Synthesis and Direct Patterning of Functional Nanostructures on Flat and Flexible Substrates towards Device Fabrication

A Thesis
Submitted for the Degree of

Doctor of Philosophy

by
B. Radha

Chemistry and Physics of Materials Unit
Jawaharlal Nehru Centre for Advanced Scientific Research
(A Deemed University)
Bangalore - 560064 (INDIA)

MARCH 2012

Dedicated to

My Parents

DECLARATION

I hereby declare that the thesis entitled *"**Synthesis and direct patterning of functional nanostructures on flat and flexible substrates towards device fabrication***"* is an authentic record of research work carried out by me at the Chemistry and Physics of Materials Unit, Jawaharlal Nehru Centre for Advanced Scientific Research, Bangalore, India under the supervision of **Professor G. U. Kulkarni** and that it has not been submitted elsewhere for the award of any degree or diploma.

In keeping with the general practice in reporting scientific observations, due acknowledgment has been made whenever the work described is based on the findings of other investigators. Any omission that might have occurred due to oversight or error in judgment is regretted.

B. Radha

CERTIFICATE

Certified that the work described in this thesis titled *"**Synthesis and direct patterning of functional nanostructures on flat and flexible substrates towards device fabrication***"* has been carried out by **B. Radha** at the Chemistry and Physics of Materials Unit, Jawaharlal Nehru Centre for Advanced Scientific Research, Bangalore, India under my supervision and that it has not been submitted elsewhere for the award of any degree or diploma.

Professor G. U. Kulkarni

(Research Supervisor)

ACKNOWLEDGEMENTS

Preface

The thesis narrates the synthesis and direct patterning of functional nanostructures on flat and flexible substrates towards device fabrication. Currently the synthesis of nanomaterials and their exploitation as device elements are two distinct activities. This thesis makes an unified approach wherein patterned synthesis of nanomaterials and their integration in devices is achieved in most straightforward ways. It is organized into four parts. **Part I** introduces the concept of nanoscale materials, their important properties and various methods which are currently in practice for patterning nanomaterials. The thesis work relies on simple metal organic complexes as single source precursors which upon thermolysis lead to desired nanomaterials with minimal carbon impurities. Two classes of molecular inks, namely metal anions complexed with tetraoctylammonium bromide (ToABr) and metal thiolates were employed. These molecular inks can innovatively be used to synthesize new nanomaterials such as anisotropic metal structures. Single crystalline Au(111) microplates obtained via simple air-thermolysis of Au anion-ToABr complex are discussed in **Part II** with an insight into the growth of the microplates**.** The presented method is a solid state route unlike conventional solution based synthesis methods, which yield much smaller plates. The obtained hexagonal and triangular microplates, although only few tens or few hundred nanometer thick, are few hundred µms wide. They can be self-supporting too. Importantly, the microplate surface is non-toxic to living cells and can enhance the fluorescence signal from fluorophores residing within the cell by an order magnitude.

The current lithography methods rely on resist action from beam sensitive polymeric species, which either remain passive or sometimes even interfere during the subsequent device processing steps. In this work, usage of conventional resists is avoided by exploiting amenability of metal organic precursors for lithographic processes. **Part III** presents the results obtained from the direct patterning of various nanomaterials on flat as well as on flexible substrates using the aforesaid simple molecular precursors as inks. The lithographic techniques namely electron beam lithography (EBL), micromolding in capillaries (MIMIC) and nanoimprint lithography (NIL) were employed to obtain micro and nanoscale patterns (often sub 100 nm) of various metals i.e., Au, Pd, Pt, Ag, Cu as well as of their alloys (AuCu), oxides (Co_3O_4, ZnO), nitrides (CoN, InN, GaN) and sulfides (Pd_4S, Ag_2S). In contrast to conventionally applying the above techniques, the direct write method involves only a single (at best two) process step with an excellent control on chemical purity and morphology of the resulting patterns. The e-resist action of the precursors originates from the extreme e-beam sensitivity of the hydrocarbon chain present in

the precursors, while direct micromolding in capillaries has been possible due to the easy flow of the precursor solution in capillaries. On the other hand for imprintability using NIL, Pd thiolate precursor was chosen which possesses a suitable melting temperature. Apart from 2D nanopatterns, hierarchically patterned 3D nanostructures were also obtained.

The seed activities of Part III have come to fruition by the fabrication of integrated nanodevices as presented in **Part IV**. Six prototype devices fabricated using functional nanostructures presented in Parts II and III. A practically useful strain gauge with high gauge factor was produced by controlled thermolysis of patterned μ-stripe grating structures to result in Pd nanocrystals distributed in residual carbon. Here, the sensing mechanism is due to the varying strength of the interparticle coupling with strain. By carrying out complete thermolysis, highly conducting Pd nanowires could be obtained on flexible substrates. Utilizing thus made nanowires, a flexible H_2 sensor sensitive down to 50 ppm, has been developed. Hierarchical metal structures described in Part III have been examined for anisotropic superhydrophobic wetting, important in microfluidic devices. Using Pd thiolate films and patterned structures, non-volatile memory devices with large on-off ratio, high endurance and high retention have been fabricated. From the Au nanocrystalline wires obtained by direct write EBL discussed in Part III, a nanoscale diode with commendable diode characteristics was obtained. Single crystalline Au microplates (discussed in Part II) have been employed as top contacting electrodes for examining electrical transport through monolayers of self-assembled molecules and a large number of vertically grown semiconductor nanowires, in capacitor geometry. **Part V** provides an outlook taking the reader beyond the thesis work. Several unexplored issues related to the thesis work as well as future directions are laid out.

TABLE OF CONTENTS

ACRONYMS

0D	Zero dimensional
1D	One dimensional
2D	Two dimensional
3D	Three dimensional
AC	Alternating current
AFM	Atomic force microscopy
AFMEN	AFM-assisted electrostatic nanolithography
C6D	Hexanedithiol
C8D	Octanedithiol
C10D	Decanedithiol
C10M	Decanemonothiol
C12M	Dodecanemonothiol
C16M	Hexadecanemonothiol
CA	Contact angle
C-AFM	Conducting atomic force microscopy
CD	Compact disc
CNTs	Carbon nanotubes
DDA	Discrete dipole approximation
DC	Direct current
DDT	Dodecanethiol
DI	Deionised
dia	Diameter
DLS	Dynamic light scattering
DNA	Deoxy-ribonucleic acid
DOF	Depth of focus
DOS	Density of states
DPN	Dip-pen nanolithography
DSC	Differential scanning calorimetry
DTT	Dithiothreitol
EBL	Electron beam lithography
ED	Electron diffraction
EDS	Energy dispersive X-ray spectroscopy
EFM	Electrostatic force microscopy
EUV	Extreme ultraviolet
EUV-IL	Extreme ultraviolet interference lithography
FA-DPN	Field assisted dip-pen nanolithography

FBS	Fetal bovine calf serum
FCC	Face centered cubic
FET	Field-effect transistor
FESEM	Field emission scanning electron microscopy
FFT	Fast fourier transform
FIB	Focused ion beam
FIBID	Focused ion beam induced deposition
F-N	Fowler-Nordheim
FOV	Field of view
FT-IR	Fourier transform infrared spectroscopy
GB	Gigabyte
HOPG	Highly oriented pyrolytic graphite
HRTEM	High resolution transmission electron micrograph
HSQ	Hydrogen silsesquioxane
IL	Interference lithography
IR	Infrared
I-V	Current-Voltage
JCPDS	Joint committee on powder diffraction standards
JV	Current density-Voltage
LAO	Local anodic oxidation
LCD	Liquid crystal display
LED	Light emitting diode
LER	Line edge roughness
LIGA	Lithography, Electroplating and Molding
LIL	Laser interface lithography (Holographic lithography)
LMCT	Ligand-to-metal charge-transfer
LPNE	Lithographically patterned nanowire electrodeposition
LTPS	Low temperature deposited polysilicon
μCP	Microcontact printing
MDNIL	Melting induced direct nanoimprint lithography
MEF	Metal-enhanced fluorescence
MEMS	Microelectromechanical systems
MESFET	Metal semiconductor field effect transistor
MIMIC	Micromolding in capillaries
μCP	Microcontact printing
μTM	Microtransfer molding
MFM	Magnetic force microscopy
MLCT	Metal-to-ligand charge-transfer
MNGP	Metal nanowire grating pattern

MOF	Metal-organic frameworks
MOSFET	Metal–oxide–semiconductor field-effect transistor
MP	Melting point
MRI	Magnetic resonance imaging
μ-stripes	Microstripes
M-Thiolates	Metal Thiolates
M-ToABr	Metal anion complexed with tetraoctyl ammonium bromide
MWNT	Multi walled carbon nanotube
NA	Numerical aperture
NAND	Not AND
NEM	Nanoentrapment molding
NEMS	Nanoelectromechanical systems
NIL	Nanoimprint lithography
NIR	Near field infrared spectroscopy
NSOM	Near field scanning optical microscopy
nTP	Nanotransfer printing
NW	Nanowire
OP	Optical profiler
OOP	Out of plane (in Raman)
PC	Polycarbonate
PDMS	Polydimethylsiloxane
PEDOT:PSS	Poly(3,4-ethylenedioxythiophene) :poly(styrenesulfonate)
PET	Polyethylene terephthalate
PL	Photoluminescence
PMMA	Poly(methyl methacrlylate)
ppm	Parts per million
PVDF	Poly vinylidene fluoride
PSI	Phase shifting interferometry
PVA	Poly vinyl alcohol
PVD	Physical vapor deposition
QD	Quantum dot
REM	Replica molding
RF	Radio frequency
RIE	Reactive ion etching
RR	Rectification ratio
RT	Room temperature
SAED	Selected area electron diffraction

SAMs	Self-assembled monolayers
SAMIM	Solvent assisted micromolding in capillaries
SAXS	Small angle X-ray scattering
SD	Secure digital
SEF	Surface enhanced fluorescence
SEM	Scanning electron microscopy
SERS	Surface enhanced Raman scattering
SFIL	Step-and-flash imprint lithography
SNAP	Superlattice nanowire pattern transfer
SP	Surface Plasmon
SPL	Scanning probe lithography
SPR	Surface plasmon resonance
STM	Scanning tunneling microscopy
STEM	Scanning transmission electron microscopy
STS	Scanning tunneling spectroscopy
SWNT	Single walled carbon nanotube
TEM	Transmission electron microscopy
TERS	Tip enhanced Raman scattering
TFT	Thin film transistor
TGA	Thermogravimetric analysis
ToA	Trioctyl amine
ToABr	Tetraoctyl ammonium bromide
TCR	Temperature coefficient of resistance
UV	Ultraviolet
UV-NIL	Ultraviolet nanoimprint lithography
UV-vis	Ultraviolet-visible
UHV	Ultra-high vacuum
VLS	Vapor-liquid-solid
VSI	Vertical scanning interferometry
VSM	Vibrating sample magnetometer
XAFS	X-ray absorption fine structure
XPS	X-ray photoelectron spectroscopy
XRD	X-ray diffraction

PART I

Introduction

I.1 ABOUT THE NANOSCALE

The dawn of nanoscience and nanotechnology is considered to be the lecture "There's plenty of room at the bottom" delivered by a visionary physicist, Richard Feynmann in 1959 [1]. Drexler elaborated this idea in his technical book *Nanosystems* [2]. Since ancient Roman times, colloidal gold has been known and was used to colour glass with intense shades of yellow, red, or mauve varying the concentration of gold. Before the name 'nano'science and technology was coined, Michael Faraday prepared colloidal Au sol and named it as a metallic divided state [3]. Nano (=dwarf in Greek) is a scale (=10^{-9}) rather than a specific discipline of science or engineering. The science of nanotechnology is basically looking at important phenomena that become apparent when one goes to very small scales. To get a feel for the nanoscale, one can take an example of a strand of human hair (~60-100 μm) width. A nanometer is ~10,000 times smaller than a single strand of hair. In simple terms, one nanometer is to a tennis ball, what a tennis ball is to the Earth. A cartoon comparison of various natural and man-made nano and micron sized systems is shown below (Figure I.1).
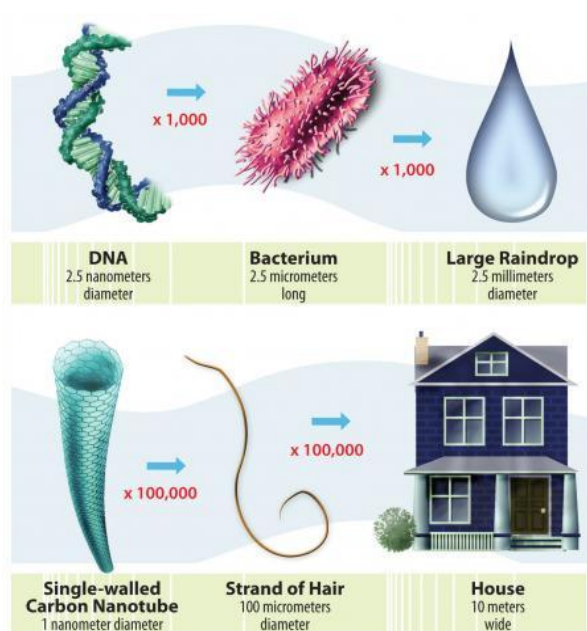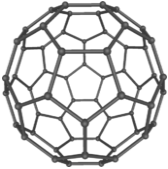
Figure I.1 Size comparison of microscopic natural, artificial and macroscopic objects [from [4]].
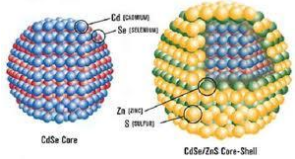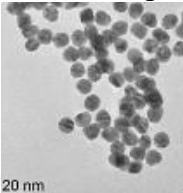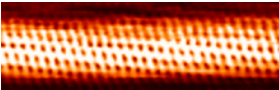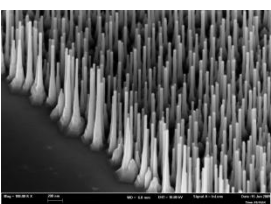
Biosystems possess many functional elements at nanodimensions. In the pioneering speech of Feynmann [5], he mentioned "*the biological example of writing information on a small scale has inspired me…a biological system can be exceedingly small. Many of the cells are very tiny, but they are very active; they manufacture various substances; they walk around; they wiggle; and they do all kinds of marvelous things-all on a very small scale. Also they store information…in DNA molecules in which approximately 50 atoms are used for one bit of information. Consider the possibility that we too can make a thing very small that does what we want-that we can manufacture an object that maneuvers at that level!*"
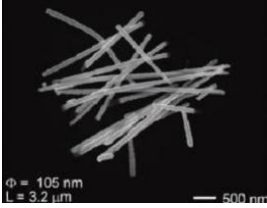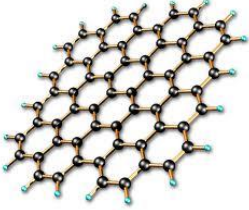
I.2 IMPORTANT NANOMATERIALS
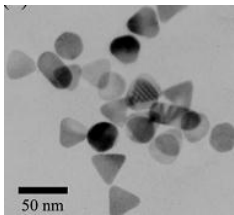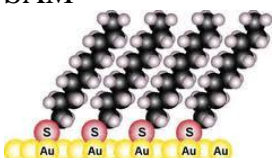
When the size of a material is reduced to a length scale typical of the interactions therein, quantum confinement of electrons sets in, leading to unusual properties that depend on the size of the system itself. Details of the quantum confinement will be described in a later section. A nanomaterial has atleast one of the dimensions in nanometric regime and depending on the number of degrees of freedom available for the bound electrons in the material, various nanomaterials are classified as 0D, 1D, 2D meaning available degrees of freedom are 0, 1 and 2 respectively. The synthetic methods for nanomaterials include bottom-up chemical and top-down physical processes and sometimes, hybrid methods as well. Any material that possesses interesting properties in the bulk state is synthesized or cast into nanomaterials of different dimensionalities and at different sizes. Examples are abounding in the recent literature - fullerenes, nanotubes and graphene, nanocrystals, nanorods, nanowires and other anisotropic structures of metals such as gold and silver, semiconductors such as ZnO etc. A number of commonly known nanomaterials are listed in Table I.1.
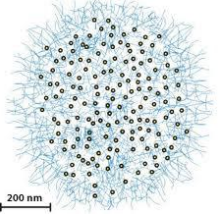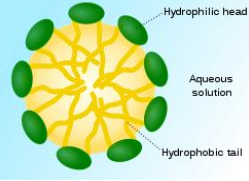
Table I.1 List of various important nanomaterials.

0D		
Fullerene	Examples	C_{60}, C_{70}, C_{50}, C_{28}
	Size	<1 nm
	Properties	Superconductivity and ferromagnetism, soft electrophile, heat resistance
	Applications	• Drug delivery • MRI contrast agents (exploiting its container properties) • Drug-delivery agents (through surface functionalization), • Fullerene-based superconductors, • Light-activated antimicrobial agents

Semiconductor nanoparticles	Examples	CdSe, CdTe, InP, InAs, PbS, PbSe, PbTe etc.
	Size	<100 nm
	Properties	Fluorescence, photoluminescence
	Applications	• Targeted tagging for medical imaging • Sensors • Lasers • LED • High density discs • Optical computing • High efficiency solar cells
Metal nanoparticles	Examples	Au, Ag, Pd, Pt, Ni etc.
	Size	<100nm
	Properties	Catalysis, SPR, Conductivity
	Applications	• Catalyst • Magnetic fluids • Diagnostics • Medical imaging and therapy • Targeted drug delivery
1D		
Carbon nanotubes	Examples	SWNT, MWNT
	Size	Few nm in diameter, length up to several cm
	Properties	Extraordinary thermal conductivity, mechanical and electrical properties Metallic to semiconducting Strongest, hardest and stiffest material
	Applications	• Additives to various structural materials • Field-effect transistors (FET) • Stab-proof and bulletproof clothing • Movable arms in upcoming nanomechanical devices • Superconductivity with a relatively high transition temperature $T_c = 12$ K • Tips for AFM • In tissue engineering, CNTs can act as scaffolding for bone growth • Paper batteries • Solar cells • Ultracapacitors
Semiconductor nanorods and nanowires	Examples	Si, ZnO, InGaN, SiC, GaN, InP etc.
	Size	Dia. 1-100nm
	Properties	Quantum confinement (strong photon, phonon, and electron confinement within the semiconductor nanowires); size dependent properties (tuning) and unique one-dimensionality
	Applications	• Electronics and photonics • Life science applications

		• Fabricating electronic, optoelectronic, electrochemical and electromechanical nanodevices • For energy conversion and storage • Interfacing nanowires with living cells • Cheaper and more efficient solar cells • Batteries • High storage capacity
Metal nanorods and nanowires	Examples	Ag, Au, Pt, Ni etc.
	Size	Dia. 1-100nm
	Properties	Aspect ratio; size dependent properties (tuning), unique one-dimensionality and lightning rod effect
	Applications	• Sensors • Nanotransistor • High sensitivity nanoelectrodes to meta-materials • High density perpendicular data storage • SERS, nanooptics and molecular electronics • Biological tags • Field emission electron emitters • Transparent conducting electrodes
2D		
Graphene	Examples	Graphene, Graphene oxide, MoS$_2$, etc
	Size	0.335-3 nm thick
	Properties	High electron mobility at room temperature Spin transport Graphene is one of the strongest, lightest and most conductive material It's 97.3 % transparent, but easily observable over SiO$_2$ substrates under optical microscopes Anti-bacterial
	Applications	• Spintronics • Single-molecule gas detection (sensors) • Graphene transistors • Graphene optical modulators • Integrated circuits • Electrochromic devices • Transparent conducting electrodes • Reference material for characterizing electroconductive and transparent materials • Thermal management and interfacial materials • Solar cells, ultracapacitors • Biodevices • Data and energy storage
Semiconductor thin films	Examples	CdTe, a-Si, CIS, CIGS, InAs, GaN etc
	Size	<100 nm thick

	Properties	Photoluminescence, band gap engineering, spin transport and high mobility
	Applications	• Solid state lighting • Solar cells • Transistors, diodes, memory devices • Electrochromic devices
Metal thin films	Examples	Au, Ag, Cu, Ni etc
	Size	<100 nm thick
	Properties	Conductivity Optics Different defect structures from bulk Strongly influenced by surface and interface effects Magnetic properties
	Applications	• Heads-up displays for military aircraft • Audio visual projection systems for film and TV • Telescope mirror surfacing, anti-refective coatings • Optoelectronic devices, Infrared systems, medical equipment • Periscopes range finders and conductive coatings • Gas sensors • Microelectronics - electrical conductors, electrical barriers, diffusion barriers • STM substrates
Metal nanoplates/sheets	Examples	Au, Ag, Ni, Co etc.
	Size	Several microns wide with <100 nm thickness
	Properties	Localized surface plasmon resonance (SPR) Metal-enhanced fluorescence Au: Excellent biocompatibility and nontoxicity
	Applications	• TERS, SERS • Au: Photonics, optical sensing, biological labeling, and near-IR light absorbing, cancer hyperthermia
Molecules as nanomaterials		
SAM	Examples	Aliphatic and aromatic thiols, amines, dithiocarbamates etc.
	Size	Few nms
	Properties	Flexibility with respect to the terminal functionalities of the organic molecules allows the control of the hydrophobicity or hydrophilicity of metal surface i.e., surface functionalisation
	Applications	• Nanoelectronic devices, sensor arrays, supercapacitors, catalysts, lubricants

		• SAM on metal: chemical sensing, control of surface properties like wettability and friction, corrosion protection, patterning, semiconductor passivation, and optical second harmonic generation • Molecular engineering (switching, gating, rectification, amplification etc) • Biosensors and molecular recognition • Electrochemistry, electronics, nanoelectromechanical systems (NEMS) and microelectromechanical systems (MEMS) • SAMs are invaluable substrates in bioanalytical, organometallic, physical organic, bioorganic and electrochemistry • SAM modified surfaces are highly useful for investigating several fundamental phenomena or observation of molecular events such as coulomb staircase, single electron transfer etc., on artificially designed nanostructures
Polymer nanoparticles 200 nm	Examples	Poly(N-isopropylacrylamide), polystyrene, polymethylmethacrylate, polydimethylsiloxane, Chitosan, Gelatin, Sodium alginate, Albumin etc.
	Size	Few hundred nms
	Properties	Easy to process, reversible deformation, don't break easily, thermo-sensitive, conductivity (can be tunable using methods of synthesis), antistatic materials, better dispersability, biodegradable.
	Applications	• Corrosion Inhibitors • Compact capacitors • Anti-static coatings • Smart windows • Light weight batteries • Solar cells • Drug delivery vesicles • In drug targeting to particular organs/tissues, as carriers of DNA in gene therapy, and in their ability to deliver proteins, peptides and genes through an oral route of administration.
Micelles	Examples	Dodecylphosphocholine, Epirubicin, poly(L-histidine) etc.
	Size	Few tens to hundred nms
	Properties	Emulsification, wetting, pH sensitive
	Applications	• Detergents • Antibiotics • Targeted drug delivery

I.3 NANOMATERIALS: HOW ARE THEY DIFFERENT FROM BULK?

'Nano' has assumed importance as the materials of nanosize reveal unique size-dependent properties due to mainly, large surface area to volume ratio and quantum confinement. As compared to the surface area available with a non-porous bulk cube, nanosized cubes of the same mass from the same material offer surface area which may be few thousand times of the former (Figure I.2 inset). The fraction of atoms on the surface of the particle (P_s, percentage) can be estimated using the simple relation,

$$P_s = 4N^{-1/3} \times 100$$

where N is the total number of atoms in the particle. The variation of the surface fraction of atoms with the number of atoms is shown in Figure I.2. The fraction of surface atoms becomes less than 1% only when the total number of atoms is of the order of 10^7, which for a typical metal would correspond to a particle diameter of 150 nm [6]. Thus, nanosize brings enormous amount of surface area and increased reactivity for a material, important in heterogenous catalysis.
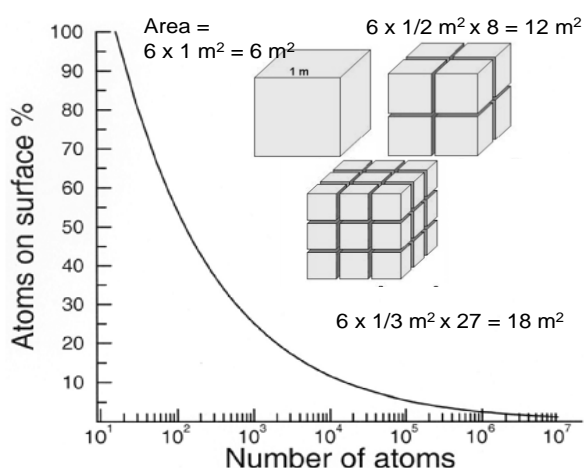
Figure I.2. Plot of the number of atoms vs. the percentage of atoms located on the surface of a particle (from [7]). The calculation of the percentage of atoms is made on the basis of the above equation and is valid for metal particles.

Nanosize regime can be considered as a staircase with atoms at the bottom of the architecture and the bulk at the top. This size evolution is shown in Figure I.3. Atoms possess orbitals, which depending on the overlap remain unperturbed (as in noble gases) or they combine to extended band structures (as in metals or semiconductors). Each atom contributes electronic states to a band so that the width of a band increases slightly when more atoms are added, but importantly the density of states (DOS) within a band increases proportionally with the number of contributing atoms. The band width amounts typically to a few eV.

The DOS scales smoothly with size, but with a scaling law that is different from that found for surface effects. To a first approximation it can be described by the 'particle in a box' model in which the size of the box is nothing but the size of the particle. A threshold is reached when the gap between the highest occupied and the lowest unoccupied state (called the Kubo gap δ) equals thermal energy. When electrons get thermally excited across the Kubo gap, a low temperature insulator becomes a semiconductor and at higher temperatures a metal.
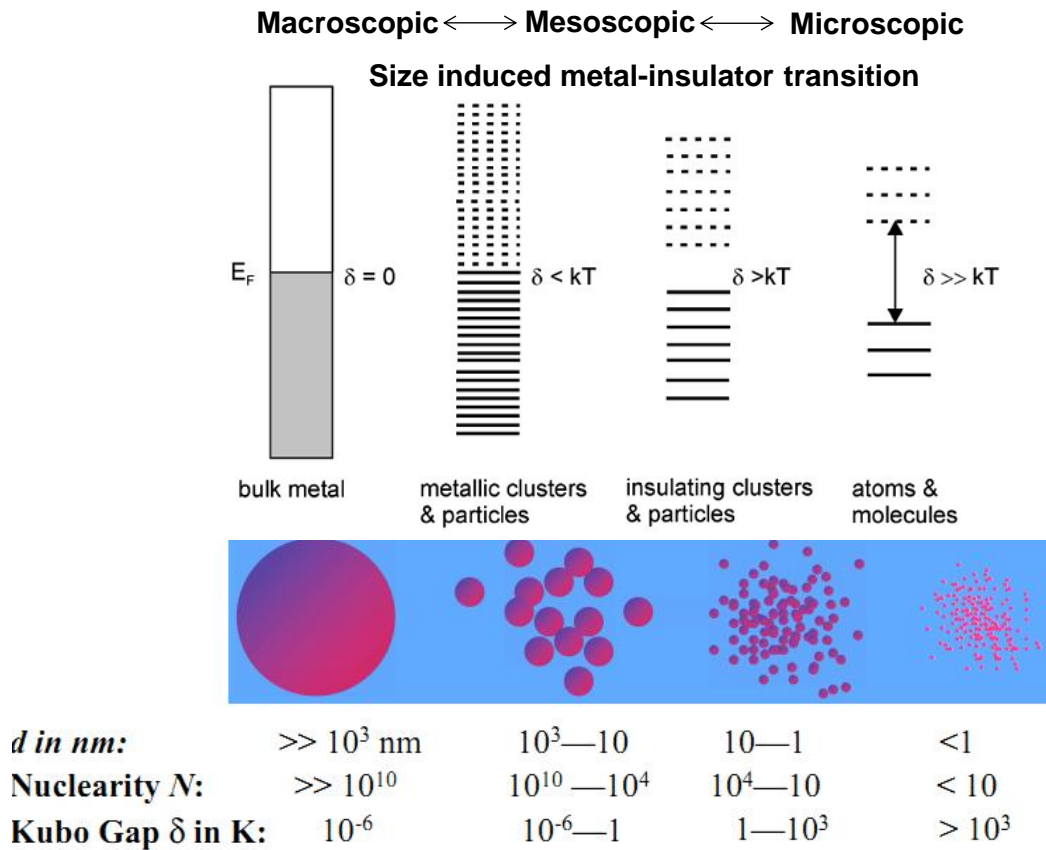
Figure I.3 Evolution of the band gap and the density of states as the number of atoms in a system increases (from right to left) (from [8]).

Thus, the Kubo gap δ, is the average spacing between consecutive energy levels, usually measured in terms of meV. The magnitude of δ varies inversely with nuclearity (the number of atoms). As the Kubo gap increases, there is a decrease in the DOS at the Fermi level. The discreteness of energy levels do not physically manifest themselves as long as the gap is less than kT, the thermal energy at temperature T. Kubo gap, is given by the equation,

$$\delta = \frac{4E_F}{3n_e}$$

where, E_F is the fermi level and n_e is the number of valence electrons.

The size effect on the band gap, discretization of quantum levels and the variation of density of states for various dimensions of the nanomaterials occurs when the physical dimensions of a solid become comparable to the mean free path of the electrons in it, i.e., when the electrons begin to feel confined. A schematic diagram of the density of states of a solid with electrons confined to one, two and three dimensions, named as 2D, 1D and 0D materials respectively, is illustrated in Figure I.4.
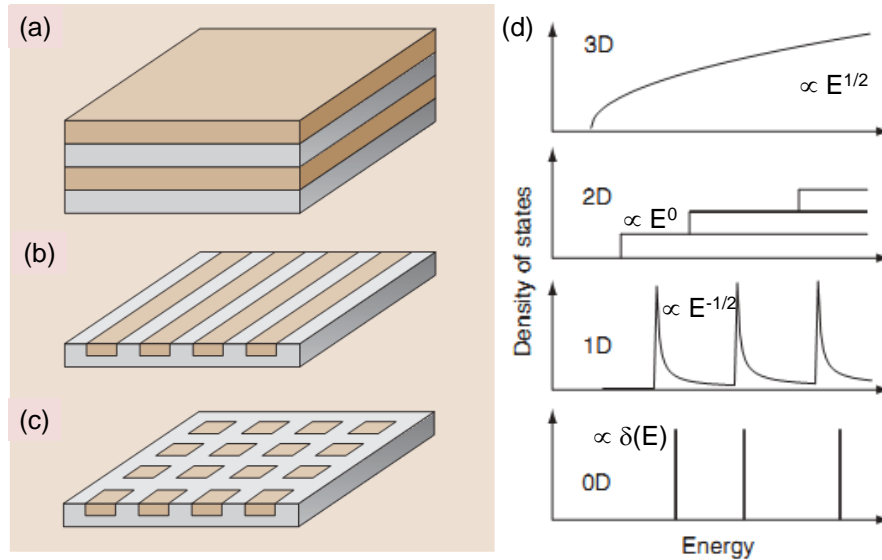
Figure I.4 The electronic density of states for a bulk semiconductor (3D), a quantum well (2D), a quantum wire (1D) and a quantum dot (0D) (from [9],[10]).

The presence of energy band gap and quantum confinement in a semiconductor can pose an interesting scenario. Quantum confinement in semiconductor nanocrystals, walks in only below a size regime, decided by the Bohr exciton radius. Here, the valence band is filled and the conduction band is completely empty at 0 K. The bands are separated with a specific energy gap, E_g. When an electron gets excited due to thermal excitations, an electron–hole pair is created. The electron in the conduction band and the hole in the valence band can be bound when they approach each other at a finite distance. The bound pair is called an 'exciton', which is delocalized throughout the crystal. An exciton Bohr radius is the distance in an electron-hole pair (Figure I.5). When a nanocrystal size is less than or of the same order as the exciton Bohr radius, quantum confinement effects are seen. For example, the exciton Bohr radius of CdSe is 5.6 nm. The mathematical relation of exciton Bohr radius is given as follows.

$$a_{exciton} = \frac{a_0 \varepsilon}{m^*/m_e}$$

where m^* is the effective mass, ε is the permittivity of the material and a_0 is the Bohr radius.
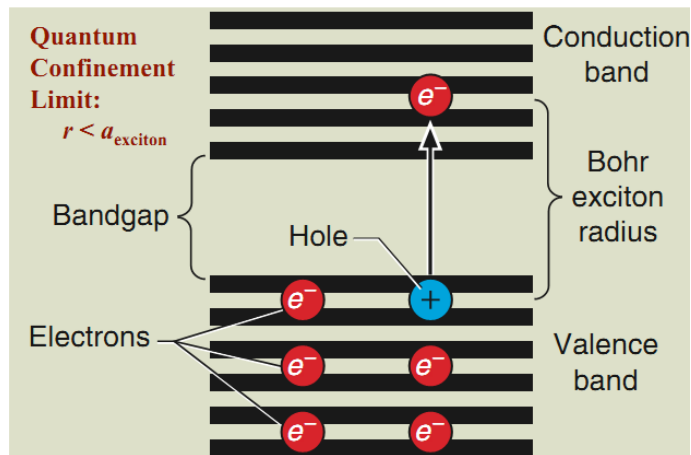
Figure I.5 Illustration of exciton pair (from [11]).

Due to the quantum confinement and surface effects, nanomaterials exhibit many interesting size-dependent properties. The change in a material property as a function of size is shown schematically in Figure I.6. At small sizes, the properties vary irregularly and are specific to each size. At larger sizes, dependence on size is smooth and scaling laws can be derived to describe the variation in this regime. The size-dependent properties of nanoparticles include electronic, optical, magnetic, and chemical characteristics. A few are dealt with in the forthcoming sections.
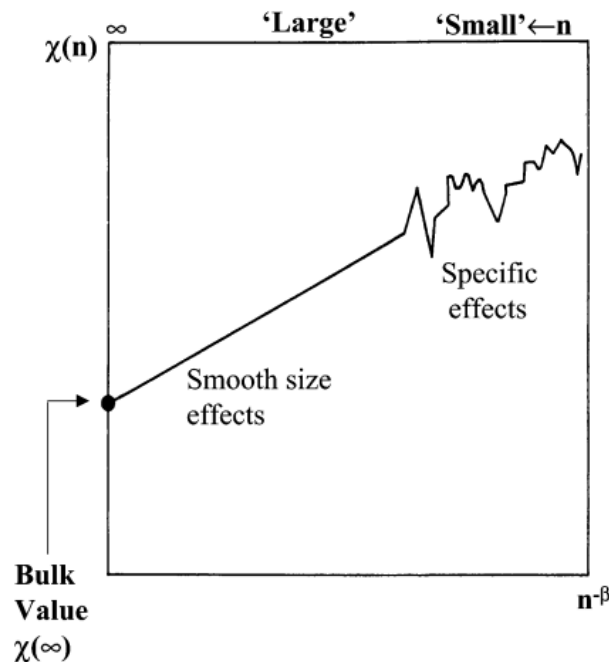
Figure I.6 The size dependence of a property $\chi(n)$ on the number of atoms (n) in a nanoparticle. The data are plotted against $n^{-\beta}$ where $\beta \geq 0$. Small nanoparticles reveal specific size effects, while larger particles are expected to exhibit a smooth size dependence, converging to the bulk value (from [7]).

I.4 SIZE-DEPENDENT PROPERTIES

I.4.1 Thermal properties – Melting point

Atoms at the surface have fewer direct neighbours than atoms in the bulk. Therefore, particles with a large fraction of atoms at the surface have a low mean coordination number (which is the number of nearest neighbours). The lower stabilisation of atoms or molecules at the surface leads the lower melting point of surface layers (Figure I.7). Ice, for example, is covered by a liquid-like layer down to below -10 °C. This, besides the pressure exerted by the weight of the skater on the sharp edge of his skates, is another factor that facilitates skating. Furthermore, this has been known since 1871 when W. Thomson [12] described that the melting point scales inversely with the radius of a particle according to equation,

$$\frac{T_m - T^*{}_m}{T^*{}_m} = \frac{\Delta T_m}{T^*{}_m} = \frac{2V_m(l)\gamma_{sl}}{\Delta H_m r}$$

which is known today as the Gibbs–Thomson equation. In this equation T_m is the melting point of the cluster with radius r, T_m* that of the bulk, $V_m(\ell)$ the molar volume of the liquid, γ_{sl}, the interfacial tension between the solid and the liquid surface layer, and ΔH_m the bulk latent heat of melting.
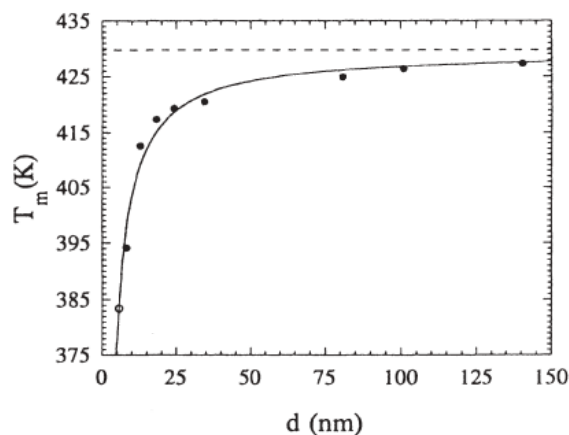
Figure I.7 Melting temperature as a function of particle diameter. The broken line represents the bulk melting point (from [13]).

I.4.2 Optical properties

The 'nanomaterials' color usually differs from that of the bulk counterpart and is vividly evident. The fascinating colors of metal nanoparticles have been utilized in many cathedrals for decorating glass windows (stained glass windows) in Europe [14]. The light absorption in metal nanoparticles instigates from an interesting phenomenon called localized surface plasmon resonance. According to the Drude–Lorentz model, the atoms in metals exist in a plasma state, having a core of positively charged nuclei surrounded by a pool of

negatively charged electrons and hence named as 'plasma electrons' [15]. In the presence of an electromagnetic radiation, the electric vector displaces the free electrons and the columbic electrostatic attraction of the nuclei will restore the electrons to the original position. This sets up an oscillating nature due to the electric field of light, and the electron cloud coherently oscillates over the surface with a resonance frequency 'ω_p'. A resonance condition is established when the frequency of this oscillation matches with that of the incident radiation; this results in an intense absorption, termed as 'surface plasmon resonance (SPR)' absorption (Figure I.8). In a nanoparticle, since the electron cloud is confined to a finite volume which is smaller than the wavelength of light, the frequency of oscillation of metal nanoparticles is determined mainly by four parameters: number density of electrons, effective mass of the electron and the size and shape distribution of the charge. This allows the tuning of the optical properties of noble metal nanoparticles by varying the size, shape and dielectric environment. Typically, the surface plasmon band for spherical Au nanoparticles having diameter of ~20 nm is observed at around ~520 nm [16].   On increasing the diameter of the Au nanoparticle from 20 to 80 nm, SPR band shifts from 520 to 550 nm which is attributed to the electromagnetic hindrance and varying dielectric function with size. The dependence of the nanoparticle diameter on the maximum of plasmon resonance band was theoretically calculated by adopting Mie theory and discrete dipole approximation method [17].
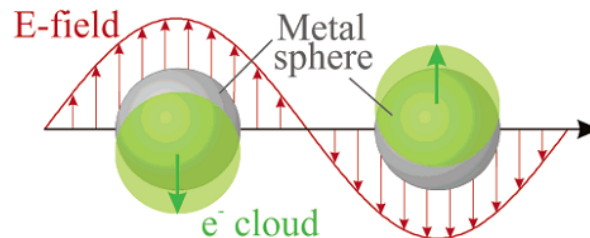
Figure I.8 Schematic of plasmon oscillation for a sphere, showing the displacement of the conduction electron charge cloud relative to the nuclei (from [15]) .

As the shape of the nanoparticle changes, the surface electron density and hence the electric field on the surface varies [17]. For example, nanorods of Au and Ag split the dipolar resonance into two surface plasmon bands wherein the induced dipole oscillates along the transverse and longitudinal axes [18]. The longitudinal surface plasmon band shifts to longer wavelengths with increase in the aspect ratio, while the position of transverse surface plasmon band remains more or less unaffected (Figure I.9). Nanoplates and prisms

possess different plasmon modes, in terms of in plane and out-of-plane dipolar as well as quadrupolar resonances.
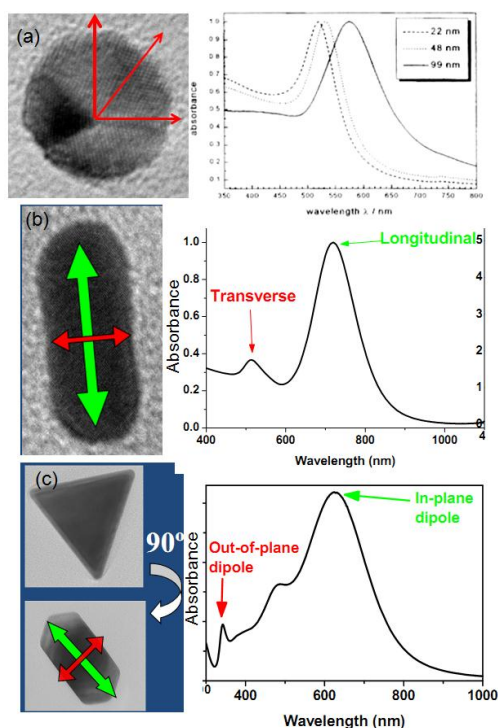
Figure I.9 Plasmon modes in spherical and anisotropic nanoparticles (from [19]).

In a semiconductor nanoparticle, quantum confinement of both the electron and hole in all three dimensions leads to an increase in the effective band gap with decreasing crystallite size. Consequently, both the optical absorption and emission of quantum dots shift to the blue (higher energies) as the size of the dots gets smaller. This has been illustrated using the well-known example of CdSe quantum dots (Figure I.10).
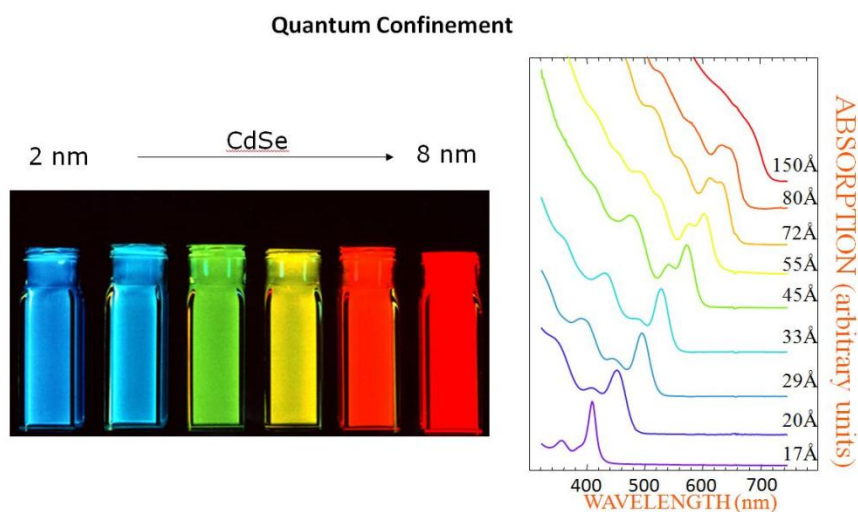
Figure I.10 Left: fluorescence image of CdSe QDs as a function of size. Right: absorbance spectrum as a function of size (from [20]).

Optical properties of nanostructures can be exploited in applications. For instance, in surface enhanced Raman scattering (SERS), the enhanced electric fields (E) of a plasmonic nanostructure can increase the Raman scattering of molecules in their vicinity by a factor of E^4 [21]. Measured enhancements range from 10^4 to 10^{15}, and even single molecules have been detected [22]. SERS is a sensitive technique and provides the unique vibrational spectrum of a molecule, a Raman fingerprint, and does not require labels or other markers. The enormous enhancement in SERS can be attributed to two mechanisms [23]. The first is a result of electromagnetic enhancement that arises due to the localized SP resonance modes, which can focus light into nanosized volumes, drastically increasing the E-field intensity near the nanoparticle. The second is chemical enhancement, which is thought to arise from interactions between the molecule and the nanoparticle as a result of changes to the molecular electronic states. This leads to resonant enhancement from molecular excitations or charge transfers between the molecule and the nanoparticle. The electromagnetic mechanism is typically thought to contribute most of the enhancement (10^5-10^8), and the chemical enhancement contributes much less (10-10^3) [24].

Another important application of the optical property of the nanostructures is to enhance the emission of resonant molecules in the vicinity of a plasmonic nanostructure through a process known as surface enhanced fluorescence (SEF) [25]. SEF occurs primarily as a result of the interactions between the excited state of a fluorophore with the near-fields of an excited metal nanostructure, increasing the optical excitation rate and the decay rate (both radiative and nonradiative) for the molecule [26]. Plasmonic nanostructures can increase the emission intensity and the enhancement factors can vary from 2 to 1000.

I.4.3 Electrical properties

As discussed in section I.3, there is an emergence of Kubo gap in a nanosystem. This leads to a size-induced metal-insulator transition when the diameter of a metal nanoparticle is less than a few nanometers. Scanning tunneling spectroscopy (STS) measurements of various metal nanoparticles have shown that the dimensions ~1 nm^3 display a definitive band gap (~ 70 meV) that decreases as the volume of the nanoparticle increases. The effect of the Kubo gap will not be apparent at room temperature, because the thermal energy is greater than this energy gap. In this case, the nanoparticles have metallic conductivity. If the thermal energy is less than the Kubo gap, the nanoparticle conductivity should be like an insulator. Thus, in a nutshell, a metal-insulator transition can be expected to occur when the Kubo gap, becomes comparable to kT. For example, Nb behaves as a bulk superconductor

with a normal metallic phase. For Nb nanoparticles with sizes in between 28 nm and 11 nm, the superconductivity decreases and the normal state resistivity increases with a reduction in size. Below 8 nm, superconductivity no longer exists and there is a size-dependent metal-insulator transition. A case of metal-insulator transition observed for Au cluster arrays capped with a monolayer of dodecanethiol (DDT) at low temperatures is illustrated in Figure I.11.
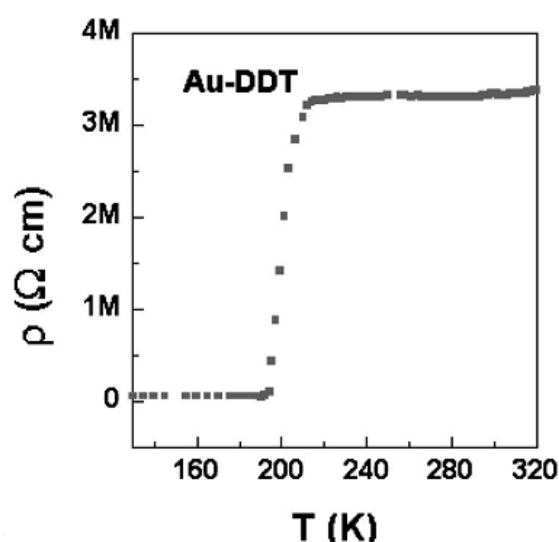
Figure I.11 Temperature dependence of resistivity (ρ) of Au metal clusters (from [27]).

Nanoparticles possess coulombic energy states which become evident during charging and discharging events. Nanocrystals possess charging energies (U) of the order of hundreds of millielectron volts, due to which charge transport would be dominated by a hopping mechanism in ensembles of nanocrystals. Au and Pd nanocrystals exhibit nonmetallic behavior (measurement was done of pellets of nanocrystals) with specific conductivities in the range of 10^6 Ω^{-1}cm^{-1} [28]. The conductivity, however, increases intensely with an increase in the diameter of the nanocrystals [29]. An insulator metal transition has been reported from pellets made of ~12.5 nm Au and Ag nanocrystals [27]. Two-dimensional arrays of metal nanocrystals have been electrically studied and the *in situ* replacement of alkanethiol with aromatic thiol increased the conductivity [30]. Interparticle spacing is an important parameter for varying the interaction energy of nanocrystals in such organizations, which in turn can be varied by changing the either by the spacer length or by applying pressure in a Langmuir-Blodgett trough while forming the array [31]. The capacitance (C) of a nanoparticle is size dependent and is related to U by

$$C = \frac{U}{2e}$$

The classical expression for the capacitance of a metal sphere (of radius R) embedded in a dielectric with a dielectric constant, ϵ_m is

$$C = 4\pi\epsilon\epsilon_m R$$

Both these equations yield capacitances of the order of 10^{-18} F (or 1 aF) for nanoparticles. In this regime of finite charging energies and low capacitances, the charging of a capacitor is no longer continuous, but is discrete. For a current to flow through a nanocrystal, an external voltage V_{ext} exceeding e/2C is required. This phenomenon of current exclusion across zero bias is called Coulomb blockade. The barrier can be overcome by applying sufficient voltage where electrons can tunnel in and out of the nanocrystal almost immediately. A continuous one electron current, I given by I =e/2RC flows through the circuit. For an additional electron to go through the nanocrystal, a voltage increase of e/C is required. This leads to steps in the IV spectra of nanocrystals which is known as Coulomb staircase [32]. A schematic illustration and an experimental observation of a Coulomb staircase observed in the IV spectra is given in Figure I.12. While Coulomb blockade is usually observed, the Coulomb staircase requires a tuning of the circuit characteristics of nanocluster. It has been proposed that, by using nanocrystals, single electron devices such as memory devices and ultrasensitive electrometers could be fabricated [33].
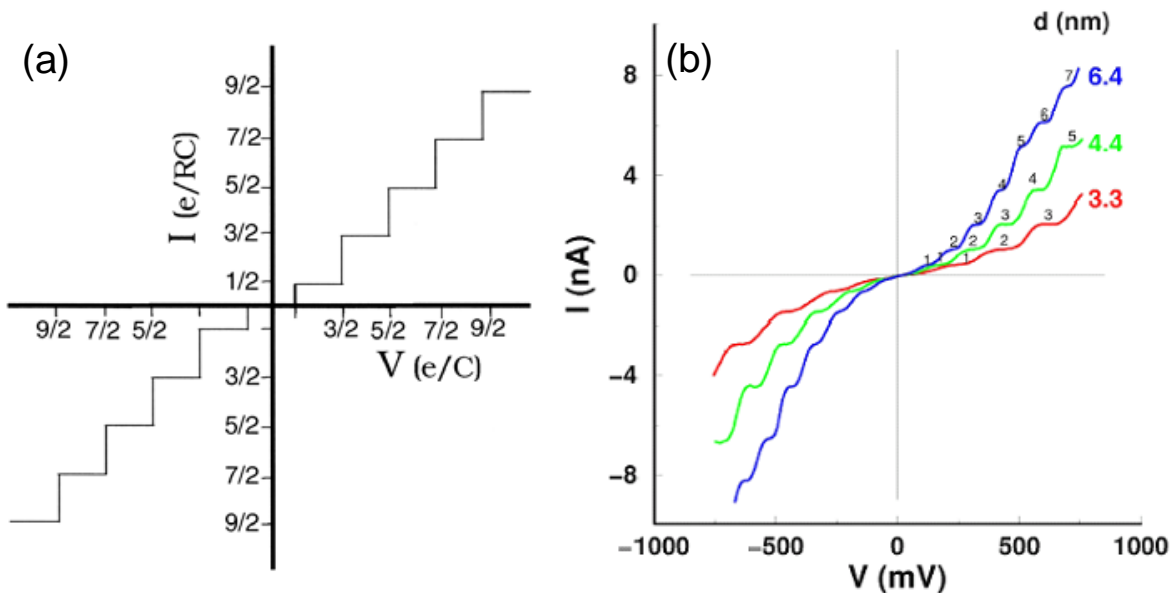
Figure I.12 (a) Schematic illustration of the Coulomb staircase behavior (from [34]), (b) I-V spectra of Pd nanocrystals of different sizes exhibiting Coulomb staircase phenomena (U ~ 100 meV) (from [35]).

1.4.4 Magnetic properties

Magnetic transitions are often observed when the particle size reduces below a certain size, since the surface energy provides a sufficient energy for domains to spontaneously switch polarization directions. For instance, ferromagnetic particles become unstable and become paramagnetic [36]. However, nanoparticle sized ferromagnetic turned to paramagnetic behaves differently from the conventional paramagnetic and is referred to as superparamagnetic. The coercivity (i.e., the intensity of the applied magnetic field required to reduce the magnetization of that material to zero after the magnetization of the sample has been driven to saturation) of a magnetic particle strongly depends on its size. Thus, if the particle is large; it supports multidomain structure, magnetization reversal occurs through a domain walls motion and thus the coercivity is low [37]. In a single-domain particle the change of direction of magnetization can occur only by coherent rotation of spins, which results in a higher coercivity compared to that of multi-domain particles (Figure I.13). When the size of the particle is reduced further, the coercivity falls off due to progressively increasing thermal fluctuations and thus leads to superparamagnetism. Thus, superparamagnetic nanoparticles rapidly respond to an applied magnetic field but exhibit negligible residual magnetism and coercivity. These features make superparamagnetic nanoparticles very attractive for a wide range of applications [38]. Self-assembly for forming large complex nanoparticle structures provides an attractive strategy to controllably increase magnetization while retaining superparamagnetic characteristics. For instance Fe_3O_4 nanoparticle arrays have been realized [39].
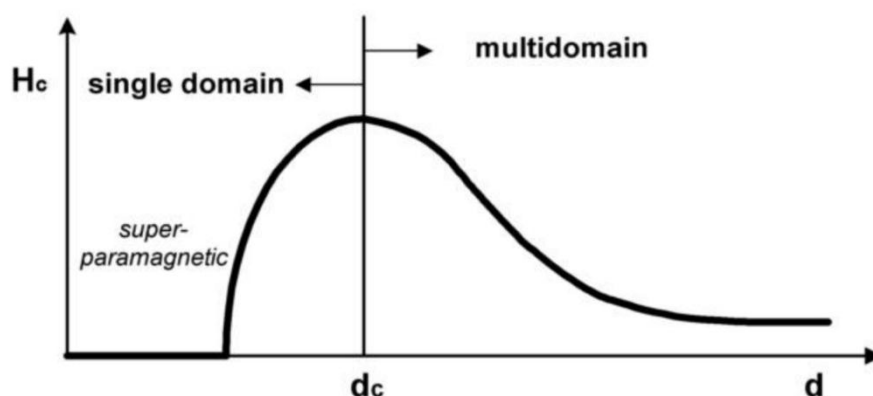
Figure I.13 Particle coercivity H_c versus size, d. The largest coercivity is observed at the particle size d_c corresponding to the transition from multidomain to single-domain structure (from [40]).

I.5 NANOMATERIALS – FROM PROPERTIES TO APPLICATIONS

In contrast to simply establishing the valuable properties of various nanostructures as has been done in the past, the main goal in the present era of nanoscience, is to realize the device applications tailor controlled for the specific purpose. To use a nanomaterial for its fascinating properties, it has to be patterned and placed in a device layout and addressed. This calls for a paradigm shift from the conventional approaches of present day fabrication.

In many of the common day to day devices, important functional materials find their place, where each material is addressed by a set of electrodes. This is all at the tens of micrometer scale. Few examples are listed in Figure I.14. A pixelated display in touch screen of a cell phone consists of Si transistors. An ink-jet printer cartridge consists of patterned heater elements to guide the printing of ink droplets. In a television liquid crystal display (LCD), liquid crystal molecules' response to an applied electric field is made use of through patterned pixel arrays. There are many lithography techniques which enable such device fabrication. Below is a brief survey of commonly used conventional lithography techniques.
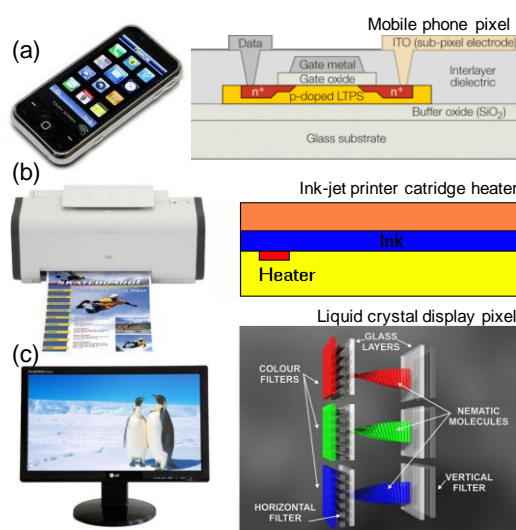
Figure I.14 (a) A mobile phone pixel of the display consists of a thin film transistor (TFT) made up of low temperature deposited polysilicon (LTPS) (from [41]. (b) Aschematic of a ink-jet printers cartridge (from [42]). (c) A LCD internal pixel structures with liquid crystalline molecules sandwiched between electrodes (from [43]).

I.6 MICROLITHOGRAPHY – PUSHED TO NANOSCALE

The process of patterning a material is called lithography (in latin, litho = stone, graphein = writing) i.e., transferring geometric shapes on a mask to the surface of a desired substrate [44]. This can be done using photons, electrons, ions or even sharp tips. Based on the source employed, various lithography techniques have emerged, which will be discussed below.

I.6.1 Photolithography

Photolithography is an optical means for transferring patterns onto a wafer. It draws parallelism with the well-known photography process, which was invented in 1826 by Joseph Nicephore Niepce [45]. Almost 100 years later, Louis Minsk developed the synthetic photosensitive polymer, polyvinylcinnamate, the first negative photoresist. Later on, so many organic materials have been discovered which act as resists. The resists are generally classified as positive or negative resists depending on the solubility of exposed area in a developer. In a positive resist, molecular weights of exposed region are decreased by polymer chain scission and the exposed area is dissolved much faster during development. In a negative resist, crossliking occurs during exposure, making exposed region much less soluble in a developer.

In the first step, the wafers are chemically cleaned to remove particulate matter on the surface as well as any traces of organic, ionic, and metallic impurities. There are various recipes established for cleaning surfaces of Si, glass and other substrates. Typically, 2-5 min. soak in acetone, methanol, double distilled deionised (DI) water with ultrasonic agitation is followed in series. For drying, spin-rinse dry for wafers or nitrogen blow-off dry for small substrates can be employed. Substrate or wafer is kept on a rotated chuck by vacuum and resist is applied by spin coating (Figure I.15). Typically 3000-6000 rpm for 15-60 sec. Resist thickness depends on resist viscosity and spinning velocity. Most resists are 1-2 micron thick (SU-8 up to 200 micron). Pre bake is done in an oven or hot plate to evaporate the solvent from the resist after spin coating. Hot plate is usually preferred as it is faster, controllable and does not trap solvent like in oven. Prebaking improves adhesion, uniformity, etch resistance, line-width control and light absorbance characteristics of photoresist.
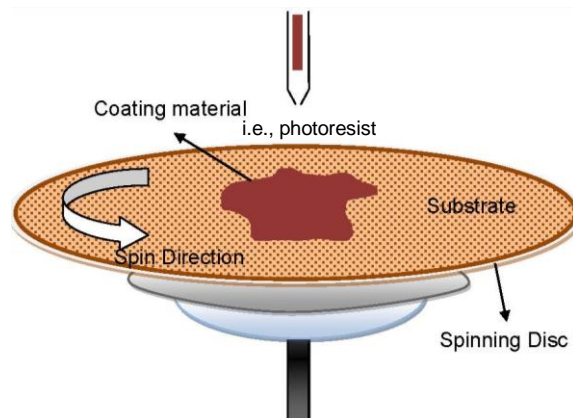
Figure I.15 Spincoating process of a photoresist (from [46]).

Next step is the mask alignment, which is one of the most important steps in the photolithography process. A photomask is generally a quartz plate with a patterned metal film on top. Quartz i.e., hard mask is expensive and fragile; it is generally used for fine features. For patterning features >50 µm size, soft masks i.e., polyethylene terephthalate (PET) sheets printed with black ink lines can be used. The mask is aligned with the wafer, so that the pattern can be transferred onto the wafer surface. For multiple patterning, every time mask must be aligned to the previous pattern. Once the mask has been accurately aligned with the pattern on the wafer's surface, the photoresist is exposed through the pattern on the mask with a high intensity ultraviolet light. There are three primary exposure methods: contact, proximity, and projection. They are shown in Figure I.16.

	Contact	Proximity	Projection
Resolution(µ)	0.1-1	2-4	0.1-1
Image quality	best	poor	good
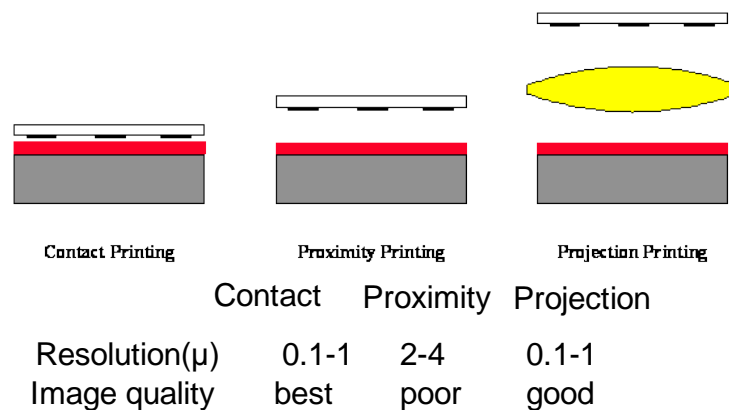
Figure I.16 Methods of exposure of UV light in photolithography (from [47]). Lithographic printing in semiconductor manufacturing has progressed from contact printing (in the early 1960s) to projection printing (from the mid 1970s to today).

In contact printing, the resist coated wafer is brought into physical contact with the photomask. The wafer is held on a vacuum chuck, and the whole assembly raised until the wafer and mask contact each other. The photoresist is exposed with UV light while the wafer is in contact position with the mask. Because of the contact between the resist and mask, very high resolution is possible in contact printing. The problem with contact printing is that debris, trapped between the resist and the mask, can damage the mask and cause defects in the pattern. The proximity exposure method is similar to contact printing except that a small gap, 10 to 25 microns wide, is maintained between the wafer and the mask during exposure. This gap minimizes (but may not eliminate) mask damage. Approximately 2 to 4 micron resolution is possible with proximity printing. Projection printing, avoids mask damage entirely. An image of the patterns on the mask is projected onto the resist-coated wafer, which is many centimeters away. Only a small portion of the mask is imaged. This small image field is scanned or stepped over the surface of the wafer. Projection printers that step

the mask image over the wafer surface are called step-and-repeat systems, which are capable of approximately 1 μm resolution.

Each commercial photoresist has its recommended developer, a chemical that dissolves exposed/unexposed areas of the photoresist. The tone of a resist i.e., positive or negative, decides the behavior of the resist in developer (Figure I.17a). The response curves for negative and positive resist after exposure and development are shown in Figure I.17b. At low-exposure energies, the negative resist remains completely soluble in the developer solution. As the exposure is increased above a threshold energy E_T, more of the resist film remains after development. At exposures two or three times the threshold energy, very little of the resist film is dissolved. For positive resists, the resist solubility in its developer is finite even at zero-exposure energy. The solubility gradually increases until, at some threshold, it becomes completely soluble. These curves are affected by all the resist processing variables: initial resist thickness, prebake conditions, developer chemistry, developing time, and others.
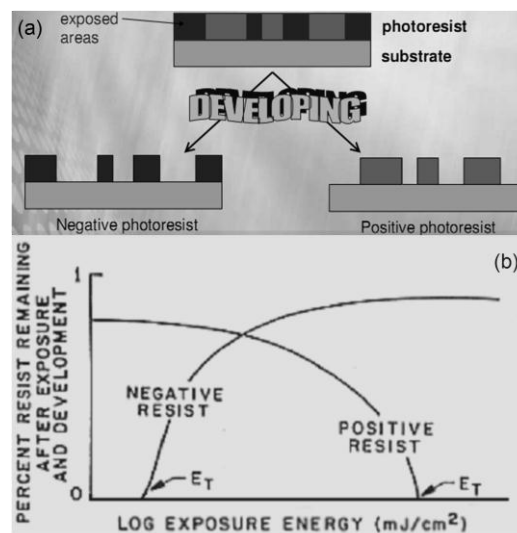
Figure I.17 Development process and typical dose response curves (from [48]).

Hard baking is necessary in order to harden the photoresist and improve adhesion of the photoresist to the wafer surface. In this step, photoresist will undergo plastic flow with sufficient time and temperature. It also removes any residuals of the coating solvent and developer. In order to transfer the pattern from the photoresist to the desired material, either the material is coated as a thin-film by deposition or the substrate coated with material is used for photolithography process. In the former case, lift off is performed to remove the photoresist from the undesired areas. In the latter case, etching is done to remove the exposed material. This is illustrated in Figure I.18.

The final step of the process is the photoresist stripping i.e., removal. Simple solvents are generally sufficient for this purpose. The patterned wafer is mildly sonicated in solvents such as acetone, trichloroethylene (for positive photoresist) or methyl ethyl ketone, methyl isobutyl ketone (for negative photoresist). Some photoresists (for ex., SU-8) are very hard to remove and thus can be as parts of a final device.
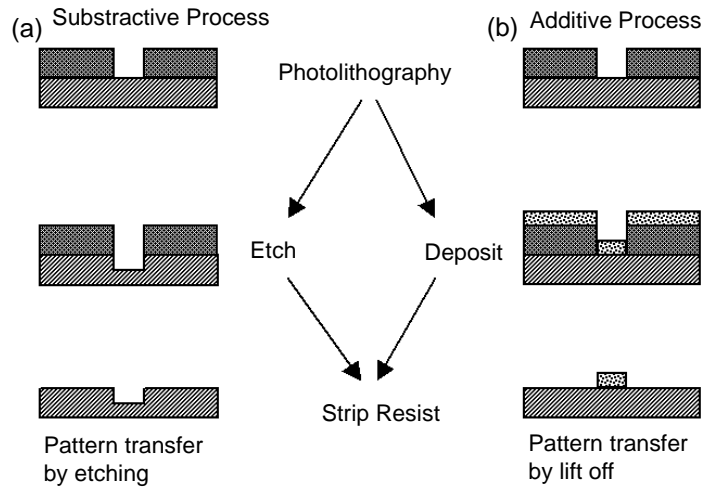
Figure I.18 (a) Pattern transfer from patterned photoresist to underlying layer by etching (b) Pattern transfer from patterned photoresist to overlying layer by lift-off (from [49]).

Photolithography Resolution

Resolution is limited by the diffraction of the light used for exposure. In the case of contact and proximity photolithography

$$2b_{min} = 3\sqrt{\lambda\left(s + \frac{t}{2}\right)}$$

where b_{min} is minimum feature size; λ, wavelength; s, mask-photoresist spacing; t, photoresist thickness and in projection lithography,

$$2b_{min} = \frac{k_1\lambda}{NA}$$

k_1 is a coefficient that encapsulates process related factors, and typically equals 0.4 for production. NA is numerical aperture. The depth of focus (DOF) is also a concern in the process, which is given by

$$DOF = \pm\frac{k_2\lambda}{(NA)^2}$$

Here, k_2 is another process related coefficient. The depth of focus restricts the thickness of the photoresist and the depth of the topography on the wafer. Thus, a balance between DOF and $2b_{min}$ is sought after.

To overcome the diffraction limit and achieve the highest resolution, the exposure system can use:

- shorter wavelengths of light (ArF excimer laser at 193 nm, Hg-vapors lamp, Xe-lamp) (Figure I.19)

- high numerical aperture lenses to project the light (immersion lithography)
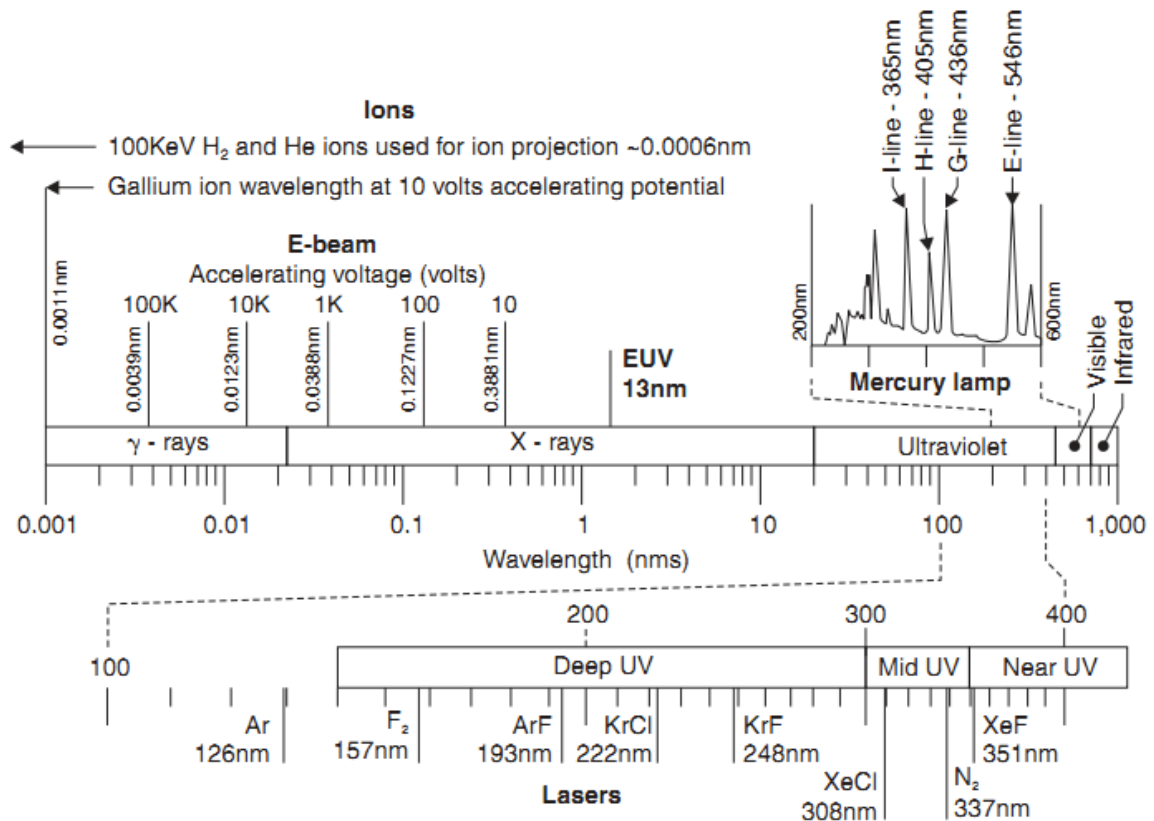
Figure I.19 Exposure sources and wavelengths (from [50]).

The process of photolithography is a vital step in chip manufacturing by industries (Figure I.20). Currently, the optical shrink or die shrink has advanced up to 22 nm half-node in 2011, as predicted by International Technology Roadmap for Semiconductors [51]. 'Optical shrink' refers to a simple scaling of semiconductor devices, mainly transistors. The act of shrinking a die is to create a somewhat identical circuitry using advanced fabrication process, usually involving an advance of lithographic node (i.e., process). This reduces overall costs of a chip company allowing more processors to be manufactured on the same piece of silicon wafer, resulting in greater revenue per product sold.

In order to achieve minimum feature sizes, lower wavelengths i.e., deep UV, extreme UV, even X-rays have been employed as photon source. Each of these lithography processes

comes with pros and cons. The optics become complicated and the set of photoresists and photomasks vary from process to process.
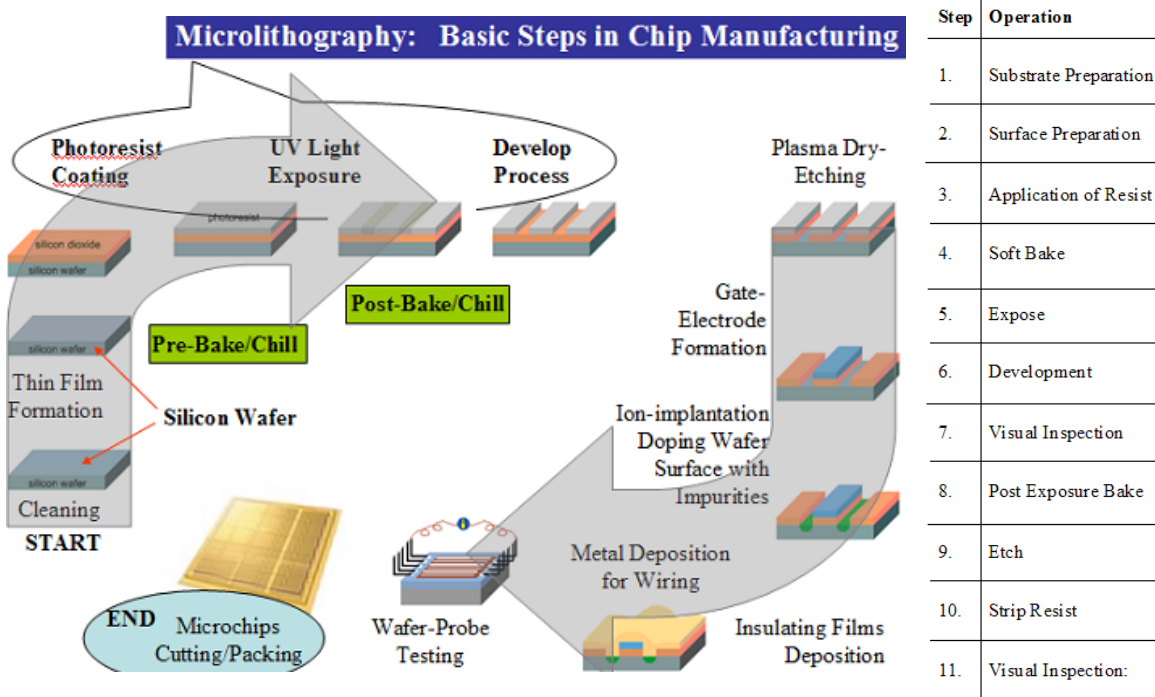
Figure I.20 Sequence of steps involved in the manufacture of a computer chip (from [52]).

I.6.2 Electron beam lithography

Electron beam lithography (EBL) utilizes electrons for patterning and provides excellent resolution due to the small wavelength and a small probe size, whereas the resolution in optical lithography starts to become limited by the wavelength of the light that is used for exposure [53]. It is a serial technique, aimed at finer features, and high density packaging. There are two main e-beam writing strategies; projection printing and direct writing. In projection printing, a large e-beam pattern is projected parallel through a mask onto a resist coated substrate by using a high-precision lens system (much like photolithography). In direct writing, a small e-beam spot is moved with respect to the wafer to expose the wafer one pixel at a time, eliminating the expensive and time-consuming production of masks. Typically the writing field, which is defined by the maximum deflection range of the e-beam, is of the order of a few hundred micrometers. Larger patterns require mechanical stage movements, which need to be very accurate in order to precisely stitch consecutive writing fields. The process steps involved in EBL are similar to that of the photolithography. Poly(methyl methacrlylate) (PMMA) has been the most widely used and high resolution positive-tone resist and hydrogen silsesquioxane (HSQ), a relatively new resist material, is a high resolution negative-tone resist [54].

One of the most important parameter of the EBL process is the resolution of a resist. It is defined as the smallest line-width which can be consistently patterned. Lower the molecular weight of the polymeric resist, higher the resolution. For positive resist, it is related to rate of chain scission and the rate of solubility with the molecular weight. For a negative resist, the limiting factor is something else. The exposed portions of a negative resist swell as their unexposed areas are dissolved by the developer. This swelling, which is simply volume increase due to the penetration of the developer solution into the resist material, results in distortions in the pattern features. This swelling phenomenon can limit the resolution of a negative resist. The unexposed regions of positive resists do not exhibit swelling and distortions to the same extent as the exposed regions of negative resists. This allows positive resists to attain better image resolution.

Physical limitation of the resolution is the proximity effect (Figure I.21), which is re-exposure of the resist with the backscattered secondary electrons. To suppress the proximity effect, increased electron energy can be used. Primary beam scattering occurs when electrons in the beam elastically collide with atomic nuclei in the material and their trajectory is subsequently altered. It is commonly described as two sub processes: forward scattering and backscattering.
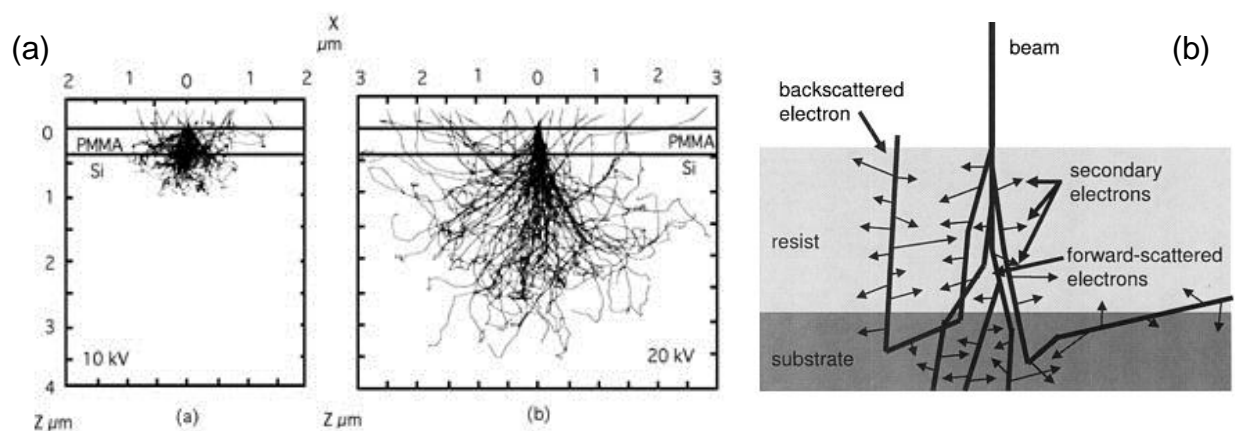
Figure I.21 Monte Carlo simulation of electron scattering in resist on a silicon substrate at a) 10 kV and b) 20 kV (from [55]). (b) Schematic illustration of the various processes that influence the point-spread function. An electron beam traveling through a resist film can interact with particles both elastically) producing forward scattering and beam broadening) and inelastically (producing secondary elections) (from [56]).

Forward scattering

As the electrons penetrate the resist, some fraction of them will undergo small angle scattering events, which can result in a significantly broader beam profile at the bottom of the resist than at the top. The increase in effective beam diameter in nanometers due to

forward scattering is given empirically by the formula $d_f = 0.9 \, (R_t / V_b)^{1.5}$, where R_t is the resist thickness in nanometers and V_b is the beam voltage in kilovolts. Forward scattering is minimized by using a thin resist and high accelerating voltage.

Backscattering

As the electrons continue to penetrate through the resist into the substrate, they will experience large angle scattering events and may return back through the resist at a significant distance from the incident beam, causing additional resist exposure. This is called the electron beam proximity effect. The range of the electrons (defined here as the distance a electron travels in the bulk material before losing all its energy) depends on both the energy of the primary electrons and the type of substrate.

Secondary electrons – actual resist exposure

After the primary electrons slow down, their energy is dissipated via secondary electrons (energies, 2 to 50 eV). They are responsible for the major portion of the actual resist exposure. Since their range in resist is only a few nanometers, they contribute little to the proximity effect. Instead, the net result can be considered to be an effective widening of the beam diameter by roughly 10 nm. This largely accounts for the minimum practical resolution of 20 nm observed in the highest resolution electron beam systems and contributes (along with forward scattering) to the bias that is seen in positive resist systems, where the exposed features develop larger than the size they were nominally written. A small fraction of secondary electrons may have significant energies, on the order of 1 keV. These so called fast secondaries can contribute to the proximity effect in the range of a few tenths of a micron. In the following paragraphs, the most important properties that an e-beam resist must have in order to become a suitable candidate for nanolithography will be discussed.

Electron dose is the number of electrons per unit area (expressed as $\mu C.cm^{-2}$) required to achieve the desired chemical response in the resist. The optimum dose refers to the dose at which the measured linewidth after development is equal to the designed linewidth. Dose test is performed to arrive at the correct dose parameter. In this test, the same pattern is exposed at different doses and after the development, the optimum dose can be determined through inspection via SEM, AFM or optical microscope. The electron dose influences the actual size of the patterned feature. When a pattern is exposed at lower doses compared to the optimum dose (underexposure), the actual structure width is smaller than the designed structure width but the pattern irregularities also exist. On the other hand, overexposure (dose higher than the optimum dose) leads to widening of the pattern size. In

general, the electron dose of a resist should be low in order to achieve high sensitivity and throughput. Contrast and sensitivity characteristic properties of e-beam resist. Response/contrast curves, which can be obtained by plotting the remaining thickness after the development process versus the e-dose (Figure I.22) are used for determining these properties. The sensitivity is defined as the critical dose required for removal (positive) or retention (negative) of half the thickness of the resist film. Resist sensitivity increases with increasing molecular weight. The sensitivity of a resist can be obtained from its contrast curve. Contrast (γ), also called 'the vertical contrast', is defined as the slope of the linear portion of the falling edge (positive resist) of the remaining resist thickness versus log (dose) curve. An ideal e-beam resist should have both a high contrast and a high sensitivity. But in general, an increase in one of these parameters leads to a decrease in the other. A high sensitivity will provide a high throughput (e.g. reduction of the writing time), but leads to a shallower slope for the contrast curve, hence a lower contrast.

$$\gamma_{p=(log(d_c/d_0))^{-1}}$$

$$\gamma_{n=(log(d_0/d_c))^{-1}}$$

where d_c is the maximum dose at which still no film is lost (see the illustration in Figure I.22 plots on top) and d_0 is the minimum dose at which all the resist thickness is lost.
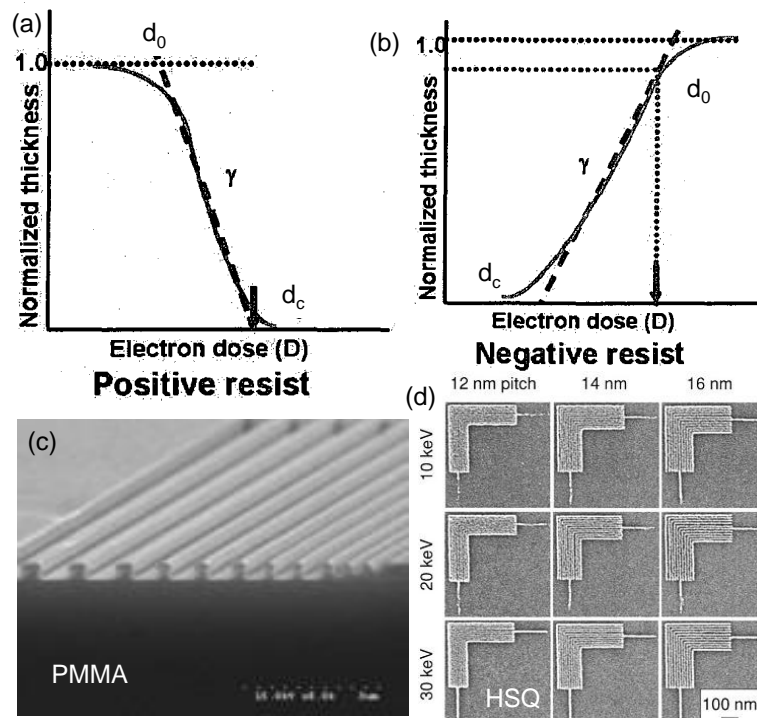
Figure I.22 Response curves of (a) positive and negative resists. The slope of curves give the contrast parameter of the resist [from [57]]. Examples of patterns made using (c) PMMA (from [58]) and (d) HSQ resists (from [56]). Dose test for HSQ resist is shown in (d).

For thick resist layers and large structures, these curves are easy to obtain. In general, the remaining resist thickness after the development process is measured with a surface profilometer. When thin resist layers are used (<10 nm), reliable measurements are difficult to get, even when using an atomic force microscope (AFM) operating in tapping mode. In this case, the 'horizontal contrast' is measured; this is defined as the slope of the linear portion of the graph of the linewidth measured after the development plotted versus the logarithm of the dose.

Line edge roughness (LER) or the linewidth fluctuation becomes a serious issue when the pattern size shrinks. For nanolithography, the LER should be as small as possible in order to avoid pattern distortion or deterioration of the resolution. Finally, etch resistance represents the ability of the resist to withstand an etching process (which follows the development process).

I.7 PARADIGM SHIFT WITH THE INTRODUCTION OF UNCONVENTIONAL PATTERNING TECHNIQUES

Although conventional lithography methods have served for decades in patterning a variety of materials over large areas, these processes are in general not compatible for patterning nanomaterials on surfaces which are usually sensitive to process conditions and attract contaminants. In addition, other compromises are to be made. Realizing high resolution patterning over large areas is rather challenging with nanomaterials. Further complications arise nanomaterials are to be patterned in the context of plastic electronics or bio applications, latter applications typically employ special biomaterials designed for a given purpose. Patterning on non-planar, curved surfaces is another challenge using the conventional lithography.

I.7.1 Scanning probe lithography

Scanning probe lithography (SPL) is a promising method for nanopatterning. It makes use of the probe tip - surface interaction, which is confined to the nanoscale, due to which high-resolution patterning at the nanoscale can be realized. Numerous AFM-based lithographic techniques have been developed in the last two decades. Usually, these techniques can be classified into two groups based on their operational principles: (i) force-assisted and (ii) bias-assisted AFM nanolithography. In the former, a large force (larger than those used for AFM imaging) is applied to the tip for pattern fabrication mechanically, whereas in the latter, AFM tip is biased to create patterns (see Figure I.23a and b). Typical

force-assisted   AFM   methods   include   mechanical   indentation,   nanoplowing, thermomechanical writing, nanomanipulation, dip-pen nanolithography (DPN) etc.

During mechanical indentation and plowing, a rigid AFM tip is used to mechanically modify a soft sample surface by applying certain load in the range of 1000~1500 nN, depending on the substrate. More rigid cantilevers and greater loads are needed for harder samples. Thus, arrays of regularly organized gaps have been produced by local indention, with the size of the gaps controllable by the shape of the top and its penetration depth [59]. Nanopatterns were fabricated on various materials, e.g., diamond-like carbon thin films, polymer and single crystal silicon [60], metal surfaces (Ni, Cu, Au), metal chalcogenide [61], nanocluster films [62] using this technique. In thermomechanical writing, a resistively heated AFM probe (~400 °C) writes a data bit by scanning over a polymer surface (Figure I.23c). Here, the combined effect of heat and mechanical force of the tip is the reason for the polymer flow, which can be of potential use in writing data bits in a storage medium [63]. In dip pen lithography (DPN), the tip is used as a nanoscale pen to directly deposit collections of ink materials onto the substrate to define a functional structure [64, 65]. In this direct-write lithographic technique, an AFM tip coated with ink, which consists of organic molecules in solution. This ink is transferred from the tip to a substrate through the water meniscus that forms at the tip-sample junction under ambient conditions (Figure I.23d). DPN in general and is applicabile to immobilize a large diversity of organic materials, and in particular biomolecules, for constructions of (bio) functional surface arrays [64].

As for bias-assisted AFM nanolithography, the AFM tip is biased to create a localized electric field in the regime of 10^8 V/m to 10^{10} V/m, due to which tip acts as a source of current injection or collection. Under such a high localized field, pattern formation can be due to processes or interactions such as electrostatic, electrochemical, oxidation etc. The variable here are the tip bias and the substrate material; the application of tip voltage can be used for anodic oxidation [66, 67], electrostatic attraction [68], electrochemical deposition [69] as well as nanoscale explosion and shock wave propagation [70].

Local anodic oxidation (LAO) is a standard method used for the fabrication of nanosized oxide structures [67]. It is based on direct oxidation of the sample by negative voltage applied to the AFM tip with respect to the sample oxidized. The process utilizes the presence of a water bridge created between the sample and the tip [71]. For local electric field larger than the critical one, 10^9 V/m or (1 V/nm) [71], the water molecules split into H^+ and OH^- ions. OH^- ions are transported to the positively biased sample surface in the

direction of the electric field, which react with the surface atoms, and form oxides (Figure I.23e). LAO technology can be applied to various metallic, semiconducting, or insulators samples. The bias voltage, substrate, separation between tip and sample surface, duration, and ambient humidity all have significant effect on the oxidation.
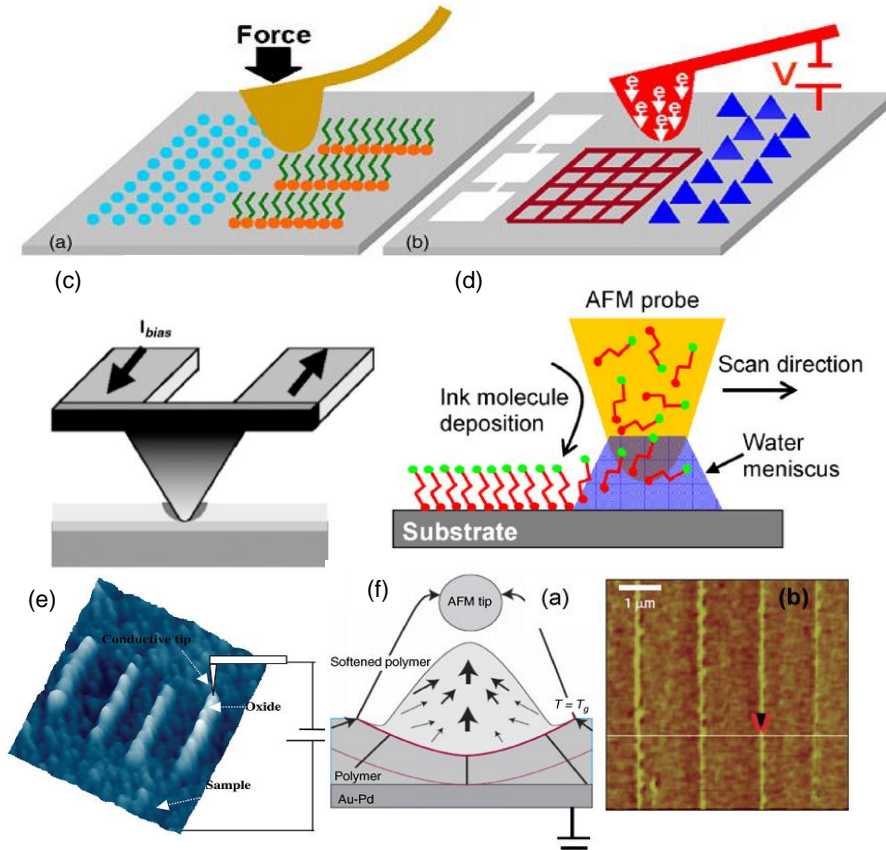
Figure I.23 (a) Force-assisted, (b) bias-assisted AFM nanolithography, (c) shows the schematic of resistively heated cantilever used for thermomechanical writing, (d) dip pen nanolithography - schematic showing the transport of ink from the AFM tip to the substrate through the water meniscus (from [65]). (e) A schematic plot of AFM tip-directed oxidation (from [66]), (f) AFM electrostatic nanolithography for polymer pattern formation and (g) Periodic lines created on PMMA by electrostatic deformation (from [69]).

Another technique, AFM-assisted electrostatic nanolithography (AFMEN) generates nanoscale polymeric features by Joule heating [68]. In this technique, current flowing from the biased tip leads to mass transport of polymer films via local softening. The viscoelastic polymer is polarized due to the non-uniform electric field gradient gets attracted towards the tip apex, thus leading to the formation of protruding structures on the film (Figure I.23f). Figure I.23g shows raised periodic lines and letter patterns created by this method on PMMA. Thermal characteristics of the polymer, such as glass transition temperature Tg, thermal conductivity and temperature dependence of the viscosity play a key role on the obtained feature sizes [68]. The resolution of polymeric features does not directly depend on the tip radius, distinguishing this technique from other AFM nanolithographic methods.

I.7.2 Soft lithography

An alternate lithography method that could afford rapid prototyping as well as patterning of a wider range of materials was highly desirable. Unconventional soft lithography techniques, developed in 1993 by Whitesides group at Harvard University have met some of these needs and hold a great promise. Learning lessons from our ancestors and from routinely used seal stamping, soft lithographic techniques take a step forward to micro and nanopatterning. In the historical times, baked clay tubes with relief designs were used by the Olmecs in Mexico around 1000–800 BC, to print patterns on their bodies or onto cloth. Metals, wood and stone were also used as stamps and were later replaced by rubber [72]. A seal which is used to create impression of signature is another macroscopic analogue to this technique. The modern version of this kind of creating impressions is the soft lithography. It is a group of techniques in which an elastomeric stamp or mold transfers a pattern to the substrate [73]. The term "soft" refers to the use of materials involved in stamping - elastomers as well as organic molecules. To date, besides conventional methods, patterned microstructures have been produced on nonplanar surfaces. Complex and 3D intricate patterns have been fabricated and also shown to work as microelectronic devices [74]. Sub-100 nm patterning by soft lithography is a reality [75]. Soft lithography, parallel large area patterning technique, should be regarded as a complement to common lithography and has several advantages apart from not being limited by diffraction. To name a few, soft lithography can be used to pattern

- UV sensitive materials without degrading the performance
- non-UV reacting materials
- on non-planar surfaces
- control the chemistry during the patterning in a better way
- 3D structures
- clean room free operation
- low cost

The soft lithography tool-kit comprises of the stamp, inks and substrates, of which the key element is the stamp. One of the most successful stamp materials is poly(dimethyl siloxane) (PDMS) also called as Sylgard 184 which is a resilient silicone elastomer [76]. It is a environment friendly elastomer and has been used for nose/ear implants and in pacemakers etc. It can deform reversibly at a microscopic level to conform to even non-planar surfaces, a property which enables it to replicate features on the master with high fidelity [77]. PDMS is

optically transparent down to ~300 nm and is homogeneous and isotropic, ideal while combining soft lithography with optical methods. It is chemically inert, thermally stable although permeable to gases [78].

Siloxane prepolymer   Siloxane cross-linkers
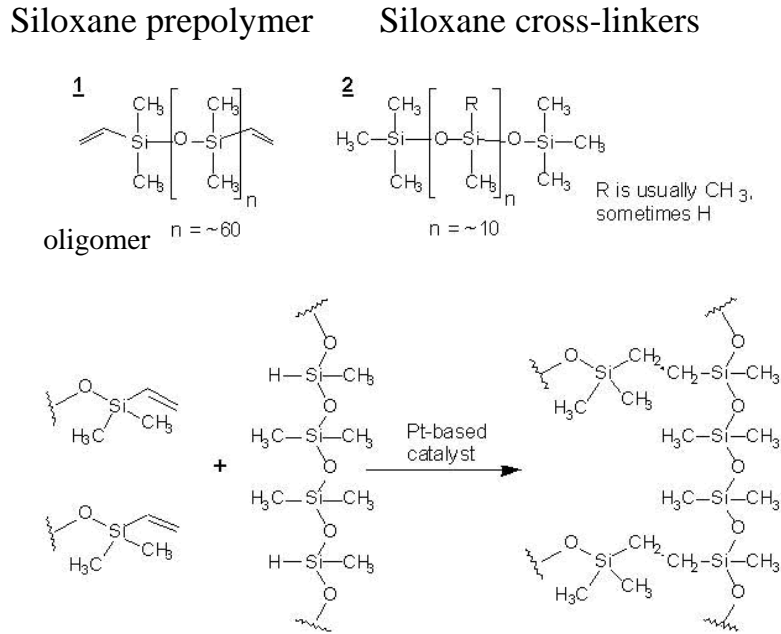
Figure I.24 Cross-linking (curing) reaction of the PDMS (from [79]).
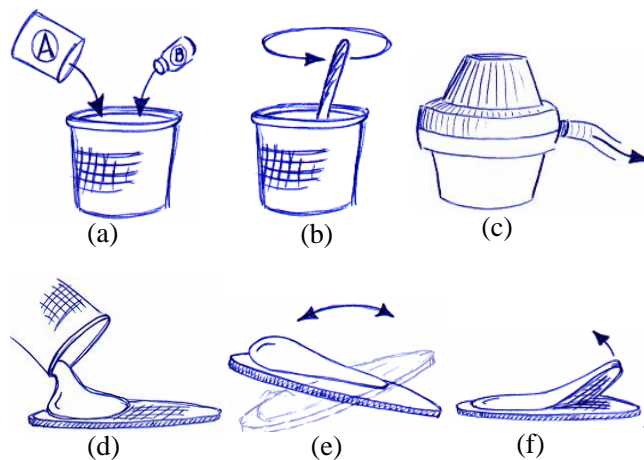
Figure I.25 Protocol for PDMS stamp preparation (from [80]).

Precursors to PDMS are commercially available (e.g., Dow corning); they are vinyl terminated siloxane prepolymer (base material) and siloxane cross-linking agent (curing agent). Curing or cross linking involves addition reaction i.e., hydrosylilation [78] between the two components, forming a three-dimensionally crosslinked elastomer (see Figure I.24). The curing temperature and the ratio of the two components decide the Young's modulus of the formed elastomer [81]. PDMS possesses a low surface energy due to the low

intermolecular forces between the methyl groups. For the stamp fabrication, the base material and curing agent are mixed in the desired ratio (popular ratio is 1:10), the mixture is stirred well and degassed by placing in vacuum, then poured onto the master pattern to be replicated. For cross-linking the PDMS, the setup is placed in an oven at desired temperature and time (commonly 60 °C for 6 hrs). A protocol for the replication of a patterned structure is given in Figure I.25 with detailed illustration of the steps below.

In a plastic cup, base elastomer and curing agent (1:10 by weight) are weighed (Figure I.25a). A plastic spoon can be used to mix the base and the curing agent and should be mixed for at least few minutes on an average of 100 strokes. While mixing, a lot of air gets incorporated in the solution, which can be removed in the next step (Figure I.25b). The silicone mixture will be filled with air bubbles and needs degassing. This can be done in a vacuum dessicator by putting the plastic cup after removing the spoon (Figure I.25c). During the degassing, the silicone expands and starts to look like foam and may overflow. When the silicone is completely clear and transparent, the degassing is complete. The mixture is poured onto the template and dispensing the material at the center of the template minimizes the risk of trapped air (Figure I.25d). To aid the PDMS spreading, the template can be tilted in different directions (Figure I.25e). It can be left as such for a minute in order to get a flatter top surface. Stamps thickness can range from ~0.1 to 5 mm or more. The elastomer can be cross-linked by thermal curing which can be done from less than room temperature to 150°C. PDMS has temperature dependant shrinkage (Figure I.26). For instance, curing at 140 °C (~15 min) will make the stamp shrink almost exactly 3% whereas curing at 60 °C (>24 hours) shrinks PDMS by <1%. The final step is to peel off the stamp from the template. First the borders can be peeled off and then at a low speed entire stamp can be peeled in a direction parallel to most structures (Figure I.25f). The properties of thus made PDMS are listed below [80].

As supplied		*As cured*	
Mix ratio A:B	10:1	Appearance	Transparent
Viscosity (mixed)	3900 centipoise	Tensile strength	6.2 MPa
Specific gravity	1.05	Elongation	100%
Pot life (25 ^{0}C)	2 h	Surface state	Hydrophobic
		Water adsorption	0.1%
		Refractive index	1.430
		Dielectric constant	2.65 - 2.7
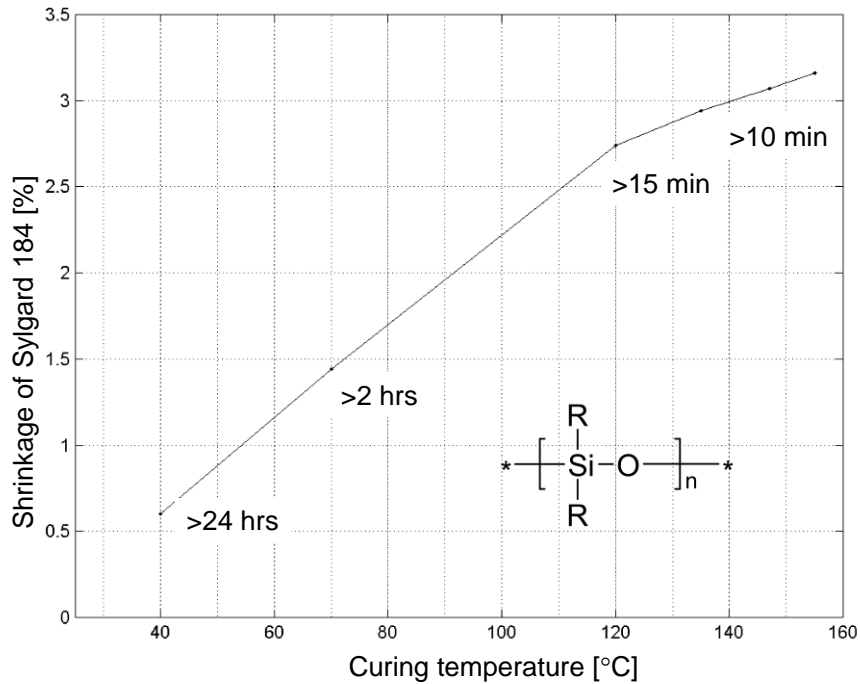
Figure I.26 Plot of shrinkage versus curing temperature (from [80]).
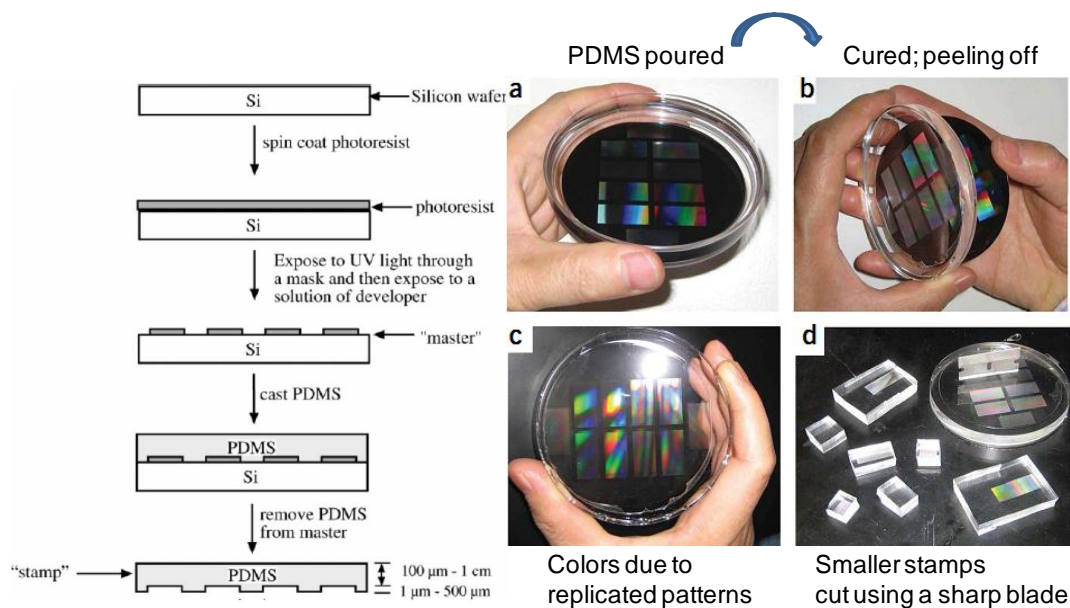
Figure I.27 Schematic of PDMS stamp fabrication with illustrating photographs (from [82], [83]).

As discussed thus far, this technique requires a master - the material on which the features to be transferred to the stamp, are produced by photolithography, or electron beam lithography or the like (Figure I.27). The strength of soft lithography is in replicating the master. Using the aforementioned steps, the process of replicating is illustrated below with photographs. If the stamp contains periodic structures with dimensions in the range of 0.5–10 μm, diffraction color viewed from an angle is a quick check for the quality of the stamp

(Figure I.27a-d). The same master can be used to fabricate many PDMS stamps provided the master pattern has been kept in a covered petridish or other containers to avoid contamination of its surface by dust particles.

Since the stamp is deformable, there are limits on the aspect ratios of the features [84], which can be replicated (Figure I.28a). If the height (H) is much greater than the width (L) of the feature, the stamp features collapse laterally while peeling off from the master or during the inking process due to capillary forces (Figure I.28b). On the other hand, if the height is much less than the distance (D) between features, the roof of the stamp sags under its own weight while printing or molding, causing contact between the stamp and the substrate in regions where it is not desired (Figure I.28c). Sagging can be eliminated by fabricating a submicron thick stamp on a rigid support [85]. To minimize the deformation, a composite stamp that retains the structure of nanoscale topographic patterns containing a base layer of h-PDMS is employed [86]. It may be interesting to note that stamp deformations have been exploited widely in producing unusual patterns [87]. Stamp collapse due to overpressure has also been exploited in contact printing of features with reduced size [88] as well as for creating new shapes [89].
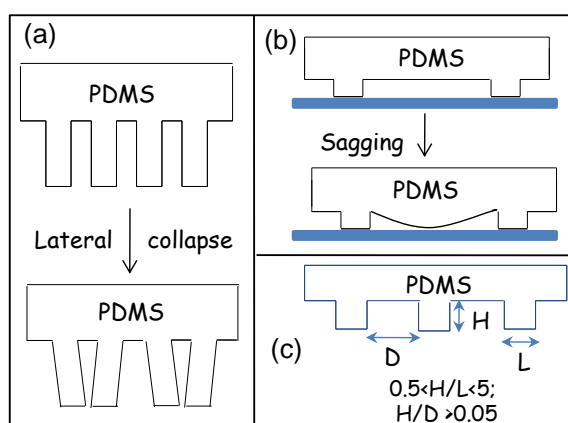
Figure I.28 Schematic illustrating the failure events in PDMS

Once the stamp is fabricated with the desired relief features, it can be used for many purposes such as molding, printing, embossing, imprinting etc. Below, the molding method is discussed in detail, as an illustrative example for soft lithography and a brief sketch of other related techniques is also provided.

Molding

Molding is casting the topographic pattern from one material to another by a liquid precursor which is solidified while being molded. This method is specifically called Replica molding (REM) [90] (Figure I.29). The name is justified as it shares similarity with the

conventionally used wax molding. Another approach of molding is microtransfer molding (µTM). In this method, the polymer precursor is dropped onto the surface of the PDMS mold and excess material is removed. Then, the prepolymer is cured after placing the mold onto another substrate. In this method, a residual thin layer of polymer is generally found connecting the isolated features, which could be removed by reactive ion etching (RIE). To prevent the formation of this residue, PDMS molds with appropriate surface chemistry (e.g. fluorinated silanes) can be used to dewet the prepolymer from the relief features of the PDMS mold [91].
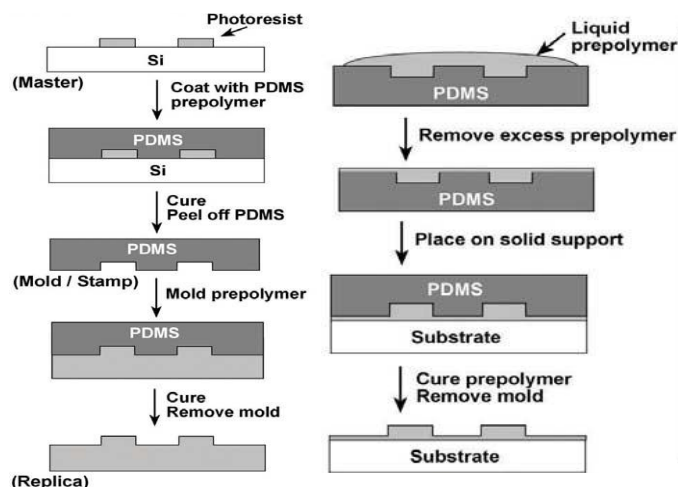
Figure I.29 Schematic illustration of REM and µTM (from [92]).
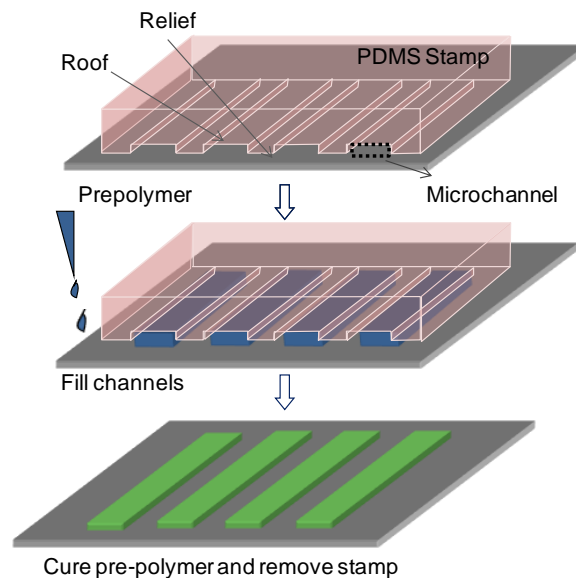
Figure I.30 Schematic illustration of MIMIC process.

Micromolding in capillaries (MIMIC) is yet another technique to mold isolated features [93]. When a patterned PDMS mold is placed onto a substrate, the relief features conform to the substrate, thus forming a network of microchannels. Injecting a solution at

one end of the channels, the liquid is made to fill the channels by capillarity which either deposits or removes material in the exposed regions of the underlying substrate [91]. Deposited materials include polymers, prepolymers [94], sol-gel precursors [95], proteins [96] and colloids [97] (Figure I.30). Various materials such as polymers, prepolymers [94], sol-gel precursors [95], proteins [96], and colloids [97] etc., have been patterned by this method. Using this technique, sub-wavelength optical devices, waveguides and optical polarizers, have been devised which could be used in optical fiber networks and in optical computers [98]. Microfluidic and nanofluidic devices for producing biochemical chips are other examples of MIMIC [99]. Few examples of patterned microstructures formed by this method are shown in Figure I.31.
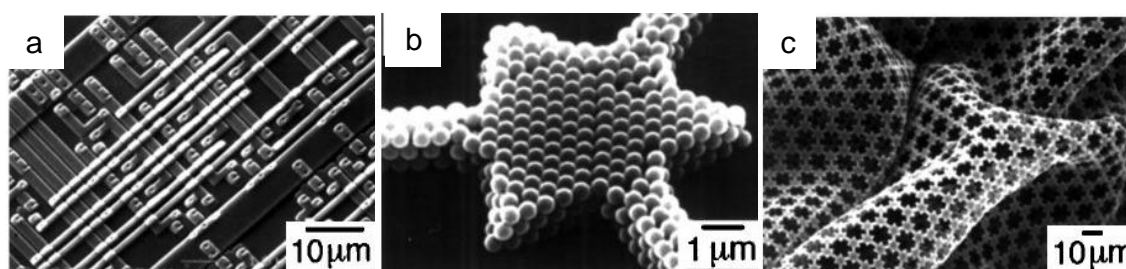
Figure I.31 SEM images of microstructures of various materials fabricated using MIMIC. (a) Quasi-three-dimensional structures of polyurethrane formed on Si/SiO_2. (b) Patterned microstructures polystyrene beads and (c) free-standing microstructured membranes of polyurethane (from [73]).

The criteria for choosing the 'ink' and the substrate are well established. For micromolding, the viscosity of the liquid 'ink' chosen should be low enough to allow fast filling of the microchannels and it should atleast partially wet the PDMS stamp. This can be further understood in terms of the following classical equation for the capillary filling [100].

$$dl/dt = (\gamma r \cos \theta) / 4\eta l$$

where dl/dt is the rate of penetration of the liquid in the capillary; l, distance penetrated into a cylindrical capillary of radius, r in time t; θ, angle between liquid and surface; γ, interfacial free energy of liquid and η is the viscosity of the liquid.

The solvent of the 'ink' should be chosen in such a way that the interfacial energy is minimum. For example, PDMS being hydrophobic, water is not a good medium for MIMIC. If water has to be used as a solvent, either a surfactant or an organic solvent such as ethanol is required to achieve the capillary flow through the channel. The liquids with low interfacial free energies (e.g., methanol, ethanol) and low viscosity fill the channels rapidly.

As regards the substrate, an important issue is the sticking of the material being molded (whether to the PDMS stamp or to the substrate), which is determined by the

interfacial free energy (γ); the material sticks to a surface which has higher γ. As the interfacial free energy of the PDMS stamp is very low [73], (γ_{SV}(PDMS) = 21.6 dyn/cm) compared to the commonly used substrates for patterning, (for e.g., γ_{SV}(Si/SiO$_2$) = 72 dyn/cm), the molded material selectively adheres to the substrate rather than to PDMS.

Apart from solution 'inks', MIMIC has been explored with gas phase 'inks' as well [101]. After placing the PDMS stamp in conformal contact with the substrate, the open channels are exposed to an organosilane saturated environment. The silane molecules diffuse into the microchannels, and condense preferentially along the interfaces upon contacting the substrate in the channels [101].

MIMIC allied technique-SAMIM

Solvent assisted micromolding in capillaries (SAMIM) [102] produces patterns on the surface of a material using a solvent that can dissolve the material. The PDMS mold is wetted with the solvent and brought into contact with the surface of the material to be patterned (generally polymers). The solvent dissolves or swells a thin layer of the material, which gets molded by the PDMS. When the solvent evaporates, the patterned surface gets defined as the replica of the mold surface. The solvent chosen should not affect the PDMS mold. It should evaporate rapidly, thus solvents having high vapor pressure are suitable for this. For using solvents such as water which do not wet the PDMS surface, a pre-treatment to make it hydrophilic, is generally employed. Unlike MIMIC, this technique generates features which are connected by a residual layer. The patterns generated by SAMIM are affected by various parameters such as mold rising angle (angle between substrate and mold sidewall), concentration of the material being molded and its amount [103]. The capillary rise of the material upon softening with the solvent can be controlled with the time of contact of the mold. Thus miniaturized edge-confined structures have been prepared by bringing the swollen PDMS stamp into contact with polystyrene for half a minute [104].

Printing

The principle underlying contact printing by soft lithography is similar to what is used in day-to-day seal stamping. A patterned PDMS stamp is inked with a specific molecular ink and is transferred onto a desired substrate. As the relief features of the stamp contact the substrate, the ink gets transferred, defining a pattern similar to that of the stamp. This is the process of microcontact printing (Figure I.32). This method is simple, straightforward and multiple printing can produce intricate patterns [105]. Initial

demonstration of the microcontact printing was the patterning of thiol self-assembled monolayer (SAM) onto Au surfaces and the transfer of the SAM ink was based on the chemisorption onto Au surface [106]. Later, the contact printing technique has been used to pattern molecules, colloids, nanoparticles, organic reactants, biomolecules etc [76].
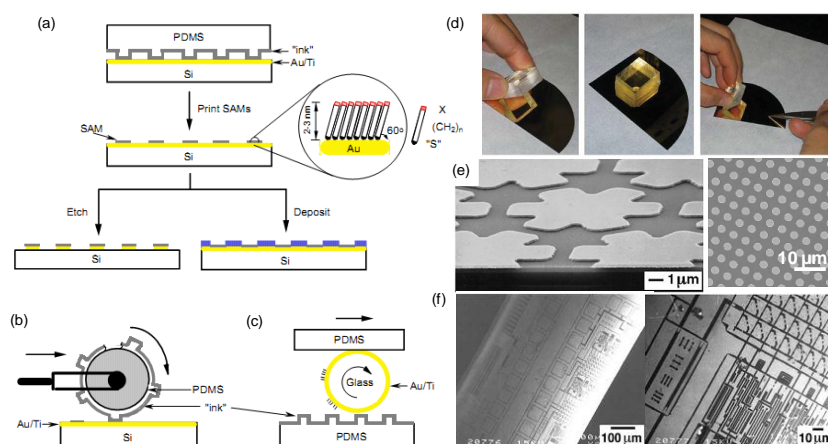
Figure I.32 Schematic procedures for µCP of hexadecanethiol on the surface of gold: (a) printing on a planar surface with a planar stamp (b) printing on a planar surface over large areas with a rolling stamp (c) printing on a nonplanar surface with a planar stamp (d) Photographs of the steps involved in microcontact printing of alkanethiol on gold, left initiating contact between the PDMS stamp and the gold surface from the edge with an angle to avoid trapping air bubbles between them; middle, leaving the stamp in contact with gold for 10 s; and right, separating the stamp from the gold surface, (e,f) SEM images of patterned strucutres on planar and non-planar surfaces (from [77], [83]).

The technique can be used to pattern discontinuous structures but is a surface patterning technique. The stamp and surface can be planar or non-planar and roll-to-roll type of printing is possible with this technique. However the limitation of this technique is that, the recessed features of the stamp can deform on the nanoscale and cause distortions in the pattern [73]. Transfer of the material from PDMS stamp to the substrate can also be assisted by applying a bias voltage, and this method is called electrical microcontact printing [107].

PDMS stamp can not only be used to transfer inks, but also metal patterns by nanotransfer printing (nTP). Patterned PDMS stamp is coated with a desired metal and brought in contact with the pre-treated substrate. The pre-treatment involves coating a SAM on the substrate, so as to mediate the transfer of the metal from PDMS to the substrate by covalent bonding. The metal gets transferred only from the relief features of the stamp thus producing a similar pattern as that of stamp. Interesting shapes such as Au nanocones have been fabricated using nTP [108]. The technique works fairly well with Au, but for metals such as Cu, the diffusion of PDMS oligomers makes the transfer printed patterns non-conductive. The solution to print conductive patterns in such cases is to leach the PDMS

stamps prior to transfer printing [109]. One can substitute the covalent bonding step with heat treatment which alters the surface energy of PDMS. This weakens the adhesion of material to the PDMS surface, thus enabling the transfer of the material to the substrate. SWNT networks have been transfer printed using this method [110]. Kinetic control of the adhesion is also exploited to transfer print variety of materials [111]. For example, p–n junctions and photodiodes have been transfer printed onto highly curved surfaces by kinetically controlled switching between adhesion and release of materials [111].

I.7.3 NIL-Large area next generation lithography technique

Various types of printing and molding techniques employing soft stamps have been dealt with. Before soft lithography becomes a general strategy for microfabrication, there are few technical problems to be addressed. The volume of the stamp material PDMS shrinks by »1% upon curing and thus can be readily swelled by a number of nonpolar organic solvents such as toluene and hexane after curing [86]. It poses a serious threat to the high registration of the patterns, if the process flow involves such solvents. Also, the softness of an elastomer limits the aspect ratio of microstructures in PDMS. The aspect ratio of the relief features in PDMS has limitations, in order to obtain defect-free stamps or molds. Because of all these factors, soft lithography fails in the case of multiple layers that must stack 'precisely' on top of one another [98]. This calls for a rigid stamp than an elastic one. Thus emerged a technique called Nanoimprint lithography (NIL) developed by Stephen Y Chou which employs a rigid master (generally made of Si or quartz) for embossing a film of polymer (Figure I.33) that has been heated to a temperature near its melting point to facilitate the embossing process [112]. It is a parallel patterning with high throughput and is viewed as a potential candidate for 'Next generation lithography'. To date 5 nm features and 14 nm pitch features have been fabricated using this technique [113]. Generally this method is used for imprinting polymers and then the pattern in the polymer is transferred into the desired material by etching. In another technique called step-and-flash imprint lithography (SFIL) employing preferably UV-transparent stamp, the stamp is pressed against a thin film of liquid polymer and is exposed to ultraviolet light, which solidifies the polymer to create the desired replica [114]. This technique is particularly useful when repeat periodic patterns have to be fabricated on a substrate. Of course, as the stamp is rigid, these techniques employ huge amount of pressures to ensure proper contact between the stamp and the substrate. Anti-sticking layer over the stamp surface also plays a critical role in deciding the pattern transfer to the substrate.
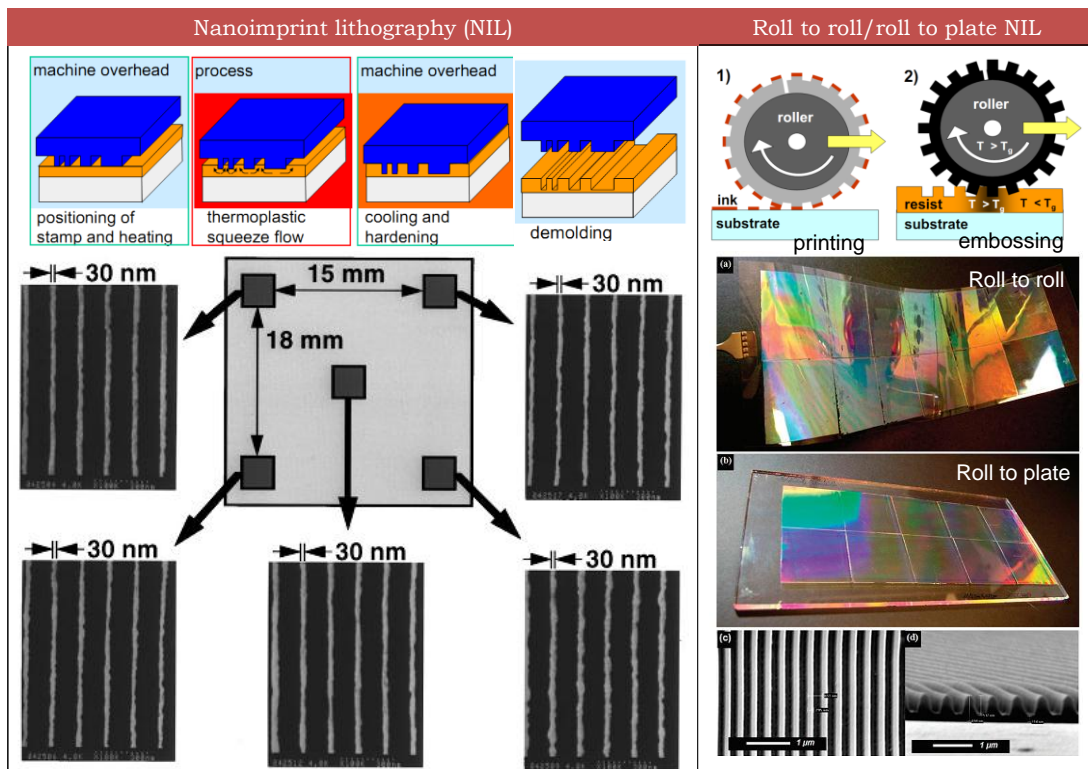
Figure I.33 NIL process flow (left) along with SEM images of the printed patterns of various dimensions on the same substrate (from [115]); Roll-to-roll printing and embossing schematic (right) along with photographs of the samples imprinted using the process (from [116]).

Summary
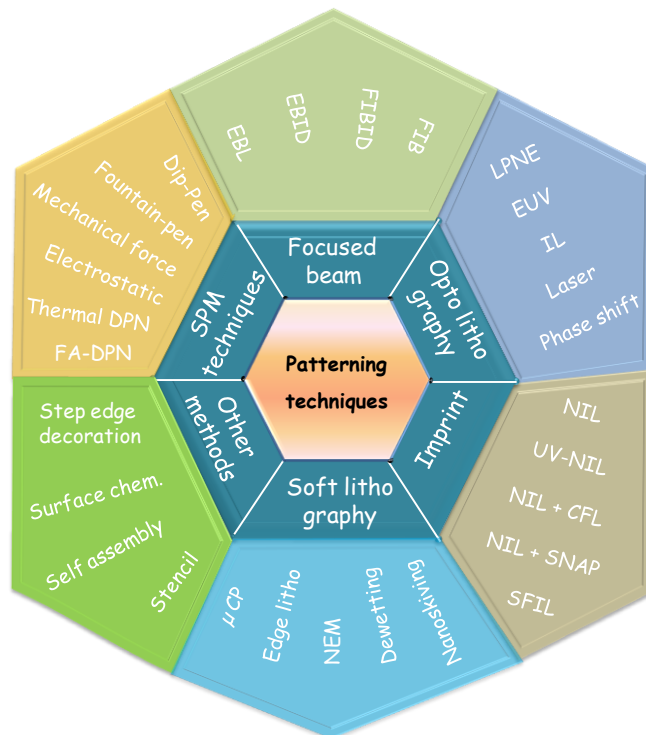
Figure I.34 A palette displaying various fabrication techniques for patterning.

Thus as discussed, there have been a number of conventional as well as innovative lithography processes to achieve sub-100 nm patterns, which is pictorially presented in Figure I.34. They are classified under scanning probe and focused beam based techniques, optolithography, nanoimprint and soft lithography. Many hybrid methods are also shown. The collage of course is not exhaustive.

1.8 NANOMATERIALS TO APPLICATIONS

Many physical, chemical and electrochemical methods have been devised for synthesizing assorted nanomaterials such as carbon nanotubes, graphene, semiconductor nanowires etc., with unique properties. The major task is to realize the devices comprising these nanomaterials. On the other hand, using exotic nanolithography and fabrication methods, tiny objects and machines (Figure I.35) have been made. Manipulating atoms precisely and writing alphabets with atoms also has been achieved.
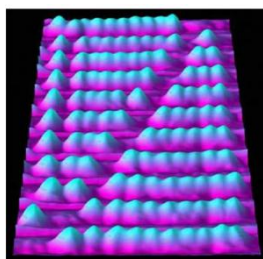
Figure I.35 The nanoscale abacus - individual bumps are molecules of C_{60}, which are about 1 nm wide (from [117]).

But one question remains. How does one connect such tiny nanoobjects to macroscopic real world? It is important not only to be able to make such tiny machines and diverse nanomaterials, but also to realize practical applications. Many prototype devices have been devised such as single electron transistor, single molecule switch, resonant tunnelling diode and many more, the common aspect in all of them being the method of realization of the functional device is through localised sophisticated measurement on the molecule. The contacts and the related instrumentation around these devices are much more than million times the size of the actual device itself. In short, this scenario is suitable for studying fundamental phenomenon but not scalable to devices for industrial production.

This awareness has taken the research in a different direction. For instance, when graphene, a 2D sheet of carbon with excellent electronic and optoelectronic properties, is synthesized, it is quite important to mention how large sheets of graphene can be made laterally, maintaining the thickness of one atomic layer [118]. In the case of anisotropic nanoparticles, for e.g., nanowires, length of the nanowires is sought after to be more than

tens of µms keeping the diameter in few nms [119]. Another important class of materials, metal-organic frameworks (MOF) often synthesized as small crystals or powders evidenced a burgeoning challenge [120] in the field i.e., to prepare these MOFs with shapes tailored for specific purposes, for example as thin films or patterned structures. All these point to the fact that the nanoobjects are ultimately to be connected to the real world, keeping the nano-component intact. Nature does this in quite an elegant way. For instance, in the case of cellulose fibres, the internal structure is composed of separated nanofibrils, but entangled to form microfibril and macrofibrils (see Figure I.36). As said rightly by Feynman [121], "*Nature uses only the longest threads to weave her patterns, so that each small piece of her fabric reveals the organization of the entire tapestry*".
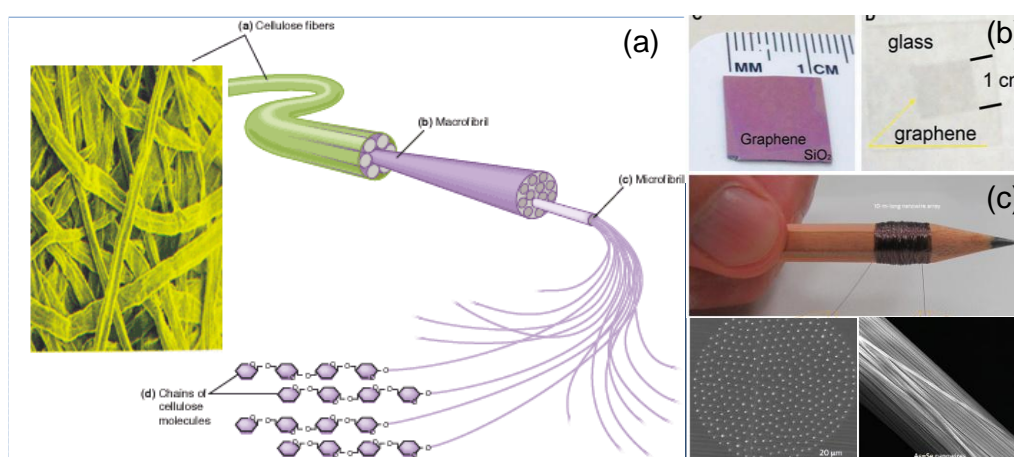
Figure I.36 (a) Cellulose fibre structure (from [122]). (b) Photograph showing a large area graphene grown on SiO_2 and glass substrate (from [118]). (c) A polymer-embedded nanowire array rolled around a pencil truly spans macroscopic and nanoscale worlds. Cross-sectional SEM micrographs from a 10 m long polymer fibre that contains hundreds of As_2Se_3–PVDF core–shell nanowires; side view of the free NWs is also shown alongside (from [119]).

I.8.1 Key to utilize the nanostructures effectively in man-made devices

Various nanostructures as discussed thus far have been synthesized and the key to utilize them, to draw out interesting electrical, optical, magnetic etc properties in the device applications lies in contacting them through the desired means. For instance, fabricating memory devices, photovoltaics, transistors etc., out of inorganic compounds or molecules requires establishing electrical contacts. Particularly scientists have synthesized interesting molecules with different structures suitable for efficient energy generation in photovoltaics [123], spin state dependent conduction [124] etc. Owing to their small size, top contacting has been the method of choice for contacting molecules (Figure I.37a). Of course, small nanometric junctions such as break junctions have also been tried to measure the molecular

properties [125]. On the other hand, important one dimensional structures such as vertically grown carbon nanotubes and semiconductor nanowires, clearly foreseen as realistic candidates for post-modern electronic applications, such as energy storage, sensing, power generation, light emitting diodes, and solid stage lighting [126]. Thus, top contacting vertically grown NWs is also of presumed importance (Figure I.37b).
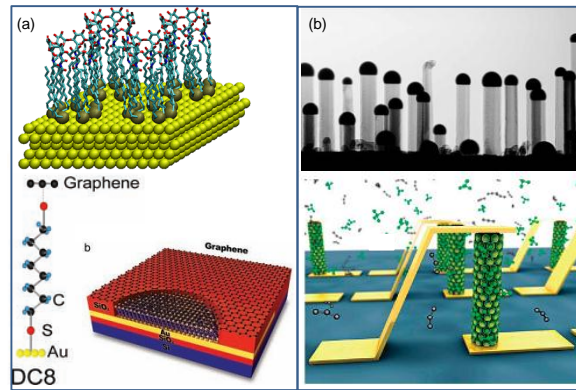
Figure I.37 (a) SAM molecules on a metal surface. Graphene used as a top electrode material for molecular contact (from [127]). (b) TEM image of the vertically grown semiconducting nanowires and a schematic showing one of the top contacting methods for nanowires (from [49]).

I.9 CHARACTERIZATION TECHNIQUES

Several spectroscopic and microscopic techniques have been used to characterize the prepared samples reported in this thesis. In the following paragraphs, the details of instruments used and the sample preparation methods are described.

Powder X-ray diffraction measurements were performed using a Siemens Seifert 3000TT diffractometer employing Cu Kα (λ = 1.5406 Å) radiation. Samples were prepared by depositing the materials in the form of films on glass slides and typical scan rate was 1 deg.min^{-1}. The X-ray tube was set at 40 kV and 30 mA. With a receiving slit of 0.3 mm wide and a scintillation counter as detector, the θ -2θ scans were performed.

High-purity silicon powder was used as an internal standard. The coherently diffracting crystallographic domain size (D) of the nanoparticles was calculated from X-ray diffraction (XRD) line broadening after subtracting the contribution from the Cu Kα component (Rachinger correction) and correcting for the instrumental width. The integral line width was used in the Scherrer formula [128] to calculate d$_{XRD}$ of the high intensity peak.

$$D = \frac{0.9\lambda}{\beta_{1/2}\cos\theta}$$

where λ is the wavelength of the X-ray beam, $\beta_{1/2}$ is the angular width at the half-maximum intensity and θ is the Bragg angle.

Transmission electron microscopy (TEM) measurements were carried out with a JEOL-3010 instrument operating at 300 kV (λ = 0.0196 Å) and selected area electron diffraction (SAED) patterns were collected at a camera length 20 cm (calibrated with respect to the standard polycrystalline Au thin film). Samples for TEM were prepared by depositing a drop of the nanomaterial on a holey carbon copper grid, allowing it to dry in a desiccator overnight. The diameters of the nanomaterials were obtained from transmission electron micrographs and generally represent averages obtained from a few hundred nanocrystals. Atomic resolution TEM (HRTEM) image has been taken in a TITAN[3] 80-300 kV transmission electron microscope in an aberration corrected mode with a negative C_s of ~ -30 µm and a positive defocus Δf of ~ +8 nm (bright atom imaging contrast) [129].

Scanning electron microscopy (SEM) was performed using a Nova NanoSEM 600 equipment (FEI Co., The Netherlands). Energy dispersive spectroscopic (EDS) mapping was performed using EDAX Genesis V4.52 (USA) attached to the SEM column. The EDS mapping was performed at 10 kV (energy window, 10 eV) with a beam current of 1.1 nA, the dwell time per pixel being 25 µs. STEM (scanning transmission electron microscopy) and low vacuum imaging were performed on the same instrument using STEM and helix detectors respectively.

Electron beam lithography (EBL) was performed using a Nova NanoSEM 600 equipment (FEI Co., The Netherlands). Patterning was done under high vacuum conditions, typically 10^{-6} Torr. The substrates used were usually Si, Si/SiO_2 or Au coated glass. Before patterning, the sample was well grounded to avoid any charging while patterning, as charging can broaden the patterned feature. The patterns were created using a e-beam write software available with the instrument. The e-beam energy was varied between 5-30 kV. For fine structures, higher kVs were employed whereas for larger area patterning, lower kVs were preferred. The patterning was performed in parallel mode. The beam current was varied between 91 pA to 24 nA. The dwell time, i.e., exposure time per pixel was varied from 0.1-50 µs. Number of passes was varied from 1-16000.

Nanoimprint lithography (NIL) was carried out in an Obducat imprinter (Obducat, Sweden). Before imprinting, the Si molds were cleaned and coated with SAM (self-assembly monolayer of perfluorodecyltrichlorosilane) to reduce their surface energy so that it is removed easily leaving behind the imprinted nanostructures on the substrate.

Thermogravimetric analysis were carried out with a Mettler Toledo Star instrument (Weinheim, Germany) in the temperature range $30 - 450\,°C$ under N_2, H_2 or O_2 atmosphere at a flow rate of 100 mL/min and a heating rate of $5\,°C$/min. Typically using 5-25 mg of the sample in solid form mounted on a porcelain boat. Differential scanning calorimetry (DSC) was performed with a TA Q100 instrument.

X-ray photoelectron spectroscopy (XPS) was carried out with OMICRON spectrophotometer (1×10^{-10} Torr vacuum) with X-ray source of Al $K\alpha$ (1486.6 eV). Samples for XPS (solid substrates) were mounted on the stub using high vacuum compatible Ag paint and drying in a vacuum. For sputtering the samples, a beam (focus 1 keV) energy of 1 keV with a current of 44. 2 μA was used at a base pressure of 10^{-5} mbar.

UV-visible spectra were recorded using a Perkin-Elmer Lambda 900 UV/vis/NIR spectrophotometer. The photoluminescence (PL) spectra were taken with different excitation wavelength from the spectroflurometer. PL was measured on Perkin- Elmer LS55 Luminescence spectrometer.

Fourier transform infrared (FTIR) measurements were done using a Bruker IFS66v/s spectrometer with a resolution of $\sim 2\ cm^{-1}$. The optical images were procured with the microscope of Laben, India. The confocal images were taken by using a Zeiss LSM 510 laser scanning confocal microscope. Raman measurements were performed using LabRAM HR apparatus (Horiba, USA) with an excitation wavelength of 632.8 nm and 5 $mW.cm^{-2}$. Signal accumulation was performed for 10 s with a spot size of $\sim 1\ \mu m$.

Atomic force microscopy (AFM) experiments were carried out using Veeco Dimension 3100 SPM with Nanoscope-IV controller and Veeco diInnova SPM with Nanodrive controller. Tapping and contact (lateral force) mode imaging was carried out using standard etched Si or Si_3N_4 cantilevers respectively. The scanner was calibrated using a standard Pt coated Au grid with a pitch of 1 μm. Both height and deflection/ amplitude information were recorded at a scan rate of 1 Hz, and stored in a 512x512 pixel format. Images were processed using the Nanoscope version 7.15 software. The magnetic force microscopy (MFM) was performed using a magentic coated (CoCr-coated) Si tip. It was magnetized vertically along the tip axis, thereby allowing detection of the perpendicular component of the stray field emanating from the sample surface with a spatial resolution of ~ 50 nm. Conducting-atomic force microscopy (C-AFM) measurements were performed using Pt/Ir coated Si tips operated in contact mode. The conducting tip is brought into contact with the substrate until a preset loading force is reached. The bias voltage on the

sample is then varied while the resulting current is measured. For scanning tunnelling microscopy experiments, the instrument used was a Veeco diInnova Scanning Probe Microscope with Nanodrive controller. Platinum-Iridium Precision Cut Wire (Model no. CLST-PTBO) of 0.5 mm diameter and 20mm length was used. Both height and current channels were recorded at a scan rate of 10-15 Hz with a 512x512 pixels. The images were processed using SPM lab analysis software.

For film thickness measurements, a Wyko NT9100 (Veeco, USA) optical profiler (OP) and a stylus profiler Dektak 6M (Veeco, USA) were used. In OP, the vertical scanning interferometry (VSI) for roughness of samples more than 160 nm and phase shifting interferometry (PSI) mode for roughness of samples less than 160 nm were employed with a field of view and objective lens magnifications from 0.5x – 2x and 5x – 50x respectively.

For contact angle measurements, a Rame´-Hart digital contact angle (CA) goniometer was used to measure the surface wetting properties of hierarchical Pd films at room temperature. A deionized (DI) water droplet (3uL) was deposited gently on the sample surface using an automatic pipet, and a photograph of the water droplet was taken immediately with the goniometer camera. CA values were given by the DROP image advanced software measurement; the CA values obtained from the software were also cross-checked with the CA values measured manually on the printed photograph of the water droplet. An average was taken after a few point measurements. For each point, a few images were recorded and measured. The typical error of the CA measurements is ±3°.

Au metal (99.99% pure) was physically deposited by resistive heating using 12" vacuum coating unit, (12A4D, HindHivac system, Bangalore) under 10^{-6} Torr vacuum. In order to fabricate gap electrodes, thin carbon fiber served as a mask. Conducting Ag paint was used for electrical contacts. An external multimeter (Keithley 236) served as the source and measurement unit for current-voltage characteristics. I-V ramp was carried out generally for ±5 V with a dwell time of 0.1-100 ms between data points. The current compliance was generally set at 100 mA.

Magnetic measurements were carried out either a vibrating sample magnetometer (VSM 7300, Lakeshore).

REFERENCES

[1]   R. P. Feynman, Caltech Engineering and Science 23 (1960) 22.

[2]   K. E. Drexler, Nanosystems: Molecular Machinery, Manufacturing, and Computation, Wiley, New York, 1992.

[3]   M. Faraday, Philosophical Transactions of the Royal Society of London 147 (1857) 145.

[4]   http://www.nano.gov/nanotech-101/what/nano-size

[5]   R. P. Feynman, Journal of Microelectromechanical Systems 1 (1992) 60.

[6]   http://www.uwgb.edu/dutchs/GRAPHIC0/GEOMORPH/ SurfaceVol0.gif

[7]   C. N. R. Rao, P. J. Thomas, and G. U. Kulkarni, eds., Nanocrystals: synthesis, properties and applications, Springer, Heidelberg, 2007.

[8]   P. P. Edwards, R. L.Johnston, and C. N. R. Rao, in Metal Clusters in Chemistry (L. A. O. P. Braunstein, P. R. Raithby, ed.), Wiley, Weinheim, 1999.

[9]   R. M. Brydson and C. Hammond, in Nanoscale Science and Technology (R. W. Kelsall, I. W. Hamley, and M. Geoghegan, eds.), Wiley, New York, 2005.

[10]   B. Bhushan, ed., Springer Handbook of Nanotechnology, Springer, Berlin, 2004.

[11]   http://inside.mines.edu/~zhiwu/courses/550/lecture14.pdf

[12]   W. Thomson, Philosophical Magazine 42 (1871) 362.

[13]   E. Roduner, Chemical Society Reviews 35 (2006) 583.

[14]   http://www.metmuseum.org/toah/hd/glas/hd_glas.htm

[15]   K. L. Kelly, E. Coronado, L. L. Zhao, and G. C. Schatz, The Journal of Physical Chemistry B 107 (2002) 668.

[16]   N. N. Long, L. V. Vu, C. D. Kiem, S. C. Doanh, C. T. Nguyet, P. T. Hang, N. D. Thien, and L. M. Quynh, Journal of Physics: Conference Series 187 (2009) 012026.

[17]   P. K. Jain, K. S. Lee, I. H. El-Sayed, and M. A. El-Sayed, The Journal of Physical Chemistry B 110 (2006) 7238.

[18]   C. J. Murphy, T. K. Sau, A. M. Gole, C. J. Orendorff, J. Gao, L. Gou, S. E. Hunyadi, and T. Li, The Journal of Physical Chemistry B 109 (2005) 13857.

[19]   http://www.imaginenano.com/GENERAL/Presentations/PPM_LizMarzan.pdf

[20]   http://nanocluster.mit.edu/research.php

[21]   P. L. Stiles, J. A. Dieringer, N. C. Shah, and R. R. Van Duyne, Annual Review of Analytical Chemistry 1 (2008) 601.

[22]   M. J. Banholzer, J. E. Millstone, L. Qin, and C. A. Mirkin, Chemical Society Reviews 37 (2008) 885.

[23]   G. McNay, D. Eustace, W. E. Smith, K. Faulds, and D. Graham, Applied Spectroscopy 65 (2011) 825.

[24]   S. E. J. Bell and N. M. S. Sirimuthu, Chemical Society Reviews 37 (2008) 1012.

[25]   E. Fort and S. Grésillon, Journal of Physics D: Applied Physics 41 (2008) 013001.

[26]   J. Lakowicz, C. Geddes, I. Gryczynski, J. Malicka, Z. Gryczynski, K. Aslan, J. Lukomska, E. Matveeva, J. Zhang, R. Badugu, and J. Huang, Journal of Fluorescence 14 (2004) 425.

[27]   M. Aslam, I. S. Mulla, and K. Vijayamohanan, Applied Physics Letters 79 (2001) 689.

[28]   M. Brust, D. J. Schiffrin, D. Bethell, and C. J. Kiely, Advanced Materials 7 (1995) 795.

[29]   U. Simon, R. Flesch, H. Wiggers, G. Schon, and G. Schmid, Journal of Materials Chemistry 8 (1998) 517.

[30]   R. G. Osifchin, W. J. Mahoney, J. D. Bielefeld, R. P. Andres, J. I. Henderson, and C. P. Kubiak, Superlattices and Microstructures 18 (1995) 283.

[31]   G. Markovich, C. P. Collier, S. E. Henrichs, F. Remacle, R. D. Levine, and J. R. Heath, Accounts of Chemical Research 32 (1999) 415.

[32]   C. W. J. Beenakker, Physical Review B 44 (1991) 1646.

[33]   D. L. Feldheim and C. D. Keating, Chemical Society Reviews 27 (1998) 1.

[34]   J. H. Fendler, ed., Nanoparticles and Nanostructured Films, Wiley-Vch, Weinheim, 1998.

[35]   P. J. Thomas, G. U. Kulkarni, and C. N. R. Rao, Chemical Physics Letters 321 (2000) 163.

[36]   G. Cao, ed., Nanostructures & nanomaterials synthesis, properties and applications, Imperial College Press, London, 2004.

[37]   D. L. Leslie-Pelecky and R. D. Rieke, Chemistry of Materials 8 (1996) 1770.

[38]   N. Bao and A. Gupta, Journal of Materials Research 26 (2011) 111.

[39]   T. Ogawa, Y. Takahashi, H. Yang, K. Kimura, M. Sakurai, and M. Takahashi, Nanotechnology 17 (2006) 5539.

[40]   G. Schmid, Nanoparticles, From Theory to Application, WILEY-VCH Verlag GmbH & Co. KGaA, Weinheim, 2004.

[41]   http://www.electroiq.com/articles/mlw/print/volume-16/issue-4/featured/lithography-for-mobile-displays.html

[42]   http://mimech.com/printers/inkjet-printer-technology.asp

[43]   http://commons.wikimedia.org/wiki/File:V%C3%A4rviline_LCD.png

[44]   http://www.kettererkunst.com/dict/lithography.shtml

[45]   http://en.wikipedia.org/wiki/Nic%C3%A9phore_Ni%C3%A9pce

[46]   http://www.seas.upenn.edu/~umab/research.html

[47]   http://www.lithoguru.com/scientist/lithobasics.html

[48]   http://www.ece.gatech.edu/research/labs/vc/theory/photolith.html

[49]   P. Offermans, M. Crego-Calama, and S. H. Brongersma, Nano Letters 10 (2010) 2412.

[50]   http://www.icknowledge.com/misc_technology/PhotoChapter.pdf

[51]   http://en.wikipedia.org/wiki/22_nanometer

[52]   http://www.nonoscience.info/2008/02/27/introduction-to-microlithography/

[53]   A. A. Tseng, C. Kuan, C. D. Chen, and K. J. Ma, IEEE Transactions on Electronics Packaging Manufacturing 26 (2003) 141.

[54]   A. E. Grigorescu and C. W. Hagen, Nanotechnology 20 (2009) 292001.

[55]   D. F. Kyser and N. S. Viswanathan, Journal of Vacuum Science and Technology 12 (1975) 1305.

[56]   B. Cord, J. Yang, H. Duan, D. C. Joy, J. Klingfus, and K. K. Berggren, Journal of Vacuum Science & Technology B: Microelectronics and Nanometer Structures 27 (2009) 2616.

[57]   S. K. Choi, Vol. Doctor of Philosophy (Ph.D.), University of Illinois at Urbana-Champaign, 2009, p. 106.

[58]   http://www.itrc.narl.org.tw/Research/Product/Nano/ebeam-e.php

[59]   P. Chen, J. Gu, E. Brandin, Y.-R. Kim, Q. Wang, and D. Branton, Nano Letters 4 (2004) 2293.

[60]   T. A. Jung, A. Moser, H. J. Hug, D. Brodbeck, R. Hofer, H. R. Hidber, and U. D. Schwarz, Ultramicroscopy 42-44, Part 2 (1992) 1446.

[61]   E. Delawski and B. A. Parkinson, Journal of the American Chemical Society 114 (1992) 1661.

[62]   S. L. Brandow, W. J. Dressick, C. S. Dulcey, T. S. Koloski, L. M. Shirey, J. Schmidt, and J. M. Calvert, Journal of Vacuum Science & Technology B: Microelectronics and Nanometer Structures 15 (1997) 1818.

[63] P. Vettiger, G. Cross, M. Despont, U. Drechsler, U. Durig, B. Gotsmann, W. Haberle, M. A. Lantz, H. E. Rothuizen, R. Stutz, and G. K. Binnig, IEEE Transactions on Nanotechnology 1 (2002) 39.

[64] H. Zhang, Z. Li, and C. A. Mirkin, Advanced Materials 14 (2002) 1472.

[65] X. N. Xie, H. J. Chung, C. H. Sow, and A. T. S. Wee, Materials Science and Engineering: R: Reports 54 (2006) 1.

[66] T. Qian, S. San-Qiang, and Z. Limin, Journal of Nanoscience and Nanotechnology 4 (2004) 948.

[67] A. Fuhrer, A. Dorn, S. Lüscher, T. Heinzel, K. Ensslin, W. Wegscheider, and M. Bichler, Superlattices and Microstructures 31 (2002) 19.

[68] S. F. Lyuksyutov, R. A. Vaia, P. B. Paramonov, S. Juhl, L. Waterhouse, R. M. Ralich, G. Sigalov, and E. Sancaktar, Nature Materials 2 (2003) 468.

[69] Y. Li, B. W. Maynor, and J. Liu, Journal of the American Chemical Society 123 (2001) 2105.

[70] X. N. Xie, H. J. Chung, C. H. Sow, K. Adamiak, and A. T. S. Wee, Journal of the American Chemical Society 127 (2005) 15562.

[71] R. Garcia, M. Calleja, and H. Rohrer, Journal of Applied Physics 86 (1999) 1898.

[72] T. F. Carter, ed., The invention of printing in China and its spread westward, Ronald Press Co., 1955.

[73] Y. Xia and G. M. Whitesides, Angewandte Chemie - International Edition 37 (1998) 551.

[74] B. D. Gates, Q. Xu, J. C. Love, D. B. Wolfe, and G. M. Whitesides, Annual Review of Materials Research 34 (2004) 339.

[75] X.-M. Zhao, Y. Xia, and G. M. Whitesides, Journal of Materials Chemistry 7 (1997) 1069.

[76] B. D. Gates, Materials Today 8 (2005) 44.

[77] Y. Xia and G. M. Whitesides, Annual Review of Materials Science 28 (1998) 153.

[78] C. SJ and S. JA, eds., Siloxane Polymers, Englewood Cliffs, NJ: Prentice Hall, 1993.

[79] http://mrsec.wisc.edu/Edetc/background/PDMS/index.html

[80] http://www.ifm.liu.se/applphys/biorgel/education/mikrosystem-nanobiologi-t/material-samt-tipstricks/Soft_Lithography_for_Dummies.pdf.

[81] D. Armani, C. Liu, and N. Aluru, in Twelfth IEEE International Conference on Micro Electro Mechanical Systems 1999, p. 222.

[82] R. S. Kane, S. Takayama, E. Ostuni, D. E. Ingber, and G. M. Whitesides, Biomaterials 20 (1999) 2363.

[83] D. Qin, Y. Xia, and G. M. Whitesides, Nature Protocols 5 (2010) 491.

[84] E. Delamarche, H. Schmid, B. Michel, and H. Biebuvck, Advanced Materials 9 (1997) 741.

[85] A. Bietsch and B. Michel, Journal of Applied Physics 88 (2000) 4310.

[86] H. Schmid and B. Michel, Macromolecules 33 (2000) 3042.

[87] Y. Y. Huang, W. Zhou, K. J. Hsia, E. Menard, J.-U. Park, J. A. Rogers, and A. G. Alleyne, Langmuir 21 (2005) 8058.

[88] Q. Guo, X. Teng, and H. Yang, Nano Letters 4 (2004) 1657.

[89] X. Fan, D. T. Tran, D. P. Brennan, and S. R. J. Oliver, Journal of Physical Chemistry B 110 (2006) 11986.

[90] Y. Xia, J. J. McClelland, R. Gupta, D. Qin, X. M. Zhao, L. L. Sohn, R. J. Celotta, and G. M. Whitesides, Advanced Materials 9 (1997) 147.

[91] B. D. Gates, Q. Xu, J. C. Love, D. B. Wolfe, and G. M. Whitesides, Annual Review of Materials Research 34 (2004) 339.

[92]   Y. Xia, J. A. Rogers, K. E. Paul, and G. M. Whitesides, Chemical Reviews 99 (1999) 1823.

[93]   E. Kim, Y. Xia, and G. M. Whitesides, Nature 376 (1995) 581.

[94]   E. Kim, Y. Xia, and G. M. Whitesides, Journal of the American Chemical Society 118 (1996) 5722.

[95]   M. J. Lochhead and P. Yager, Materials Research Society Symposium - Proceedings 444 (1997) 105.

[96]   H. W. Shim, J. H. Lee, B. Y. Kim, Y. A. Son, and C. S. Lee, Journal of Nanoscience and Nanotechnology 9 (2009) 1204.

[97]   W. Huang, J. Li, C. Luo, J. Zhang, S. Luan, and Y. Han, Colloids and Surfaces A: Physicochemical and Engineering Aspects 273 (2006) 43.

[98]   G. M. Whitesides and J. C. Love, Scientific American 285 (2001) 38.

[99]   G. M. Whitesides, E. Ostuni, S. Takayama, X. Jiang, and D. E. Ingber, Annual Review of Biomedical Engineering 3 (2001) 335.

[100]   D. Myers, Surfaces, Interfaces, and Colloids, VCH, New York, 1991.

[101]   A. George, D. H. A. Blank, and J. E. ten Elshof, Langmuir 25 (2009) 13298.

[102]   E. King, Y. Xia, X.-M. Zhao, and G. M. Whitesides, Advanced Materials 9 (1997) 651.

[103]   S.-H. Lee, H.-N. Kim, R.-K. Kwak, and K. Y. Suh, Langmuir 25 (2009) 12024.

[104]   X. Yu, Z. Wang, R. Xing, S. Luan, and Y. Han, Polymer 46 (2005) 11099.

[105]   J. A. Rogers and R. G. Nuzzo, Materials Today 8 (2005) 50.

[106]   A. Kumar and G. M. Whitesides, Applied Physics Letters 63 (1993) 2002.

[107]   H. O. Jacobs and G. M. Whitesides, Science 291 (2001) 1763.

[108]   T.-i. Kim, J.-h. Kim, S. J. Son, and S.-m. Seo, Nanotechnology 19 (2008) 295302.

[109]   K. Felmet, Y.-L. Loo, and Y. Sun, Applied Physics Letters 85 (2004) 3316.

[110]   S.-H. Hur, D.-Y. Khang, C. Kocabas, and J. A. Rogers, Applied Physics Letters 85 (2004) 5730.

[111]   M. A. Meitl, Z.-T. Zhu, V. Kumar, K. J. Lee, X. Feng, Y. Y. Huang, I. Adesida, R. G. Nuzzo, and J. A. Rogers, Nature Materials 5 (2006) 33.

[112]   Q. Xia and S. Y. Chou, in Proceedings of SPIE - The International Society for Optical Engineering, Vol. 5725, 2005, p. 180.

[113]   M. D. Austin, H. Ge, W. Wu, M. Li, Z. Yu, D. Wasserman, S. A. Lyon, and S. Y. Chou, Applied Physics Letters 84 (2004) 5299.

[114]   D. J. Resnick, S. V. Sreenivasan, and C. G. Willson, Materials Today 8 (2005) 34.

[115]   S. Y. Chou, P. R. Krauss, and P. J. Renstrom, Journal of Vacuum Science and Technology B: Microelectronics and Nanometer Structures 14 (1996) 4129.

[116]   S. H. Ahn and L. J. Guo, ACS Nano 3 (2009) 2304.

[117]   M. T. Cuberes, R. R. Schlittler, and J. K. Gimzewski, Applied Physics Letters 69 (1996) 3016.

[118]   X. Li, W. Cai, J. An, S. Kim, J. Nah, D. Yang, R. Piner, A. Velamakanni, I. Jung, E. Tutuc, S. K. Banerjee, L. Colombo, and R. S. Ruoff, Science 324 (2009) 1312.

[119]   M. Yaman, T. Khudiyev, E. Ozgur, M. Kanik, O. Aktas, E. O. Ozgur, H. Deniz, E. Korkut, and M. Bayindir, Nature Materials 10 (2011) 494.

[120]   R. E. Morris, Nature Chemistry 3 (2011) 347.

[121]   R. Feynman, The Character of Physical Law, The M.I.T. Press, 1965.

[122]   http://nutrition.jbpub.com/resources/chemistryreview9.cfm

[123]   A. Hagfeldt and M. Grätzel, Accounts of Chemical Research 33 (2000) 269.

[124]   J. J. Parks, A. R. Champagne, T. A. Costi, W. W. Shum, A. N. Pasupathy, E. Neuscamman, S. Flores-Torres, P. S. Cornaglia, A. A. Aligia, C. A. Balseiro, G. K.-L. Chan, H. D. Abruña, and D. C. Ralph, Science 328 (2010) 1370.

[125] J. He, O. Sankey, M. Lee, N. Tao, X. Li, and S. Lindsay, Faraday Discussions 131 (2006) 145.

[126] C. Thelander, P. Agarwal, S. Brongersma, J. Eymery, L. F. Feiner, A. Forchel, M. Scheffler, W. Riess, B. J. Ohlsson, U. Goesele, and L. Samuelson, Materials Today 9 (2006) 28.

[127] G. Wang, Y. Kim, M. Choe, T.-W. Kim, and T. Lee, Advanced Materials 23 (2011) 755.

[128] B. D. Cullity and S. R. Stock, Elements of X-Ray Diffraction, Prentice-Hall Inc., 2001.

[129] C. L. Jia, M. Lentzen, and K. Urban, Science 299 (2003) 870.

PART II

Movable Au Microplates - Synthesis, Characterization and Important Properties*

SUMMARY

Single crystalline Au(111) surface is the most sought after platform for studying molecular and other interesting phenomenon. Here, synthesis of giant Au(111) single crystalline hexagonal and triangular Au microplates was performed. The single crystal surfaces are smooth and possess areas extending over ~1,00,000 μm^2 with thickness in the range of 30 to 2000 nm. The synthesis method is simple involving a one-step thermolysis process i.e., heating on a hot plate, of $(AuCl_4)^-$-tetraoctylammonium bromide complex. The microplates are self-supporting and can be easily manipulated using a sharp pin, a property which enables them to serve as substrates for living cells. The microplate surface is non-toxic to living cells and can enhance the fluorescence signal from flurophores residing within the cell by an order magnitude. The microplates are atomically flat, ideal as microscopy substrates and molecular electrodes. The growth process of these microplates was also studied in detail. Scanning electron microscopy performed using a heated stage showed nucleation of nanoparticles into dendrimeric structures and rudimentary shapes, which took several minutes to anneal into well formed single crystalline triangles and hexagons. Amazingly quite often, the plates were held vertical to the substrate surface during the growth even at large sizes, as evidenced by in situ optical microscopy. Three growth modes namely nucleation of tiny nanoparticles into dendrimeric structures which assemble into specific shapes, atom-by-atom addition from the precursor feedstock and fusion of the 3D particles to the growing microplates, have been inferred from this study using real time microscopy.

II.1 INTRODUCTION

Anisotropic metal nanostructures form an interesting area of research [1] with potentially important applications in diverse fields such as catalysis [2], multicolor diagnostics [3] and optoelectronics [4]. An anisotropic structure is almost anything that is not even approximately spherical, obvious examples being prismatic [5] and elongated nanoparticles (the latter also known as nanorods), triangular [6] and hexagonal [7] plate-like structures, decahedra, icosahedra, and truncated tetrahedral structures [8]. Other structures include nanobelts [9], tetrahexahedral nanocrystals [10], rice-shaped particles [11], pentagonal bipyramidal [12] and star-shaped particles [13]. As a triumph of bottom-up approaches using chemical methods, there is much impetus on growing polygonal plate-like structures [14,15] with projected applications in infrared absorbing optical coatings [16], surface plasmon resonators [17], high activity electrocatalysts [18], STM substrates [19] etc., and as substrates for surface enhanced Raman spectroscopy [20]. For such applications it is desirable to have plates as large as possible but of submicron thickness, however, not compromising with the flatness and surface smoothness. Towards this end, there have been close to 100 reports in the literature during the last one decade (Table II.1).

Table II.1 Literature reports which are related to synthesis of plate-like structures. This table is comprehensive but not exhaustive.

Sl. No.	Metal nanostructure	Edge length (µm)	Reference
1.	Au-nanoplates	0.5 – 2	[21]
2.	Ag- nanoprisms	0.1-0.5	[22]
3.	Au- nanorings	0.08	[23]
4.	Au- nanowires & sheets	1-10	[24]
5.	Au-nanoplates	0.3 - 1.8	[14]
6.	Au-nanoplates	0.1 - 0.8	[25]
7.	Au-nanoplates	1-10	[26]
8.	Au-micrometer plates	0.5 – 2	[15]
9.	Au-nanoplates	0.08 - 0.5	[27]
10.	Au-nanoplates	2 – 10	[28]
11.	Au-nanoplates	5 – 30	[29]
12.	Au-nanocrystals	5 – 30	[30]
13.	Au-nanoplates	0.5-5	[31]
14.	Au-nanoplates	0.08	[32]
15.	Au-nanoplates	0.08 – 2	[33]
16.	Au-nanoplates	2	[16]
17.	Au-nanoplates	5-40	[34]
18.	Au-nano and microplates	0.1 - 10	[35]

19.	Au-nanogears	0.4	[36]
20.	Au-polygons	0.5 - 2	[37]
21.	Au-nanoplates	2 - 15	[38]
22.	Au-nanoplates	2 - 10	[39]
23.	Au-microplates	5 - 20	[40]
24.	Au-nanoplates	12 - 35	[41]
25.	Au- nanoplates	10 - 40	[42]
26.	Au-nanosheets, belts	7 - 20	[43]
27.	Au-microplates	0.5 - 2	[44]
28.	Au-micrometer sized crystals	10 - 50	[45]
29.	Ag, Au, Pd, Pt-microplates	0.04 - 0.8	[46]
30.	Au nanoplates	0.1-5	[47]
31.	Au-µPn	0.05 - 3	[48]
32.	Ag-triangular silver nanocrystals	0.1 - 0.4	[49]
33.	Au nanoplates and nanorods	0.5	[50]
34.	Au-nanoplates	0.03 - 15	[51]
35.	Au-nanoplates	1 - 5	[52]
36.	Au-microplates	10 - 500	[53]
37.	Au nanoplates	0.5 - 2	[54]
38.	Au-nanoplates	0.6 - 3	[55]
39.	Au-nanogears	0.2 - 0.6	[56]
40.	Au nanobelts	2 - 21	[9]
41.	Au-nanoplates	0.05 - 0.5	[57]
42.	Au-nanoplates	2 - 20; 100 (cup like)	[58]
43.	Au-micrometer crystals	5 - 30	[59]
44.	Au-hexagonal nanoparticles	0.035	[60]
45.	Ag-nanosheets	3 - 8	[61]
46.	Au-nanoplates	1 - 5	[62]
47.	Au-microplates, nanotadpoles, nanokites	1 - 3	[63]
48.	Au-nano and microstructures	10 - 40	[64]
49.	Au- nanoplates	0.5 - 2	[65]
50.	Au nanowires	40	[17]
51.	Au- icosohedral	Few hundred nm	[66]
52.	Multishaped Au nanoparticles	Few hundred nm	[11]
53.	Au-nanoplates	1 - 5	[67]
54.	Au-nanoplates	10 - 30	[68]
55.	Au-nanoplates	4 -15	[69]
56.	Au- nanoprism	0.2 - 2.5	[18]
57.	Au-nanoplates	4 - 50	[70]
58.	Multishaped Au nanoparticles	Few hundred nm	[71]
59.	Pd-nanohexagons	0.025	[72]

60.	Au-Nanocorolla	Few hundred nm	[73]
61.	Au-nanoplates	0.5	[74]
62.	Au-nanoplates	0.1 – 1	[75]
63.	Au-nanoplates	1 – 2	[76]
64.	Au-nanoplates	0.015 - 0.5	[77]
65.	Au-nanoplates, twinned plates	0.1-15	[78]
66.	Au-nanoflowers	Few hundred nm	[79]
67.	Au-nanosheets & polyhedral	5 – 20	[80]
68.	Au-nanoplates	0.5 – 2	[81]
69.	Au-nanoplates	0.2-0.5	[82]
70.	Au-triangular nanoplates	0.1	[83]
71.	Au-microplates	4 – 10	[84]
72.	Au- nanoplates	Few hundred nm	[7]
73.	Au-microplates	10	[85]
74.	Au-nanoplates	2 – 10	[86]
75.	Au-nanotriangles	0.2 - 0.5	[6]
76.	Au-nanoplates	0.08 - 0.2	[87]

While the literature in the last one decade is abundant with reports on the synthesis and properties of such anisotropic structures, aspects related to growth is still being actively pursued [30]. Theoretical models [88-90] based on the energy minimization, have addressed how different shapes can emerge from a tiny nucleus and what all factors could be at play. There have been many experimental attempts as well, employing techniques such as in situ high resolution transmission electron microscopy (HRTEM) [91], small angle X-ray scattering (SAXS) [92,93], X-ray absorption fine structure (XAFS) [94], X-ray diffraction (XRD) [95], dynamic light scattering (DLS) [96] and UV-Vis absorption spectroscopy [97-100]. Employing in situ XAFS and optical measurements, Murayama et al. evidenced the growth of Ag triangular nanoplates as the aggregation of small spherical nanoparticles [94]. The anisotropy of the growing particle expresses itself as increasing absorption at longer wavelengths due to longitudinal plasmon. From total energy calculations, it is proposed that the energy required to build larger anisotropic structures could be less than the one required to build isotropic structures [88]. Several growth studies have been carried out ex situ by arresting the growth at intermediate stages. The spontaneous transformation process of aggregated nanoparticles to triangular and hexagonal nanocrystals confined by a dendrimeric structure has been reported [47]. Seed formation followed by fusion of aggregates and recrystallization leading to Au nanoplate formation has been observed [7]. In the case of nanobelts, it was observed that nanotriangles assemble in 1D manner and recrystallize to

form single-crystalline nanobelts [9]. Small nanoplates connecting together along the {110} lateral planes produce large hexagonal and triangular nanoplates which was confirmed using TEM analysis [101]. Based on the above studies, it may be stated that where organic moieties are part of the synthetic process, their preferential adsorption to specific nanocrystal surface sites or facets, may poison or accelerate the addition of fresh adatoms thus inducing anisotropy. Such restrictions may also occur in micellar organization formed by surfactants. Another factor responsible for anisotropic growth is the presence of twin planes in the nanocrystal.

II.2 SCOPE OF THE PRESENT INVESTIGATION

The present investigation pertains to the synthesis of giant, flat, single crystalline Au microplates. While most reports relate to sub-micron and few micron sized Au hexagonal and triangular plates, wider plates with sides extending over tens of microns are not commonly found (Table II.1); in the reported instances [29,43,53,58], the plates seem fragile containing defects and are found mingled with other nanostructures. The separation of desired plates from the mass is like removing a needle from haystack! Top-down methods too, have aimed at producing faceted structures for use as substrate in STM studies [102]. Generally, these structures bear unfriendly geometries and macroscopic thickness, making them unsuitable for many of the applications. The manipulation and organization of the as-made plates has proved rather difficult. In one recent instance, the separation and assembly of small Au triangles was made possible by selective precipitation [103]. Thus, it has not been trivial to produce metal microplates with the mentioned qualifiers.

Previous studies on growth of Au microplates have all been carried out in the solution phase [7,10,47,101] as these plates are typically few hundred nanometers to few microns. Real time imaging of the growth of plates on solid substrates from nanometer size to few tens of microns using high resolution scanning electron microscopy and optical microscopy, therefore could not be thought of. The present study with large microplates is based on solid state synthesis and attempts to gain insight into growth using real time imaging.

II.3 EXPERIMENTAL DETAILS

Hydrogen tetrachloroaurate(III) hydrate, tetraoctylammonium bromide (ToABr) and toluene were obtained from Sigma Aldrich and used without further purification. The water used throughout this investigation was double distilled and deionised. The precursor for microplate synthesis is essentially a complex containing $(AuCl_4)^-$ ions stabilized in ToABr

(25 mM in toluene), termed as $(AuCl_4)^-$-ToABr. It was prepared following a literature procedure [104]. The precursor was prepared by phase transfer of $(AuCl_4)^-$ ions from an aqueous solution (25 mmol/L, 3.2 mL) to toluene (8 mL) using ToABr (50 mmol/L) as phase transfer agent. This corresponds to a $(AuCl_4)^-$ to ToABr ratio of 1:4.4. Likewise, the phase transfer was carried out with varying ratios of $(AuCl_4)^-$ and ToABr (1:1 to 1:8.8). The two-phase mixture was vigorously stirred until all the $(AuCl_4)^-$ ions were transferred into the organic layer. As the phase transfer proceeded, the yellow colored bottom aqueous layer became colorless and the top organic layer developed a red color.
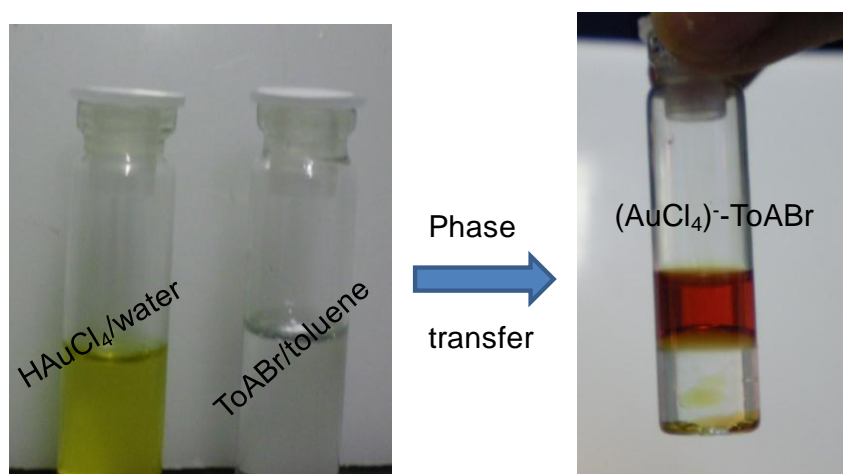
Figure II.1 Photographs illustrating the phase transfer process.

The organic layer was separated and drop coated onto the chosen substrate. Different substrates have been tried out - Si, glass, stainless steel, mica or HOPG and flexible substrates such as polyimide, polydimethylsiloxane - almost any smooth surface that can stand temperature and remain insoluble in the solvent should serve for this purpose. Thermolysis was carried out in air at 130-250 °C for 1-55 hrs. In our experience, the thermal treatment was most effective in producing microplates than using external reducing or stabilsing agents. All such attempts led to nanoparticle formation. Following thermolysis, a gentle wash in toluene was done to remove the undecomposed precursor, if any.

Cell Culture and Immunofluorescence

The KB or H1299 or 3T3 cells were grown continuously as a monolayer at 37°C and 5% CO_2 in DMEM medium (Sigma). The DMEM medium was supplemented with penicillin (100 units/ml), streptomycin (100 mg/ml), and 10% heat-inactivated fetal bovine calf serum (FBS) before use. To visualize the effect of Au microplates onto the cellular system KB, H1299 or 3T3 cells were cultured as monolayer on cover slips (coated with Au microplates) in DMEM medium. Cells were grown for 24 hrs, then immunofluorescence was carried out

[105]. Fixed cells were probed with anti-acetylated histone H3 (Calbiochem) polyclonal antibodies followed by secondary antibody conjugated with Alexa 488 (Invitrogen). In case of tubulin, fixed cells were probed with antitubulin monoclonal antibody (Cabiochem) followed by secondary antibody conjugated with Alexa 568 (Invitrogen). To stain the chromosomal DNA Hoechst 33528 (Sigma) was used.

II.4 RESULTS AND DISCUSSION

II.4.1 Synthesis and characterization of giant Au microplates

The precursor is essentially $(AuCl_4)^-$ ions stabilized by tetraoctylammonium bromide in toluene (25 mM), termed as Au-ToABr. The synthesis process involves two steps, drop coating or spin coating of Au-ToABr precursor onto a given substrate and thermolysing it at 130 °C in air to give rise to reduced Au (see scheme in Figure II.2a). After thermolysis, the unreacted Au-ToABr was washed off in toluene. After 24 hrs of thermolysis, the reduced Au was in the form of microplates, with many of them having edge lengths above 100 μm. The optical microscopy images of a few typical plates are shown in Figure II.2b. As shown in the histogram in Figure II.2c, microplates with areas 5000 - 10000 $μm^2$ were commonly seen. The thickness was more frequently sub-100 nm (Figure II.2d). The area and thickness had no definite relation, in the two such cases given in Figure II.2e, the smaller hexagon (top) is ~1 μm thick while the thickness of the bottom truncated triangle is only ~ 100 nm. Figure II.2f shows a typical low magnification SEM image with several microplates covering the substrate; there are very few particulates.

$(AuCl_4)^-$-ToABr is a crystalline molecular solid complex, as shown by XRD data (see Figure II.3). The thermolysis process initially melts the precursor (m.p. 85 ºC) and brings about the reduction of Au(III) to Au(I) by the formation of colorless $AuBr_2^-$, followed by the reduction of Au(I) to Au(0), which typically goes on for several hours. The reaction is essentially unaided by any solvent. Figure II.3 shows the powder XRD pattern from a film of $(AuCl_4)^-$-ToABr precursor thermolysed at 250 °C for 30 min. The peaks in XRD could be indexed to the standard face centered cubic (FCC) crystalline structure of Au (a = 4.078, JCPDS PDF No. 040784). There is essentially one intense sharp peak assignable to (111), indicating the high purity and single phase nature of the obtained Au microplates. Furthermore, the relative diffraction intensity of (111) to (200) is 100:0.02, which is much lower than the corresponding value from bulk Au (100:52, JCPDS PDF No. 040784).
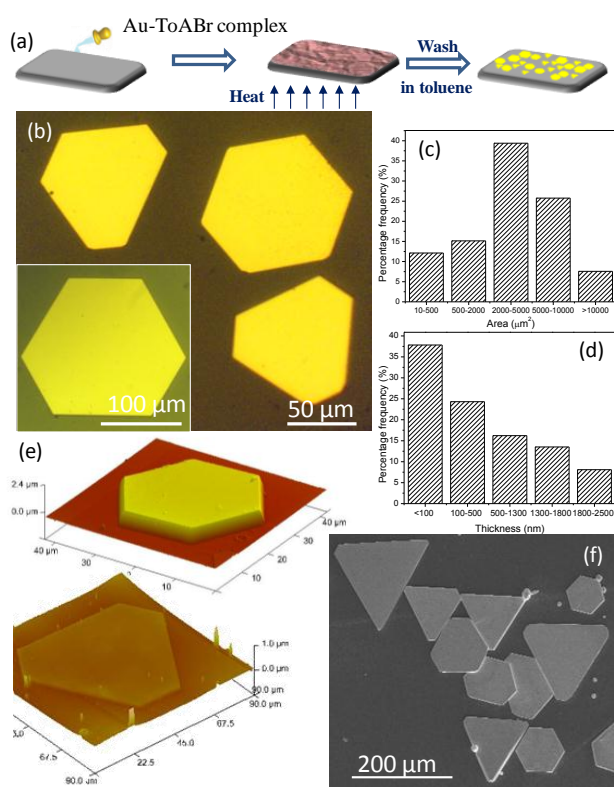
Figure II.2 (a) Schematic showing the procedure for making Au microplates. First, Au-ToABr solution is coated onto a given substrate and then thermolysed at 130 °C. (b) Optical image showing the microplates, a large one with the area of ~12000 μm^2 is shown in the inset. (c) and (d) are the histograms of the area and thickness of the plates respectively. (e) AFM topography images of a thick microplate along with the thin one at the bottom. (f) A low magnification SEM image showing several Au microplates on the substrate.
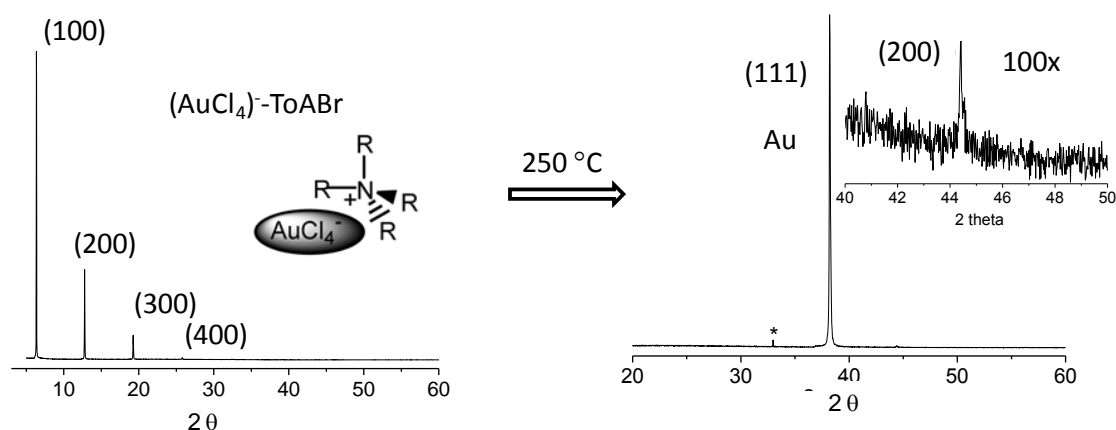
Figure II.3 XRD pattern of the thermolysed Au-ToABr with the peaks matching with the JCPDS (PDF #040784), * corresponds to a peak from the Si substrate. The inset shows the (200) peak with its intensity multiplied by 100 times.

The process of transformation of Au(III) to Au(0) to form microplates was followed by in-situ FTIR and TGA measurements (Figure II.4). Prior to thermolysis, the room temperature FTIR spectrum of (AuCl$_4$)$^-$-ToABr displays characteristic C-H stretches of the

methylene and the end methyl groups of the alkane chain in the 2800-3000 cm^{-1} region (Figure II.4a). The symmetric and anti-symmetric methylene C-H stretches appear around 2851 and 2920 cm^{-1}. The methyl symmetric and antisymmetric stretches are centered around 2875 and 2953 cm^{-1}. As the thermolysis progresses above 130 °C, these peaks seem to shift upwardly by at least 4 cm^{-1}. This is possible existence of defects in alkane chains [106] at elevated temperatures. The FTIR spectrum at 250 °C is featureless, indicating complete metallization. At 250 °C, the residual weight (10.4%) in TGA data nearly corresponds to the Au content in the complex with no residual from the hydrocarbon. This marks the complete removal of ToABr. If the residue of 10.4% in TGA (see region IV in Figure II.4b) is taken to be the metallic species (which is supported by the XRD in Figure II.3), the starting precursor would correspond to $N^+(C_8H_{17})_4AuCl_4^-.2N(C_8H_{17})_4Br$ (molecular weight, 1899.25). This is somewhat less compared to the starting ratio (1:4.4); some loss of ToABr units is expected at the aqueous-organic interface.
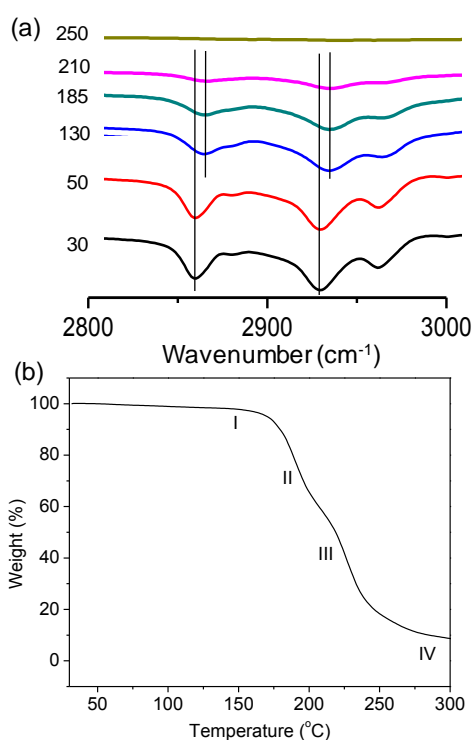
Figure II.4 (a) In-situ FTIR spectra of the $(AuCl_4)^-$-ToABr precursor subjected to thermolysis in air at various temperatures. (b) Thermogravimetric analysis of the precursor prepared with $(AuCl_4)^-$ and ToABr ratio of 1:4.4. The weight loss in TGA occurs in four steps - region I (5.04%), regions II (51.2%), region III (33.25%) and region IV (residue, 10.4%) correspond respectively to the solvent evaporation, decomposition and desorption of ToABr, ToA and chloride ions, and the metallic residue.

With the quest for obtaining giant Au microplates, the recipe was optimized further. Freshly prepared Au-ToABr precursor solution (100 µL, 200 mM) was drop coated onto a well cleaned thin glass slide and heated at 130 °C in air on a hot plate for 55 hrs to produce

large Au single crystals. Thus formed Au microplates are visible even to the unaided eye. These microplates possess significantly larger areas ~80000 to 1,00,000 μm^2 i.e., ~ 0.1 mm^2 (Figure II.5). In terms of synthesis, the present recipe differs in certain parameters in that, keeping the thermolysis temperature as low as possible i.e., at 130 °C, the annealing time was increased from few hrs to few days. The slower kinetics seems to play an important role in yielding larger microplates. Also, the concentration of the precursor does not proportionately increase the size of the microplates, instead there was an optimum concentration i.e., 200 mM above or below which smaller microplates were obtained. Importantly, a freshly prepared Au-ToABr solution unexposed to ambient light was found to be much more effective than an aged solution left in the ambient. As is well known [107], aged $(AuCl_4)^-$ solutions contain some reduced Au species which may follow a different trend of growth than those from the molten precursor and in effect, hinder the latter growing into large sized single crystals.
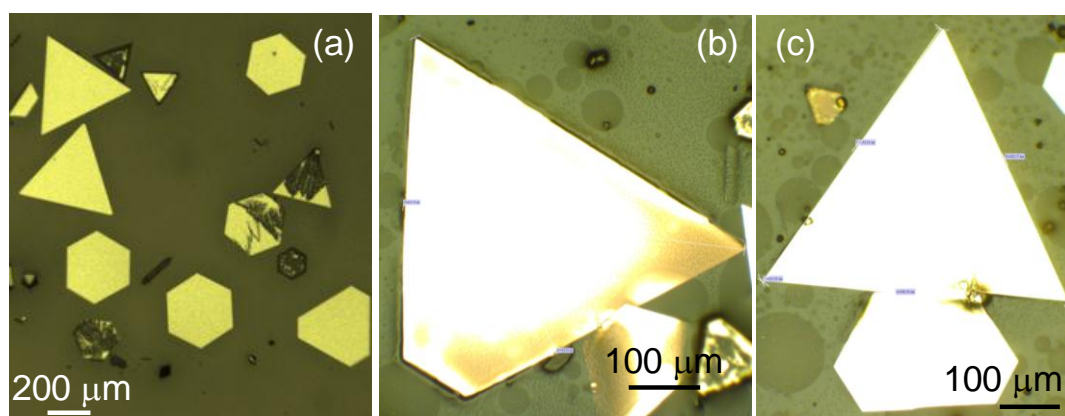
Figure II.5 Giant Au microplates: (a) Optical images of the as-synthesized microplates. Dark traces on some of the microplates are due to the unreacted precursor. (b) and (c) show the magnified images of the giant Au microplates. Thermolysis was done at 130 °C for 55 hrs.

The surface of the microplates is devoid of possible contaminants such as carbon as revealed by EDS mapping data (Figure II.6). X-ray photoelectron spectra in the C1S core-level region (284 eV) had negligible intensity. The $Au4f_{7/2}$ core level spectrum was intense with peak position at ~ 84 eV, typical of metallic Au (Figure not shown).

The microplates present themselves as ideal as scanning probe microscopy substrates. Firstly, Au microplates are atomically smooth (surface roughness, <1 nm over tens of micrometers, see Figure II.7a and b). They are easily identifiable on a given substrate owing to their large size. The microplates being made up of Au, can be easily functionalized. A STM image from Au microplate surface obtained in a preliminary study, is shown Figure II.7c.
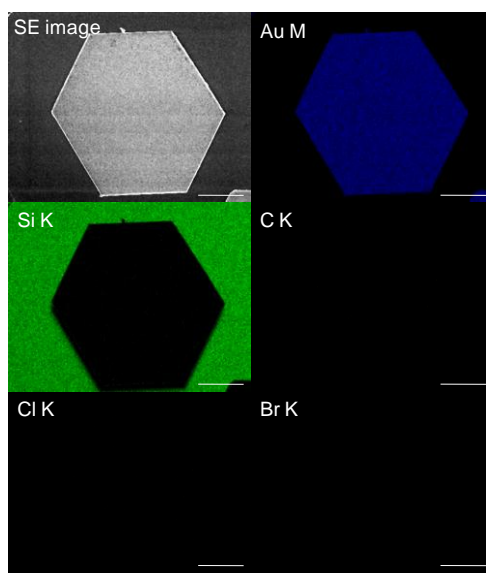
Figure II.6 EDS map of a Au hexagonal microplate. All scale bars correspond to 20 μm. No features are visible in the C K, Cl K, BrK EDS maps.
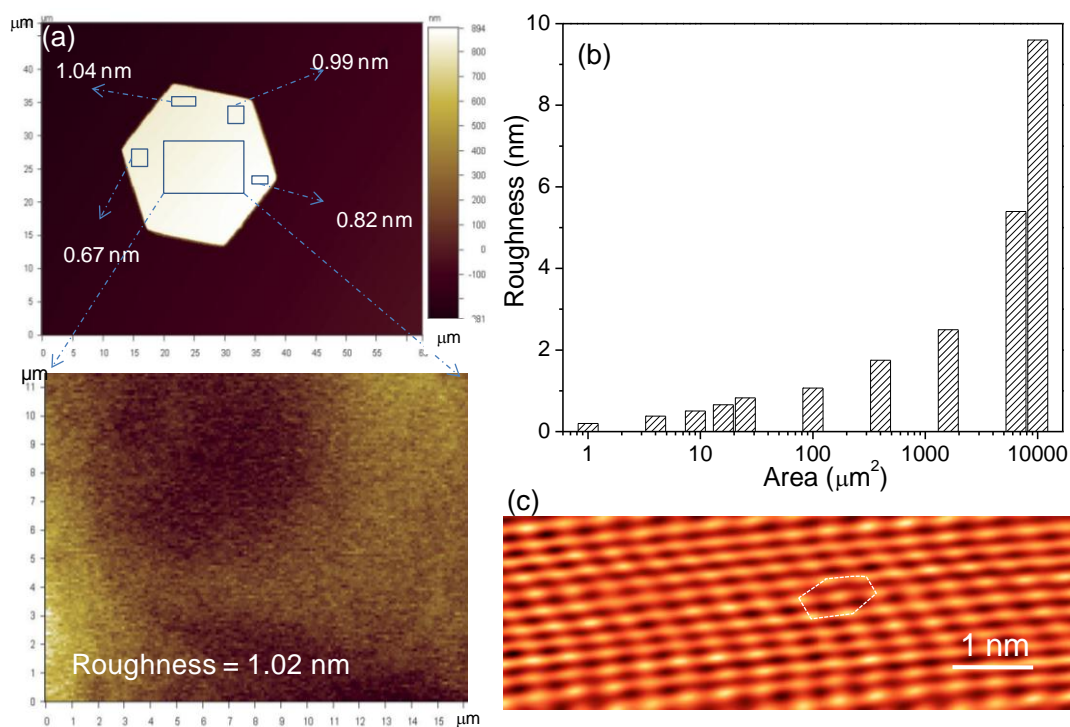
Figure II.7 Ideal scanning probe microscopy substrates: (a) Optical profilometric image showing a hexagonal microplate with roughness from various marked regions shown as indicated by arrows. (b) Average roughness vs area from which roughness was calculated. (c) STM image of a Au microplate, showing typical (111) orientation (see dotted line). The noise and drift in the image is due to the instrument instability.

Figure II.8a shows TEM image of a truncated triangular plate. The contours seen in the image originate from the diffraction effects arising due to slight bending of the thin plate on the TEM grid surface [101]. The selected area electron diffraction (SAED) pattern shown in the inset is hexagonally symmetric and corresponds to Au (FCC) crystalline lattice viewed

along the <111> direction. The spots representing {220}, {422}, {440} bragg planes are clearly visible. Importantly, no kinematically forbidden spots such as 1/3{422} were observed, which have been attributed to the presence of two or more twin planes in the nanoplates [55,101]. HRTEM image of the along <111> zone axis in Figure II.8b reveals Au atoms (white dots) in hexagonal packing with a spacing of ~1.4 Å between the rows, which correspond to the {220} planes. This observation goes well with the geometric model of a FCC crystal, when viewed along the <111> direction.
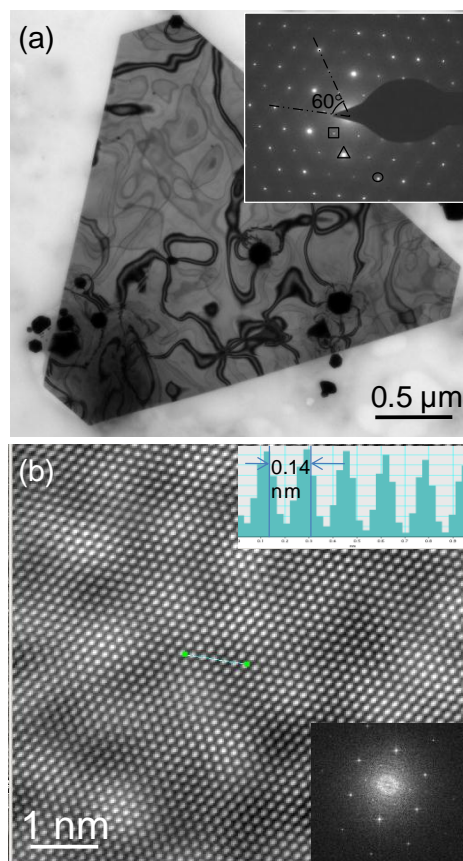
Figure II.8 (a) TEM image of the Au microplate, with the SAED pattern shown as inset. The ED is hexagonally symmetric and the spots marked by square, triangle and circle correspond to {220}, {422}, {440} planes respectively. (b) HRTEM image of the microplate; corresponding FFT is shown as inset. Bright dots are Au atoms with the spacing marked in the top inset.

The UV-visible absorption spectrum of the Au microplates is shown in Figure II.9. It shows a broad band extending from 500 to 900 nm due to plasmon absorption from metallic Au. As there is not much absorption around 520-530 nm, the population of isolated nanoparticles may be negligible. Notably, the metallic plates are IR absorbing. The synthesis of the Au microplates can be carried out on various substrates, such as Si, glass, stainless steel, polyimide, polydimethylsiloxane (PDMS), mica or HOPG etc. In fact, almost any substrate that can stand the thermolysis temperature and remain insoluble in the solvent (i.e.,

toluene) can be used. Figure II.10 shows the SEM images of the Au microplates synthesized on various substrates, at a thermolysis temperature of 250 °C for 3 hrs. Even on a rough surface such as textured Si, Au microplates could grow but with small cracks on the surface. Among others, Si and coverslip substrates prove to be the best for growing giant unbroken Au microplates with good yield (Figure II.10).
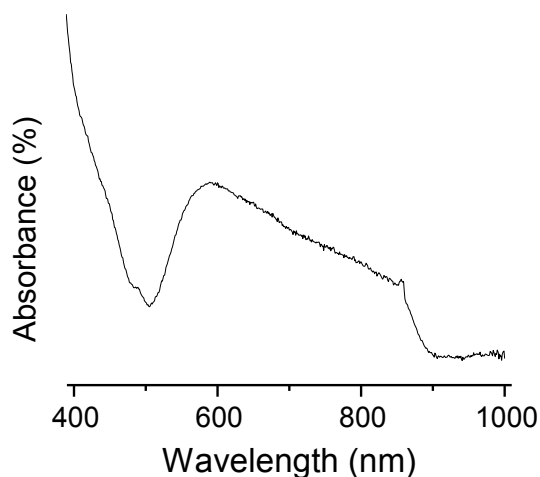
Figure II.9 UV-Visible absorption spectrum of the Au microplates on glass substrate.
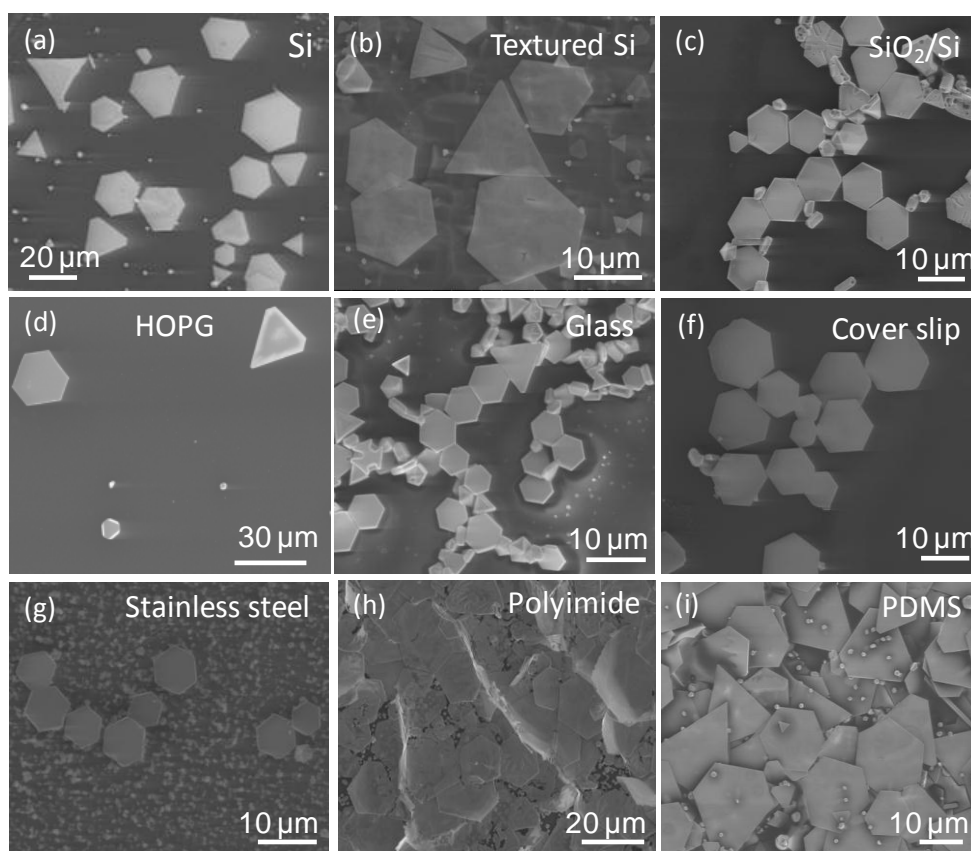
Figure II.10 SEM images of the Au microplates synthesized on various substrates, indicated over the image. Thermolysis was done at 250 °C for 3 hrs.

The effect of varying the ratio, $(AuCl_4)^-$ to ToABr, during the preparation of the precursor for Au microplates has been examined. As the ToABr proportion in the precursor increased from being 1:1, the edge lengths of the resulting microplates increase (Figure II.11a). The ratio of 1:4.4 for $(AuCl_4)^-$:ToABr proves to be the most effective to yield large microplates at 130 °C. A further increase in the ToABr content makes the overall Au content less and the resulting microplates have reduced sizes. The effect of thermolysis temperature was also examined. As shown in Figure II.11b, large edge lengths are found with 130 °C treatment. With the increase in the thermolysis temperature, the decomposition kinetics is expected to be faster, influencing adversely the growth of the plates. Thus at elevated temperatures, small sized plates are obtained along with Au nanoparticles. Below 130 °C, the decomposition of $(AuCl_4)^-$-ToABr does not seem possible at all.
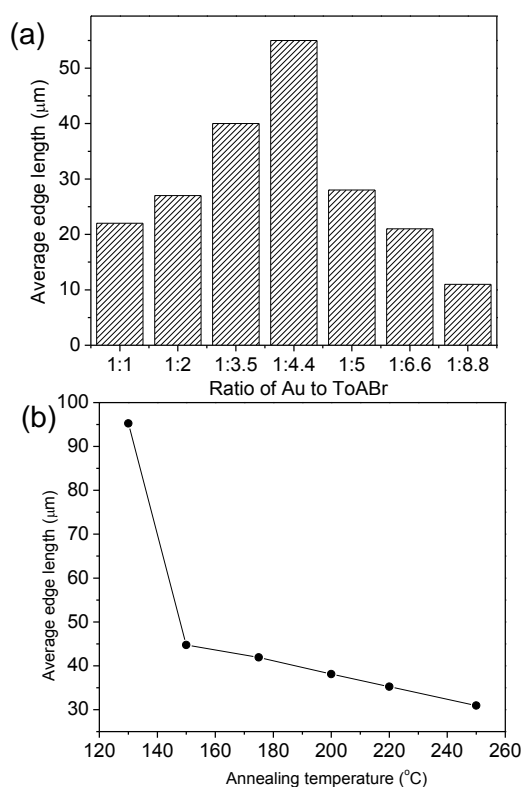
Figure II.11 (a) A histogram of the longest edge length of microplates obtained with different $(AuCl_4)^-$: ToABr ratios (Thermolysis conditions, 130 °C, 6 hrs). (b) Variation in the longest edge length with respect to the thermolysis temperature. The ratio chosen for the precursor synthesis was 1:4.4. Temperature ramp, 2 °C/min and thermolysis time was 24 hrs.

The variation of alkyl chain length in tetraalkylammonium bromide was also done to study the effect on the growth. Tetraoctylammonium bromide gives the largest Au microplates among all (see Table II.2).

Table II.2 Effect of alkylchain length of tetraalkylammonium bromide on the size of Au microplates. The thermolysis was carried out at 130 °C for 24 hrs on Si substrate.

No. of carbons in tetraalkylammonium bromide	Average edge length of microplates(µm)
4	35±15
8	100±50
10	40±20
16	70±20

II.4.2 Growth mechanism of Au microplates

The growth of Au microplates was monitored at two different length scales using SEM and optical microscopy. The initial growth of Au nanostructures was monitored *in situ* at 130 °C inside the FESEM chamber (Movie II.S1 in CD). Within 5 min, nanoparticles were seen nucleating to form dendrimeric structures (Figures II.12a, b and c). Interestingly, these are essentially rudimentary shapes of triangles and hexagons. After 15 min, the nanoparticles fused to form well defined shapes (Figure II.12d). As the structures grew, a halo was commonly seen surrounding the structures, corresponding to the metal precursor in its molten state (melting point 85 °C). This formed a feedstock of Au atoms for the growing structures. Besides the structures shown, bigger particles with 3D shapes such as prismatic and dodecahedral, were also seen occasionally.
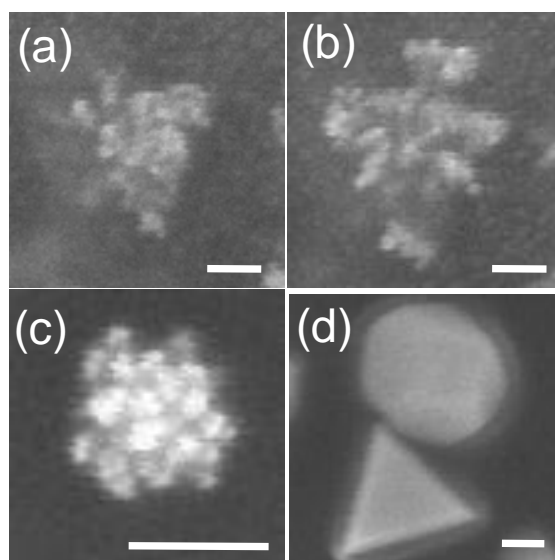
Figure II.12 SEM images: (a, b) Initiation of dendrimeric growth and triangular shapes emerging from aggregation, (c) a hexagonal shape, (d) the fusion of nanoparticles is near complete to form a well-defined triangle. (b) is the image taken of the same triangular aggregation as in (a) after 60 s. The halo seen around the particles in (d) represents the $(AuCl_4)^-$-ToABr feedstock. Scale bar corresponds to 100 nm.

During further growth, there is a competition between the plate-like structures and particles with 3D shapes. It is seen from the various examples shown in Figure II.13 where the 3D particles are connected to corners and edges of triangular and hexagonal microplates. Based on this observation, one may speculate that the 3D structures dissolve away and merge with the microplates as the plates represent the lowest surface energy (111) plane [108] against which the higher surface energy structures sacrifice. Accordingly, the 3D structures were rarely seen in the final product obtained after extended thermolysis.
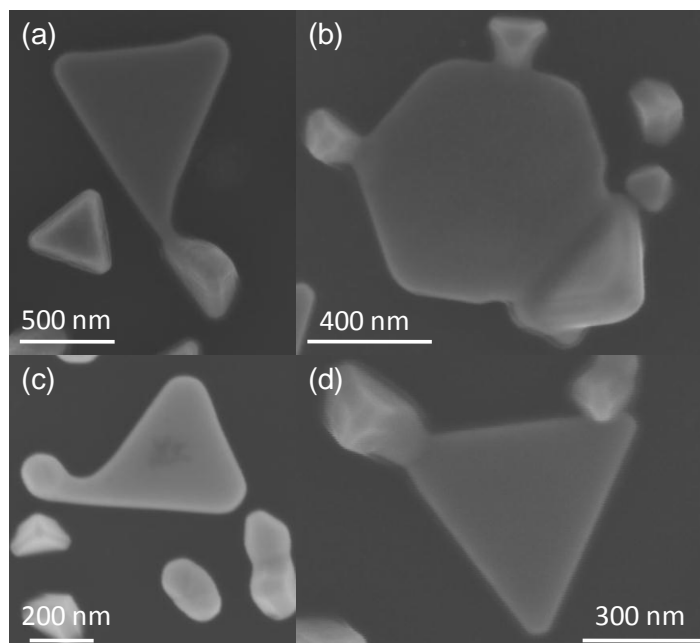
Figure II.13 SEM images of the 3D Au nanostructures sacrificing to merge with the 2D nanoplates.

Under an optical microscope, something very interesting was observed, perhaps for the first time in the literature. As growth continues at large length scale, a number of tiny microplates were seen all over, often vertical to the substrate. In Figure II.14a, few microplates are seen brightly reflecting (marked 1-5) and these must be lying flat. There are other plates (6-10), which appear as elongated rod-like structures. A careful observation of the structures marked 11-15 in Figure II.14a, reveals that these microplates are standing vertical to the substrate but slightly slanted. Indeed, the rod-like appearing structures with darker contrast (6-10) are also microplates standing vertically. The vertically standing microplates are seen more clearly in the SEM image shown in Figure II.14b. It is observed that the initial growth of the Au microplates (60-70%) happens vertically to the substrate, which was monitored in real time employing in situ optical microscopy (Movie II.S2 in CD) snapshots of which are shown in Figure II.14c-e. After certain growth, the microplates fall

off flat to the substrate, as the feedstock surrounding them gets depleted. As shown in Figure II.14c, a triangular microplate appears as if one of the corners of the microplate is pinned to the substrate. The growth proceeds along the free, standing-up corners and as a result the two corners seem to move away from each other. After certain growth, the microplate falls off flat (Figure II.14d) and continues to grow along the same corners. It now looks brighter as it lies flat on the substrate. Another tiny microplate is seen to nucleate in the neighborhood. In such circumstances, the neighboring plates usually come closer and reorient as shown in Figure II.14e.
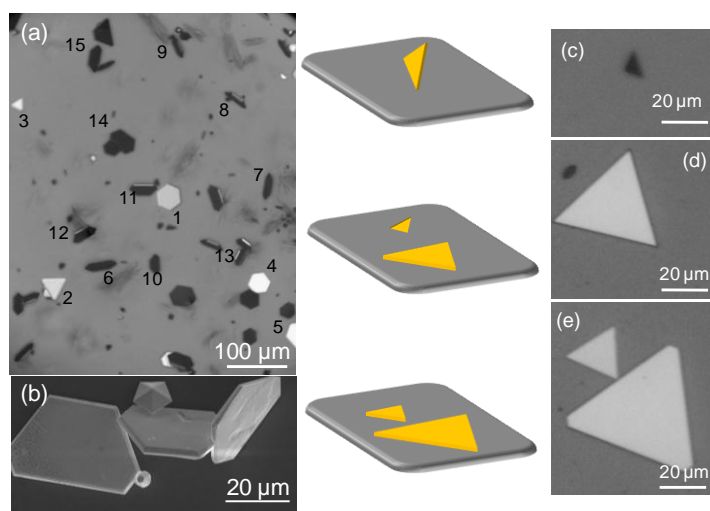
Figure II.14 (a) Optical image of a region showing many vertical (marked 6-15) Au microplates along with few plates lying flat (1-5). (b) SEM image of three microplates which are slanted and vertical to the substrate. Two 3D particles with pentagonal prismatic and dodecahedral shapes are also seen. Optical images (c, d, e) of a triangular Au microplate as it grew, with a schematic on the left. The darker shade of the microplates in c and d is due to its angle with respect to the optical axis.

The vertical growth of the microplates can be partially understood, by drawing parallelism with the well-known vapor-liquid-solid (VLS) growth for nanotubes/nanowires. Vertical growth using a metal catalyst particle has much to do with the adsorption of precursor vapor on the particle surface which induces precipitation leading to nanowire/nanotube growth. In the case of Au microplates, the initial seed particle itself acts as catalyst and the surrounding precursor in the liquid form supplies Au atoms from all directions in the plane of the substrate. For this reason, growth therefore appears to be restricted to a vertical plane. After certain growth, the vertical plates fall off as the pinning point of the plates becomes stressed or due to depletion of the surrounding precursor.

Most often, the growth of the Au plates takes place in the molten precursor feedstock as described above. In some cases, the liquid front moving away, with microplates staying

outside. In the following stages, dendrimeric offshoots were observed as if originating from the vertices (Movie II.S3 in CD). As seen in Figure II.15, the particulate structures established a connection with the microplate in course of time. These dendrimeric connections are more clearly visualized in the SEM image as shown in the inset taking the example of a different microplate.
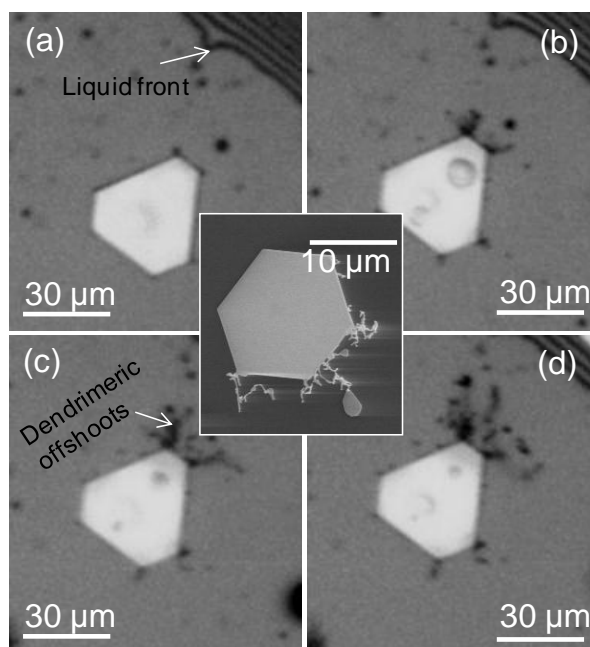
Figure II.15 Optical images of a Au microplate lying just outside of the precursor feedstock captured at successive intervals, (a) 30 min, (b) 40 min (c) 50 min and (d) 60 min. Inset shows the SEM image of a hexagonal Au microplate under similar conditions where the growth was stopped at an intermediate stage.

The dimensions of the growing plates were noted using optical microscopy (Figure II.15), taking both hexagonal and triangular shapes as case examples. At 130 °C (Figure II.16a), the areas of the microplates are seen to increase linearly with the time of annealing, which essentially translates to a linear dimension going as square root of growth time. Thus, it implies that the growth is diffusion limited [109], especially at sizes relevant to optical microscopy. Indeed, this is first experimental observation of a diffusion limited growth of an anisotropic structure at such large length scale. Of course, the slope of the growth curve can be different for different plates with different shapes (see Figure II.16a), although no systematic dependence can be expected based on shape alone. For the examples chosen in Figure II.16, the triangles outscore the hexagons in terms of slope. Among many parameters at play (which is unclear to us at present), the slope should depend on the local concentration of the precursor and the annealing temperature. At 180 °C, the growth of the microplates was in general faster as also seen in the case of plates shown in Figure II.16b, although the

ultimate sizes attained were much larger at 130 °C. It is also commonly observed that in the case of triangular microplates, the corners get rounded after a while and further growth actually led to the truncation of the triangles (see images shown in Figure II.16). This is reflected in the slope of the growth curve. Perhaps an increase in the perimeter because of truncation, leads to a faster growth as there is increased interface between the growing plate and the precursor feedstock. Thus, many truncated triangular or asymmetric hexagonal microplates are commonly seen.
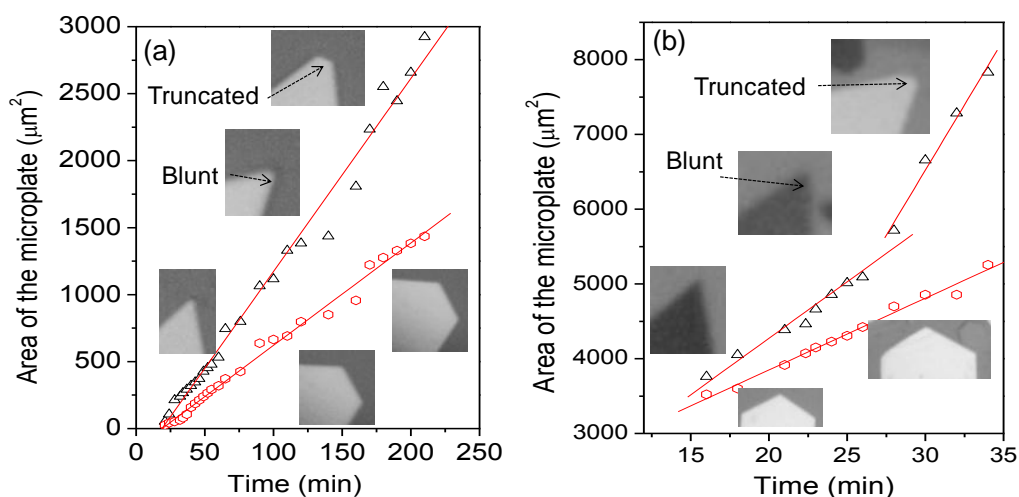
Figure II.16 Area of the triangular and hexagonal microplates versus the thermolysis time at (a) 130 °C and (b) 180 °C. The $(AuCl_4)^-$-ToABr precursor is taken in the ratio of 1:4.4. The deviation from the slope is the point of initiation of bluntness of the corner of the triangular microplates, followed by truncation at later stages. Please note that the darker contrast for the initial triangular microplates shown in Figure II.16b is because the triangle is not exactly perpendicular to the incident beam.

From the above observations, at least three different modes of growth, not necessarily sequential, may be identified namely, the nucleation of tiny nanoparticles into dendrimeric structures which assemble into specific shapes [47], atom-by-atom addition to the formed platelets [7] from the precursor feedstock and fusion of the 3D particles to growing microplates [51]. While all the three modes are found in the literature reports, their occurrences in the present study deserve some discussion (see Schematic diagram in Figure II.17). Ours is not a solution based method but more like a solid state synthesis. The reaction is essentially unaided by any solvent. Moreover, the precursor is highly enriched with Au (10 wt%) and the thermolysis product is reduced metal with hardly any trace of impurities. The microplate growth condition is such that the temperature is just above the solvent boiling point at which the precursor remains in the molten state (melting point, 85 °C). A modest temperature of 130 °C can slow down the kinetics (see Figure II.16b for the

decomposition steps), ideally suited for ultra-slow growth of Au nanostructures amidst the molten precursor. A slow growth is expected to induce high anisotropy along with well-formed facets in the obtained structures [46]. The nucleation of nanoparticles takes place in this feedstock and leads to dendrimeric structures. As the nanoparticles come together while afloat in the liquid feedstock with facets guiding their orientations, they anneal themselves into definite shapes (mostly triangular or hexagonal) amidst the fluidic precursor. Once a well annealed anisotropic structure starts emerging, its growth is entirely dependent on atom-by-atom addition from the fluidic precursor (see Figure II.17) with no addition of nanoparticles. Such a distinct stage of atom-by-atom addition has not been commonly observed [7],[51]. Further growth of the microplate can also take place by the addition of 3D nanoparticles. Thus it has been realized that such a slow reaction kinetics is possible with $(AuCl_4)^-$-ToABr complex, leading to Au microplates formation [46] rather than spherical particles.
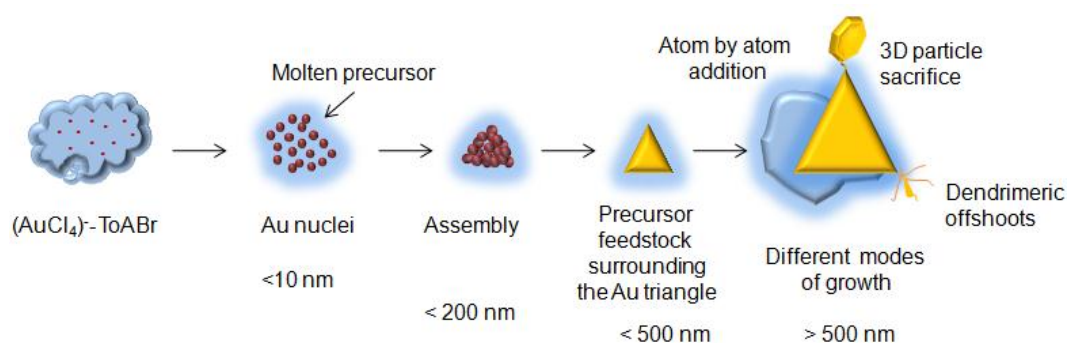
Figure II.17 A schematic showing various growth modes, along with the relevant length scales.

In an effort to throw more light on the proposed mechanism, thermal studies on the Au microplates were performed. If the microplates were to form by the fusion of tiny platelets, it is reasonable to expect that they would disintegrate into particles [41]. But something very different was observed. In the present study, when the Au microplates were annealed at 350 °C for longer time (6 hrs), microplates do defragment, but the mode of defragmentation is found to be quite different from that was observed previously [42]. In the examples shown in Figure II.18, it is clear that the metal has flown outwardly thinning the middle region and in some cases even rupturing to form holes near the vertices. This process as follows. A fully grown microplate is essentially a well annealed single crystal with little defects. When subjected to higher temperatures (350 °C) on a hot plate (Figure II.18), the middle region of the microplates melts readily as expected due to restricted heat flow, and as

a result the metal flows outwardly making the polygons appear thicker at the edges. This effect is more pronounced at the vertices (see Figure II.18a and d). If the vertices are closer as in the case of truncated triangular plates, this leads to a crack (Figure II.18b and e). The propagation of this crack creates interesting shapes as shown in Figure II.18c and f. For the microplates reported in the literature, elevated temperatures cause cracking and degeneration [41]. For such plates formed by particle fusion, the presence of impurities along particle boundaries (from reagents used in the synthetic process) can lead to breaking up of the microplate into particulate islands, from which the microplate had formed.
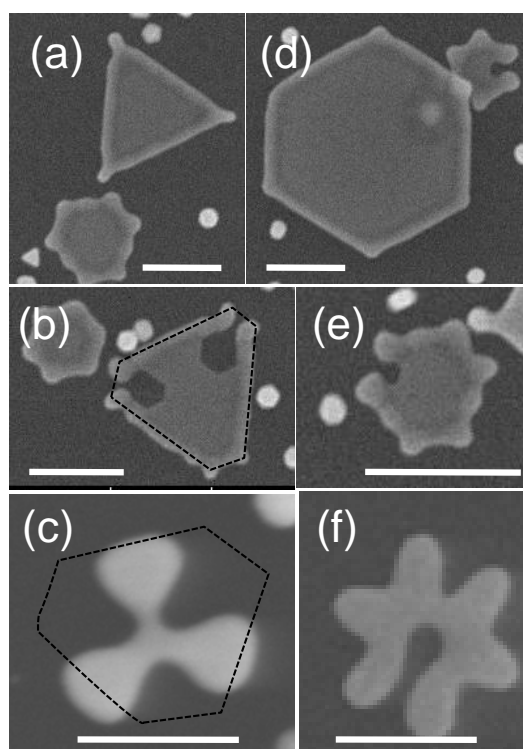
Figure II.18 SEM images of Au microplates heated to 350 °C in air. Images in a, b and c correspond to transformations in triangles while (d, e and f) are from hexagons. Initial edge thickening (a and d), cracking initiated along the corners (b and e) and final morphology attained (c and f). The dashed outline in b and c stand for the shape of the microplates before heating. Scale bars, 1 μm.

II.4.3 Manipulation of Au microplates

Another attractive feature is that the microplates can be detached from the substrate rather easily. A sharp pin carrying an Au microplate is shown in Figure II.19a. Shown in Figure II.19b is a pattern of the microplates organized using the sharp pin. The transferred microplates are quite mobile on PDMS surface under little force (see Figure II.19d for the sequence of the arrangement of the microplates). In one report, manipulation of a nanowheel made from Au nanoplate was shown using a nanomanipulator inside a FIB system [36]. In

the present case, the process is much simplified because of the large size of the microplates, thus not demanding the sophisticated instrumentation for manipulation. These microplates can also be dropped into microwells as shown in Figure II.19c.
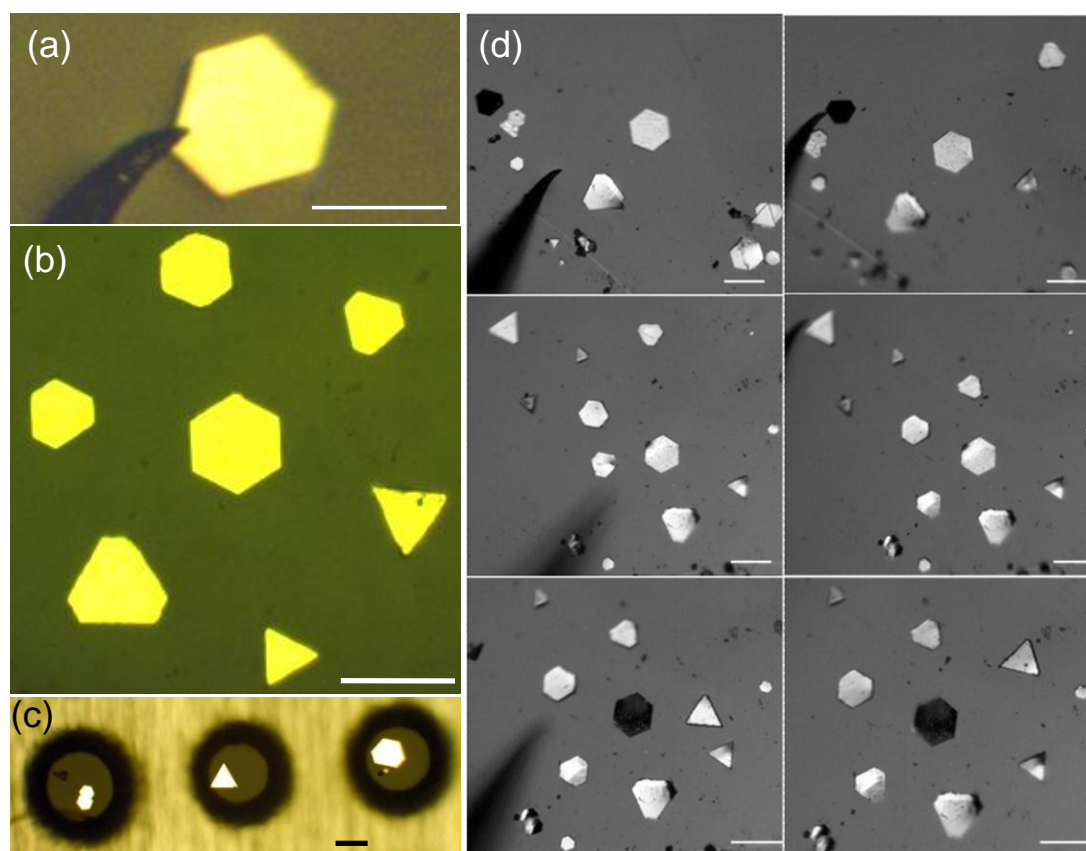
Figure II.19 (a) Optical image of a sharp pin carrying a Au microplate. (b) Au microplates arranged in a pattern on a PDMS substate. For this purpose, the as-made Au microplates are dispersed in toluene, and then a drop of toluene containing Au microplates is placed onto PDMS surface. Thus spread plates are manipulated using the pin. (c) Microplates placed in microwells formed between a stencil and a glass substrate. A drop of toluene containing Au microplates was spread on a stencil. As the solvent evaporates, Au microplates get arranged in the wells, presumably one in each, because the size of the wells is chosen to be similar to that of the microplates. (d) Different stages of organizing microplates using a pin. All scale bars correspond to 100 μm.

As-synthesized Au microplates are transferrable to other substrates, which is important in properties such as site selective wettablity, cytophilicity, etc. How Au microplates could be embedded in a polymer matrix is explained in Figure II.20a. The polymer chosen here was poly(dimethylsiloxane) (PDMS), which is extensively used as a biomaterial in ear and nose implants, pacemaker insulation, catheters, drainage tubing, for membrane oxygenators, etc [110]. In the recent past, use of PDMS for replicating nanostructures with high fidelity is well acknowledged and it forms the heart of a branch of lithography named soft lithography. PDMS elastomer mixed with curing agent was poured

over the microplates on a given substrate and the entire setup was kept in oven at 50 °C overnight for curing the PDMS. After cooling to room temperature, cured PDMS was peeled off from the substrate, leading to Au microplate embedded PDMS (Figure II.20b). PDMS hosting Au microplates presents a unique platform for hosting live cells, as the cells can be selectively adsorbed only onto the microplates as the microplate surface is cytophilic while the PDMS surface, as known [111], should inhibit the cell adhesion. Instead of PDMS the Au microplates can also be transferred to a scotch tape by simply peeling them off from a glass or Si substrate (Figure II.20c).
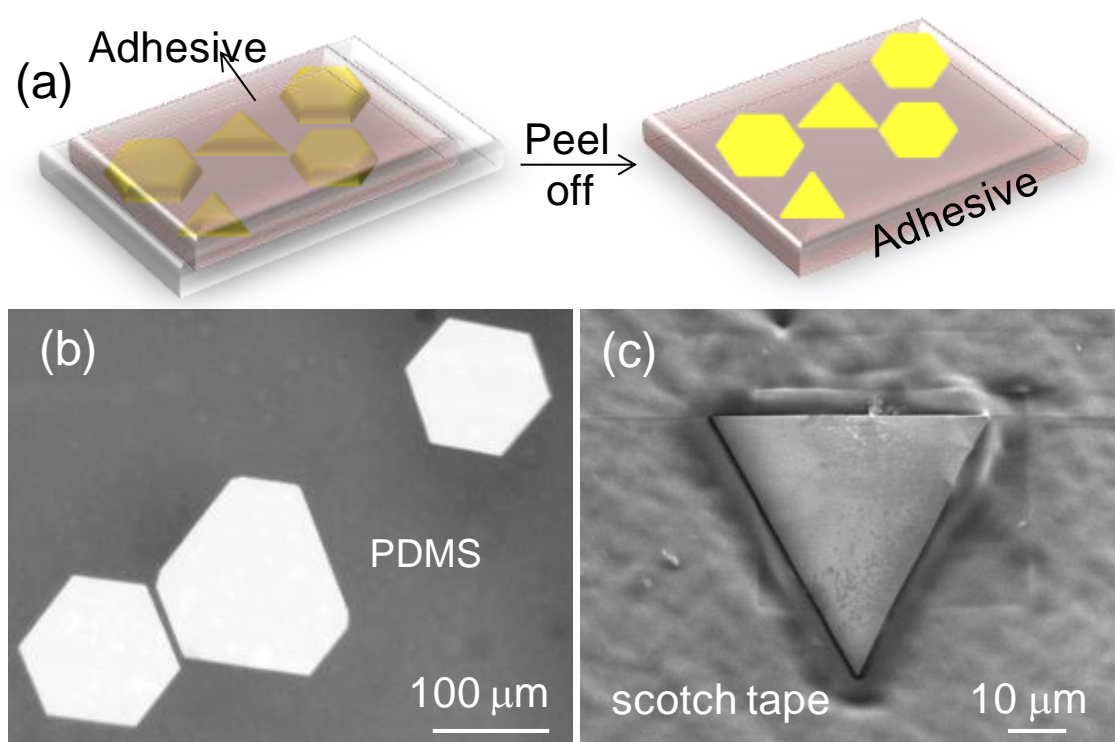
Figure II.20 Transferability of Au microplates to other substrates: (a) Schematic illustration of the process; The adhesive, i.e., either a scotch tape or a polymer such as PDMS which can be cured, is brought over the microplates on a substrate and peeled off. (b) Optical image (in reflection mode) of the cured PDMS peeled off from the substrate. (c) SEM image showing the faithful transfer of Au microplates to scotch tape.

There are other possibilities relevant to technological applications. Nanopatterning was attempted on the surface of the microplates. Ion beam milling of metal surfaces to create nanoelectronic circuits is well-documented [112]. Au nanoplates have also been milled through ion-beam to produce nanocomponents such as nanowheels [36] and nanoresonators [113]. Recently, plasmonic nanocircuits such as nanoantennas have been realized on single crystal Au microplates by focused ion milling [114]. These giant Au microplates could also be used efficiently for producing high quality single crystalline components. As shown in

Figure II.21, even a low energy electron beam (5 kV) is able to create trenches on a Au microplate surface. The trenches created were about ~7 nm deep.
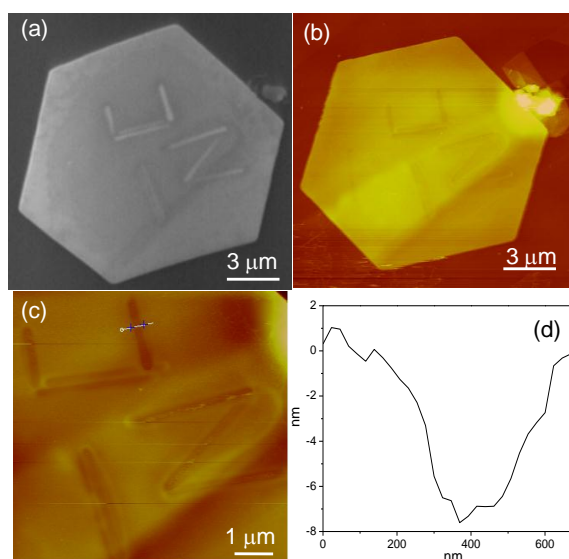
Figure II.21 (a) SEM and (b) AFM images showing the nanotrenches in the form of alphabets made by EBL (10 kV, 0.6 mC/cm) on Au microplate surface. (c) Magnified AFM image and the corresponding *z*-profile in (d).

II.4.4 Metal enhanced fluorescence - Microplates as platforms for cells and organic crystals

The microplates presented above have some unique properties- large, flat, clean and movable. These qualities prompted us to explore their utility as platforms for hosting live cells. Previously, Ishihara et al. [115], have fabricated mobile parylene microplates which could host adherent cells. Transparent SiO_2 microplates [116] are also studied for the same purpose. Most often such surfaces require a plasma pretreatment for chemical modification to attach the cell. There have been reports on cell patterning on Au substrates by surface engineering [117,118] with extracellular matrix proteins. The cellular behavior in terms of adaptation and signaling depends crucially on the environment. In the present study, coverslips coated with Au microplates were used for growing three different cell lines- KB (human oral cancer), H1299 (human lung carcinoma) and 3T3 (mouse fibroblast) cells. The cells were seen attached to the microplates as well as on other regions of the coverslips (Figure II.22). Importantly, they were as healthy on the plates as on the coverslip surface itself, implying that there is no cellular toxicity arising from the microplates. Here, it is noteworthy that no surface chemical modification was done for the attachment of cells. Electrostatic interactions between the cell membrane and the Au surface as well as specific interactions involving amine groups from cell surface proteins may be responsible for the

cell attachment to the microplates. Thus, the microplates provide an opportunity to carry out cellular studies, free of any inevitable affects caused by the surface modifications. In a recent work Brunetti et al., [119] have shown the possible role of nanoroughness in deciding the cytophilic and cytophobic nature of the surface for neuronal cells. The cells are directed preferentially towards the flat regions of the surface (cytophilic). Although the cell line used here is different, the surface smoothness of the microplate would be advantageous in attracting live cells. The microplate is also seen to enhance the fluorescence of Hoechst 33528 dye in the nucleus, as shown in Figures II.22a and b.
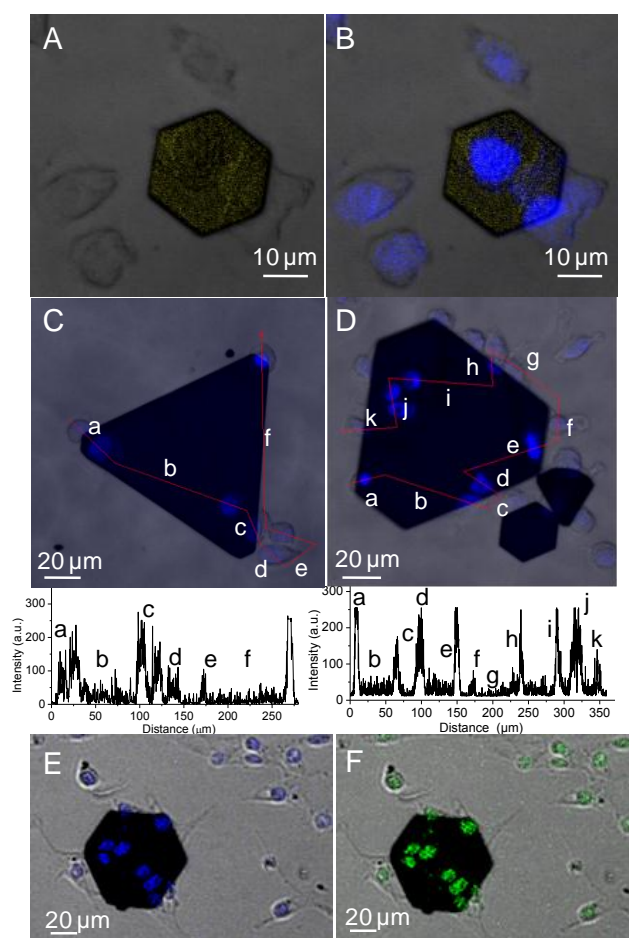
Figure II.22 (a) and (b) Confocal images showing Au microplate hosting H1299 cells in which chromosomal DNA in the nucleus has been stained by Hoechst 33528. (c) and (d) show two microplates hosting KB cells with Hoechst 33528 staining. The fluorescence enhancement is shown quantitatively beneath, a-k are guide to the trace. (e) and (f) are confocal images of a Au microplate hosting mouse 3T3 cells, stained with Hoechst and Alexa 488 to visualize nucleus and the acetylated histone H3, respectively.

This is akin to metal-enhanced fluorescence (MEF) [120] which increases the fluorescence emission from a fluorophore. MEF arises due to the increase in the electric field near the metal surface in presence of the incident light [121]. It is being increasingly used for cell imaging as the chosen fluorophores may possess low quantum yields, making it difficult

to visualize particularly in lower concentrations [121]. However, it is known that the fluorescence is enhanced only when the fluorophore is localized at an optimal distance close to the metal surface, in the range of 5-30 nm [121]. As shown in Figures II.22a and b, the cell situated in the middle of the plate is seen with a bright contrast while the cells around the plate resting on the coverglass are seen lightly colored. Another cell is half placed on the plate and half on the coverglass. Fluorescence enhancement by the microplate surface is clearly evident. The extent of enhancement is quantitatively expressed in Figures II.22c and d. In some cases, the enhancement is nearly 10 times compared to plain regions of the coverglass, the average value being 5. Another important observation is that the blue emission is from the intracellular parts. As Hoescht is known to stain specifically the chromosomal DNA in the nucleus, as shown in Figures II.22b-d clearly refer to the cell nuclei, of course within the MEF range. In some occasions, MEF may not be all that favorable to image a cell nucleus [122]. The excitation of plasmon modes at the metal surface is known to yield intense optical fields at short distances from the metal surface (a few tens of nanometers, typically) which may not play a significant role in case of micrometer-sized samples [119]. In the context of this study, the microsized fluorophore object (part of stained cell) is held beyond the distance relevant for surface plasmon effects (> 30 nm, as the cell membrane is typically thicker), only classical effects seem to influence the fluorescence. In a previous study where plasmonic structures have been employed, little to no enhancement was observed from nuclear dyes [122]. Another noteworthy advantage is that the 'mirror-type' classical enhancement is applicable to all visible wavelengths unlike plasmonic enhancement which is wavelength dependent. Figures II.22e and f illustrate 3T3 cells on the microplate, with the fluorescence enhancement evident for Hoechst 33528 and Alexa 488 dye. Further, another dye (Alexa 568) conjugated secondary antibody was used to visualize tubulin protein in the cell. Importantly, the fluorescene signal was better obtained from cells present on the Au plates (see Figure II.23).
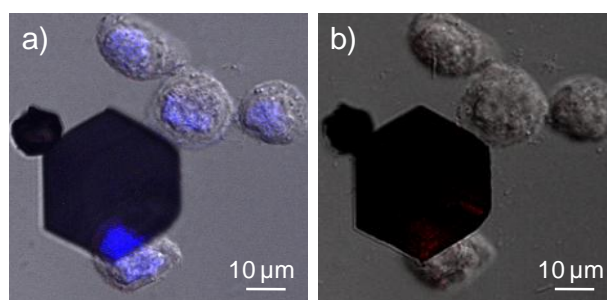
Figure II.23 Au microplate hosting KB cells. MEF from (a) Hoechst 33528 dye (blue) which stains chromosomal DNA (nucleus), and (b) Alexa 588 dye used to visualize tubulin. Please note that better fluorescence signals were obtained from cells grown on Au plates.

Comparing the relative sizes, it is clear that the microplate can essentially act as single cell platforms (Figure II.24).
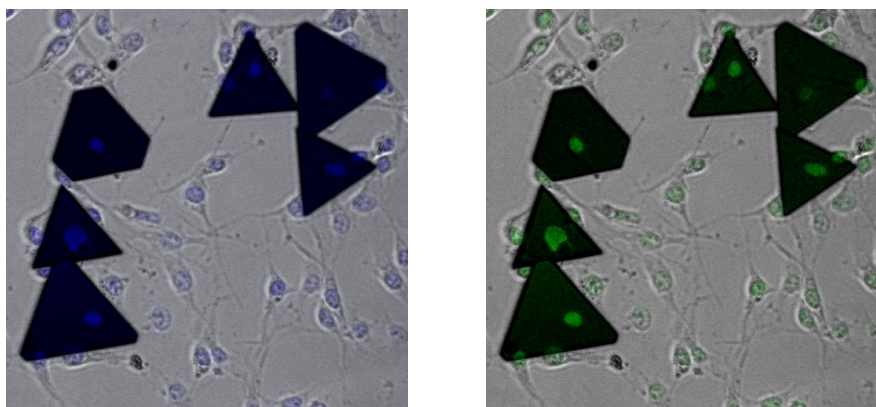
Figure II.24 Au microplates each hosting a single cell (3T3 cell) growth; Alexa 488 (green) and Hoechst 33528 (blue) dyes are used to visualize acetylated Histone H3 and nucleus respectively.
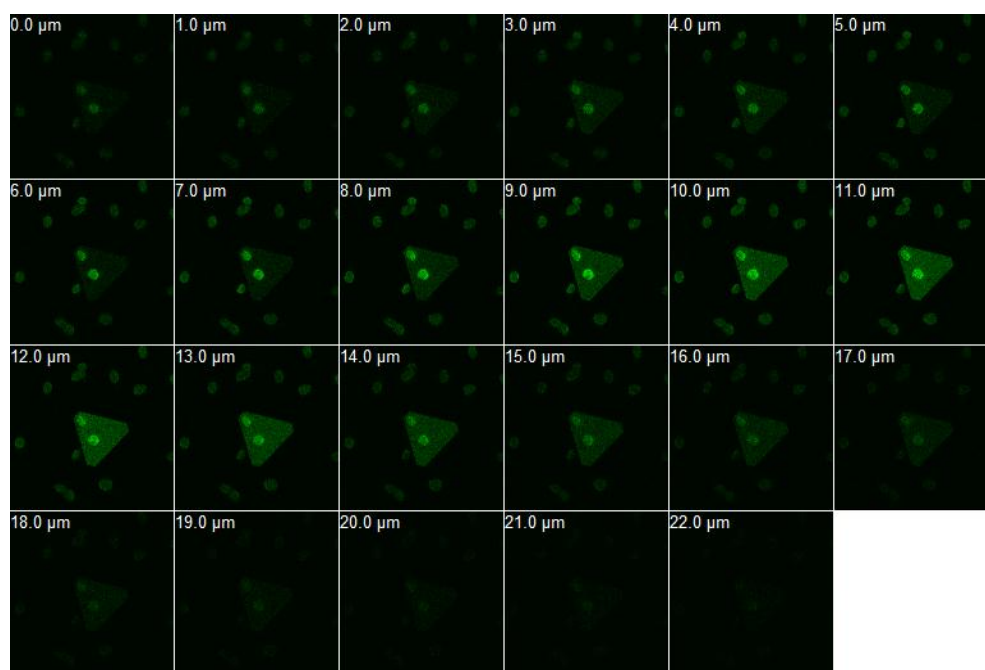
Figure II.25 Optical slices showing 3T3 cells hosted on the coverslip as well on Au microplate. Each slice is 1 μm apart.

As fluorescence enhancement of cell nucleus is evident, different z-section confocal images of the cell nucleus have been analysed, to understand the distance dependence of the fluorescence enhancement. This is shown in Figure II.25, sections with z ~ 10 μm show maximum fluorescence enhancement. Since the Au microplates can enhance fluorescence of dyes, the utility was extended to enhance the fluorescence of molecular crystals. In general, organic fluorophores display very low quantum yield in the solid state. Strong fluorescence in solid state is important if one wants to use such molecules in device applications. A

concept experiment of fluorescence enhancement for molecular crystals is demonstrated using 1,4-bis(phenylethynyl)-2,5-bis(n-propoxy)benzene as a model system. Crystals of this molecule are known to exhibit fluorescence around 515 nm in the solid state, with a high quantum yield of 0.53 [123]. A crystal was grown on Au microplates by drop-casting a toluene solution of the molecule onto Au microplates. Slow evaporation of the solvent at room temperature led to crystal growth on the microplate surface (Figure II.26). Confocal imaging of the crystals on Au microplates showed enhanced fluorescence compared to the ones grown on glass slide as control. Thus, it can be envisaged that the solid state quantum yield of industrially important organic molecules can be increased by using Au microplates as platforms.
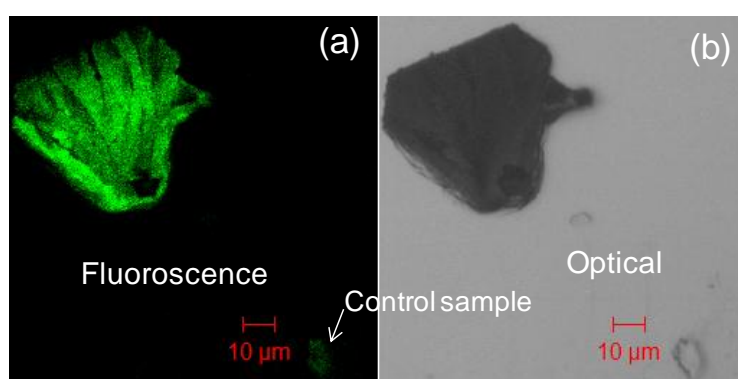
Figure II.26 Metal enhanced fluoroscence: (a) dark field confocal and (b) optical images of an organic fluoroscent crystal (oligo(phenyleneethynylene)) on a Au microplate.

II.4.5 Au Microplates – SERS

Au being a plasmonic metal [124], it is interesting to investigate the prospects of using the surface of the microplates for surface enhanced Raman spectroscopy. For this purpose, a 1 mM solution of a Raman marker (thiophenol) was chemisorbed onto the surface of a hexagonal microplate by self-assembly. Raman spectra recorded on the corners of the microplate is shown in Figure II.27a along with that recorded on the glass slide coated with 1 mM thiophenol solution. Figure II.27b shows the Raman mapping of the 1000 cm^{-1} peak across the entire Au microplate surface. Owing to the smoothness of the Au microplate, there was no enhancement at the center of the Au microplate, and the enhancement in the Raman signal was clearly evident only at the corners. In order to understand this phenomenon, electrostatic force microscopy (EFM) was performed on the Au microplates (Figure II.27c). EFM measures local electrical properties by measuring the electrostatic force between a biased AFM tip and the sample surface [125]. Figure II.27c shows the topography image of a Au microplate. While applying different bias values, EFM images were recorded

at a lift height of ~150 nm as shown in Figure II.27c. With increased tip bias i.e., at 10 V, the edges and corners of the microplate appeared brighter (with either positive or negative bias), indicating a higher electric field in those regions. This observation goes well with the literature reports [126] that along the sharp edges and corners of metal nanostructures, there will be an enhanced electric field and hence enhanced Raman signal.
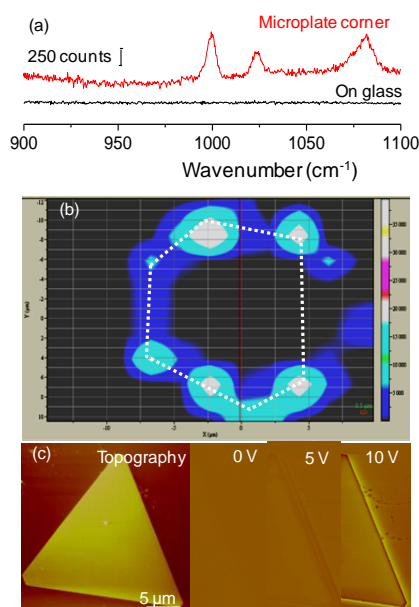
Figure II.27 (a) Raman spectrum of thiophenol chemisorbed on a Au microplate, recorded on a corner. (b) Raman mapping of 1000 cm^{-1} peak recorded on the hexagonal microplate (shown as dotted line). Corners show enhanced Raman signal. (c) AFM topography image of a Au microplate and the corresponding EFM images at 0 V, 5 V and 10 V respectively. The lift height was 150 nm.

II.4.6 Other anisotropic Au microstructures

Au-ToABr precursor can also be used for obtaining other interesting anisotropic structures. When the thermolysis of the precursor was carried on a substrate in a heat confined environment (i.e., by placing a cured PDMS flat piece on top of the precursor film on a substrate), microstars were obtained, instead of microplates (see Figure II.28a and b).
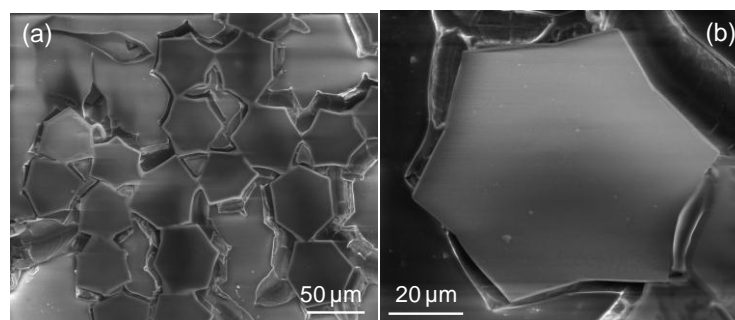
Figure II.28 Other interesting anisotropic structures: (a) SEM image of the Au microstars synthesized by confined heat treatment of Au-ToABr, (b) shows magnified image of a single microstar.

II.5 CONCLUSIONS

Au microplates have been synthesized using a single step thermolysis of a simple Au organic precursor. The microplates bear edge lengths of ~100-450 μm amounting to area of 10,000-1,00,000 μm^2, the thickness being in the range of 30 nm – 2 μm. This process is very different from the known methods in the literature which invariably report synthesis in solution. Many experimental parameters such as precursor concentration, temperature and time have been varied. The optimal conditions for large microplates have been: $AuCl_4^-$:ToABr ratio of 1:4.4 for phase transfer, thermolysis at 130 °C for 55 hrs. Electron diffraction data obtained in TEM as well as XRD data revealed that each microplate is a well formed (111) oriented single crystal with no detectable deformation, unlike most reports on microplates. To understand the growth mechanism, the images of the Au microplate embryonic state as well as of later stages as they grow in size into microplates have been captured. At synthetic temperature of 130 °C, the precursor is essentially devoid of the solvent (toluene) but remains molten, through which Au nanoparticles nucleate and grow into rudimentary shapes. These shapes eventually anneal as well as grow into tiny triangles and hexagons, as seen in SEM. There were also some pentagonal prismatic, dodecahedral and other 3D structures surrounded by a halo of the molten precursor. There were many instances where 3D structures were seen merging with the microplates. Interestingly, the plates were held vertical to the substrate surface during the growth even at large sizes, as evidenced by in situ optical microscopy. To sum up, three growth modes namely nucleation and assembly, atom-by-atom addition and fusion of the 3D particles can be inferred from this study using real time microscopy.

The microplates are atomically smooth and highly crystalline with the Au(111) face forming the polygonal surface, a property which should qualify them as ideal microscopy substrates and electrodes in molecular electronics. The microplate surface was found to be non-toxic to living cells and can enhance the fluorescence signal from cell nucleus (Hoechst 33528 dye) by an order magnitude. The process of electromagnetic enhanced SERS along the edges and corners of the microplate was clearly evident, which was supported further by EFM measurements. Importantly, the plates can be picked up using a pin and placed at a desired location and organized. Hence, this experimental platform offers exciting opportunities for single cell based studies and in probing complex and dynamic relationships between cells and their local environment.

REFERENCES

[1]   T. K. Sau, A. L. Rogach, F. Jäckel, T. A. Klar, and J. Feldmann, Advanced Materials 22 (2010) 1805.

[2]   J. Watt, S. Cheong, M. F. Toney, B. Ingham, J. Cookson, P. T. Bishop, and R. D. Tilley, ACS Nano 4 (2009) 396.

[3]   R. Jin, Y. Cao, C. A. Mirkin, K. L. Kelly, G. C. Schatz, and J. G. Zheng, Science 294 (2001) 1901.

[4]   C. J. Murphy, T. K. Sau, A. M. Gole, C. J. Orendorff, J. Gao, L. Gou, S. E. Hunyadi, and T. Li, The Journal of Physical Chemistry B 109 (2005) 13857.

[5]   S.-H. Ciou, Y.-W. Cao, H.-C. Huang, D.-Y. Su, and C.-L. Huang, The Journal of Physical Chemistry C 113 (2009) 9520.

[6]   M. Kasture, M. Sastry, and B. L. V. Prasad, Chemical Physics Letters 484 (2010) 271.

[7]   G. Lin, W. Lu, W. Cui, and L. Jiang, Crystal Growth & Design 10 (2010) 1118.

[8]   D. Seo, C. I. Yoo, I. S. Chung, S. M. Park, S. Ryu, and H. Song, The Journal of Physical Chemistry C 112 (2008) 2469.

[9]   J. Zhang, H. Liu, Z. Wang, and N. Ming, Applied Physics Letters 91 (2007) 133112.

[10]   D. Y. Kim, S. H. Im, and O. O. Park, Crystal Growth & Design 10 (2010) 3321.

[11]   H. M. Chen, R.-S. Liu, and D. P. Tsai, Crystal Growth & Design 9 (2009) 2079.

[12]   H.-L. Wu, C.-H. Chen, and M. H. Huang, Chemistry of Materials 21 (2008) 110.

[13]   E. Nalbant Esenturk and A. R. Hight Walker, Journal of Raman Spectroscopy 40 (2009) 86.

[14]   S. S. Shankar, A. Rai, B. Ankamwar, A. Singh, A. Ahmad, and M. Sastry, Nature Materials 3 (2004) 482.

[15]   S. Xuping, D. Shaojun, and W. Erkang, Angewandte Chemie International Edition 43 (2004) 6360.

[16]   S. S. Shankar, A. Rai, A. Ahmad, and M. Sastry, Chemistry of Materials 17 (2005) 566.

[17]   B. J. Wiley, D. J. Lipomi, J. Bao, F. Capasso, and G. M. Whitesides, Nano Letters 8 (2008) 3023.

[18]   Y. Xia, Y. Xiong, B. Lim, and S. E. Skrabalak, Angewandte Chemie International Edition 48 (2009) 60.

[19]   D. H. Dahanayaka, J. X. Wang, S. Hossain, and L. A. Bumm, Journal of the American Chemical Society 128 (2006) 6052.

[20]   A. Sabur, M. Havel, and Y. Gogotsi, Journal of Raman Spectroscopy 39 (2008) 61.

[21]   A. Sanyal and M. Sastry, Chemical Communications (2003) 1236.

[22]   R. Jin, Y. Charles Cao, E. Hao, G. S. Metraux, G. C. Schatz, and C. A. Mirkin, Nature 425 (2003) 487.

[23]   Y. Sun and Y. Xia, Advanced Materials 15 (2003) 695.

[24]   J. U. Kim, S. H. Cha, K. Shin, J. Y. Jho, and J. C. Lee, Advanced Materials 16 (2004) 459.

[25]   Y. Shao, Y. D. Jin, and S. J. Dong, Chemical Communications (2004) 1104.

[26]   L. Y. Wang, X. Chen, J. Zhan, Z. M. Sui, J. K. Zhao, and Z. W. Sun, Chemistry Letters 33 (2004) 720.

[27]   C. S. Ah, Y. J. Yun, H. J. Park, W.-J. Kim, D. H. Ha, and W. S. Yun, Chemistry of Materials 17 (2005) 5558.

[28]   H.-C. Chu, C.-H. Kuo, and M. H. Huang, Inorganic Chemistry 45 (2005) 808.

[29]   Z. Li, Z. Liu, J. Zhang, B. Han, J. Du, Y. Gao, and T. Jiang, The Journal of Physical Chemistry B 109 (2005) 14445.

[30]   C. Lofton and W. Sigmund, Advanced Functional Materials 15 (2005) 1197.

[31]   T. Masaharu, H. Masayuki, N. Yuki, K. Masatoshi, and T. Takeshi, Chemistry - A European Journal 11 (2005) 440.

[32]   S. Porel, S. Singh, and T. P. Radhakrishnan, Chemical Communications (2005) 2387.

[33]   A. Rai, A. Singh, A. Ahmad, and M. Sastry, Langmuir 22 (2005) 736.

[34]   X. Sun, S. Dong, and E. Wang, Langmuir 21 (2005) 4710.

[35]   L. Wang, X. Chen, J. Zhan, Y. Chai, C. Yang, L. Xu, W. Zhuang, and B. Jing, The Journal of Physical Chemistry B 109 (2005) 3189.

[36]   Y. J. Yun, G. Park, C. S. Ah, H. J. Park, W. S. Yun, and D. H. Ha, Applied Physics Letters 87 (2005) 233110.

[37]   A. Ali Umar and M. Oyama, Crystal Growth & Design 6 (2006) 818.

[38]   Z. Guo, Y. Zhang, Y. DuanMu, L. Xu, S. Xie, and N. Gu, Colloids and Surfaces A: Physicochemical and Engineering Aspects 278 (2006) 33.

[39]   Z. Guo, Y. Zhang, Y. Mao, L. Huang, and N. Gu, Materials Letters 60 (2006) 3522.

[40]   P. Jiang, J.-J. Zhou, R. Li, Y. Gao, T.-L. Sun, X.-W. Zhao, Y.-J. Xiang, and S.-S. Xie, Journal of Nanoparticle Research 8 (2006) 927.

[41]   C. Kan, G. Wang, X. Zhu, C. Li, and B. Cao, Applied Physics Letters 88 (2006) 071904.

[42]   C. Kan, X. Zhu, and G. Wang, The Journal of Physical Chemistry B 110 (2006) 4651.

[43]   C. C. Li, W. P. Cai, B. Q. Cao, F. Q. Sun, Y. Li, C. X. Kan, and L. D. Zhang, Advanced Functional Materials 16 (2006) 83.

[44]   X. Sun and Y. Luo, Materials Letters 60 (2006) 3145.

[45]   L. Xiaogang, W. Nianqiang, H. W. Benjamin , J. B. Robert , Jr., and S. Francesco, Small 2 (2006) 1046.

[46]   Y. Xiong, I. Washio, J. Chen, H. Cai, Z.-Y. Li, and Y. Xia, Langmuir 22 (2006) 8563.

[47]   D. J. Wang and T. Imae, Chemistry Letters 35 (2006) 1152.

[48]   C.-C. Chen, C.-H. Hsu, and P.-L. Kuo, Langmuir 23 (2007) 6801.

[49]   A. Courty, A. I. Henry, N. Goubet, and M. P. Pileni, Nature Materials 6 (2007) 900.

[50]   K. Furuya, Y. Hirowatari, T. Ishioka, and A. Harata, Chemistry Letters 36 (2007) 1088.

[51]   W.-L. Huang, C.-H. Chen, and M. H. Huang, The Journal of Physical Chemistry C 111 (2007) 2533.

[52]   X. Jianping, L. Jim Yang, I. C. W. Daniel, and T. Yen Peng, Small 3 (2007) 672.

[53]   H. Kawasaki, T. Yonezawa, K. Nishimura, and R. Arakawa, Chemistry Letters 36 (2007) 1038.

[54]   K. Y. Lee, M. Kim, Y. W. Lee, M. Y. Choi, and S. W. Han, Bulletin of the Korean Chemical Society 28 (2007) 2514.

[55]   J. Xie, J. Y. Lee, and D. I. C. Wang, The Journal of Physical Chemistry C 111 (2007) 10226.

[56]   Y. Yong Ju, C. S. Ah, S. Kim, W. S. Yun, B. C. Park, and D. H. Ha, Nanotechnology 18 (2007) 505304.

[57]   J. Zhang, B. Zhao, L. Meng, H. Wu, X. Wang, and C. Li, Journal of Nanoparticle Research 9 (2007) 1167.

[58]   J. Zhu, Y. Shen, A. Xie, L. Qiu, Q. Zhang, and S. Zhang, The Journal of Physical Chemistry C 111 (2007) 7629.

[59]   T. s. Base, Z. Bastl, M. Slouf, M. Klementova, J. Subrt, A. Vetushka, M. Ledinsky, A. n. Fejfar, J. Machacek, M. J. Carr, and M. G. S. Londesborough, The Journal of Physical Chemistry C 112 (2008) 14446.

[60]   W. Chen-Hsun, C.-C. Huang, C.-S. Yeh, H.-Y. Lei, and G.-B. Lee, Journal of Micromechanics and Microengineering 18 (2008) 035019.

[61]   Z. Deng, M. Mansuipur, and A. J. Muscat, The Journal of Physical Chemistry C 113 (2008) 867.

[62]   Z. Guo, Y. Zhang, A. Xu, M. Wang, L. Huang, K. Xu, and N. Gu, The Journal of Physical Chemistry C 112 (2008) 12638.

[63]   B. Lim, P. H. C. Camargo, and Y. Xia, Langmuir 24 (2008) 10437.

[64]   L. Ren, L. Meng, Q. Lu, Z. Fei, and P. J. Dyson, Journal of Colloid and Interface Science 323 (2008) 260.

[65]   Z. Wang, J. Yuan, M. Zhou, L. Niu, and A. Ivaska, Applied Surface Science 254 (2008) 6289.

[66]   J. Xu, S. Li, J. Weng, X. Wang, Z. Zhou, K. Yang, M. Liu, X. Chen, Q. Cui, M. Cao, and Q. Zhang, Advanced Functional Materials 18 (2008) 277.

[67]   J. Heo, Y. W. Lee, M. Kim, W. S. Yun, and S. W. Han, Chemical Communications (2009) 1981.

[68]   S. J. Hsu and I. J. B. Lin, Journal of the Chinese Chemical Society 56 (2009) 98.

[69]   K. Y. Lee, M. Kim, and S. W. Han, Materials Letters 63 (2009) 480.

[70]   Z. Li, V. Lapeyre, ronique, V. Ravaine, rie, S. Ravaine, and A. Kuhn, Journal of Nanoscience and Nanotechnology 9 (2009) 2045.

[71]   P. Mukherjee and A. K. Nandi, Langmuir 26 (2009) 2785.

[72]   N. Semagina and L. Kiwi-Minsker, Catalysis Letters 127 (2009) 334.

[73]   T. Soejima and N. Kimizuka, Journal of the American Chemical Society 131 (2009) 14407.

[74]   Y. N. Tan, J. Y. Lee, and D. I. C. Wang, The Journal of Physical Chemistry C 113 (2009) 10887.

[75]   A. A. Umar, M. Oyama, M. M. Salleh, and B. Y. Majlis, Crystal Growth & Design 9 (2009) 2835.

[76]   K. Xu, Z. r. Guo, and N. Gu, Chinese Chemical Letters 20 (2009) 241.

[77]   D. Zhang, P. Diao, and Q. Zhang, The Journal of Physical Chemistry C 113 (2009) 15796.

[78]   L. Zhang, C. Z. Huang, Y. F. Li, and Q. Li, Crystal Growth & Design 9 (2009) 3211.

[79]   L. Zhao, X. Ji, X. Sun, J. Li, W. Yang, and X. Peng, The Journal of Physical Chemistry C 113 (2009) 16645.

[80]   C. Bouvy, G. A. Baker, H. Yin, and S. Dai, Crystal Growth & Design 10 (2010) 1319.

[81]   Y. W. Cheng, C. C. Qiu, H. Y. Ma, X. K. Zhang, and X. H. Gu, Nanoscale 2 (2010) 685.

[82]   G. S. Ghodake, N. G. Deshpande, Y. P. Lee, and E. S. Jin, Colloids and Surfaces B: Biointerfaces 75 (2010) 584.

[83]   S. Donthu, Z. Pan, B. Myers, G. Shekhawat, N. Wu, and V. Dravid, Nano Lett. 5 (2005) 1710.

[84]   A. Leslie, L. Byungkwon, C. Peter, J. Young-Shin, and X. Younan, Chemistry - An Asian Journal 5 (2010) 123.

[85]   S. Toshio and A. Paschalis, Macromolecular Symposia 289 (2010) 18.

[86]   F. Xu, C. Guo, Y. Sun, Z. Liu, Y. Zhang, and Z. Li, Colloids and Surfaces A: Physicochemical and Engineering Aspects 353 (2010) 125.

[87]   Y. Xia and H. Xiao, Materials Chemistry and Physics 122 (2010) 333.

[88]   T. C. R. Rocha, F. Sato, S. O. Dantas, D. S. Galvao, and D. Zanchet, The Journal of Physical Chemistry C 113 (2009) 11976.

[89]   S. J. Kwon, The Journal of Physical Chemistry B 110 (2006) 3876.

[90]   J. L. Fransaer and R. M. Penner, The Journal of Physical Chemistry B 103 (1999) 7643.

[91]   H. Zheng, R. K. Smith, Y.-w. Jun, C. Kisielowski, U. Dahmen, and A. P. Alivisatos, Science 324 (2009) 1309.

[92]   A. Henkel, O. Schubert, A. Plech, and C. SoÌ‚nnichsen, The Journal of Physical Chemistry C 113 (2009) 10390.

[93]   K. Biswas, N. Varghese, and C. N. R. Rao, Small 4 (2008) 649.

[94]   H. Murayama, N. Hashimoto, and H. Tanaka, Journal of Physics: Conference Series 190 (2009) 012132.

[95]   S. Cheong, J. Watt, B. Ingham, M. F. Toney, and R. D. Tilley, Journal of the American Chemical Society 131 (2009) 14590.

[96]   R. Jagannathan, A. S. Parmar, S. Adyanthaya, A. Prabhune, M. Muschol, and P. Poddar, The Journal of Physical Chemistry C 113 (2009) 3478.

[97]   L. Cao, T. Zhu, and Z. Liu, Journal of Colloid and Interface Science 293 (2006) 69.

[98]   M. Chen, Y.-G. Feng, X. Wang, T.-C. Li, J.-Y. Zhang, and D.-J. Qian, Langmuir 23 (2007) 5296.

[99]   D. Senapati, A. K. Singh, and P. C. Ray, Chemical Physics Letters 487 (2010) 88.

[100] K. Subrata, S. Panigrahi, S. Praharaj, S. Basu, S. K. Ghosh, A. Pal, and T. Pal, Nanotechnology 18 (2007) 075712.

[101] X. Bai, L. Zheng, N. Li, B. Dong, and H. Liu, Crystal Growth & Design 8 (2008) 3840.

[102] B. Voigtlander, U. Linke, H. Stollwerk, and J. Brona, Journal of Vacuum Science & Technology A: Vacuum, Surfaces, and Films 23 (2005) 1535.

[103] T. H. Ha, Y. J. Kim, and S. H. Park, Chemical Communications 46 (2010) 3164.

[104] M. W. Mathias Brust, Donald Bethell, David J. Schiffrin and Robin Whyman, Journal of the Chemical Society, Chemical Communications 7 (1994) 801.

[105] B. R. Selvi, D. Jagadeesan, B. S. Suma, G. Nagashankar, M. Arif, K. Balasubramanyam, M. Eswaramoorthy, and T. K. Kundu, Nano Letters 8 (2008) 3182.

[106] N. S. John, P. J. Thomas, and G. U. Kulkarni, The Journal of Physical Chemistry B 107 (2003) 11376.

[107] N. Jiali, Z. Tao, and L. Zhongfan, Nanotechnology 18 (2007) 325607.

[108] P. Jiang, J.-J. Zhou, R. Li, Y. Gao, T.-L. Sun, X.-W. Zhao, Y.-J. Xiang, and S.-S. Xie, Journal of Nanoparticle Research 8 (2006) 927.

[109] M. H. Yukselici, Journal of Physics-Condensed Matter 14 (2002) 1153.

[110] R. W. H. S.A. Visser, and S.L. Cooper, Polymers. Biomaterials Science, Academic Press, 1996.

[111] H.-J. Bai, M.-L. Shao, H.-L. Gou, J.-J. Xu, and H.-Y. Chen, Langmuir 25 (2009) 10402.

[112] A. Dhawan, M. Gerhold, A. Madison, J. Fowlkes, P. E. Russell, T. Vo-Dinh, and D. N. Leonard, Scanning 31 (2009) 139.

[113] E. J. R. Vesseur, R. de Waele, H. J. Lezec, H. A. Atwater, F. J. G. de Abajo, and A. Polman, Applied Physics Letters 92 (2008) 083110.

[114] J.-S. Huang, V. Callegari, P. Geisler, C. Brüning, J. Kern, J. C. Prangsma, X. Wu, T. Feichtner, J. Ziegler, P. Weinmann, M. Kamp, A. Forchel, P. Biagioni, U. Sennhauser, and B. Hecht, Nature Communications 1 (2010) 150.

[115] H. Ishihara, K. Kuribayashi, and S. Takeuchi, in IEEE 22nd International Conference on Micro Electro Mechanical Systems, MEMS-2009, 2009, p. 367.

[116] H. Onoe and S. Takeuchi, Journal of Micromechanics and Microengineering 18 (2008) 095003.

[117] M. Veiseh, B. T. Wickes, D. G. Castner, and M. Zhang, Biomaterials 25 (2004) 3315.

[118] M. N. Yousaf, B. T. Houseman, and M. Mrksich, Proceedings of the National Academy of Sciences of the United States of America 98 (2001) 5992.

[119] V. Brunetti, G. Maiorano, L. Rizzello, B. Sorce, S. Sabella, R. Cingolani, and P. P. Pompa, Proceedings of the National Academy of Sciences 107 (2010) 6264.

[120] E. L. Moal, E. Fort, S. Lévêque-Fort, F. P. Cordelières, M. P. Fontaine-Aupart, and C. Ricolleau, Biophysics Journal 92 (2007) 2150.

[121] K. Aslan, I. Gryczynski, J. Malicka, E. Matveeva, J. R. Lakowicz, and C. D. Geddes, Current Opinion in Biotechnology 16 (2005) 55.

[122] J. Zhang, Y. Fu, D. Liang, R. Y. Zhao, and J. R. Lakowicz, Langmuir 24 (2008) 12452.

[123] R. Thomas, S. Varghese, and G. U. Kulkarni, Journal of Materials Chemistry 19 (2009) 4401.

[124] X. Lu, M. Rycenga, S. E. Skrabalak, B. Wiley, and Y. Xia, Annual Review of Physical Chemistry 60 (2009) 167.

[125] G. Paul, Nanotechnology 12 (2001) 485.

[126] J. Hu, Z. Wang, and J. Li, Sensors 7 (2007) 3299.

PART III

Patterned Synthesis of Nanomaterials by EBL, MIMIC and NIL*

SUMMARY

The study explores the possibility of using metal anions complexed with tetraoctylammonium bromide (ToABr) and metal thiolates as single source direct write precursors in e-beam, soft and nanoimprint lithography processes to obtain micro and nanoscale patterns of various metals i.e., Au, Pd, Pt, Ag, Cu as well as of their alloys (AuCu), oxides (Co_3O_4, ZnO), nitrides (CoN, InN, GaN) and sulfides (Ag_2S, Pd_4S). The obtained precursors are easily processable as they have reasonable solubility in common solvents and are obtainable as smooth films, both being important for high resolution patterning. The e-resist action of the precursors originates from the extreme e-beam sensitivity of the hydrocarbon chain present in the precursors, while direct micromolding and NIL has been possible due to the easy flow of the precursor solutions in capillaries. The easy removal of the hydrocarbon from patterned regions by thermolysis on a hot plate in the ambient or in controlled atmosphere enables to form the desired product. This method can be easily generalized for many materials.

III.1 INTRODUCTION

As discussed in the Part I, conventional lithography techniques involve multiple process steps. Particularly in the crucial process steps such as metal etching and lift off, there is a high probability to contaminate the patterned material from the external etching agents or lift-off solution. The multiple process steps are cumbersome, time consuming and cost prohibitive. Due to this reason, direct write techniques [1] are becoming popular in many beam based techniques (electron beam, focused ion beam, laser lithography), which reduce the number of steps in the lithography process flow (Figure III.1). Very recently, direct methods are thought of for large area patterning techniques such as soft lithography and nanoimprinting as well [2]. Single source precursors which can be made to flow into narrow microchannels of the mold are highly desirable. In direct MIMIC and NIL, the development, etching and lift-off processes are removed, thus making the process flow much simpler. In the context of direct write lithography techniques, there is an increasing emphasis on processable single source precursors, which can directly lead to the desired materials.
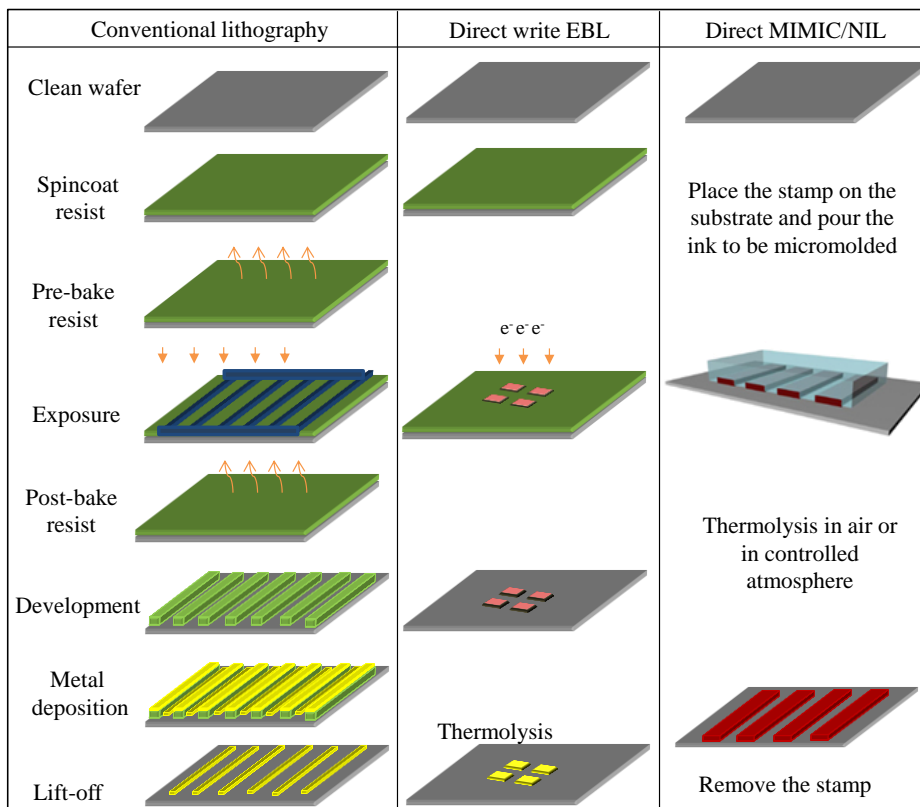
Figure III.1 Conventional lithography vs direct lithography methods.

On the other hand, single step synthesis of materials as thin films from single source precursors is well known. Even though physical methods such as pulsed laser ablation and RF sputtering making use of powder pellet of the compound, produce smooth films [3], they

require vacuum and elevated temperatures and can be time consuming as well as expensive. Also, chemical vapor deposition techniques rely on gaseous forms of precursors for which suitable precursors with low vapor pressures are not always available [4]. Thus, if one finds a suitable precursor solution to work with, the simplest method would be to coat a few drops on a substrate and converting to the desired composition by preferably a single step processing. For example, oximate [5] and naphthenate [6] complexes were utilized as single source precursors for preparing ZnO films. Triazidogallium and derivatives have been shown to serve as single-molecule precursors for the deposition of polycrystalline GaN thin films [7]. Platinum carbonyl clusters coated from a solution and subjected to pyrolysis above 100 °C produce thin films of Pt [8]. The preparation of Cu sulphide thin films was possible by the thermal decomposition of drop coated dithiocarbamate complexes in Ar atmosphere [9]. Many other compounds pose difficult situations. As an example, the case of Pd_4S may be noted. Pd sulfides form an interesting class of compounds i.e., metal rich sulphides - Pd_4S, Pd_3S, $Pd_{16}S_7$, $Pd_{2.2}S$ besides PdS [10]. Especially, Pd_4S conducts like a metal [11], but unlike Pd, is impermeable to H_2 [12]. The Pd-Pd distance being close to that of Pd metal [13], it is not surprising that it behaves metallic. Pd_4S, although not studied well in its pure phase, is believed to be the primary component in catalysts that remove Hg from coal gas streams [14], catalysts that are resistant to acidic solutions used for the electrolytic deposition of Cu while manufacturing circuit boards [15]. It is also projected to be a material for high temperature electrodes [16], as well as in solar cells [17-20]. Conventional synthesis of Pd sulphides is done by heating of the elements in requisite proportions in an evacuated tube, grinding and annealing the obtained powder product for several days [21,22]. For Pd sulfide films, usually Pd metal films are sulfidised [23]. Recently, O'Brien and co-workers reported deposition of thin films of mixtures of Pd sulphides by aerosol-assisted chemical vapour deposition using dithiocarbamate precursors [24]. Similarly, dithiocarbamate and dithiolate complexes have also been used as single source precursors for Pd sulphides [25]. Chalcogenolato-bridged allyl complexes have served as versatile precursors for Pd sulfides [26,27]. The precursor synthesis can be tedious with low yields. In all the above mentioned cases, the obtained films are not always of high quality, nevertheless suffice for many applications.

Patterning of functional materials is an important step in realizing the applications of the materials. The use of a single source precursor which is lithographically adaptable reduces the arduous steps, making the process less tedious [28]. The increasing interest in

direct write e-beam lithography (EBL) with single source precursors is evident in the recent years. Au nanoparticles capped with alkanethiol ligands [29] and Pd clusters protected by ToABr [30] have served as e-beam resists to write metal nanopatterns. Instead of nanoparticle films, metal-organic precursor films are preferred as they are relatively more sensitive requiring less e-dosage. Tailor-made metal organic complexes like Au(I)-thiolate [31] and Pd acetate [32] have been employed as resists in EBL to generate nanopatterns of Au [31] and Pd [32] respectively. Using Ni naphthenate direct write e-beam resist, sub-10 nm Ni lines have been fabricated [33].While using a metal organic precursor as a direct write resist, an additional advantage is that the patterned precursor can be transformed into a desired functional material, besides metal, by appropriately choosing the thermolysis conditions. Working with metal-organic precursors, soft lithography methods such as micromolding in capillaries (MIMIC) [34] can also be an attractive possibility, especially for large area patterning. Direct MIMIC has been explored in the literature with various soluble functional material inks. For instance, Greco et al. [8], fabricated conductive Pt stripes using a Pt carbonyl cluster precursor. Another variation of stamping i.e., imprinting has been utilized for direct imprinting of various materials such as metal nanoparticles [35], ceramics [36] and metal oxides [37] etc. Direct NIL using hard Si or quartz stamps to produce functional material patterns over large area is also possible, if one could adjust the viscosity of the precursor material and prevent the sticking of the imprinting material to the stamp. High resolution TiO_2 nanostructures were directly imprinted recently using thermally polymerizable liquid precursors containing titanium methacrylate [38].

Direct patterning of a functional material as discussed is itself a difficult task and to obtain the feature sizes below 100 nm over large areas is even more challenging. The fabrication of nanostructures with lateral resolution down to 50 nm has been achieved by special techniques such as microtoming [39], phase shift lithography employing composite masks [40], nanocontact printing [41], edge spreading lithography [42], capillary force lithography [43,44], transfer printing [45], block copolymer templates [46], shrinking hydrogels [47] etc. All these methods however are indirect, and consist of multiple steps.

III.2 SCOPE OF THE PRESENT INVESTIGATION

Neither a generalized single source precursor nor a simple method exists thus far in the literature for direct writing a range of nanomaterials. Where there is some general route [33,48,49], sensitivity, throughput and nature of the patterns are not sufficiently satisfactory.

The right choice of the precursor material is very critical to have the highly precise definition of the patterned features by direct write lithography methods, with minimum amount of impurities left, keeping the process temperature low at the same time. The precursors are ought to be highly soluble in organic solvents. Importantly, they should leave behind very little carbon impurity in the final structures following thermolysis. In this context, the use of metal alkanethiolates as single source precursors for metal and metal sulphides attracts attention [50,51]. The use of Pd alkanethiolates as single source precursors to produce Pd sulfides was not explored thus far which will be discussed in the present part of the thesis.
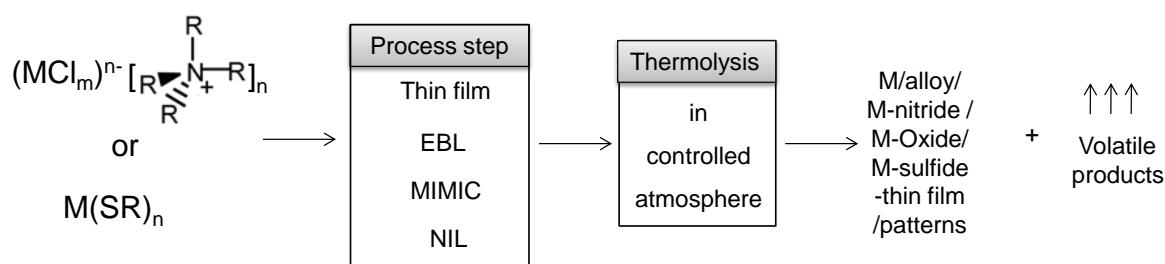
Scheme III.1 The process flow for the preparation of patterns and thin films of metals and their alloys, metal nitrides, oxides and sulfides.

This scheme of process is essentially direct write lithography which in contrast to conventional lithography methods, does not use polymeric resists taken through a number of process steps such as exposure, development, metal deposition and lift-off or etching; the latter steps although crucial often lead to incorporation of contaminants into the patterned materials. Various single source precursors exist for various materials as discussed in III.1, nevertheless the precursors are specific to the material, and a general precursor for obtaining patterns of various materials was not addressed thus far. In this part of the thesis, two generic classes of single source precursors i.e., metal anion-tetraoctylammonium bromide complexes and metal thiolates are discussed, which are amenable to direct write EBL, MIMIC and NIL.

III.3 EXPERIMENTAL DETAILS

Si(100) substrates (n-doped, 4–7 Ω.cm) and glass substrates were cleaned by ultrasonicating in acetone and double distilled water and dried under flowing N_2. The e-resist film was made by spin-coating of the M-ToABr or M-thiolate solution at 2000 rpm for 1 min. EBL was performed using a Nova NanoSEM 600 instrument (FEI Co., The Netherlands). The electron beam energy employed for patterning was 5-10 kV. For direct micromolding, elastomeric stamps were fabricated by replica molding of polydimethylsiloxane (PDMS) on a commercially available compact disk (Sony CD-R).

PDMS was prepared by mixing Sylgard 184 curing agent (Dow Corning) and its elastomer in the ratio of 1:10 by weight. This ratio was preferred as it results in a flexible stamp with a Young's modulus of 0.75 MPa and poisson's ratio of ~0.5. The mixture was then degassed under vacuum for 30 min. PDMS was poured onto the polycarbonate backing of the master (CD) and then cured in the oven at 60 °C overnight. The stamp peeled off from the master contained protruding line features of 505 nm width separated by 950 nm channels which were ~160 nm high. When Sony DVD-R was used as a master, feature widths were ~350 nm separated by ~400 nm, with height ~140 nm. The stamp was ~2 mm thick and usually weighed ~2.4-2.5 g. Cured PDMS stamps were cleaned using hexane and further ultrasonicated in ethanol to remove any low molecular weight, uncured oligomers. After keeping the PDMS stamp on the substrate, 60 μL of the precursor solution is injected at the interface of the stamp and the substrate using a micropipette. The entire setup was heated slowly at a ramp of 10 °C/min to 250 °C. In order to pattern metal nanolines via modified micromolding, pressure (100 Pa to 1010 Pa) was applied on top of the PDMS by placing appropriate weight and then a 60 μL of the precursor solution is injected at the interface of the stamp and the substrate using a micropipette. The whole setup was then heated to 250 °C at a ramp of 30 °C/min and held for 30 min on a hot plate. Following annealing, the stamp is removed leaving behind the nanolines. For nanoimprinting, Si substrates and molds were cleaned with piranha solution at 140 °C for 2 hrs, followed by rinsing with deionized water and blow drying using a nitrogen gun. The substrates were kept in a dry area while the Si molds were treated with perfluorodecyl-trichlorosilane for 5 hrs to reduce their surface energy in order to facilitate a clean demolding after imprinting. Three types of molds were used for imprinting, namely, 250 and 100 nm gratings with equal line width and spacing and a dimple mold with 200 nm holes which were 200 nm deep. Imprint lithography was carried out in an Obducat imprinter (Obducat, Sweden). For electroless deposition of Cu onto Pd or CoN, the copper plating bath [52] contained 3 g of $CuSO_4$, 14 g of sodium potassium tartrate mixed with 4 g of NaOH in 100 mL of distilled water (Solution A). Solution B was an aqueous formaldehyde solution (37.2 wt%). A and B solutions were mixed in a 10:1 ratio. The plating was carried out by immersing the desired substrate into the mixture for varying times of 30-300 s. The process was stopped by removing the sample and rinsing with distilled water. For electrolytic deposition of Cu film onto Pd_4S, an applied voltage of -0.5 V was used with Pd_4S as working electrode employing the standard procedure [15], using $CuSO_4$ mixed with H_2SO_4 as the electrolyte.

The synthesis procedures adopted for the direct write precursors are as follows.

M-ToABr: All metal salts were obtained from Sigma Aldrich, tetraoctylammonium bromide (ToABr) from Spectrochem and dodecylamine (DDA) was purchased from Merck; they were used without further purification. The water used throughout this investigation was double distilled and deionized. To 50 mM aqueous metal solution, 50mM ToABr was added. In some cases conc.HCl was used to aid the formation of metal anions. The gravimetry for M-ToABr (M=metal) was done by taking metal salt solution (for example $HAuCl_4$ as mother liquor) and aqueous phase left after phase transfering with ToABr. Approximately 100µL solution of both mother liquor and aqueous phase was coated on preweighed coverslips and thermolyzed at 100 °C for 1h. After cooling to room temperature, the coverslip was weighed again and from the weight difference, the amount of metal which did not phase transfer was calculated. Detailed experimental of the formation of metal anions and the phase transfer process are illustrated below (Table III.1 and Figure III.2).

Table III.1 Procedure of phase transfer to ToABr for various metal anions.

M-ToABr (M)	Starting material	Metal anion	Phase transferred solution color
Pd	H_2PdCl_4	$PdCl_4^{2-}$	Dark red
Pt	K_2PtCl_4	$PtCl_4^{2-}$	Light orange
Ag	$AgNO_3$ + HCl	$(AgCl_2)^-$	Colorless
Au	$HAuCl_4$	$(AuCl_4)^-$	Dark red
Pb	$Pb(CH_3COO)_2$ + HCl	$(PbCl_4)^-$	Colorless
Cu	$CuCl_2$ + HCl	$(CuCl_4)^{2-}$	Red
In	In_2O_3 + HCl	$(InCl_4)^-$	Colorless
Co	$CoCl_2$ + HCl	$(CoCl_4)^-$	Blue
Ga	Ga_2O_3 + HCl	$(GaCl_4)^-$	Light milky
AuCu	$HAuCl_4$ + $CuCl_2$+HCl	$(AuCl_4)^-$ + $(CuCl_4)^{2-}$	Dark maroon
Zn	$Zn(CH_3COO)_2$	--	Colorless

Ag-DDA/Cu-DDA: Ethanolic dodecylamine (DDA) (100 µl in 5 mL of ethanol) was added to 5ml of $AgNO_3$/ $CuSO_4$ (1 mM) while stirring. To this mixture, toluene was added on top. DDA mediates the phase transfer of Ag to toluene. The phase transferred toluene solution is coated on substrate and thermolyzed at 250°C for 1 hr in N_2 atmosphere.
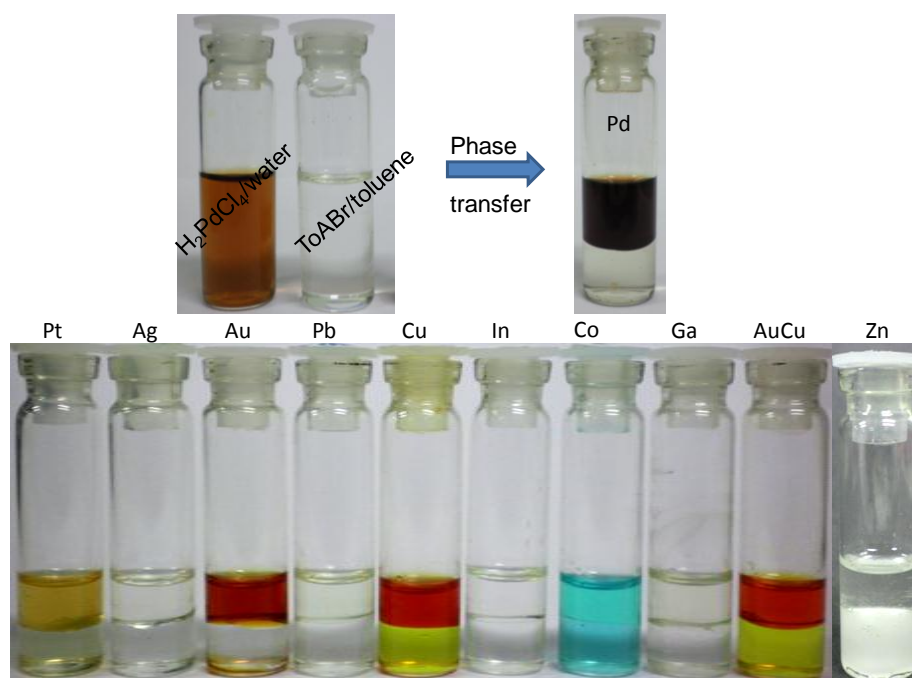
Figure III.2 Photographs showing the phase transferred complexes of various metals.

M-Thiolates

Pd thiolate: To 5 mmol of Pd(OAc)$_2$ (Sigma Aldrich) in toluene (7 mL) was added 5 mmol of octanethiol or benzylthiol (Fluka, 99%) in toluene (3 mL), and the resulting mixture was stirred vigorously. Following the reaction, the solution became viscous, and the yellow color deepened to orange-yellow. The obtained thiolate was washed with methanol and acetonitrile to remove excess thiol and finally dissolved in toluene or chloroform to obtain a solution of desired concentration.

Au thiolate: First, Au(PPh$_3$)Cl was synthesized based on a recipe reported in the literature [53,54]. The solvents were degassed prior to use by bubbling argon for 2 min. Hydrogen tetrachloroaurate (HAuCl$_4$.xH$_2$O, x~3, 1 g, 2.54 mmol) was introduced into a 250 mL round bottomed Schlenk flask equipped with a stopcock and backfilled with argon. Degassed 95% EtOH (analytical grade, 35 mL) was made to dissolve the precursor. To this solution was added under argon, a solution of PPh$_3$ (1.364 g, 5.20 mmol) in 50 mL of degassed 96% EtOH, using glass pipette. The reaction mixture became colorless immediately, and a white precipitate appeared after a few seconds.

$$HAuCl_4 + 2PPh_3 + H_2O \longrightarrow AuCl(PPh_3) + 3HCl + O=PPh_3$$
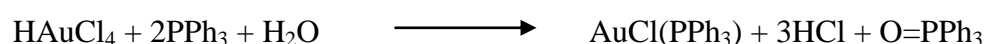
The mixture was stirred for 2 min, and the product was then removed by filtration, washed with Et$_2$O (analytical grade, three 15 mL portions), and dried in vacuum. The obtained solid was then directly dissolved in CH$_2$Cl$_2$ (10 mL) in a 250 mL Schlenk flask. Slow addition of

pentane (60 mL) and cooling to -25° C resulted in the formation of white needles of Au(PPh$_3$)Cl. Dodecylthiol from Sigma-Aldrich was used as supplied along with the prepared Au(PPh$_3$)Cl precursor for the preparation of Au(I) thiolate.

III.4 RESULTS AND DISCUSSION
III.4.1 M-ToABr as direct write precursors

Although the interaction of metal anions with quaternary ammonium salts to form complexes is well known and widely applied for the extraction of metals from aqueous solutions [55,56] these complexes had not been commonly employed in materials research. A notable exception was the Brust method, where (AuCl$_4$)$^-$ ions extracted using tetraoctylammonium bromide (ToABr) in toluene served as precursor for controlled synthesis of alkanethiol capped Au nanoparticles in solutions [57]. Since then, colloidal sols of Pt [58], Pd [59], Ag [60], Au [57], alloys such as AgAu [61], have been prepared by stabilizing the respective anions with ToABr, thus establishing usefulness of the ToABr complexes [62]. The method has been varied to obtain various anisotropic nanostructures of Au, Ag, Cu etc., by playing with the reducing agent [63]. However, these complexes have not been explored as precursors in lithography processes. It was realized that the precursors are easily processable as they have reasonable solubility in common solvents and are obtainable as smooth films, both being important for high resolution patterning. The hydrocarbon part is expected to be highly sensitive to the e-beam [64] and is easily detachable by thermal activation [51]. The liberated anion is reactive to produce the desired end product (Scheme III.1).

Many metal anions such as (AuCl$_4$)$^-$ exhibit visible color due to metal-to-ligand charge transfer (MLCT), which is often employed to monitor the process of transfer of the ions. Thus, the UV-visible spectrum shown in Figure III.3a, exhibits a peak at ~345 nm corresponding to corresponds to metal-to-ligand charge transfer of (AuCl$_4$)$^-$ ions [65] transferred to the organic phase. For ToABr, though the residence is organic medium, there may be some crosstalk at the interface effectively bringing a small fraction of ToABr into the aqueous medium as revealed using IR spectroscopy (Figure III.3b). This may adversely affect its transfer efficiency for metal anions. Among the examined cases (Figure III.3c), the efficiency is highest for (AuCl$_4$)$^-$ (99%), (PdCl$_4$)$^{2-}$ being at 94.5%. The anions of Pt, Cu, Ga and In get transferred by ToABr with efficiency in the range, 60-70%. The transfer efficiency is poor for Co (46%) and Pb (41%). There may be many factors [66,67] which

influence the process such as charge and size of the anion, pH of the aqueous chloroanion solution, the organic solvent (toluene) etc. which has not been investigated in further detail in this study. Besides octyl, alkyl ammonium bromides of other chain lengths (butyl, decyl and hexadecyl) have been tried out. The butyl complex is less soluble in toluene while for decyl and hexadecyl, the anion transfer efficiencies were found to be poorer (for $(AuCl_4)^-$: 85.3% and 55.9% for decyl and hexadecyl respectively compared to 99% for octyl). The formed complexes with ToABr have many important attributes – they are air stable and can be solubilised repeatedly in low boiling point solvents such as toluene, ethanol, chloroform etc. and the crystallization to solid state is rapid.
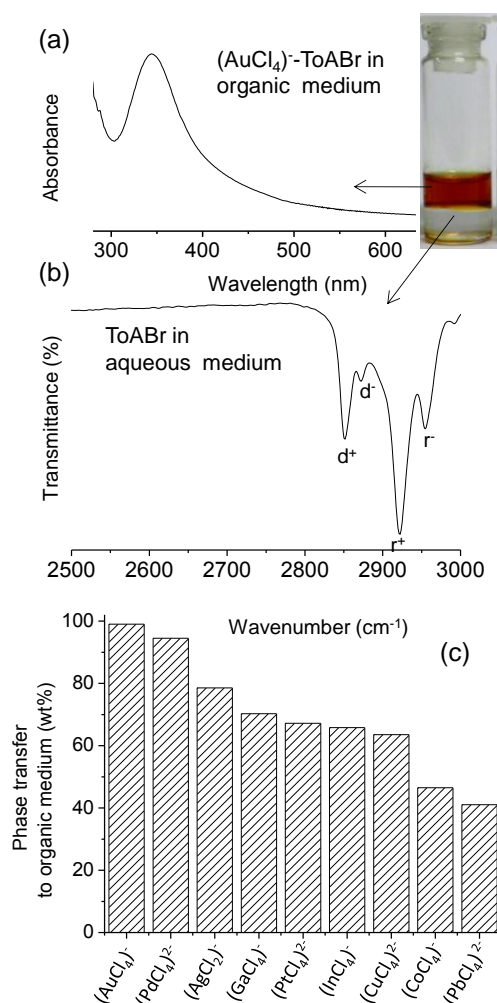
Figure III.3 Aqueous-organic phase transfer of metal anions. (a) UV-visible absorption spectrum of $(AuCl_4)^-$ phase transferred to ToABr (organic phase). Strong absorption band at 345 nm is characteristic of the MLCT band of $(AuCl_4)^-$ complex. The LMCT band at lower wavelength (260 nm) is merged with the scattering from the glass. A photograph showing the biphasic mixture is given alongside. (b) FTIR spectrum of the ToABr which got transferred to the aqueous phase. ToABr in toluene was reacted with water and the bottom aqueous solution was examined with FTIR. (c) Phase transfer efficiency of ToABr for various metal anions as estimated by gravimetry.
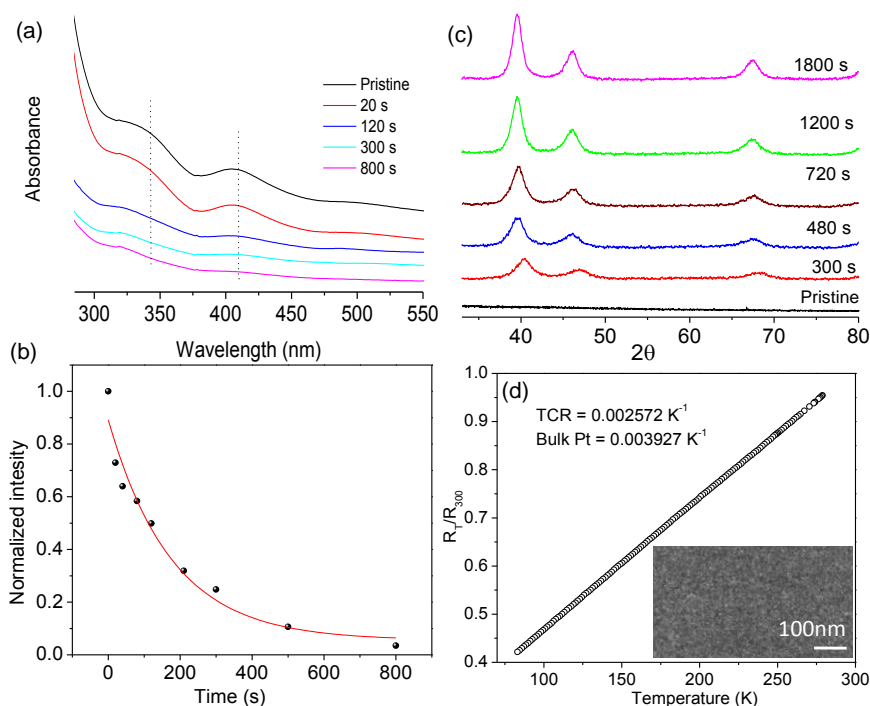
Figure III.4 Metallisation of Pt-ToABr. (a) UV-visible absorption spectra of Pt-ToABr film upon heating at 180 °C for various times as mentioned. (b) Intensity of the 342 nm band versus time of thermolysis, and (c) XRDs of Pt formed by thermolysing Pt-ToABr film for various times at 250 °C (250 °C was chosen instead of 180 °C for better crystallinity) (d) Four probe resistance measurement of the thermolysed Pt nanocrystalline film with SEM image as inset.

The metal anion-ToABr interaction is completely electrostatic which should make the separation of metal rather easy [57]. The process of metallization was carefully followed using UV-vis spectroscopy with Pt as an example. The phase transferred $(PtCl_4)^{2-}$-ToABr (Pt-ToABr for brevity) coated as a film on glass slide, shows two bands at 342 nm and 410 nm corresponding to the d-d transitions [68]. The spectra were recorded while heating the film at 180 °C for increasing duration, 20 - 800 s as shown in Figure III.4a. The d-d bands diminish in intensity gradually and almost disappear after 800 s. The decrease in the intensity of the 340 nm band is exponential (Figure III.4b) with a time constant of 175.9 sec, indicating that the process is rather slow. In addition, XRD was used as a tool to monitor the metallization process (Figure III.4c). The pristine Pt-ToABr film does not show any features in the range relevant for crystalline Pt. After thermolysing the film for 5 min, the appearance of small peaks is evident in the XRD data. With increasing time of thermolysis (Figure III.4c), the XRD peaks corresponding to crystalline Pt grew in intensity, due to an overall improvement in the crystallinity. However, the peaks were broad as the diffracting regions

were essentially nanoparticles. Using the Scherrer formula, the particle size was estimated to be ~8 nm. A corresponding SEM image shows that indeed the thermolysed Pt film is composed of polycrystalline nanoparticles (see inset in Figure III.4d and also TEM, ED in Figures III.5a and b). EDS spectrum in Figure III.5d shows that the overall content of carbon present in the spectrum is ~19 at% which is not unusual and indeed is relatively less compared to other results in the literature [69]. The metallization process (see TGA and FTIR in Figures III.5c, e and f) gives us an idea that the ToABr ligand neatly desorbs around 250 °C to give rise to Pt metal. In TGA, the total weight loss is 82.14% and the residue is 17.86%.
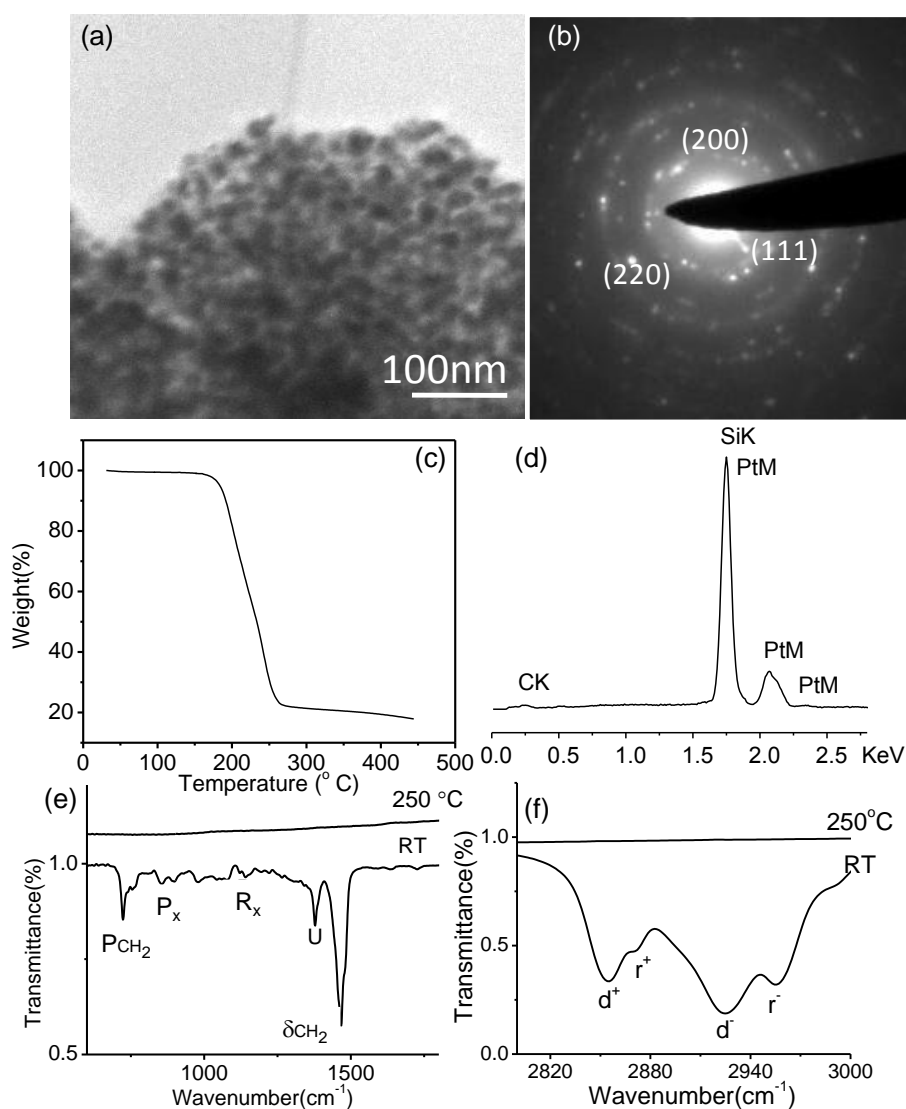
Figure III.5 (a) Transmission electron microscopy image of Pt nanoparticles and (b) the corresponding electron diffraction pattern, with the planes marked. (c) TGA of the $(PtCl_4)^{2-}$-ToABr complex, (d) EDS spectrum of the thermolysed Pt nanocrystalline film. (e) and (f) are FTIR spectra of the drop coated film of pristine complex at room temperature (RT) and after thermolysis at 250 °C for 30 min. Assignments of IR bands shown in Table III.2.

This residue corresponds to metallic Pt but for little carbon left behind. According to the weight percentage calculation, the molecular formula of the starting complex corresponds to $[N^+(C_8H_{17})_4]_2 [PtCl_4]^{2-}$. After thermolysis at 250 °C for 1 hr, all the IR bands vanished, indicating the desorption of ToABr ligand units. The band assignments for the spectra are given below (Table III.2). Four probe resistivity data of the film was measured down to 77 K (Figure III.4d). Room temperature resistivity of the film is 350 μΩ.cm. This value although higher compared to bulk Pt (10.5 μΩ.cm), is comparable to the Pt deposited by beam induced depositions and is much lower than the previously reported data on Pt obtained from metal organic precursor decomposition (see for example ref. [8], the value is ~28901 μΩ.cm). The temperature coefficient of resistance, 0.00257 K^{-1}, is close to that of bulk Pt (0.00393 K^{-1}).

Table III.2 IR bands assignments for Pt-ToABr

Wave number(cm^{-1})	Type of stretching
2954	Asym.CH$_3$ stretch r$^-$
2924	Asymm.CH$_2$ stretch d$^-$
2870	symm.CH$_3$ stretch r$^+$
2854	symm CH$_2$ stretch d$^+$
1467	CH$_2$ scissor δ
1377	CH$_2$ def (Umbrella mode) U
1138	R$_x$
854	P$_x$
724	P$_{CH_2}$

As many metals form anionic complexes which could be phase transferred to ToABr solutions (Figure III.3c), they can be exploited as single source precursors for various nanomaterial products. The precursors were drop coated as thin films onto glass substrates and thermolysed under controlled conditions. The XRD data is shown in Figure III.6 and the various results in Table III.3. While metals such as Au, Pt, Pd could be obtained by thermolysis in air, Cu and Ag formed bromides which further required reduction using NaBH$_4$. Thermolysis in H$_2$ atmosphere at 375 °C appears to be most effective for producing crystalline Pb. For the formation of nitrides, Co, Ga and In precursors were heated in N$_2$ or Ar atmosphere at 375 °C. Treating in air or O$_2$, one may obtain oxide phases such as Co$_3$O$_4$.
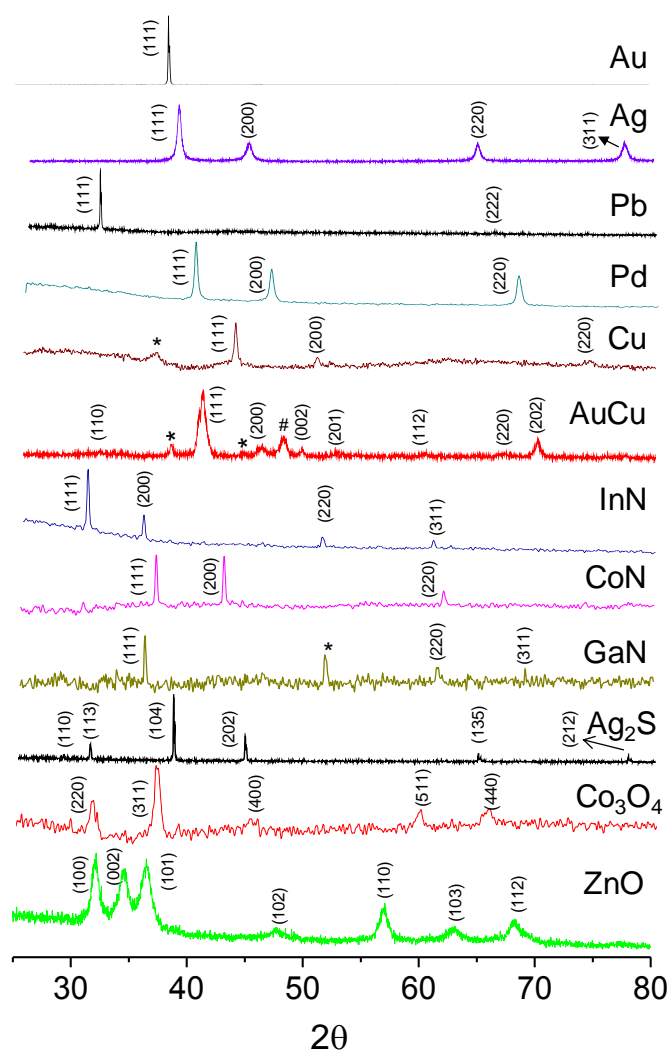
Figure III.6 XRD data of the products. The peaks are indexed following JCPDS PDF files indicated in parenthesis. Au (65-2870), Ag (89-3722), Pb (87-0663), Pd (88-2335), Cu (85-1326) (the peak marked * is due to Cu_2O. As Cu undergoes air oxidation rapidly, it may require encapsulation [70]), AuCu (89-2036) (the peaks marked * and # are due to Au and CuBr respectively), InN (88-2365), CoN (83-0831), GaN (80-0011) (the peak marked * is due to a hexagonal GaN), Ag_2S (75-1061), Co_3O_4 (65-3103) and ZnO (89-1397).

It is possible to prepare alloys as well, such as AuCu. By adding alkanethiol to the phase transferred Ag-ToABr precursor and thermolysing in H_2, Ag_2S was also prepared [71]. The anion transfer efficiency by ToABr is a matter of concern with some metals, partly because suitable anions cannot be found. Instead, even simple salts can be tried out. As a case study, $Zn(OAc)_2$ salt was used in the aqueous medium. There was hardly any complex formation with ToABr in the organic phase, rather ToABr got transferred from the organic to the aqueous phase. It is surprising that ToABr exhibits a definite interaction with $Zn(OAc)_2$, although the latter is not an anionic complex. A thermolysis in air at 250 °C produced ZnO films (Figure III.6 and Figure III.7). Perhaps the aqueous route of phase transfer is

extendable to other metals, which may not form anionic complexes readily. The morphology of the obtained thin film products was examined using FESEM (Figure III.7). While some formed smooth films, most of the products were nanoparticulate films.
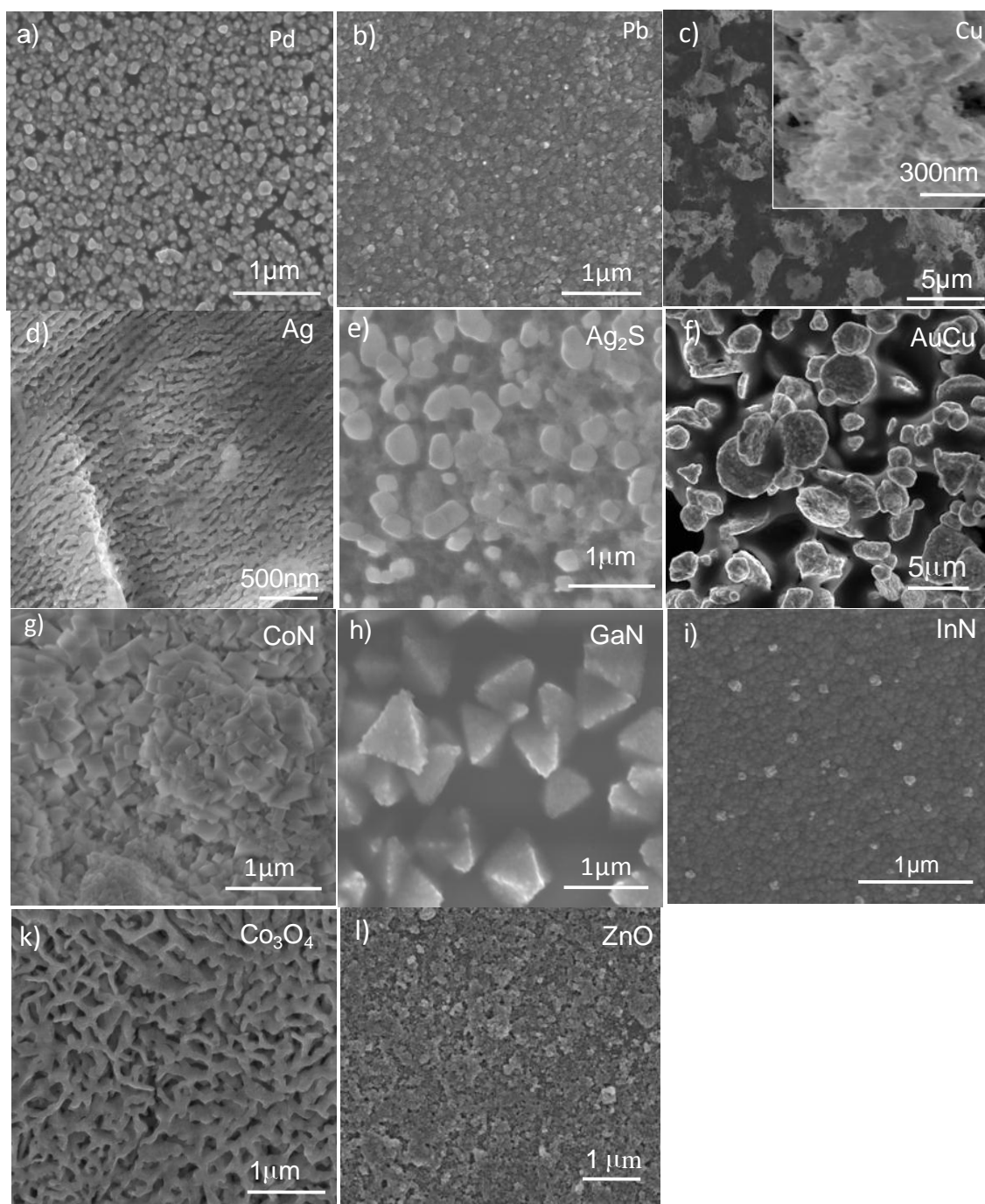
Figure III.7 SEM images of thermolysed films of various nanomaterials mentioned in Figure III.6.

Among the prepared nanomaterials, GaN and InN are important semiconductors. Band gaps of the obtained InN and GaN films were calculated using UV-visible absorption

spectrum. Band gap (Eg) of a semiconductor is related to its absorption coefficient by the equation

$$\alpha = \left(\frac{B}{h\nu}\right)\left(h\nu - E_g\right)^m$$

where α is the absorption coefficient, B is a constant, hν is the energy of incident photon, and E_g is the band gap of the material. As shown in Figure III.8, the intercept gives the band gap (Eg) to be ~1.6 eV for InN and 3.4 eV for GaN, comparable to the literature values [72,73] (InN, 1-1.5eV; GaN, 3.4eV).
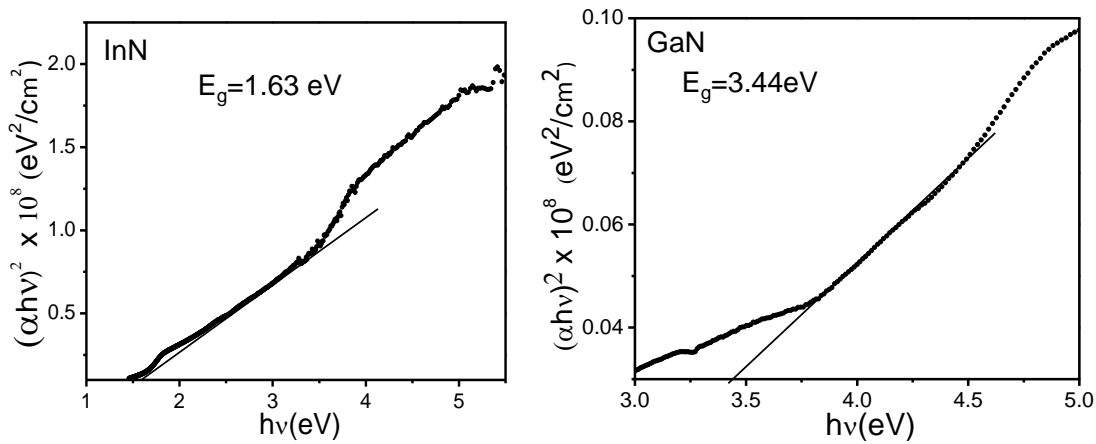
Figure III.8 Squared absorption coefficient as a function of photon energy of InN and GaN films on glass substrate.

CoN film exhibits magnetic hysteresis at room temperature with a coercivity of ~100 Oe (Figure III.9). At 5 K, the hysteresis is pronounced with coercivity value being ~125 Oe. As the full saturation of the magnetization was not obtained, the coexistence of paramagnetic elements with some ferromagnetic entities in the cobalt nitride film can be expected [74]. The magnetization was also measured as a function of temperature down to 5 K, which shows sharp increase in the magnetization below 20 K. It is discussed in the literature [75] that such a sharp rise could be due to the presence of physisorbed oxygen in the interstitial sites. CoN, apart from being magnetic, finds application in electronic industry for Cu electroless deposition [76]. The obtained CoN thin films were tested for this property of electroless deposition of Cu. To deposit Cu, the CoN substrate was immersed in the freshly prepared Cu plating bath for 300 s at room temperature. The Cu electroless deposition occurs uniformly and homogenously as evident by XRD and EDS map (see Figure III.10) of the CoN film after Cu deposition.
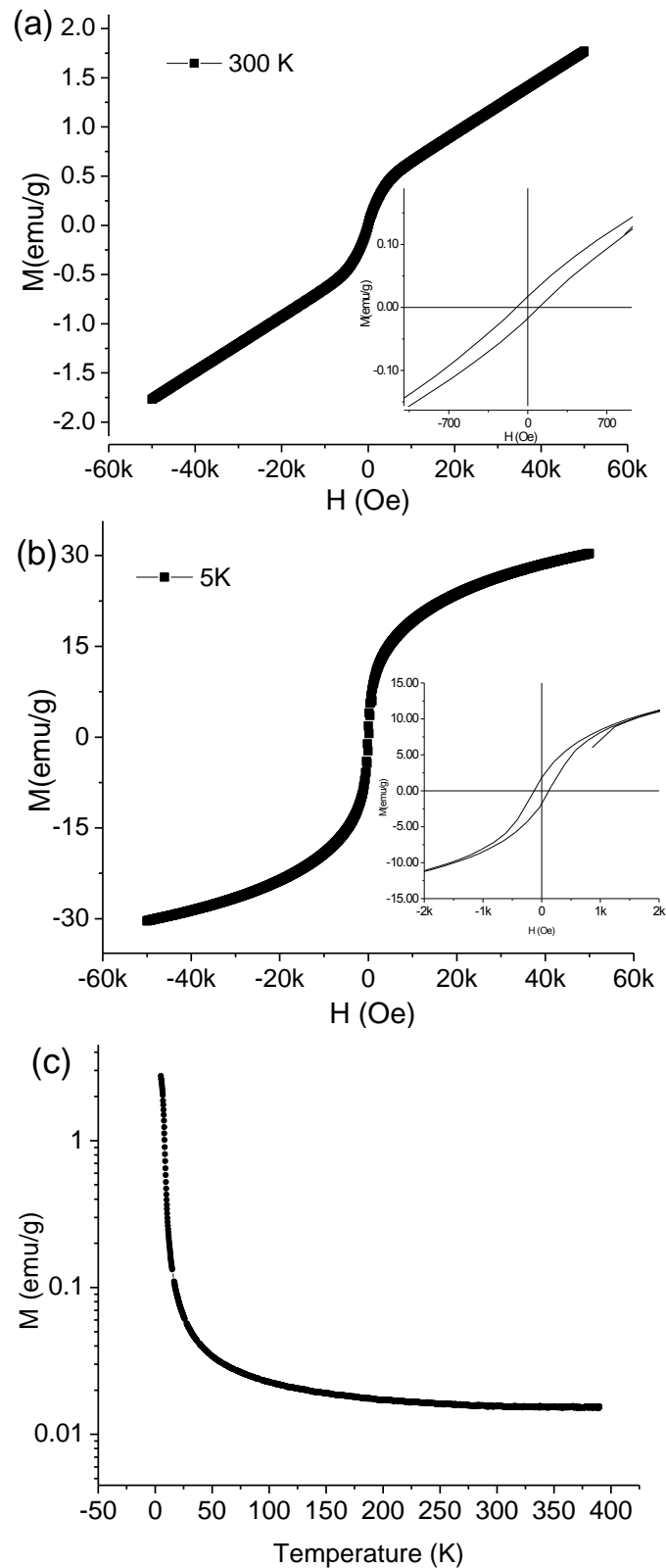
Figure III.9 Magnetization vs applied magnetic field for CoN films at 300 and 5K. Magnetization vs temperature curve for the same at an applied field of 100 Oe. CoN thin pellets were used for magnetic measurements with a vibrating sample magnetometer using a physical properties measurement system (PPMS, Quantum Design, USA).
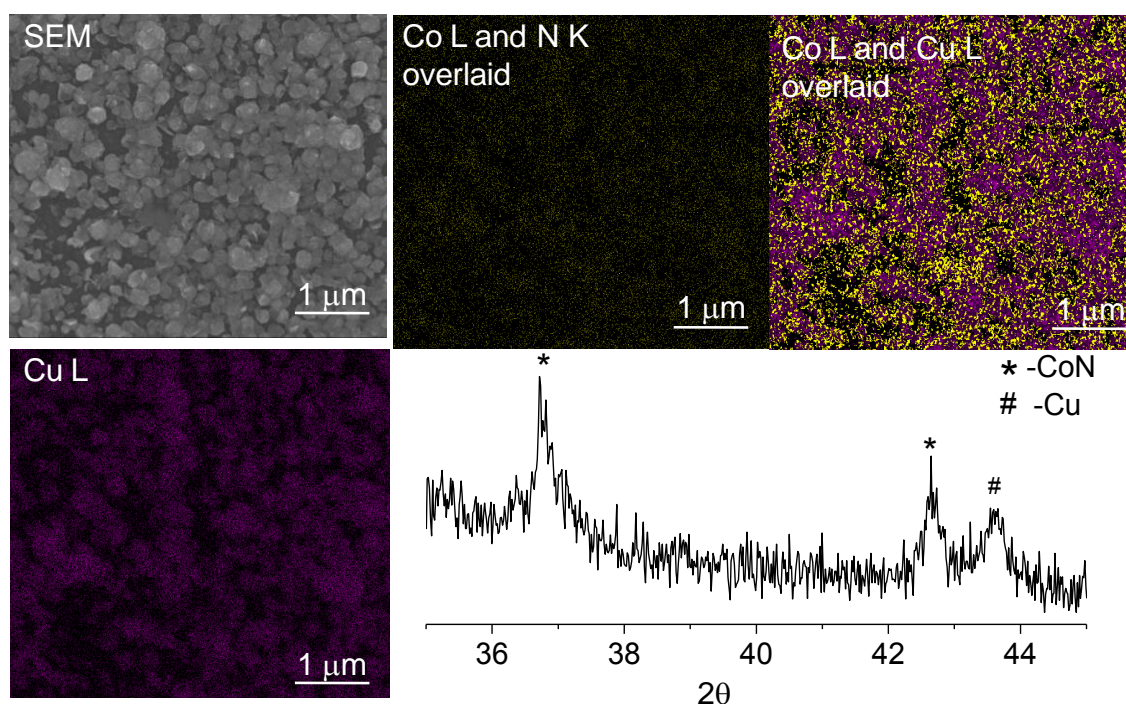
Figure III.10 SEM image of CoN film electrolessly deposited with Cu along with EDS maps. XRD pattern of the CoN film after electroless deposition shows the peak corresponding to Cu.

All the M-ToABr complexes which served as single source precursors for thin films of various materials have been summarized in Table III.3.

Direct write EBL using M-ToABr

The phase transfer and complexing agent ToABr is amenable to lithography. ToABr can form smooth films when spin coated. The average roughness of the spin coated ToABr (50 mM) film on Si substrate is ~1.5 nm. Direct write EBL process with ToABr resist is simple as illustrated in the schematic of Figure III.11a. At 5 kV, patterning was done with varying e-dosages, followed by development in toluene for 5 s. Well defined structures of ToABr were seen on the substrate wherever the e-beam was exposed, indicating the negative tone of the ToABr e-resist. Figure III.11b shows a pattern of ToABr on Si, with the corresponding EDS maps for C K, Br K and N K levels shown in Figure III.11c-e. The pattern is primarily composed of carbon. The C/Br/N elemental ratios as 80.08 : 11.80 : 3.02 were obtained for the patterned regions whereas the initial composition of the unexposed ToABr resist $(N^+(C_8H_{17})_4Br)$ was 70.40 : 14.46 : 2.51 implying that the e-dosage causes only minimal change in the overall composition.

Table III.3 M-ToABr complexes as single source precursors to various nanomaterials under controlled thermolysis conditions. The product morphology and functional properties as measured are also listed.

S.No	M-ToABr (M)	Thermolysis condition			End Product	Morphology	Particle size (nm)	Property
		Temp (°C)	Time (h)	Atm.				
1	Pt	250	1	air	Pt	particulates	5-10	• ρ =350.2 $\mu\Omega$.cm • ρ/ρ^o =33.35
2	Au	250	1	air	Au	particulates	5-40	Face centred cubic
3	Ag	250	1	air	Ag*	sheet like	25-50	• ρ =1840 $\mu\Omega$.cm • ρ/ρ^o =1159.4
4	Pb	375	1	H_2	Pb	Densely packed particles	10-150	Face centred cubic
5	Pd	250	1	air	Pd	particulates	50-200	• ρ= 67.57 $\mu\Omega$.cm • ρ/ρ^o =6.41
6	Cu	375	1	N_2	Cu*	particulates	10-20	• ρ =440 $\mu\Omega$.cm • ρ/ρ^o =262.2
7	Au:Cu 1:1	375	3	N_2	AuCu	plates	400	Tetragonal
8	In	375	3	N_2/Ar	InN	particulates	15-20	band gap ~1.63eV
9	Co	375	3	Ar	CoN	Cubic shaped particles	10-200	• NaCl like structure • Magnetic hysteresis • Cu electroless deposition
10	Ga	375	3	N_2/Ar	GaN	Pyramid shaped nanoparticulates	50-100	• Cubic structure with some hexagonal impurity (marked by * in XRD) • band gap ~3.44eV
11	Ag: C_{12} SH 1:5	375	1	H_2	Ag_2S	particulates	30-200	Monoclinic
12	Co	375	1	Air/O_2	Co_3O_4	Porous nanowalls	200	Face centred cubic
13	Zn	250	1	Air	ZnO	particulates	5-20	Wurtzite structure

ρ = resistivity and ρ^o = bulk resistivity
* - In these cases, metal bromides obtained were to be reduced by $NaBH_4$.

In order to characterize the ToABr e-resist parameters such as sensitivity and contrast, squares of 10×10 μm^2 were patterned on a film of thickness ~200 nm while gradually varying the e-dosage from 0.04 to 250 mC·cm^{-2} at 5 kV with a beam current of 4.2 nA (Figure III.11f). Following development in toluene, optical profilometric measurements were done to determine the thickness of the patterned regions. From the plot in Figure III.11f, it is possible to deduce the sensitivity of the resist, which is defined as the dose at which half the thickness of the resist is preserved. This value was found to be 65 mC/cm^2 for

ToABr, which is comparable to the polymeric resists, for instance the well-known poly(methylmethacrylate) resist sensitivity is 0.2 mC·cm^{-2} at 50 kV [77].
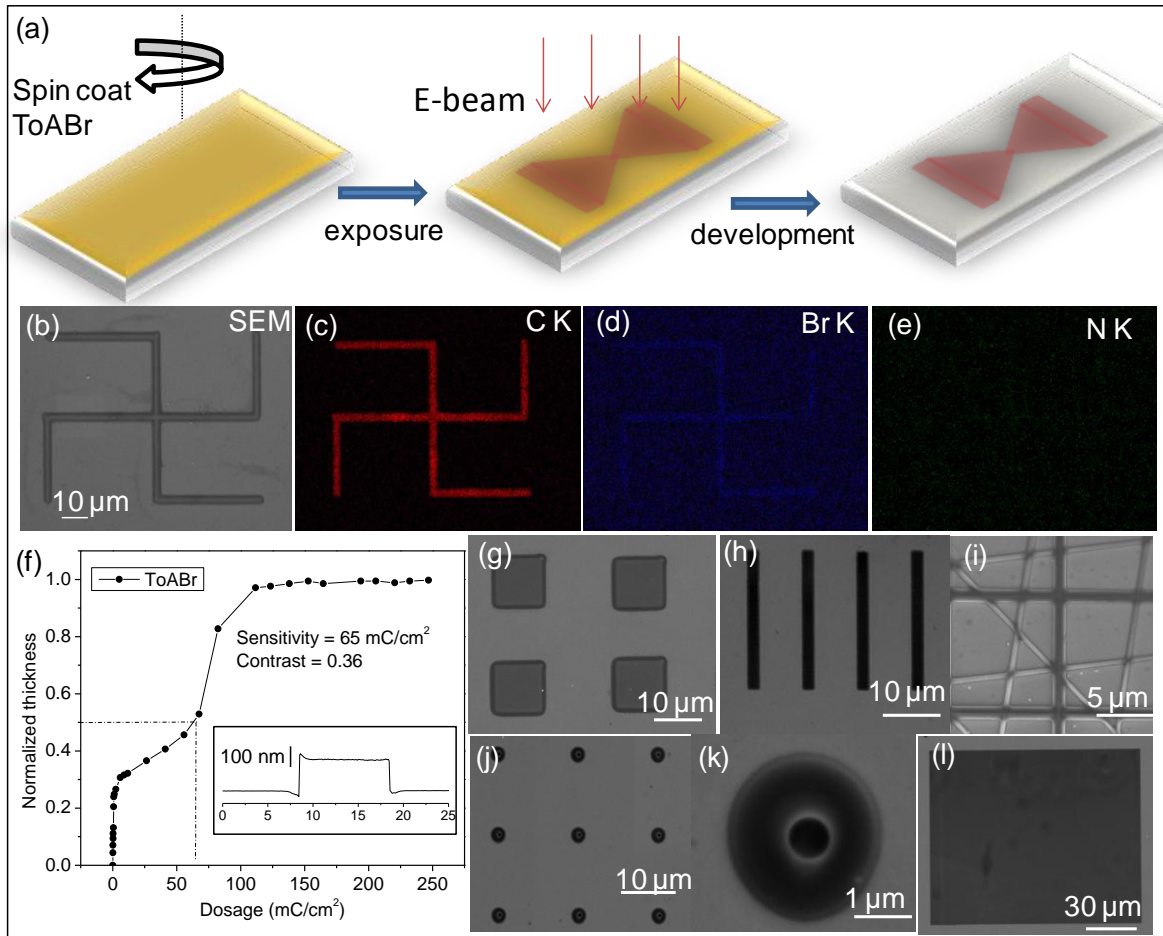
Figure III.11 ToABr e-beam resist: (a) Schematic of EBL using ToABr direct-write resist - spincoating, EBL and development. (b) SEM image showing a patterned ToABr *swastik* and (c-e) C K, Br K and N K EDS maps. (f) Variation in the film thickness (after development) normalized with respect to initial thickness, versus the e-dose (beam energy, 5 kV). Inset shows the *z*-profile of a patterned region (e-dosage, 150 mC·cm^{-2}) obtained from optical profilometric measurement. (g-k) palettes showing various patterns of ToABr e-resist. (l) A large area pattern of ToABr (e-dosage 50 mC/cm^2).

Further, the resolution achievable with a resist is defined in terms of its contrast parameter, γ: the higher the contrast, the higher the resolution. For a negative resist, $\gamma = 1/\log(d_0/d_i)$, where d_0 is the dose required to retain 100% of the resist material and d_i is the minimum dose at which resist action just begins. The measured contrast value for ToABr resist is 0.36. Figure III.11g-k show various patterns such as squares, lines, concentric circles written onto ToABr by EBL. Intricate patterns as shown in Figure III.11i were also feasible with ToABr. The edges of the patterns are quite sharp as evident in the patterns. It is also possible to pattern large areas employing low e-dosage; a patterned area of dimensions 120 x

140 μm^2 is shown in Figure III.11l. ToABr can act as an etch mask after EBL. For this experiment, the resist was spin coated on Au/Si substrate. After performing EBL (Figure III.12a), Au etching was performed utilizing ToABr as etch mask. Au beneath the ToABr patterns was protected from etching while it was removed from rest of the regions (see EDS maps shown in Figure III.12). Following washing off of the ToABr, patterned Au nanolines are shown in Figure III.12b.
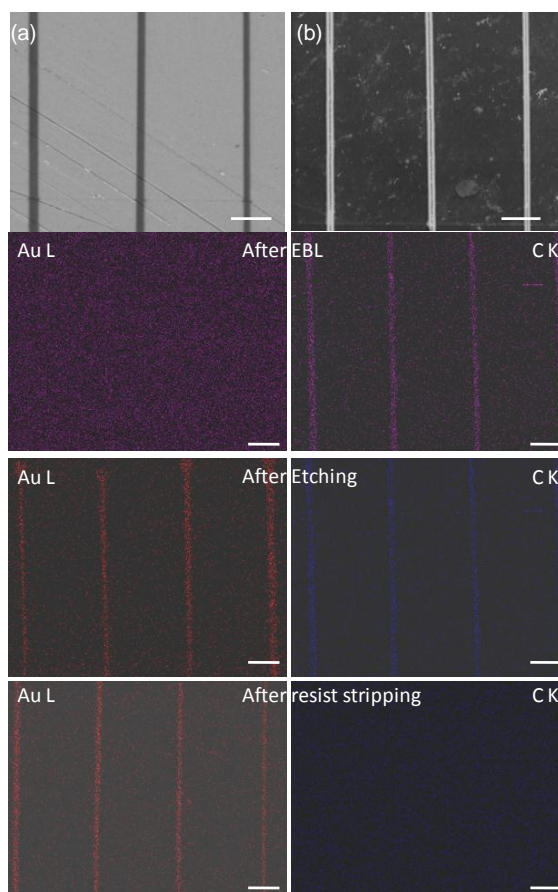
Figure III.12 (a) SEM image of the ToABr patterned nanolines on Au coated Si substrate. Below EDS maps of elemental Au and C are shown below in three process steps (after EBL, after etching and after removal of the ToABr resist). (b) SEM image of the obtained Au lines after removal of the resist. All scale bars correspond to 5 μm.

ToABr, as discussed earlier, has an additional important property that metal anions can be linked with it. Through electrostatic interaction; it can hold the negatively charged ions and transfer them from aqueous phase to the organic phase. Importantly, the ligand ToABr makes the metal highly processable. As an example, an assortment of Pt structures patterned via EBL of Pt-ToABr is shown (see Figure III.13a). Figure III.13b and c show the SEM and the corresponding EDS map of the Pt squares patterned by EBL with a 10 kV e-beam and dosage of ~800 μC/cm^2. The e-dosage required here is much lower than the

typical values reported for direct write precursors, for e.g., 15 mC/cm^2 for ZnO [49], 300 mC/cm^2 for Ni [33]. Figure III.13d, e and f are various examples of the Pt patterns revealing the continuity of the features written.
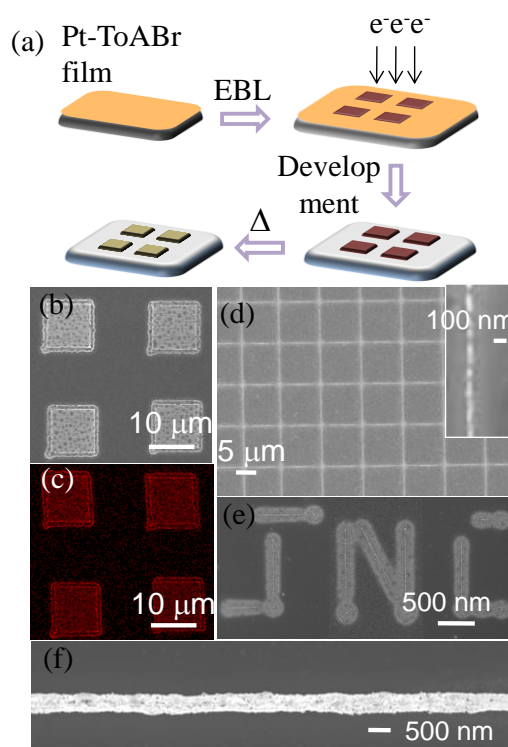
Figure III.13 Pt patterning as an example. (a) Schematic showing the direct write EBL process; precursor is spincoated on a substrate, exposed to e-beam in the desired pattern, developed in toluene for 5 s and thermolysed in air at 250 °C for 1 hr. (b) and (c) are respectively the SEM images of the Pt squares and corresponding Pt M level EDS map. (d) shows a Pt mesh structure drawn with EBL, line width being ~ 60 nm. SEM images of (e) Pt alphabets and (f) long Pt nanowire drawn by EBL.

All the complexes listed in Table III.3 have been subjected to direct write EBL to create diverse nanopatterns of various materials. Figure III.14a shows a Cu nanowire, with smooth morphology even at higher magnifications. Figure III.14b shows microsquares composed of Pd nanoparticles (see also Figure III.14c) with mean size of ~12 nm (see histogram in Figure III.14f). Direct write EBL of Au-ToABr (Figure III.14d) produced relatively polydisperse Au nanoparticles (see Figure III.14e) with mean size of ~20 nm (Figure III.14g). Ag nanowire was formed by performing direct write EBL on Ag-ToABr film. After development and air-thermolysis, AgBr nanowire got formed which was reduced by NaBH$_4$ to give rise to Ag nanowire. The roughness along the Ag nanowire edges came up during the reduction step (Figure III.14h). Confocal images of the patterned InN squares, nanowires and stripes on glass substrate, are shown in Figures III.14i and j. The emission is

primarily in the red region. Dots of GaN ~100 nm wide formed by direct write EBL are shown in Figure III.14k. GaN circle patterned by direct-write EBL shows green emission
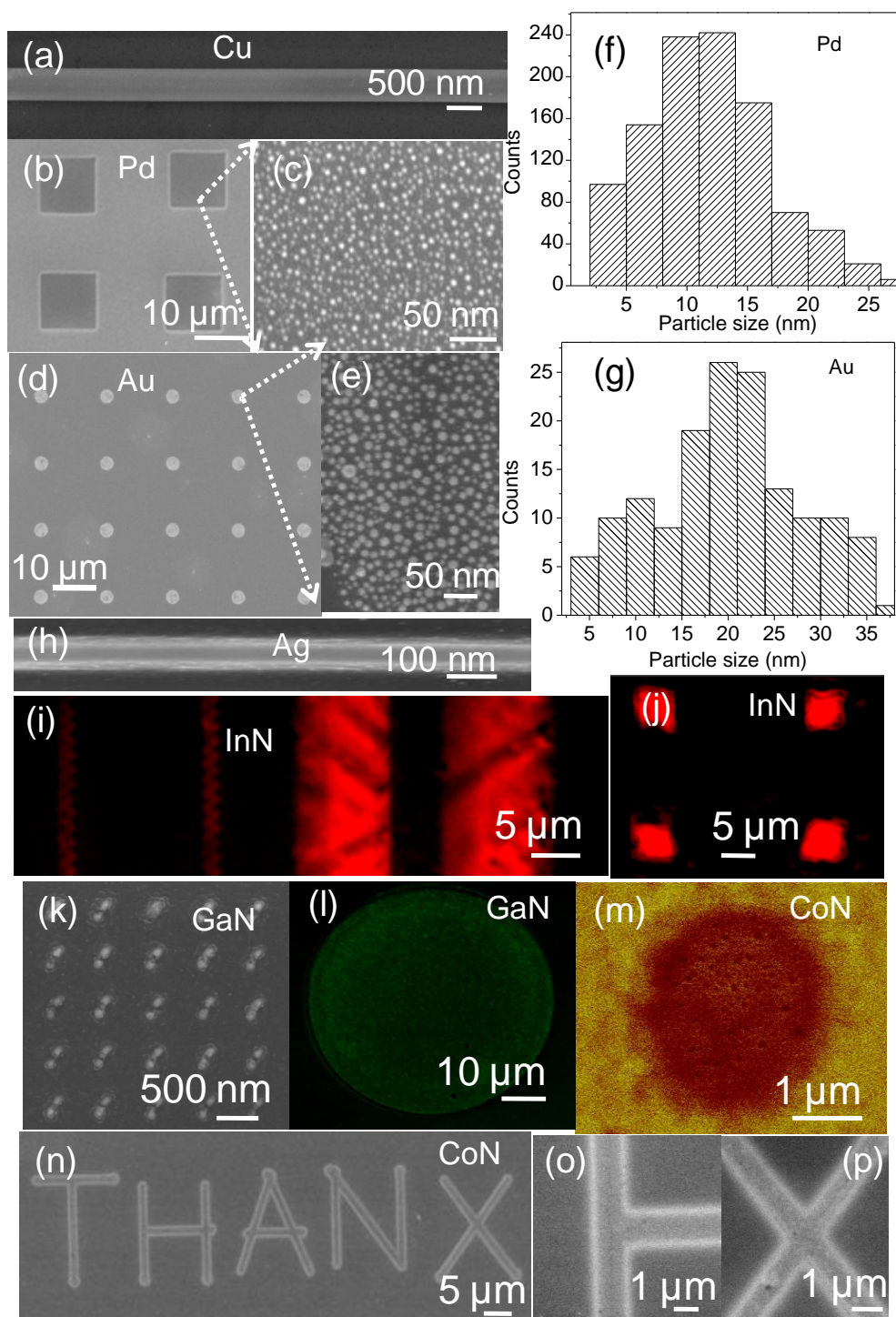
Figure III.14 Various M-ToABr precursors subjected to patterning by direct write EBL. SEM images of (a) Cu nanowire, (b, d) Pd and Au nanoparticle patterns with magnified views as indicated by arrows in (c, e) and histograms in (f, g) respectively, (h) Ag nanowire. (i, j) Confocal images of the InN EBL patterns. (k) SEM image of GaN dots, (l) confocal image of patterned GaN circle, (m) MFM image of CoN. (n) SEM image of EBL patterns of CoN with magnified views in (o) and (p).

selectively from the patterned region in confocal image (Figure III.14l). Further, the emission at different wavelengths examined by confocal imaging also emphasizes that the emission peak wavelength for InN and GaN are at ~ 620 and ~ 540 nm respectively. Tiny dots of CoN examined by magnetic force microscopy (MFM) are shown in Figure III.14m. CoN nanoparticles show darker contrast (attractive force) with either magnetization of the AFM tip, indicative of paramagnetic nature of the sample. Patterns of CoN obtained by direct write EBL show smooth line edges as shown in Figure III.14n, o and p.
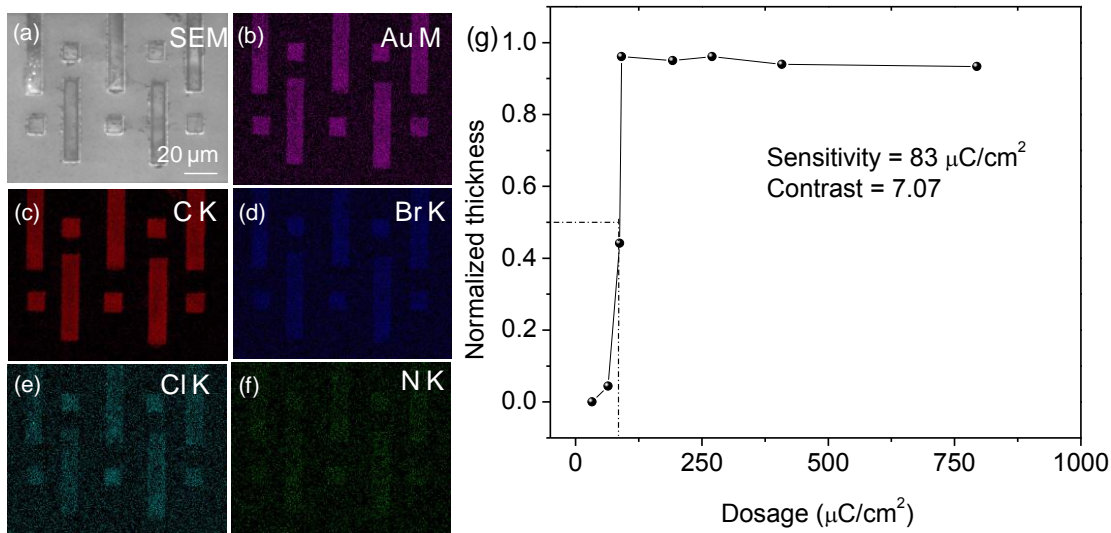
Figure III.15 (a) SEM image of patterned Au–ToABr e–resist and (b–f) the corresponding EDS maps. (g) Variation in the film thickness (after development) of Au–ToABr normalized with respect to initial thickness, versus the e–dose (beam energy, 5 kV).

Not only various metals can be directly patterned, but also importantly, the dosage required for the patterning M-ToABr is much lower as compared to ToABr itself. The sensitivity and the dosage variation was done systematically for Au-ToABr e-resist. Patterning of Au–ToABr film has been carried out under varying e–beam dosages, an example obtained using a 5 kV e–beam at 95 $\mu C \cdot cm^{-2}$ is shown in Figure III.15a. The regions exposed to the e–beam remained on the substrate after developing in toluene, thus indicating the negative–tone resist behavior of Au–ToABr. EDS images of a typical patterned region (shown in Figures III.15b–f), as expected, indicate the presence of C, Br, Cl along with that of Au in the designated areas. The Au/Cl/Br/C elemental ratios (20:11:7:62) obtained for the patterned regions agree with the initial composition (19:10:8:63) of the unexposed resist, implying that the e–dosage and developing cause only minimal change in the overall composition. Small differences seen can occur due to carbon contamination during the e–beam exposure. Importantly, the resist action of Au–ToABr is evident. This is

also reflected in the UV–visible absorption spectrum (Figure III.16a) where the characteristic features of the Au–ToABr complex disappeared. The crystalline pristine complex, which has a well-defined lamellar structure as revealed by XRD measurements in Figure III.16b, with a (001) d-spacing of 13.17Å, tends to become amorphous after the e–beam exposure as seen in the XRD data (see Figure III.16b). In order to quantify the resist action, squares of 10×10 μm^2 were patterned on a Au–ToABr film while gradually increasing the e–dosage from 35 to 800 μC·cm^{-2} on different areas (beam energy, 5 kV and beam current, 2.9 nA). The threshold dosage for the resist action was 64 μC.cm^{-2} below which the developed regions failed to exhibit a contrast. The thickness of the developed region as measured using optical profilometry increased with the e–dosage, from ~7 nm at 64 μC·cm^{-2} to ~160 nm at 800 μC·cm^{-2} clearly due to the increasing resist action (Figure III.15g). In other words, at the minimum dosage value, only about 4.4% of the original thickness is retained following developing in toluene, and this value gradually increased to 95% beyond 90 μC·cm^{-2}. The sensitivity value for Au–ToABr resist is 83 μC·cm^{-2}, which compared to other direct write resists, is commendable. The e–dosage employed here is far lower than the typical values reported for Au direct write precursors, *e.g.*, 1.5 mC/cm^2 for Au nanoparticle resist [1], 0.2 mC/cm^2 for Au–polymer composite [78] and 0.5 mC/cm^2 for Au(I)–thiolate [79]. The measured contrast value for Au–ToABr resist was 7.1 (see Figure III.15g). Generally, a higher contrast implies possibility of high–resolution patterning with the resist [80].
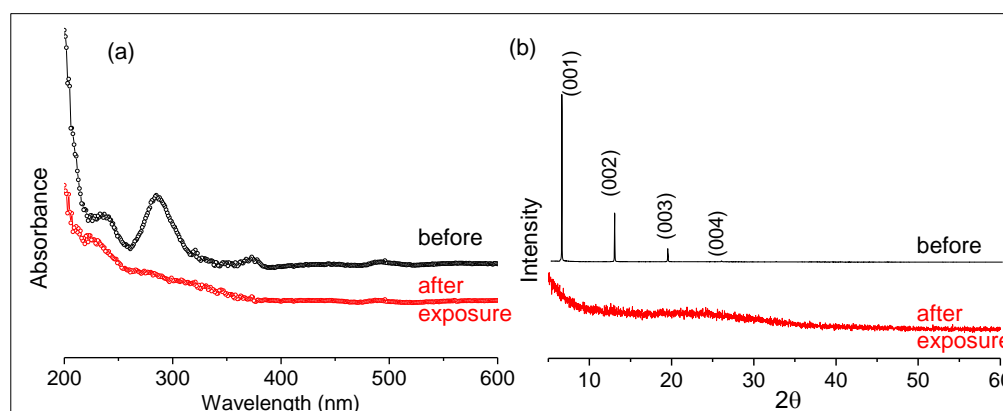
Figure III.16 (a) UV-visible spectra and (b) XRD patterns of a Au-ToABr film (~150 nm thick) before and after e-beam exposure (0.5 mC/cm^2).

In order to understand the resist action, it is important to examine the changes in the conformations of the alkyl chains on exposure to an e-beam. In Figure III.17, the IR spectra of the pristine Au-ToABr film is compared with the one exposed minimally to the e-beam (5

kV, 50 μC·cm^{-2}). In the case of pristine Au-ToABr (Figure III.17), the wag-twist progression bands (W_x+T_x, 1175-1350 cm^{-1}) are well-defined, implying that the coupling between the methylene oscillators is unaffected because the chains are all-trans, which is also evident from the C-H stretching modes (see Figure III.17b). Interestingly, these bands are greatly diminished in intensity in the case of e-beam exposed film, in spite the dosage being extremely small. The spectrum confirms the occurrence of gauche defects in the chains. The strong band at 1465 cm^{-1} due to the methylene scissoring mode (δ) seen in pristine film was clearly absent after EBL, indicating that there is deformation in the alkyl chain on exposure of e-beam. The main band at 618 cm^{-1} which represents in-plane bending
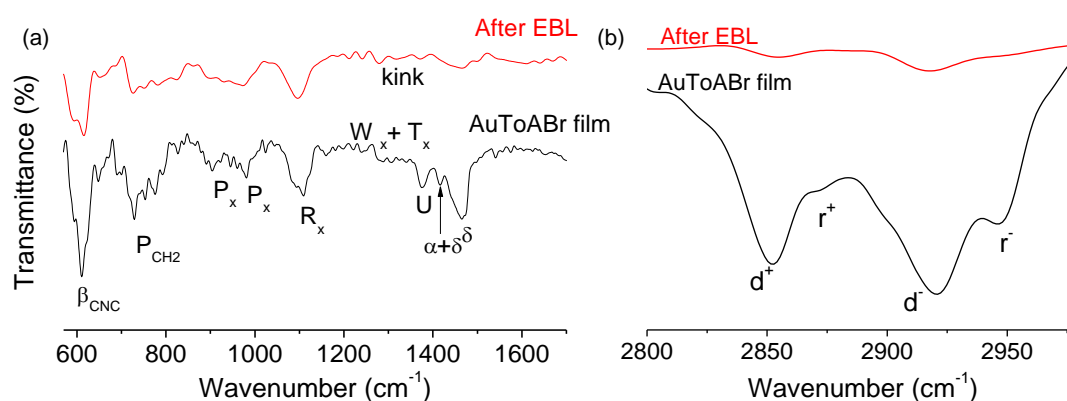
Figure III.17 FTIR spectra of Au-ToABr film before and after e-beam exposure (0.5 mC.cm^{-2}), followed by development.

of C-N-C bond (β_{CNC}), was diminished in intensity after e-beam exposure. A series of peaks observed in the region 700-980 cm^{-1} assigned to the progression bands (P_x), and those between 1000 and 1150 cm^{-1} assigned to the skeletal C-C-C vibrational modes (R_x) of the methylene chains were more prominent in the case of pristine film as compared to the one exposed to e-beam. Importantly, weak bands at 1321 and 1365 cm^{-1} due to $W_{g-t-g'}$, indicating the presence of kinks in the chain, are more vividly seen in the film exposed to e-beam. There is a broad peak observed around 1600 cm^{-1} after EBL, due to the loss of hydrogen atoms and radical formation leading to double bonds. This is also an indication of cross-linking of the chains, important in resist action. The characteristic C-H stretches of the methylene and end-methyl groups of the alkane chain appear in the 2800-3000 cm^{-1} region (see Figure III.17b). In the case of pristine Au-ToABr, the symmetric (d^+) and antisymmetric (d^-) methylene C-H stretching modes are broad with the mean positions at 2852 and 2920 cm^{-1}, respectively, which are greatly diminished in intensity after e-beam exposure. The r^+ and r^- (methyl symmetric and antisymmetric stretch respectively) modes appear around 2872

and 2950 cm^{-1}, which also diminish on exposure to the e-beam and appear as a high frequency shoulders, indicating that most methyl groups have been damaged and/or removed. Clearly, the e-beam exposure induced deformations and cross-linking of the alkyl chains of Au-ToABr make it less soluble during developing and thus an electron sensitive resist.
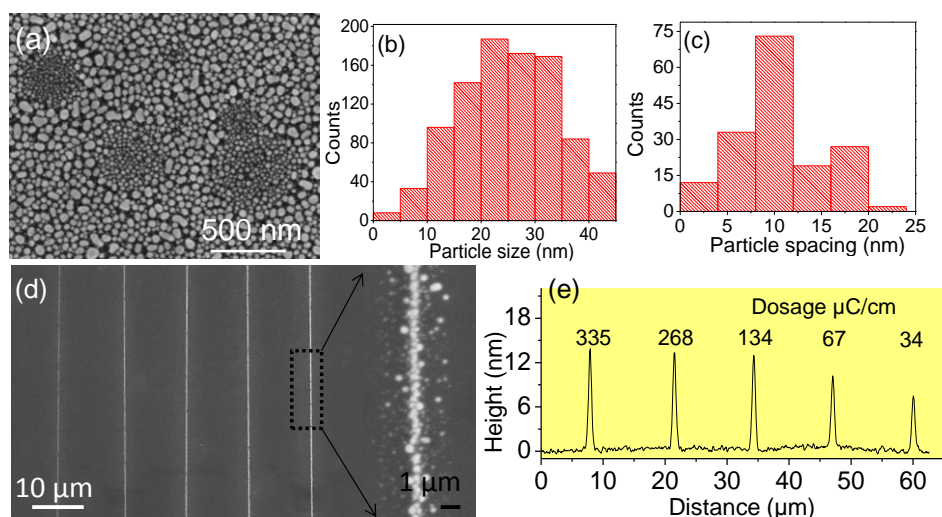
Figure III.18 (a) SEM image of a Au–ToABr film exposed to e–beam (100 μC/cm2), developed and thermolysed at 300 °C, showing tightly packed Au nanoparticles, along with histograms of particle size (b) and spacing (c). (d) SEM image of the patterned Au nanoparticle lines with a magnified view in the inset. (e) Height profile of the lines, with the dosages indicated in μC/cm.

The advantage of a direct write resist as has been discussed earlier, is its ability to produce active material with fewer processing steps. Indeed, a simple thermolysis of Au–ToABr film (300 °C, 3 hrs) removes the organic part and leaves behind only the crystalline Au metal. When not exposed to e beam, the metal product resulting from thermolysis may contain interesting structures instead of a featureless smooth film. As discussed in Part II, large plate–like polygonal Au structures were nucleated and grown starting with the Au–ToABr complex by fine–tuning the thermolysis conditions. However, a e–beam exposed film behaved very differently following thermolysis at 300 °C (Figure III.18). Upon thermolysis of the e–beam exposed Au–ToABr resist, fine Au particulates were obtained as shown in Figure III.18a. Somewhat non–spherical nanoparticles in the size range of ~5 to 40 nm packed in a roughly hexagonal array were seen in the patterns. The mean particle size was found to be ~25 nm (Figure III.18b), and the mean spacing, ~10 nm (Figure III.18c). Interestingly, 100 to 800 nm wide circular regions were observed as in Figure III.18a, in which the nanoparticles are rather small (2–20 nm) and more tightly packed. This aspect will

be dealt in the following sections. As examples of high resolution patterning, parallel lines of decreasing widths (minimum width ~70 nm) were produced as shown in Figure III.18d. The height profiles of the same in Figure III.18e indicate a remarkable control on nanoparticle line thickness based on the e-dosage.

While Pt-ToABr produced continuous features of Pt, Au-ToABr producing Au nanoparticle arrays is indeed intriguing and therefore, this aspect was investigated in some detail which is summarised in the schematic in Figure III.19a. When observed during the e–beam exposure, the pristine Au–ToABr resist film seemed to dewet leading to dark features, which with increasing time of exposure, were finely distributed all over (see movie III.S1 in CD). As these features bear a darker contrast, they may predominantly contain organic species from the resist. SEM image in Figure III.19b shows that the dewetted features have extension in the range of ~0.05 to ~1.3 μm. AFM topography image (Figure III.19c) of the features showed that they are indeed protrusions, with a mean height of ~7.7 nm (Figure III.19d) and mean width of ~0.48 μm (Figure III.19e). When this film was developed in
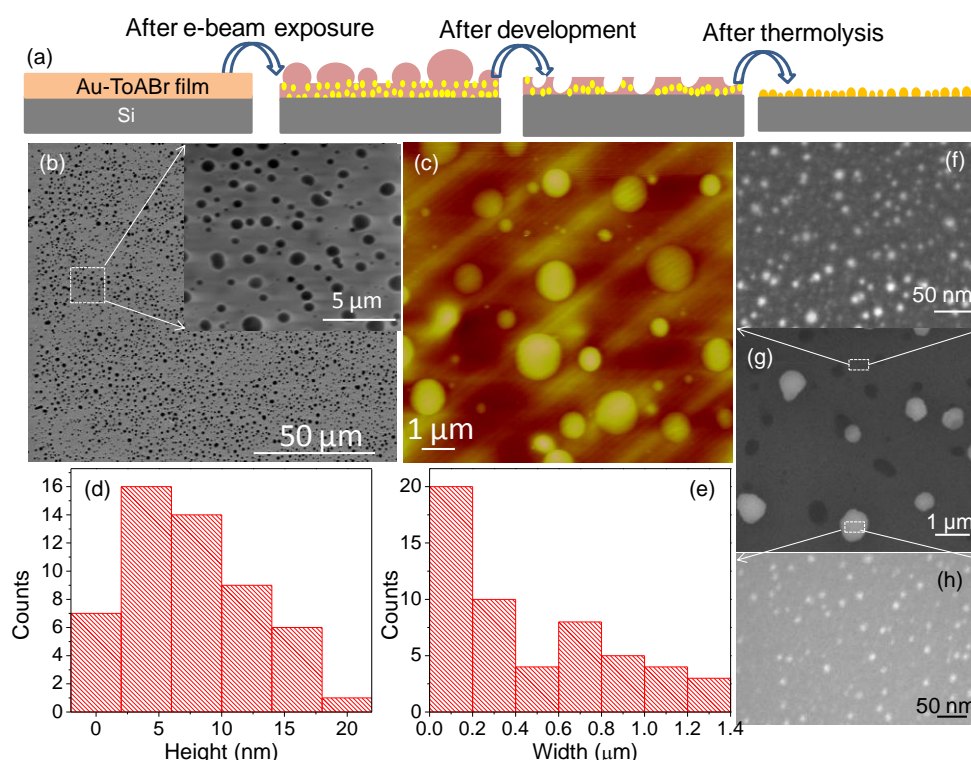
Figure III.19 (a) Schematic showing the e–beam induced dewetting of the Au–ToABr spincoated resist on a Si substrate; yellow colored dots represent Au nanoparticles. (b) SEM and (c) AFM images of a Au–ToABr film (~150 nm thick) exposed to e–beam (0.5 mC/cm^2) showing the e–beam induced dewetting. Magnified image is shown in the inset of (b). (d) and (e) are the histograms of the height and width of the blobs based on AFM. (g) SEM image after development and prior to thermolysis. Bright spots seen all over, correspond to the Si regions exposed as the blobs got washed off. Magnified portions of the dark (f) and bright (h) regions both show the presence of reduced Au nanoparticles.

toluene (10 s) and examined in SEM, the dark blobs (being organic) were almost washed away (Figure III.19g). Instead, tiny Au nanoparticles were seen all over, i.e., in dark (Figure III.19f) as well as in gray (Figure III.19h) regions. From this experiment, it is clear that e–beam induces nanoparticle nucleation (see schematic illustration in Figure III.19a). Electrostatic interactions between the $(AuCl_4)^-$-anions and ToABr perhaps enables easy liberation of Au upon mild e–beam exposures. Due to e–beam induced dewetting of the resist, only Au nanoparticles are obtained and not extended features. Although Figure III.19 is an illustration for dewetting on a larger scale, most blobs were tiny (<100 nm) as evident in the histogram in Figure III.19e where the mean value is at ~0.48 μm. It therefore appears plausible that the film dewets in nm regions which following thermolysis leads to individual Au nanoparticles. During the thermolysis, the nanoparticles are allowed to grow with the supply of Au^{3+} from the precursor available around, except in those regions, from which blobs got formed and washed away. This accounts for the occurrence of circular regions containing relatively smaller nanoparticles as shown in Figure III.18a. All the above findings point out that unlike chemically organized assemblies, in this recipe no external capping agent is required for nanoparticle array stabilization. On the contrary, the organic part of the resist gets removed during the thermolysis step! The organization of nanoparticles in arrays takes place spontaneously due to e–beam induced dewetting of the resist at different length scales followed by particle nucleation and growth.

Direct micromolding using M-ToABr

Pt-ToABr is taken as an example for illustrating direct micromolding with M-ToABr. A patterned PDMS stamp kept on a Si substrate and was showered with ~60 μL of toluene solution of Pt-ToABr while heating to 250 °C. The microchannels formed at the interface of the PDMS stamp and the substrate got filled with the solution due to capillary action (Figure III.20a). After thermolysis for 30 min, the stamp was cooled to room temperature and removed to obtain Pt grating stripes of ~1 μm wide, and spacing ~500 nm, in conformity with the stamp geometry. Figure III.20 shows the SEM image of the stripes, revealing smooth morphology. The stripes were continuous, without cracks, spread over large areas. As revealed by the AFM image, the height of the μ-stripes was around ~75±5 nm (Figure III.20b and e) with roughness of ~ 1.5 nm. EDS map in Figure III.20c shows the presence of Pt along the μ-stripes only. The formed patterns being gratings, diffraction is an ideal macroscale tool for identifying the patterns. Figure III.20f shows linear diffraction pattern formed by shining a red laser (~650 nm) onto a transmission grating of μ-stripes.
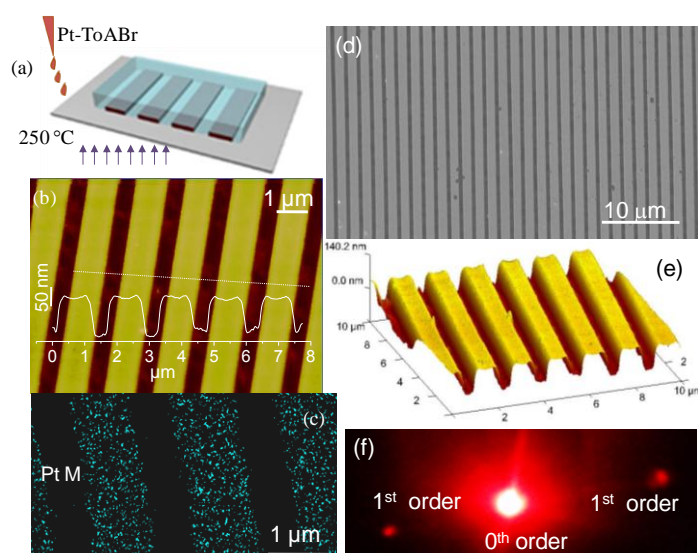
Figure III.20 Pt patterning as an example of direct micromolding. (a) Schematic showing the direct micromolding process. PDMS stamp hosting the microchannels is kept on a flat substrate, the precursor solution is dropped along one edge, thus making it flow in the microchannels. Entire setup is heated to 250 °C at a ramp of 2 °C per min, and held at 250 °C for 30 min. (b) AFM image of the formed Pt µ-stripes along with the z-profile along the dotted line, (c) Pt M level EDS map of the stripes. (d) SEM image of the continuous Pt µ-stripes over large areas, and (e) AFM image showing the three dimensional view of the µ-stripes. (f) optical diffraction pattern from the grating.

A variety of substrates (apart from Si and glass) including flexible substrates (e.g., polyimide) can be used for patterning the Pt µ-stripes, the process temperature being low. The obtained stripes were well conducting. Au electrodes were deposited by shadow masking onto Pt µ-stripes formed by micromolding on glass substrate. As shown in Figure III.21a, the stripes are joining the Au electrodes. I-V measurement (Figure III.21b) shows a nearly linear curve with a resistance of ~57.5 Ω. The resistance is a result of ~750 stripes held in parallel which implies that the resistance of single stripe is ~43275 Ω. Thus the resistivity of Pt in molded stripes is 540 µΩ.cm. This value is somewhat higher than that obtained for thin film of Pt (350 µΩ.cm). While being molded, the precursor decomposition might not be complete owing to the confined environment in the microchannel, leaving a higher percentage of carbon (~40 %) in the stripes. A rather simple step of air heating to 400 °C for 30 min, brought down the carbon in the stripes to <5% with resistivity dropping to 281 µΩ.cm.

Flowing the respective precursor solutions inside the microchannels, and thermolysing in a controlled atmosphere (same as mentioned for films), patterned µ-stripes of Pd, Pb, ZnO, CoN, Au were realized (see Figure III.22a-e). The patterns are uniform over large areas – this is clearly evident in the inset of Figure III.22b, which shows an optical

micrograph, showing the colors split by patterned Pb μ-stripe grating due to diffraction from ambient light. Also, the morphology of the μ-stripes is composed of nanoparticles. ZnO, being an important functional material in optical, electrical, piezoelectric and optoelectronic applications [81], there are several reports on patterning ZnO [48,82]. For direct micromolding of ZnO, a polymer liquid precursor is known, but the recipe demands an additional step of high temperature annealing [83]. Here, the advantage of ToABr functionality was made use of, for making a viable precursor solution but in the aqueous medium. After separating the aqueous solution from the organic phase, 3 mL of ethanol was added to 2 mL of aqueous phase. The latter was added to facilitate easy flow of the precursor during direct micromolding.Patterned ZnO μ-stripes on Si substrate are shown in Figure III.22c.
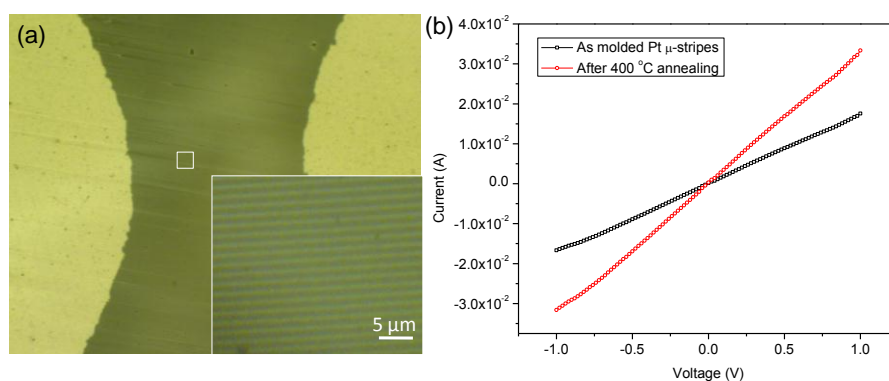
Figure III.21 (a) Optical micrograph showing Pt μ-stripes between Au electrodes on a glass substrate. Inset shows magnified image. (b) I-V characteristics of the μ-stripes.
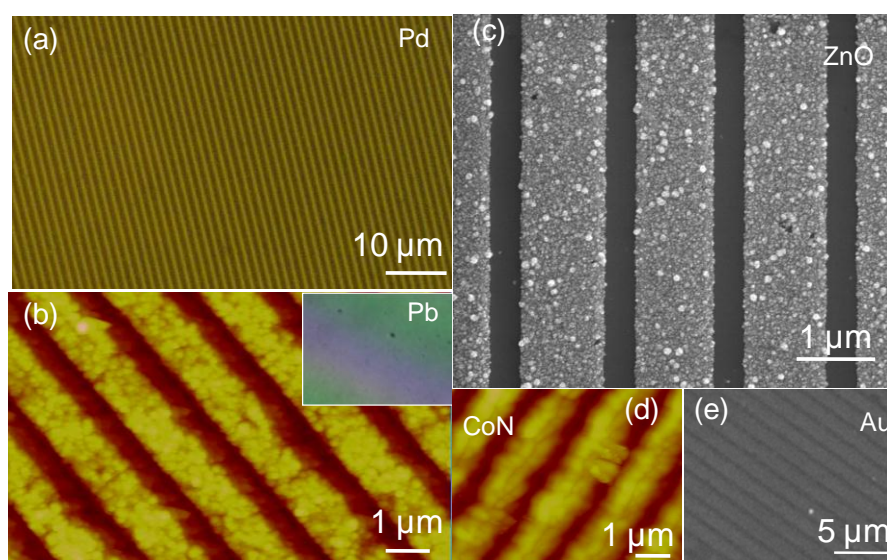
Figure III.22 Various M-ToABr precursors subjected to patterning by direct micromolding - (a) Optical image of Pd μ-stripe grating, AFM images of Pb (b) and CoN μ-stripe gratings (d). SEM images of patterned (c) ZnO and (e) Au μ-stripe gratings.

The ToABr mediated route though works well for patterning a large number of materials, in certain cases such as Ag and Cu which form bromides following air-thermolysis, an additional process step of reduction is required. In order to overcome this limitation, other phase transfer agents, devoid of halides, such as dodecylamine (DDA) have been tried [84]. DDA transfers metal ions by forming coordination complexes and it works for almost all the metals, with transfer efficiencies of ~95% [84]. When Ag-DDA and Cu-DDA complexes were used as single source precursors, crystalline metal films were obtained following thermolysis (Figure III.23a-c). DDA being a semi-solid at room temperature makes processing difficult. However, micromolding of the precursors was successful to obtain well defined patterns (Figure III.23d and e). Although the precursor responded to e-beam, the roughness of the spin-coated film (~30-50 nm) was prohibitive for further processing.
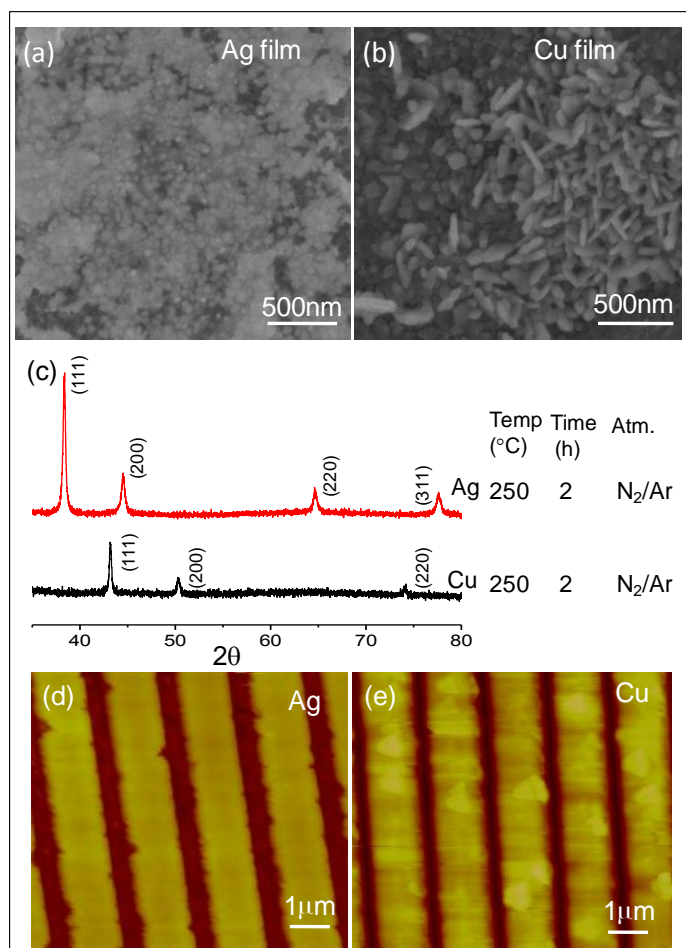
Figure III.23 Alternate routes to ToABr - SEM images (a, b) and XRD patterns (c) of of Ag and Cu films formed by thermolysis of Ag-DDA and Cu-DDA complexes with the corresponding planes in XRD indexed according to the JCPDS PDF files: Ag (89-3722), Cu (85-1326). Thermolysis conditions are mentioned. AFM images of (e) Ag and (f) Cu μ-stripes formed by direct micromolding of Ag-DDA and Cu-DDA complexes respectively, followed by thermolysis in inert atmosphere.

III.4.2 M-Thiolates as direct write precursors

Metal thiolates are another class of well known single source precursors for metal or metal sulfides by reductive elimination via thermal decomposition. Here two of the metal thiolates, Pd and Au-thiolates were chosen as direct write precursors. While all other thiolates including Au are insoluble, Pd alkanethiolates are unique in that they are soluble in common organic solvents and can be self-assembled repeatedly [85]. These compounds are highly crystalline lamellar structures and melt in the temperature range of 60 °C to 100 °C, with the melting point increasing linearly with the thiol chain length [86]. When heated to temperatures above the melting point, they undergo decomposition. Thermal decomposition occurs according to the following reaction scheme:

$$M(SR)_2 \longrightarrow M + RS\text{-}SR$$
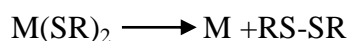
This mechanism has been reported in the case of decomposition of Au(I)-alkanethiolate producing Au nanocrystals [87]. Thioethers are the by-products when metal sulfides are formed [88]. A detailed study of the thermal decomposition of metal alkanethiolates by Carotenuto et al. [89] using differential scanning calorimetry and thermogravimetry have shown that these systems undergo melting from crystalline phase and then undergo decomposition to either metal or metal sulfides. If the metal-sulfur bond energy is lower than sulfur-carbon bond energy (714.1 kJ/mol), then the thermolysis preferentially leads to the metal with disulfide as the by-product, while it leads to the metal sulfide formation, for higher metal-sulfur bond energies.

Initially, the metallization behavior of the Pd octanethiolate, $Pd(SC_8H_{17})_2$ itself was investigated by TGA. As shown in Figure III.24, in region (i), the weight loss upto 42% corresponds to gradual solvent evaporation. Around 250 °C, ~33% weight loss was observed leaving behind 25% of the original weight with the residue. The second weight loss occurs due to the decomposition of the thiolate. Considering only the weight after solvent evaporation, the weight loss corresponding to thiol desorption is 57.7%, and the residue is 42.2%. This corresponds to a Pd : thiol ratio of 1 : 1.36. This value may be compared with the metal content in $Pd(SC_8H_{17})_2$, which is 1 : 1.35. $Pd(SC_8H_{17})_2$ coated as a film on a glass substrate and subjected to thermolysis in air, produced a film which contained closely linked Pd nanoparticle domains as revealed by FESEM and TEM images shown in Figure III.25a and b, respectively. During thermolysis, the thiol molecules seem to desorb leaving behind the metallic Pd. The carbon content was found to be less than 10% based on EDS

quantification (see spectrum in Figure III.25a), in contrast to 70% from the pristine film. HRTEM image in Figure III.25b shows the lattice fringes from a nanoparticle with the spacing (2.245 Å) closely matching the Pd(111) value (2.246 Å). The overall crystallinity of the film is evident from the XRD in Figures III.25c. The four-probe resistivity measurements (Figure III.25d) revealed the room temperature resistivity of the film to be 0.235 μΩm nearly twice that of bulk Pd (0.105 μΩm). The temperature dependence was linear, typical of a metallic species and the temperature coefficient of resistance was found to be 0.002713 K^{-1} (bulk value, 0.00572 K^{-1}).
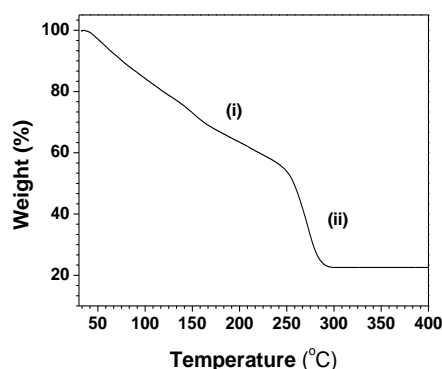
Figure III.24 Thermogravimetric analysis on Pd octanethiolate done in air. (i) Gradual loss of solvent and (ii) thiol desorption.
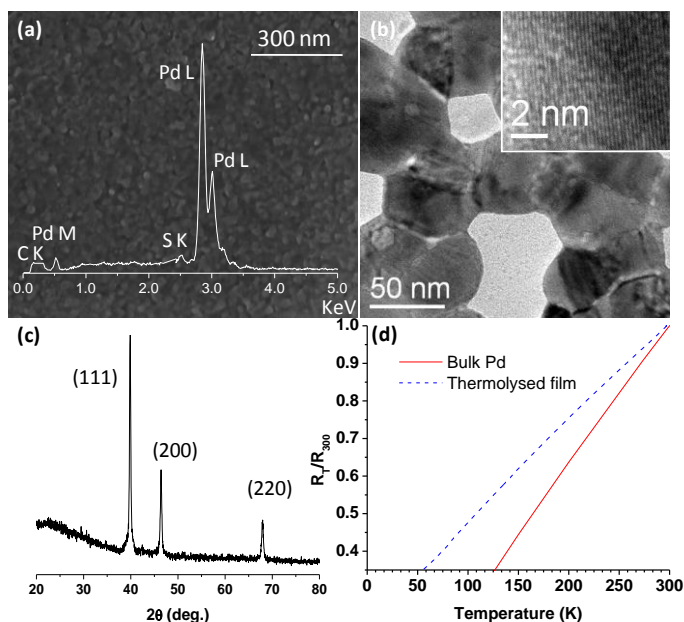
Figure III.25 (a) SEM image of the film obtained by thermolysis of Pd octanethiolate in air at 250 °C for 30 mins, The EDS spectrum is also shown. (b) A TEM image. The inset shows a HRTEM image of a nanoparticle. The lattice fringes correspond to the d(111) planes (2.245 Å) of Pd. (c) XRD data from the thermolysed film. (d) The temperature dependent four-probe resistivity for the thermolysed film (blue dotted line), along with that of the bulk Pd (red solid line, Handbook of Chemistry and Physics CRC Press 88th edition, 2007-08).

Instead of metallic Pd, a sulfidic phase such as Pd_4S can be obtained in a single step by modifying the thermolysis atmosphere to be H_2 instead of air. For this purpose, a drop-coated Pd octanethiolate solution on a glass substrate was gradually heated in H_2 atmosphere to 250 °C and was held for 30 min to obtain the desired film. XRD pattern of the film shown in Figure III.26a, contains no precursor related peaks. The obtained compound is quite crystalline with sharp diffraction peaks which are easily identifiable with the Pd_4S phase (JCPDS PDF No. 731387), importantly with no other impurity phases. Pd_4S crystallises in the space group P-42$_1$c with 8 Pd and 2 S atoms per unit cell [13]. The TGA data on the transformation of the thiolate to Pd_4S done in H_2 atmosphere showed a weight loss (56.7%) close to the expected loss of 55%. In Figures III.26b-f, the microscopy results are shown. The SEM image in Figure III.26b reveals the particulate nature of the film, with particle size in the range of 250-300 nm. Although the particulates are closely connected, cavities were observed in between. The higher magnification image in Figure III.26c shows that these particulates tend to form extended grains which interconnect across the cavities and also exhibit layered morphology. Upon close examination (see Figure III.26d), smaller particles (with 8-10 nm diameter) were found decorating each grain. AFM image in Figure III.26e shows topography with feature sizes in the range, 150-300 nm. The surface roughness of the film, as measured from several 1.5x1.5 μm^2 areas comes out to be ~36 ± 4 nm. Both SEM and AFM have shown that the film covers the substrate uniformly over several mm^2 areas. The HRTEM image (Figure III.26f) shows the internal crystallinity of an individual particulate, with lattice fringes corresponding to d spacings of 2.21 Å and 2.11 Å from d(112) and d(211) respectively. SAED pattern (Figure III.26g) from a particle is representative of its single crystalline nature. The compound formed is unambiguously Pd_4S and is highly crystalline and is a single phase. The method reported is indeed novel.

Four probe electrical measurements on a Pd_4S film (~370 nm thick), gave the room temperature resistivity value of 0.165 $\mu\Omega m$. There is one report [11] from 1959 giving a resistivity value for Pd_4S. However, the reported value (3.20 $\mu\Omega m$) is more than an order higher perhaps due to the measurement method employed. It has been observed that at lower temperatures, the resistivity value followed the classic Matthiessen's rule (Figure III.27), with a temperature coefficient of resistance (TCR) of 0.00307 K^{-1}. The TCR value of Pd_4S may be compared with that of the Pd metal itself (0.00572 K^{-1}). The electrical measurements clearly point to the metallic behavior of Pd_4S film.
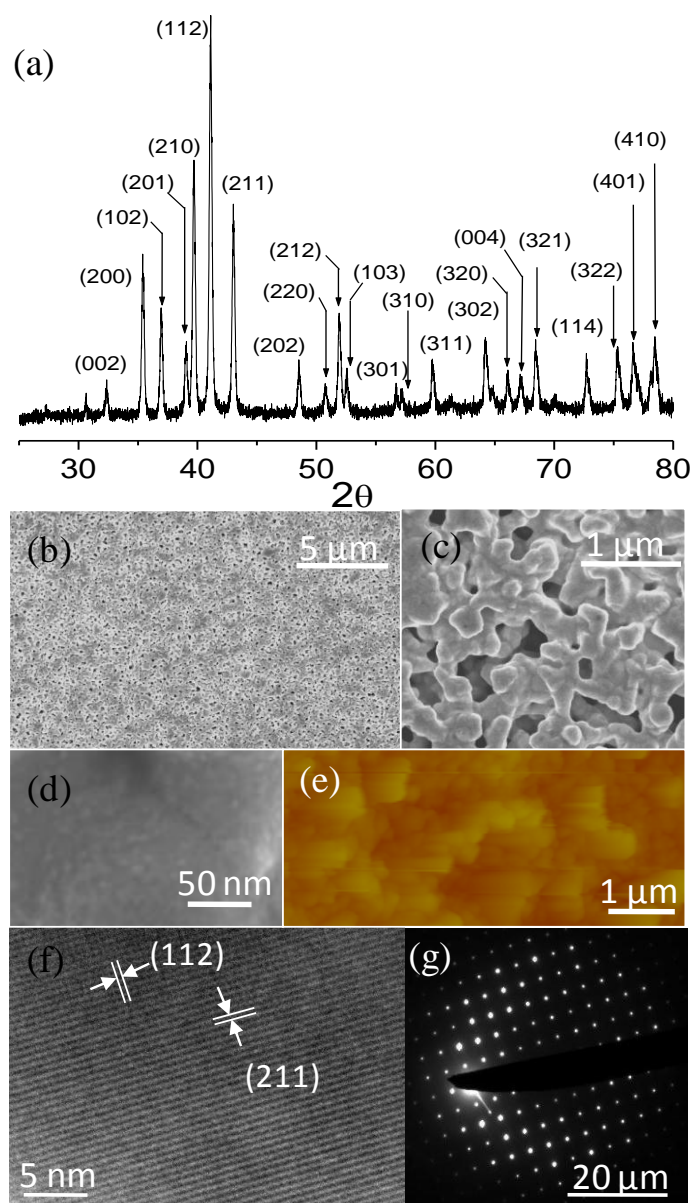
Figure III.26 (a) XRD pattern of the film by heating Pd octanethiolate in H_2 atmosphere at 250 °C for 3 hrs. Peak assignments refer to the JCPDS (PDF # 731387). (b), (c) and (d) SEM images of the film with increasing magnifications, (e) AFM image showing the topography of the film, (f) High-resolution TEM image of a grain where the (112) and (211) spacings are marked and (g) the SAED pattern.

The resistance of the film to harsh chemical environments has been examined using XRD under conditions away from the ambient (Figure III.28). The XRD data of the film heated to various temperatures in air are shown in Figure III.28a. The diffraction patterns obtained from the film held at 100 °C and 150 °C are very similar to the one obtained with the freshly prepared film (see Figures III.28a and III.26a). It is clear that the film did not undergo any compositional or structural changes. At a slightly higher temperature of 200 °C, tiny peaks identifiable with polycrystalline Pd metal (JCPDS PDF No. 461043) appeared amidst of the

Pd$_4$S peaks. After exposure to 250 °C or above, the XRD patterns contained peaks only due to polycrystalline Pd. These observations indicate that the Pd$_4$S film is stable up to 200 °C in air, above which it converts itself to Pd metal. Further, the Pd$_4$S film is stable below room temperature (-20 °C) as well. The range, -20 °C to 200 °C is important in technological applications. Also, the Pd$_4$S films were quite stable in various acid, alkali and oxidizing environments (Figure III.28b). The XRD patterns of the films recorded after dipping in concentrated HCl, HNO$_3$, H$_2$SO$_4$ and HF were similar to the pattern from the pristine film, so were the films exposed to KMnO$_4$ and a mixture of oxidizing and alkali environments such as KMnO$_4$+KOH and NH$_4$OH+H$_2$O$_2$. There was no compositional or structural change in the films as the XRD patterns are faithfully retained after exposure to harsh environments.
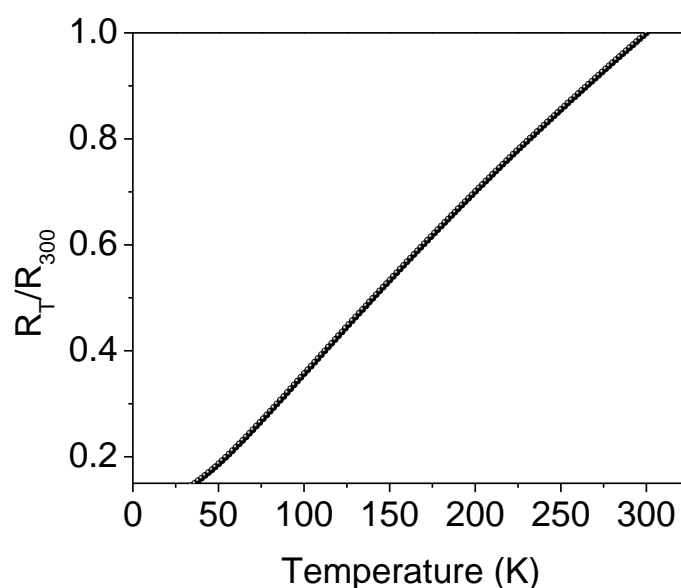
Figure III.27 Variation in the four-probe resistivity of the Pd$_4$S film (normalized with respect to the room temperature value) with lowering temperature.

This ability to conduct while withstanding harsh environments was investigated (Figure III.29). For this purpose, Pd$_4$S film was formed between Au gap electrodes (~3 mm) on a T-shaped teflon substrate, by drop coating the thiolate followed by H$_2$ treatment. The T-substrate was connected in series with an external battery and a light emitting diode (LED), the latter as an indicator for circuit continuity (Figure III.29b). The substrate was dipped in a piranha solution (caution: this mixture reacts violently with organic matter), while being in series with the electrical circuit (Figure III.29c). The LED continued to glow indefinitely clearly demonstrating the stability of the coated Pd$_4$S. There was no observable change in the circuit resistance.
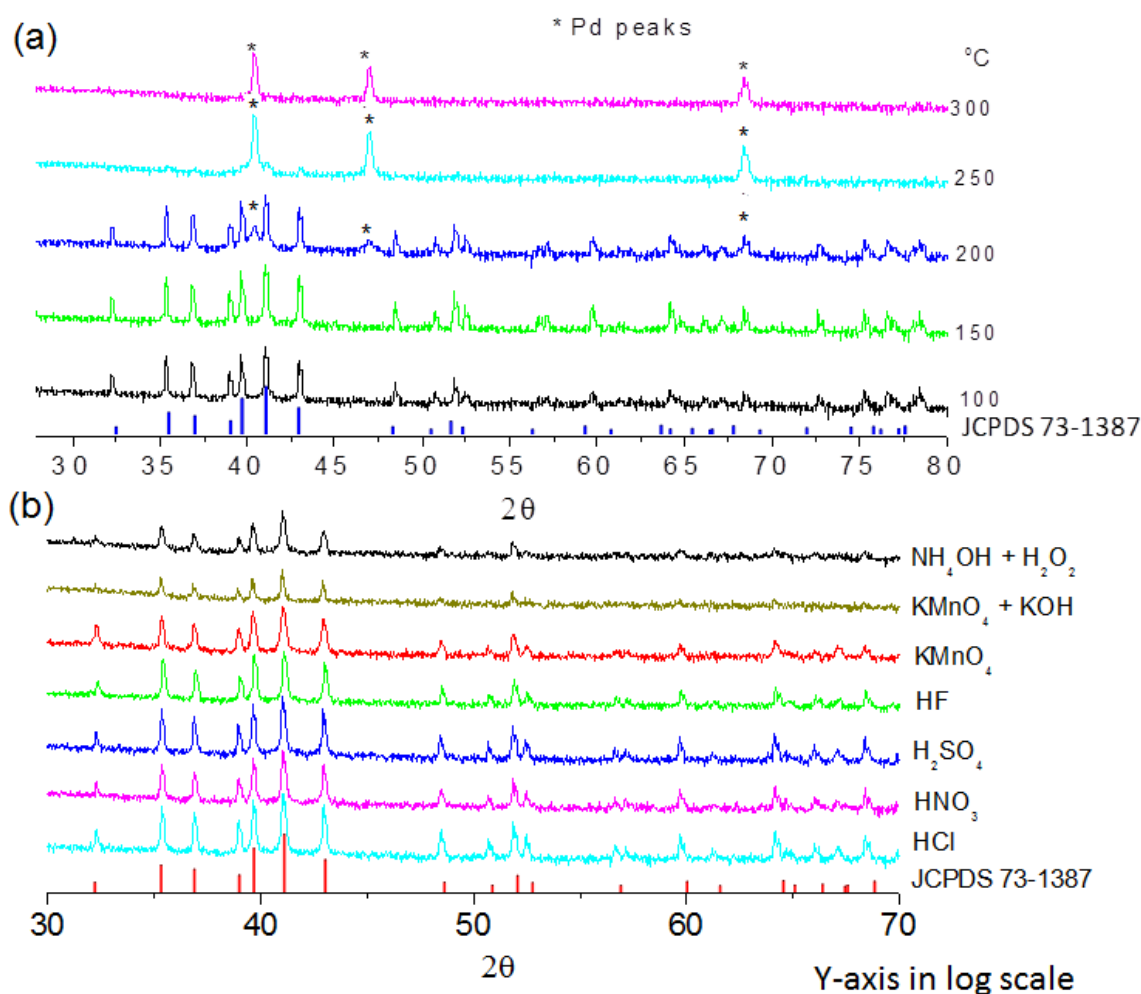
Figure III.28 (a) XRD patterns of the Pd$_4$S film heated to different temperatures for 1 hr in air. It can stand up to 200 °C, beyond which polycrystalline Pd peaks are seen in XRD pattern. (b) XRD patterns of the films exposed to different acid and alkali environments

The electroplating using Pd-S catalysts is known to be much more effective than that with Pd itself [13]. In particular, Pd$_4$S is believed to be responsible for the enhanced deposition of Cu [13], due to the presence of the bridging sulfur atom, although there is no study as pure Pd$_4$S phase. The electroplating of Cu onto Pd$_4$S films in comparison with Pd film was investigated, the latter obtained by the thermolysis of a Pd octanethiolate film in air at 250 °C. The deposition of Cu on Pd$_4$S film is evident from the EDS maps of Cu K, Pd L and S K levels (Figure III.30a). The rate of deposition on Pd$_4$S as well as on Pd films was monitored using EDS quantification (Figure III.30b). Interestingly, the deposition of Cu is relatively more on Pd$_4$S in comparison to Pd, similar to the behaviour observed with Pd-S catalysts [90-92]. This observation clearly brings out the catalytic ability of Pd$_4$S, thus substantiating earlier speculations in the literature [92].
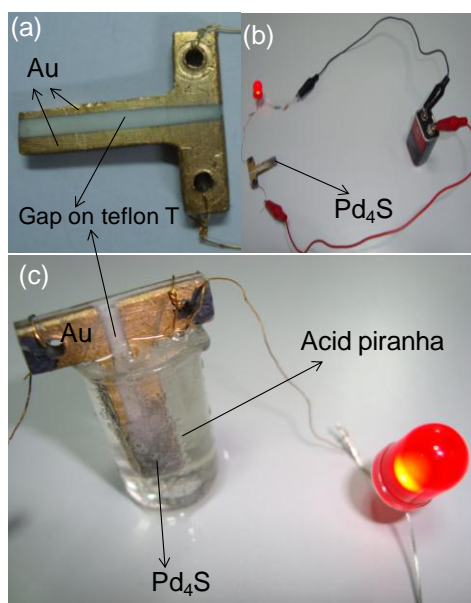
Figure III.29 Stability of Pd_4S as interconnect in harsh chemical environment. (a) Au gap electrodes on a T-shaped Teflon substrate connected to Au wires, (b) Pd_4S deposited across the gap and the associated circuit; the glowing LED is indicative of circuit continuity. (c) The T-substrate is dipped into the piranha solution of $H_2SO_4 + H_2O_2$. The the stability of Pd_4S in acid environment is evident.
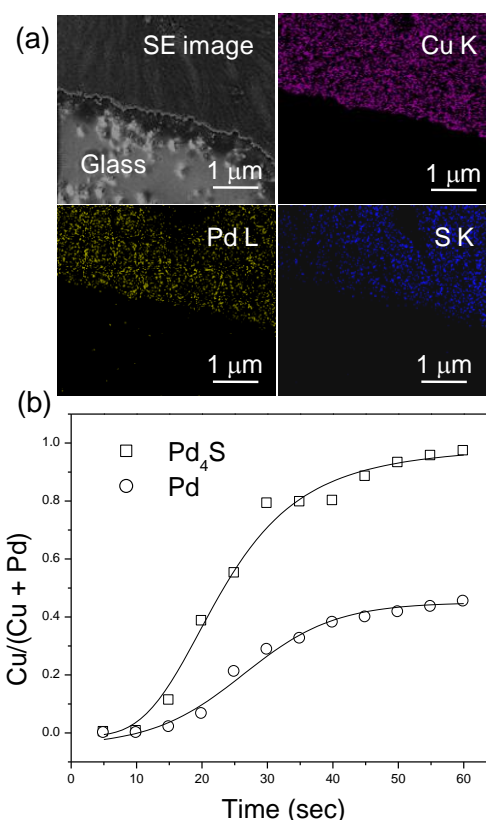
Figure III.30 (a) SEM micrograph from the edge of the film and the corresponding EDS maps indicating the Cu deposition onto Pd_4S film. (b) Based on Cu K and Pd L EDS signals, the respective atom percentage values were calculated. The variation of the ratio, Cu/(Cu+Pd), with time is shown for both Pd (circle) and Pd_4S (squares) films.

The possibility of producing other Pd sulfidic phases has also been explored as well. The precursor i.e., Pd octanethiolate itself can be designed to give specific Pd sulfide phase after thermolysis in H_2 atmosphere. As illustrated in Figure III.31, when the $Pd(OAc)_2$ to thiol ratio employed to synthesize Pd octanethiolate was 1:1.5 (as opposed to 1:1 for Pd_4S), Pd_3S can be obtained after thermolysis. When the ratio was increased to 1:2, $Pd_{16}S_7$ was obtained. To obtain $Pd_{2.8}S$, the ratio had to be enormously increased to 1:20. XRDs of the various products obtained are shown in Figure III.31.
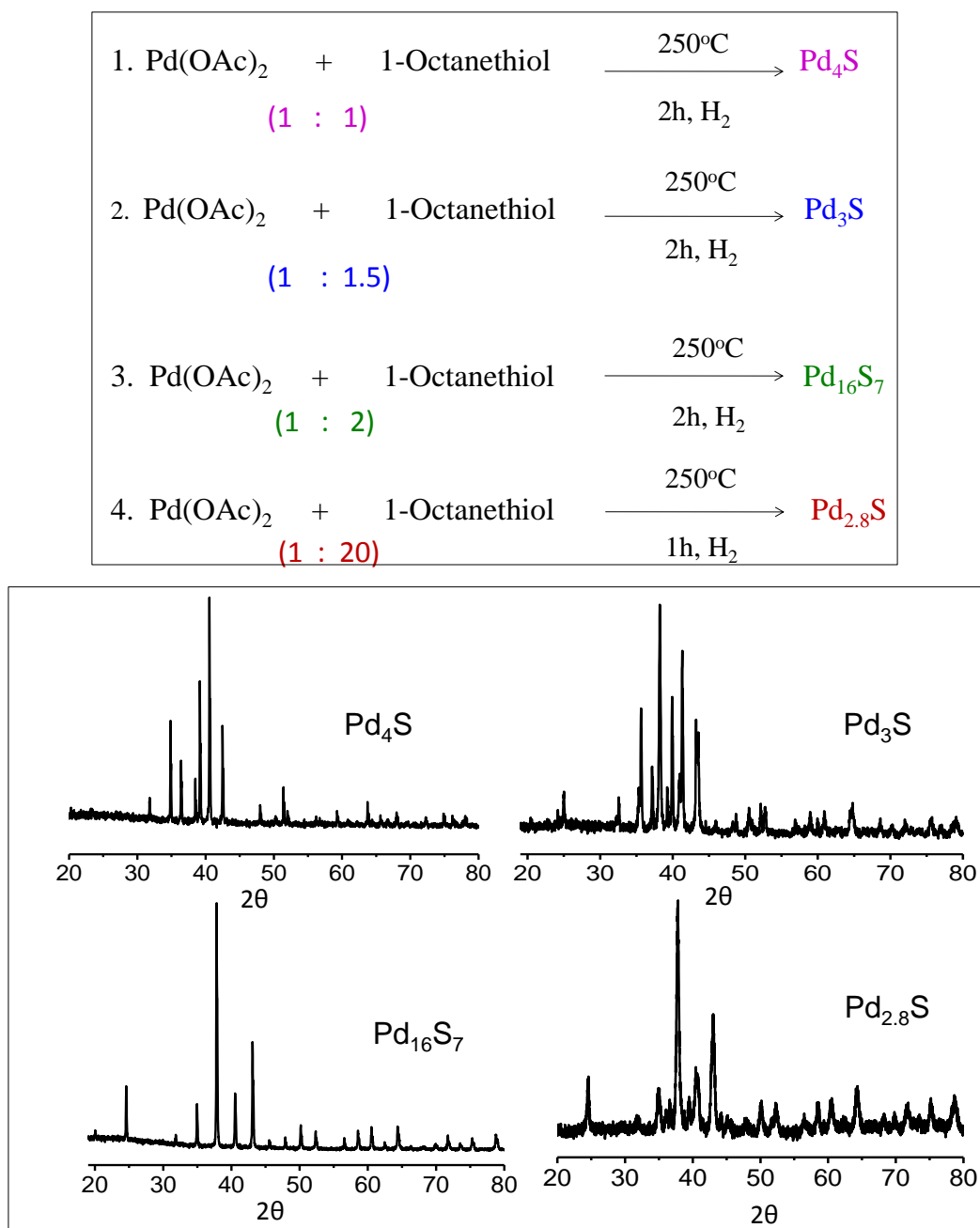
Figure III.31 Reaction scheme for synthesis of various Pd sulfides and XRDs of the products, identifiable with Pd_4S, Pd_3S, $Pd_{16}S_7$, $Pd_{2.8}S$ (JCPDS PDF #s 731387, 731831, 110001, 100334 respectively)

In the presence of inert atmosphere for thermolysis or in cases where H_2 cannot be employed for thermolysis, it is possible to obtain some of the Pd sulfidic phases. For instance, when Pd octanethiolate was heated in Ar or N_2 atmosphere at 250 °C, $Pd_{16}S_7$ phase was formed (Figure III.32a). The product is crystalline and all the peaks are identifiable with this phase. It is possible to produce PdS as well (Figure III.32b), starting with $Pd_{16}S_7$ and heating it at 250 °C in sulfur atmosphere for 3 hrs. A recent report has shown that $Pd_{16}S_7$ works well as a precursor phase for PdS [23].
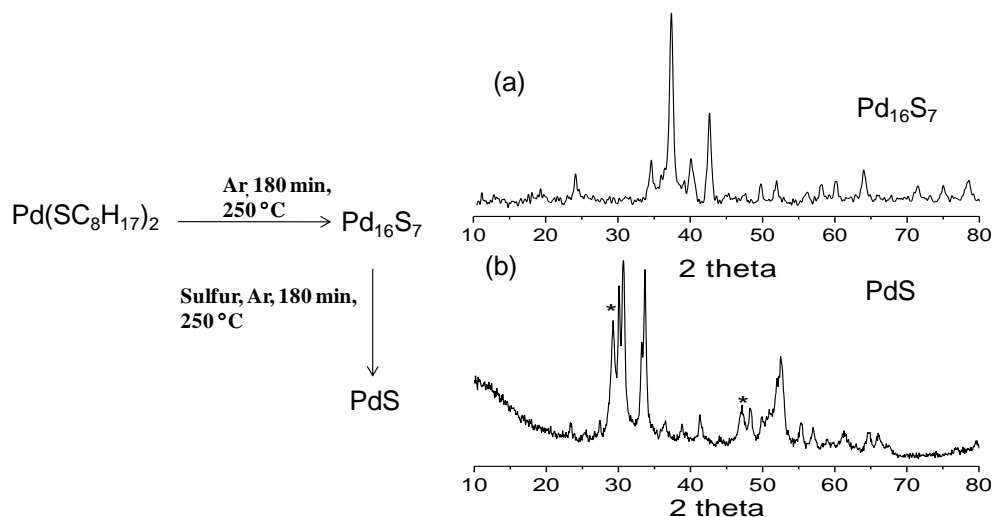
Figure III.32 Scheme showing the formation of $Pd_{16}S_7$ and PdS on thermolysis of Pd octanethiolate in different conditions as mentioned. (a) XRD pattern of $Pd_{16}S_7$ phase where the assignment is based on JCPDS PDF No. 75-2228 and (b) XRD pattern of the PdS phase obtained (JCPDS PDF No. 25-1234). The peaks marked as * could not be identified.

Direct write EBL using Pd thiolate

Previous reports from the laboratory have demonstrated the patterning capability of the precursor Pd alkanethiolates by EBL [64,93]. Utilizing the e-resist action of Pd thiolate precursor, patterns of Pd thiolate have been made by EBL. A Pd thiolate film (~60 nm) spin-coated on a Si substrate was patterned using a 5 kV electron beam at 135 $\mu C/cm^2$ and developed in toluene for 10 s. For EBL, hexadecylthiolate was used instead of octanethiolate, due to its high e-beam sensitivity [64]. The regions exposed to the e-beam remained on the substrate after developing, thus indicating the negative-tone resist behavior of the thiolate. In the follwoing step, the patterned thiolate precursor was converted to Pd_4S by thermolysis in hydrogen atmosphere. Figure III.33 shows an image of the patterned Pd_4S by EBL and the inset shows the magnified image of the pattern in which the sharpness of the pattern edges is evident. ED data spectrum laid over the image confirms the Pd:S ratio (4:1 by at %) which is preserved in the patterned Pd_4S as well.
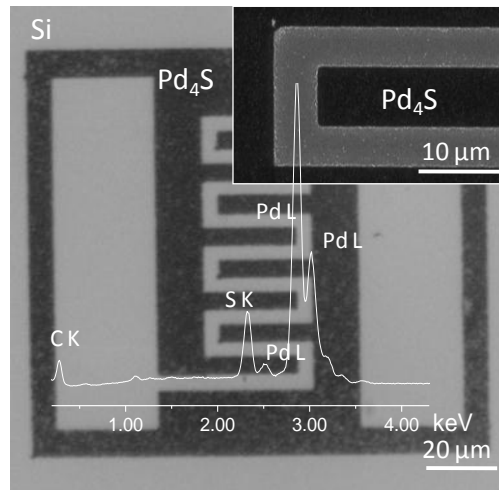
Figure III.33 (a) Pd$_4$S patterned by EBL (5 kV, 135 µC/cm^2) and the inset showing a magnified view. The corresponding EDS spectrum shown on top of the image.

The chemical resistance property of Pd$_4$S was extended to study its worthiness as an etch mask agent in lithography processes. For this purpose, a Au coated (~60 nm) Si substrate was deposited with Pd hexadecylthiolate and subjected to e-beam patterning using similar conditions as in Figure III.33, and following H$_2$ treatment, was obtained a 100 x 130 µm^2 rectangular region of Pd$_4$S on the Au film. The substrate was then dipped in a Au etching solution (KI:I$_2$:H$_2$O = 4 g : 1 g : 10 mL) for 5 min. As shown in the EDS map in Figure III.34, there was no Au signal outside of the patterned Pd$_4$S (only Si was visible), while the patterned region exhibited Au M, Pd L and S K signals. It is evident that the Au film was retained only beneath Pd$_4$S, thus demonstrating the etch mask behaviour of the latter. It is noteworthy that unlike well-known polymeric etch masks, Pd$_4$S is conducting.
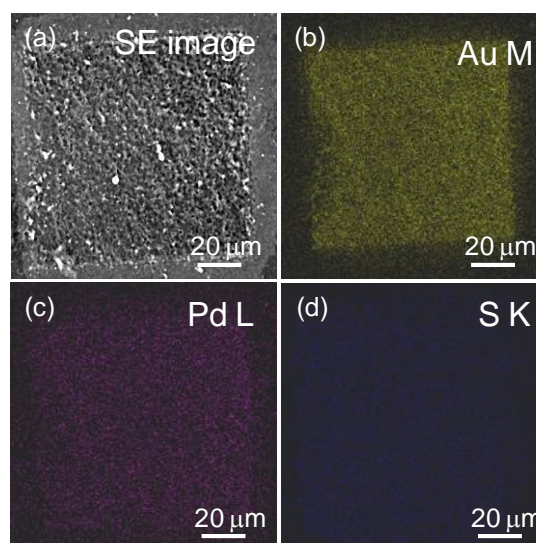
Figure III.34 Demonstrating the etch mask action of Pd$_4$S. (a) SEM image of the area masked by Pd$_4$S, (b)-(d) EDS maps obtained with Au M, Pd L and S K revealing the masked Au island.

Direct micromolding using Pd thiolate

Single source precursors such as Pd thiolate, which can be made to flow into narrow microchannels of the mold are highly desirable for direct MIMIC. The direct micromolding process consists of 3 steps (Figure III.35a) - (i) A PDMS stamp is kept on the Si substrate, (ii) the molecular precursor i.e., Pd thiolate is injected from one edge while the whole setup is heated to 250 °C and (iii) after annealing, the stamp is removed, thus micron wide stripes (μ-stripes) with uniform thickness are formed on the substrate. Figure III.35b shows the SEM image obtained after micromolding the Pd octanethiolate precursor. In Figure III.35b, a set of parallel and continuous μ-stripes of width ~1060 nm were seen. The features seen in Figures III.35b and c ought to be micromolded Pd metal stripes. The stripes are quite smooth as can be seen from the magnified images in the inset of Figure III.35b. EDS spectrum from the patterned region (Figure III.35c) shows the presence of Pd along with the Si signal from the substrate. Micromolding was possible this way due to the unique nature of Pd alkanethiolates, in that they are highly soluble in organic solvents unlike other metal thiolates.
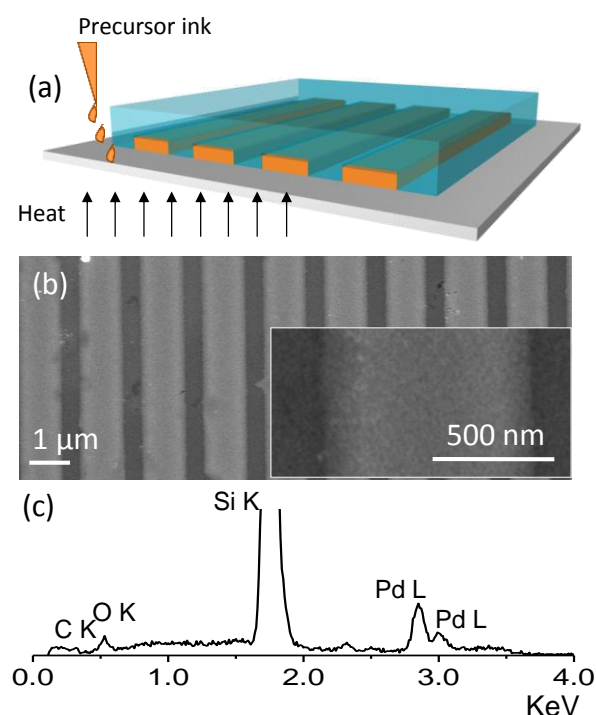
Figure III.35 Direct micromolding method: (a) Schematic showing injection of the precursor ink (Pd octanethiolate in toluene) at the interface of the PDMS stamp and the Si substrate. The μ-stripes are formed by trapping the precursor in the microchannels followed by thermolysis at 250 °C for 30 min, (b) SEM image showing the molded Pd stripes, (c) EDS from the patterned region.

Figure III.36 shows the AFM topography images of the PDMS stamp and the patterned Pd stripes. The stamp hosts relief features of width 505 nm with intermediate channels of 950 nm width. The height of the stamp features is ~160 nm. A series of microchannels of width ~ 950 nm and height ~160 nm can be easily visualized. In Figure III.36b, pairs of parallel Pd stripes, straight and continuous can be seen all over the substrate covering the molded area. They are ~1060 nm wide with spacing of ~520 nm in close compliance with the stamp geometry (see Figure III.36a). The variation in the width is rather small (standard deviation, 5 nm). The width is little larger than the microchannel, due to spreading of the precursor beyond the microchannel owing to the lower contact angle of the toluene with the Si substrate ($< 40°$). The z-profile in Figure III.36b provides the height of the patterned stripes to be approximately ~75 nm.
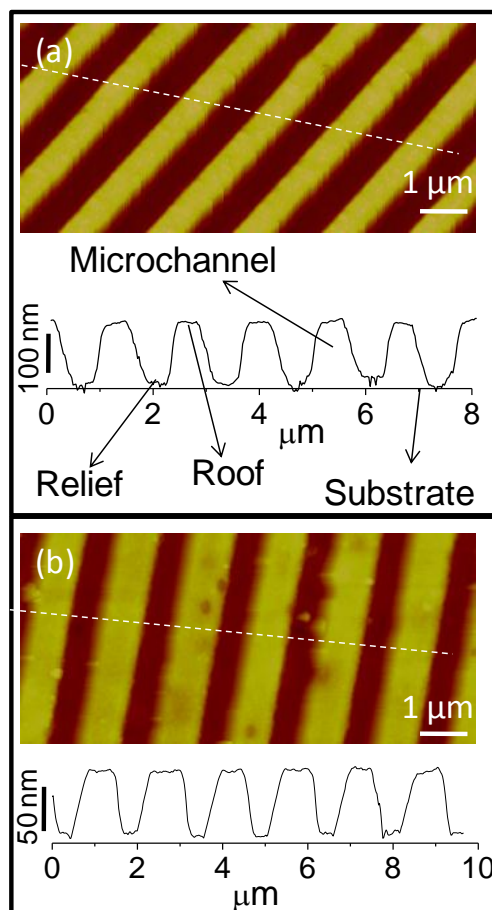
Figure III.36 Tapping mode topography images of (a) PDMS mold, and (b) molded Pd μ-stripes. The corresponding z-profiles are shown alongside. In (a), the profile is shown inverted in order to mimic the molding process.

The direct MIMIC is amenable to create patterns on varied substrates. As shown in the Figure III.37, Pd patterns could be successfully obtained on glass, SiO_2 and polyimide substrates, using similar conditions as mentioned in Figure III.35. The dimensions of the μ-

stripes are more or less the same in all cases but for slight changes in the widths. The spreading of the precursor on the substrate dictates the final dimension of the molded Pd stripes. The smearing of the ink is more in the case of glass which gives rise to slightly higher width features (~1.2 µm) than that on the SiO_2 (~1.1 µm) and polyimide (~970 nm) substrate. Polyimide being a flexible substrate, the direct molding method for patterning Pd µ-stripes onto polyimide is very encouraging. The patterning of conducting materials on flexible substrates is of assumed important while designing circuits for electronic textiles [94], sensory skins [95,96], liquid crystal displays or X-ray imaging devices [97,98].
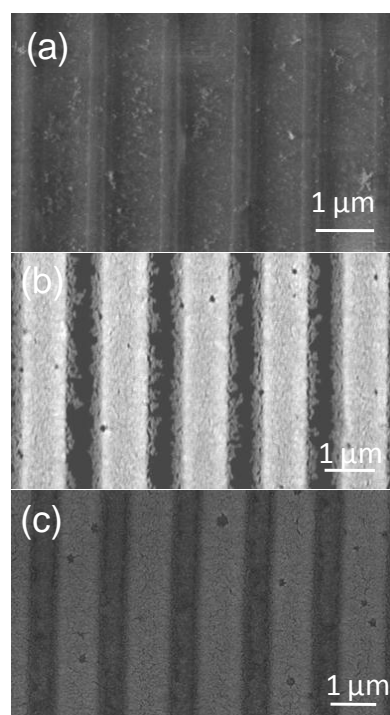
Figure III.37 SEM images of the Pd patterns molded on (a) a glass substrate, b) SiO_2/Si and on (c) a flexible polyimide substrate. The image quality is poor from the glass substrate due to e-beam induced charging.
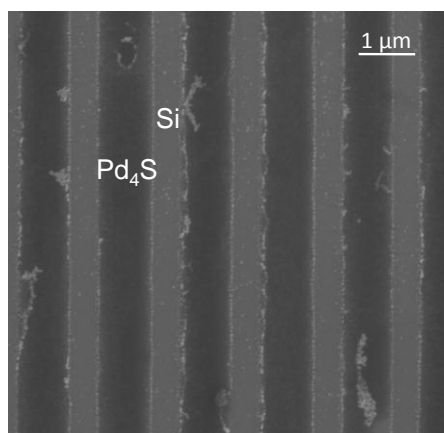
Figure III.38 A micromolded pattern of Pd_4S. The Si substrate and the stripes are marked.

Patterned Pd_4S can also be obtained by micromolding the thiolate precursor using PDMS stamp. After the thiolate pattern was obtained, it was thermolysed in H_2 atmosphere to convert to Pd_4S patterns (Figure III.38). The obtained Pd_4S patterns are in conformity with the stamp with ~1000 nm wide stripes spaced by ~495 nm.

While direct molding of Pd and Pd_4S promises widespread applications of the method to produce circuit interconnects by stamping, it also prompts one to exploit the flow conditions of the precursor inside the microchannels. In a related study, MIMIC of polystyrene has been carried out using a PDMS stamp, while heating the setup above the glass transition temperature. The resulting pattern contained replica of the parallel channels but with an important difference that trenches of width ~30 nm were found in between. The nanotrenches in polystyrene could be filled with metals by physical vapor deposition and electroless plating. In order to study this aspect with direct MIMIC, the method was modified. The modified process may be termed as 'Nanoentrapment molding (NEM)' and consists of 3 steps (Figure III.39a) - (i) A PDMS stamp is kept on the substrate, (ii) pressure is applied by placing a weight on top of the stamp, and the molecular precursor is injected from one edge while the whole setup is heated to 250 °C at a given temperature ramp, and (iii) after annealing, the stamp is removed leaving behind metallic Pd nanolines on the substrate.

For the given PDMS stamp, best results were obtained when a toluene solution of Pd octanethiolate (1 mM, 60 µL) was injected while applying an external pressure of 448 Pa on the stamp, the whole set up being heated at a temperature ramp of 30 °C/min to reach the annealing temperature of 250 °C. Figure III.39 shows the SEM and AFM images of the patterned area. Pairs of parallel lines, straight and continuous, each of width 50 nm can be seen over a large area (Figure III.39b). The variation in the width is rather small (standard deviation, ~4 nm) as can be seen from the magnified image in Figure III.39c. The AFM image in Figure III.39d provides the height of the patterned wires to be approximately 25 nm. It is astonishing that starting with a stamp with nearly micron sized features, the present recipe directly imprints truly nanometric features. It is also unique as it combines the advantages of direct patterning with the versatility of soft lithography, namely simplicity, speed, throughput as well as scalability. From Figure III.39c, the line spacing within a pair (~425 nm) is observed to be much less than the separation between the pairs (~980 nm), the two distances being close to the dimensions of the relief features (~505 nm) and the microchannel roof (~950 nm) respectively from an undistorted stamp (Figure III.36b). It is

therefore tempting to consider that under the pressure and heat treatment given, the precursor gets deposited only at the edges of the relief features leaving the channels free of any deposit (Figure III.39a). However, this process is quite different from edge lithographic techniques [99], where the molecular ink is constrained to the intersection of the roof and relief features of the stamp by employing a solvent which dewets the stamp surface, which is not the case here. Five important parameters those are responsible for the NEM process can be identified, namely the applied pressure, the solvent and the metal precursor, the heat treatment given in terms of the temperature ramp as well as the annealing temperature and finally, the stamp geometry.
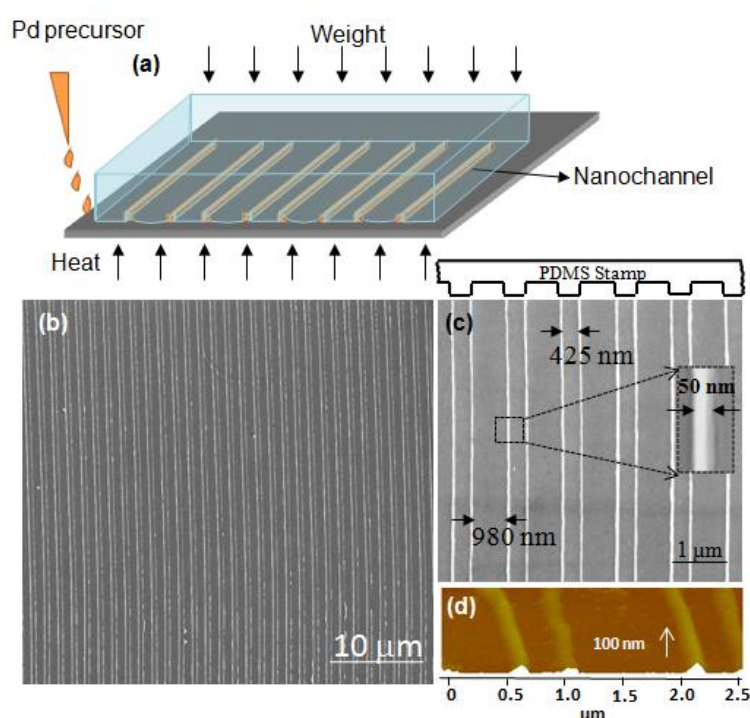
Figure III.39 Nanoentrapment molding (NEM): (a) Schematic showing the formation of nanochannels due to the near-complete microchannel roof collapse. (b) A large area SEM micrograph of patterned Pd nanolines formed on Si substrate by NEM. (c) A magnified view with the inset showing an individual nanowire of width 50 nm, and (d) AFM micrograph of the Pd lines. The observed width in AFM can have contribution from tip convolution.

When the same process was done using different applied pressures, Pd nanolines of different thicknesses were obtained (Figure III.40). While broad and continuous stripes corresponding to the stamp microchannels are seen in the absence of an external pressure (Figure III.36), with the application of a mild pressure (~110 Pa), thick lines are seen to differentiate in place of broad stripes reminiscent of their boundaries, albeit some deposits left in between. The differentiation into well-defined lines becomes evident at 127 Pa such that at any higher pressure, only lines were visible with the intervening region completely

clear. The width (W) of Pd nanowire thus obtained is varied with the applied pressure as shown in Figure III.40. In pressure regime I, the precursor ink is not strictly restricted and therefore, the deposits are seen all over the microchannel (marked D in Figure III.40a). In regime II, well defined features get formed with increasing pressure with no residual deposit on the substrate (Figure III.40a), whereas in regime III due to excess pressure, broken lines are seen (Figure III.40a). Best results (shown in Figure III.39) are obtained at the intersection of regimes II & III shown by the arrow in Figure III.40a.
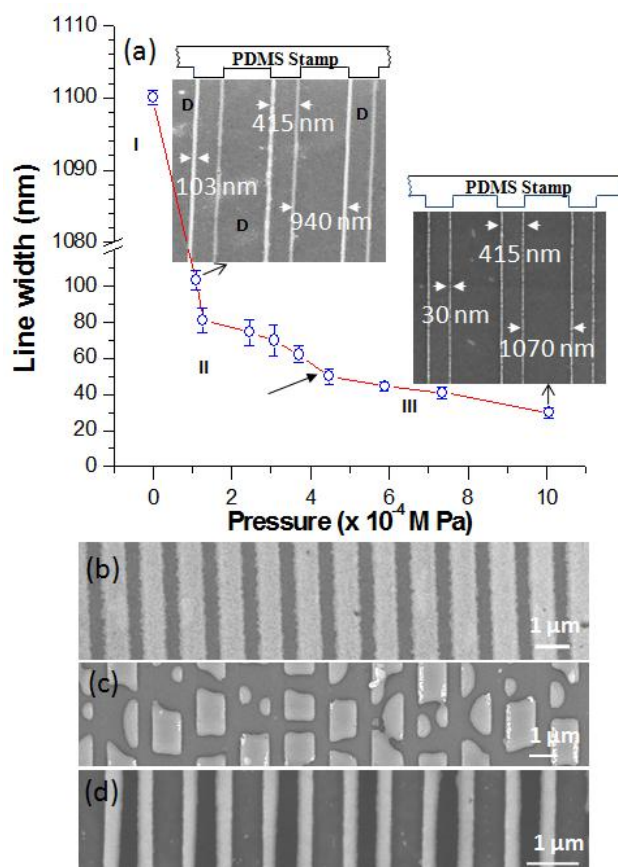
Figure III.40 (a) Variation of the Pd nanowire width with the external pressure applied on top of the PDMS stamp. In each case, the setup was heated at a ramp of 30 °C/min to 250 °C and was held for 30 mins. Here, zero pressure refers to the pressure due to the weight of the stamp itself (~54 Pa), without any external pressure. Error bars represent standard deviation in line width. SEM images corresponding to the pressures 110 Pa and 1010 Pa are also shown. The middle arrow refers to the pressure applied to obtain the pattern shown in Figure III.39. SEM images of the molded patterns obtained (b) using ethanol as the solvent, (c) with a temperature ramp of 50 °C/min. (d) with a 40 mM solution (other conditions as in Figure III.39).

In contrast to edge-patterning methods such as edge spreading lithography [42] and edge transfer lithography [99], which employ a dewetting solvent, here the solvent toluene wets the PDMS surface [100]. With solvents such as ethanol, which dewet the PDMS surface and cause negligible swelling, similar experimental conditions produced wide

patterns (~1 μm) almost equal to the microchannel width (Figure III.40b). Thus, wetting by the solvent, in some way, seems to be important in this process. The line width is sensitive to the temperature ramp as well. When the temperature was risen and held just above the boiling temperature of toluene (~110 °C) for nearly 10 min prior to annealing at 250 °C, broad features (~1 μm) were obtained as shown in Figure III.40c. Higher ramp rates, 50 °C/min instead of 30 °C/min also failed to yield narrower lines (Figure III.40c), indicating that the temperature profile influences the process. Similarly, the precursor concentration was found to influence the line width. When the concentration was much higher (40 mM instead of 1 mM), the wires were correspondingly thicker and non-uniform (Figure III.40d) while a lesser concentration (0.1 mM) yielded much fainter lines.

The discussion below provides an insight into the process by which the precursor gets deposited selectively at the edges of the relief features to produce fine wires shown in Figure III.39. It is unlikely that a lateral diffusion of the solvent into the relief features forcing the formation of a 'sedimentation cake' [101] can entirely be responsible, given that the wire formation is so neat. The line contours may instead be taken to represent the nature of the cavities which might have formed due to stamp roof collapse under the optimal conditions. Inducing roof collapse by applying external pressure on the stamp is not new. But the pressures used in such cases are usually high, ~30,000 Pa. Under the nominal pressures used in this study (~1000 Pa), cross-sectional SEM image of the stamp showed no evidence of roof collapse but instead a mild deformation (Figure III.41).
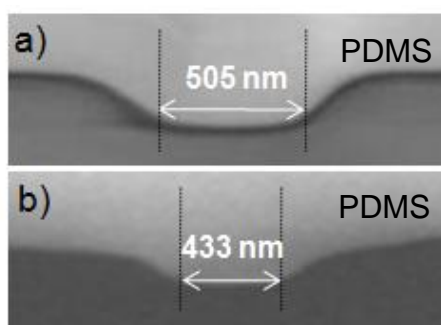
Figure III.41 Cross-section SEM image of (a) PDMS stamp with no external pressure. (b) A pressurised PDMS stamp. The contact area of the relief features decreases but no roof collapse occurs.

Accordingly, the footprint of the relief features is seen reduced from ~505 nm from an undistorted stamp to ~433 nm as marked in Figure III.41. Interestingly, the reduced footprint is close to the spacing observed within pairs of wires (~425 nm, see Figure III.39c). However, the point under discussion is the roof collapse which is far from complete. For the given stamp geometry with an aspect ratio (microchannel height/relief width) of 0.3, the

minimum amount of pressure needed for the stamp to collapse is ~ 30,000 Pa [101], but the pressure used in the present experiment is at least 30 times less. Obviously, the desired roof collapse cannot take place because of pressure alone (Figure III.42).
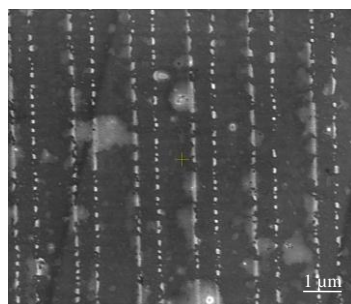
Figure III.42 Pd nanolines formed on the Si substrate by conventional micromolding using PDMS stamp which is pressurised with ~25,000 Pa on top. Stray Pd deposits are also seen in between the broken nanolines.
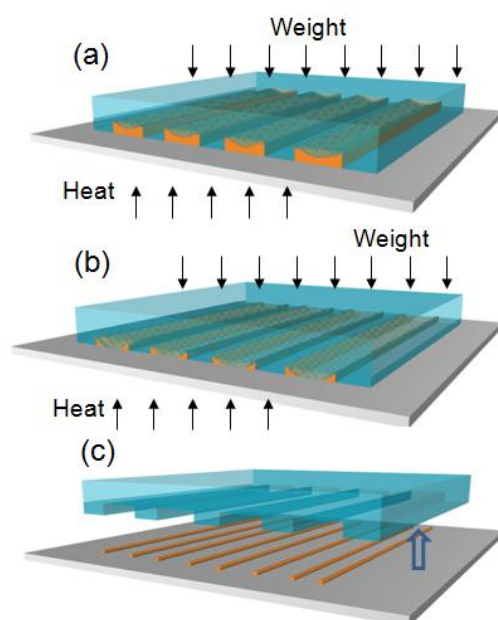
Figure III.43 Schematic showing the various stages of the entrapment of the precursor. (a) A PDMS stamp is kept on a Si surface and is pressurized on top. The Pd precursor solution is injected and heated from underneath. (b) Near complete roof collapse entrapping the Pd precursor at the edges of the relief features. (c) The entrapped Pd precursor undergoes thermolysis. The stamp is removed leaving behind patterned nanolines on the substrate.

Neither a steady state swelling due to the solvent can induce an excessive roof collapse as maximum swelling of PDMS in toluene is only 106% on weight basis [102] and moreover, such swelling is expected to be isotropic. Here, another parameter is brought for discussion, namely the temperature ramp as it controls the extent of solvent diffusion into the PDMS surface. While the diffusion rate increases with increasing temperature, the amount of solvent available itself depletes with time. Thus, the diffusion can only be skin-depth causing differential swelling of the roof surface. Perhaps, the roof surface becomes so fragile that it

may not be able to withstand even mild pressures (~100 Pa, see Figure III.40a) and collapses leading to the confinement (or pinning) of the precursor ink at geometrical obstacles i.e., feature edges (see schematic in Figure III.43). It is intriguing that the confinement is so effective leaving no trace of precursor in the intervening regions (between the pairs of lines, see Figure III.39c). One way to test this proposition is to induce some roughness of the roof surface so that, in spite of collapse, the confinement of the precursor to the edges would not be effective. For this purpose, two clean CD pieces were taken and gently rubbed against each other to create some roughness. A PDMS stamp was made using roughened CD as a master. This PDMS stamp was used for NEM. In such a case (Figure III.44), instead of narrow pairs of lines, broad Pd stripes (~1.25 µm) were observed reminiscent of the topography of the roof surface.
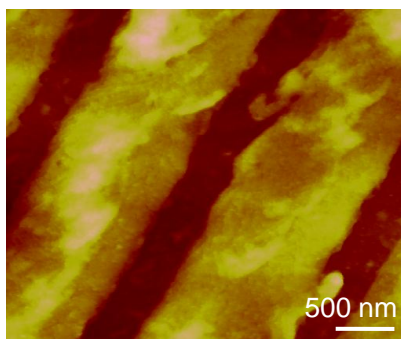
Figure III.44 AFM image of Pd patterned on Si using a PDMS stamp made of roughened CD as a master. This stamp failed to produce 50 nm Pd lines under optimal conditions. The roughness associated with the microchannel is reflected in the topography of the obtained patterns.
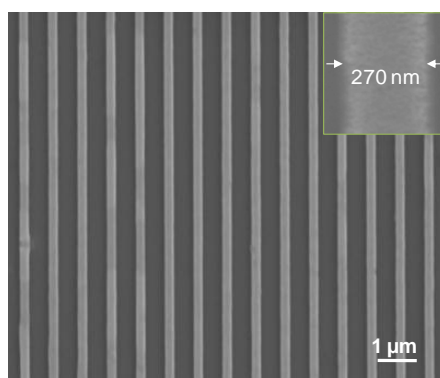
Figure III.45 SEM image of the obtained Pd nanolines using a PDMS stamp made of a DVD master; each Pd line is ~270 nm thick. The spacing distance is ~500 nm. Inset shows the magnified image of a single feature.

The optimal conditions are also linked to the initial stamp geometry. When a DVD master was used instead of a CD to produce the stamp, the above conditions produced Pd wires of width ~270 nm (Figure III.45). As the aspect ratio is 0.4, finer lines may be expected at much higher pressures.

Direct micromolding using Au thiolate

As mentioned earlier, unlike Pd thiolates, other metal thiolates are insoluble in common solvents. In order to extend the method of direct micromolding using M-thiolates, Au thiolate precursor was chosen as it is known to give rise to uniform sized Au nanocrystals upon thermolysis [87]. The choice with respect to the metal (Au) was made considering its importance in chemical and biosensing, diagnostics [103], cellular imaging [104], plasmonic activity, ease of functionalization [105], enhanced Raman scattering etc [103].
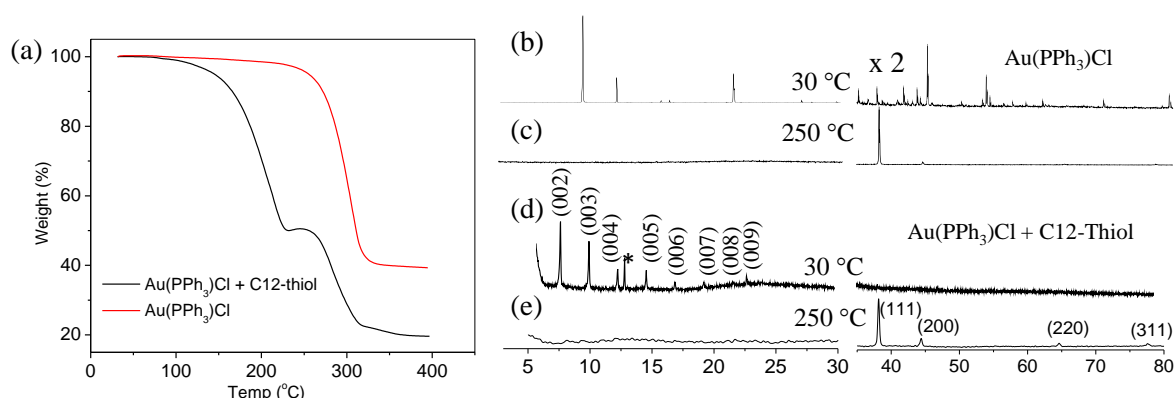
Figure III.46 (a) TGA of the $Au(PPh_3)Cl$ and its mixture (1:1) with dodecylthiol (C12-thiol). The analyte was taken in the form of viscous solution in toluene (total weight, 10 mg) in a porcelain boat. XRD data of the (b) $Au(PPh_3)Cl$ drop coated as a film, as prepared, (c) after heating to 250 °C, (d) mixture of $Au(PPh_3)Cl$ and dodecylthiol as prepared and (e) after heating to 250 °C. The peaks are compared with JCPDS PDF No. 040784 for polycrystalline Au. Some precursor $Au(PPh_3)Cl$ is still retained as revealed by the precursor peak (marked by *) in XRD.

Owing to its insolubility, *in situ* synthesis of the Au thiolate followed by its decomposition was done. The starting material was chosen as $Au(PPh_3)Cl$ in toluene (1 mM) for in situ synthesis of thiolate. Thermolysis of the $Au(PPh_3)Cl$ itself was examined first. The XRD data from a film of $Au(PPh_3)Cl$ precursor (Figure III.46b) shows clearly the formation of polycrystalline Au upon heating in air to 250 °C (Figure III.46c). This is also supported by the TGA measurement (Figure III.46a) where the total weight loss in $Au(PPh_3)Cl$ occurs above 230 °C leading to Au (39.7%, calculated 39.8%). This ink itself was used for micromolding using a topographically patterned PDMS stamp placed on a Si substrate (as depicted in scheme in Figure III.47a). A 60 μL of the $Au(PPh_3)Cl$ solution was dropped at the stamp edge so as to fill the microchannels. The set up was heated gradually to 250 °C in steps of 10 °C per min and held for 30 min. After cooling, the stamp was removed leaving behind the molded material into stripe patterns covering large areas. However, this recipe

gave rise to Au nanocrystals with large size variation (Figure III.47b). Although the stripe patterning was evident, there was little hope of getting an ordered nanocrystal array based on this recipe. Neither a lower rate of heating (5 °C per min) helped. A simple mixing of Au(PPh$_3$)Cl and dodecanethiol solutions at room temperature leads to the formation of Au(I)-thiolate as shown in the XRD data in Figure III.46d. When subjected to thermolysis at 250 °C in air, the corresponding XRD (Figure III.46e) showed peaks corresponding to polycrystalline Au. From TGA of the mixture of Au(PPh$_3$)Cl and thiol, the total weight loss was 78.9% with a residue of 21.1% (Figure III.46a). The residue corresponds to Au metal going by the weight percentage. The weight loss occurs in two major steps. The initial weight loss at ~175 °C is due to the loss of PPh$_3$ and Cl ligands leading to Au with thiol molecules present around. Around 250 °C, much of the thiol is desorbed leaving behind Au with some chemisorbed thiol.
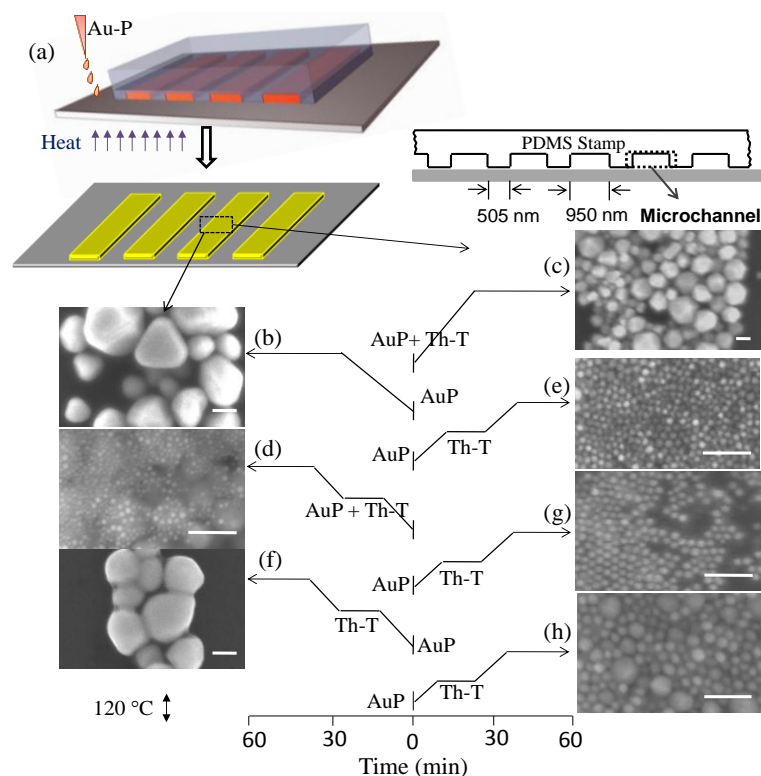
Figure III.47 Direct patterning of Au nanocrystal superlattices by micromolding, (a) schematic showing introduction of the precursor inks at the interface of the PDMS stamp and the Si substrate followed by thermolysis at 250 °C. Stamp geometry is shown alongside. (b-h) SEM images showing Au nanocrystal arrays obtained by varying preparative conditions. Au nanocrystal superlattices formed by the one-step introduction of (b) Au-P and (c) Au-P + thiol in toluene at room temperature; (d) Au-P + thiol at 120 °C. Au nanocrystal superlattices formed by the two-step introduction of Au-P at room temperature and thiol (in second step) at (e) 120°C, (f) 140 °C, (g) 80 °C, and (h) 100 °C. Au(PPh$_3$)Cl = Au-P; Th = Thiol; T = Toluene; Temperature ramp = 10 °C/min. Total reaction time was 60 min. All scale bars correspond to 100 nm.

Then the mixed toluene solutions of Au(PPh$_3$)Cl and dodecanethiol (1mM, 60 μL each) into the stamp mold and heated to 250 °C (Figure III.47c). Nanocrystals in the size range of 50-100 nm are seen with some indications of close packing but contain voids in between. Mixing the ingredients prior to molding seems to accelerate the nanocrystal growth. Introducing the mixed solutions at 120 °C (slightly above the solvent bp. 110 °C), gave rise to tiny Au nanocrystals (8-15 nm) amidst larger ones (50-100 nm) with little improvement in packing (Figure III.47d). It is clear that a sudden evaporation of the solvent may hold the key for small nanocrystal formation. Taking clues from the above experiments, a two-step synthesis was resorted – introducing Au(PPh$_3$)Cl solution into the mold at room temperature and dodecanethiol solution at elevated temperatures (Figure III.47e-h). This was followed by thermolysis at 250 °C. The introduction of thiol at 120 °C gave rise to fine nanocrystals as seen Figure III.47e with more details shown in Figure III.48. The second step at 120 °C seems crucial. A higher temperature (140 °C) can steam out the solvent destabilising possible formation of the array (Figure III.47f). Lower temperatures, 80 °C or 100 °C, also were not much helpful (Figures III.47g and h, respectively). Beyond 120 °C however, introducing the solution is rather difficult as the whole setup gets agitated resulting in just a rudimentary network of particles (Figure III.47f).
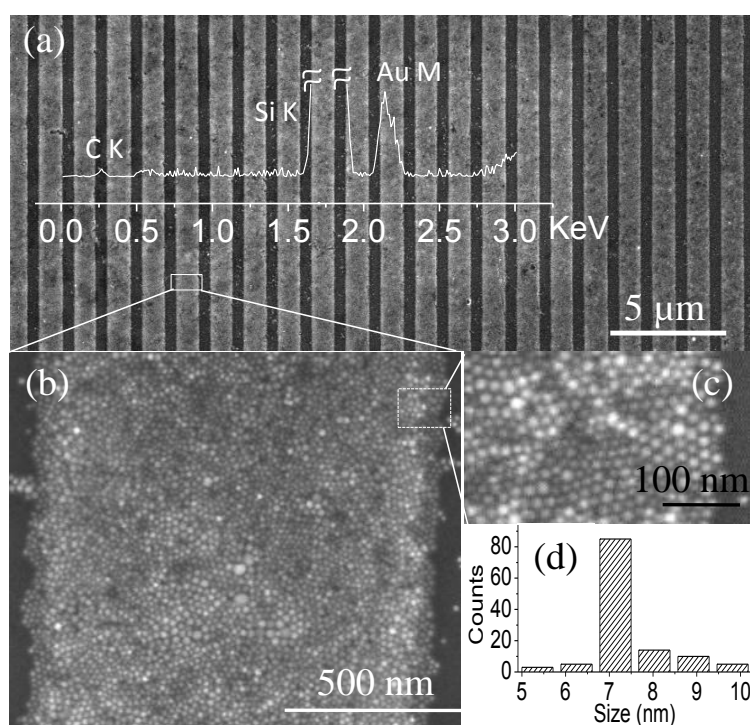
Figure III.48 (a) A SEM image showing the patterned Au nanocrystal superlattices formed by thermolysis at 250 °C for 30 min, with the EDS data from the patterned region overlaid, magnified views in (b) and (c), (d) Histogram of the Au nanocrystals from (c).
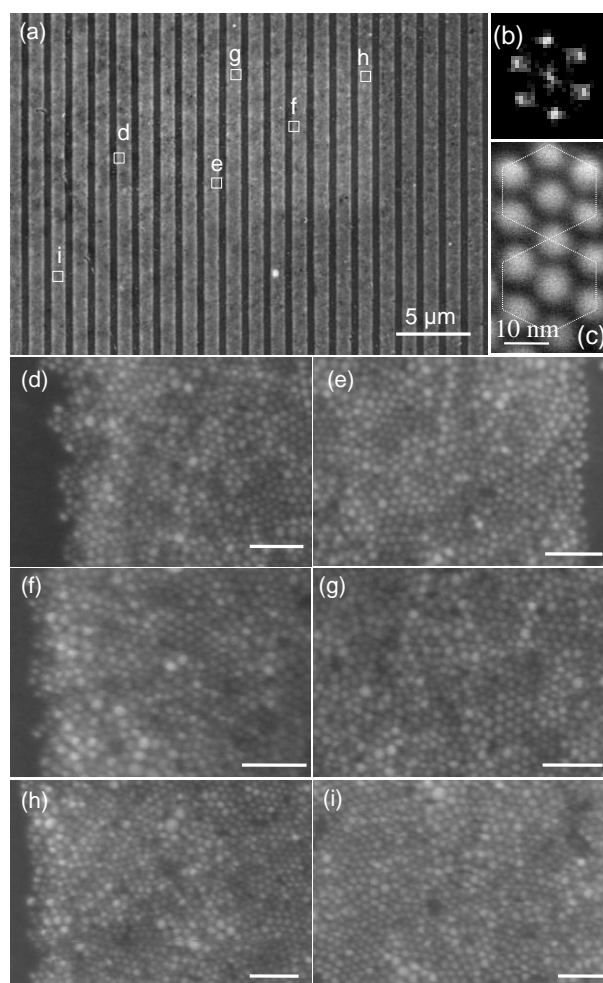
Figure III.49 SEM images (d-i) of ordered arrays of Au nanocrystals from different regions of the patterned area shown in a. The nanocrystal ordering is quite uniform along the edges as well as in the middle of the stripes. All scale bars correspond to 100 nm. FFT from one of the regions is shown in (b). (c) A magnified view showing the Au nanocrystals arranged as centred hexagons which are labeled by dashed lines.

Thus in the parameters window used, the two step MIMIC - introduction of Au(PPh$_3$)Cl solution at room temperature and dodecanethiol solution at 120 °C - followed by thermolysis at 250 °C - gave rise to fine well patterned nanocrystal superlattices (Figure III.48). The nanocrystal stripes are seen over large areas (Figure III.48a) and the EDS spectrum showed the presence of Au. The stripes measured ~1.08 μm across corresponding to the microchannel width of ~950 nm (see Figure III.47a). From Figure III.48b and c, it is seen that each stripe is essentially a colony of Au nanocrystals organised into a superlattice. Careful observation reveals the multilayer structure of the patterned stripe. SEM images from various locations (Figure III.49d-i) on the patterned stripes (Figure III.49a) reveal remarkable uniformity of the nanocrystal ordering. The fast fourier transform (FFT) of the hexagonal ordering is shown in Figure III.49b. The internal hexagonal ordering in the superlattice is evidenced from the magnified image shown in Figure III.49c. Hexagonal

ordering is favored based on entropy consideration [106,107], and is commonly observed in the absence of a directing agent or a template. The histogram of the Au nanocrystals (Figure III.48d) shows the mean particle size of ~7.5 nm, with a mean interparticle separation of ~1.5 nm. This distance can arise from the dodecanethiol molecules chemisorbed on the nanocrystal surface [108]. Indeed, IR and Raman spectroscopy measurements revealed the presence of the thiolate species (Figure III.50). While excess of molecules may desorb at the annealing temperature of 250 °C, those chemisorbed on nanocrystal surface may stay on further [37] and induce hexagonal ordering of the nanocrystals [38]. The average height of the stripes was found to be ~ 60 nm based on AFM corresponding to ~8 nanocrystal layers (Figure III.51).
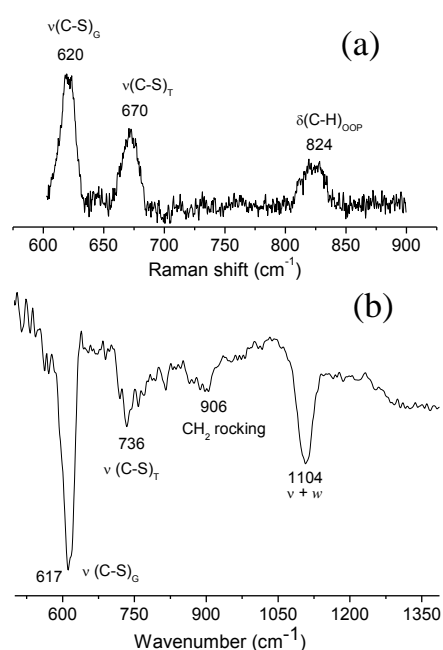
Figure III.50 (a) Raman spectrum from the patterned stripes with the peaks assigned (G-Gauche, T-Trans, OOP-out of plane), (b) FTIR spectrum of the Au ordered array showing C-S stretch modes along with C-H rocking and bending modes.
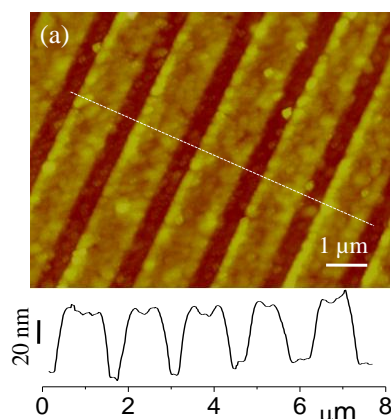
Figure III.51 AFM image of the patterned microstripes of Au nanocrystals with the z-profile at the bottom.

Micromolding offers additional advantages. As discussed previously, one may manipulate the fluid flow conditions inside the microchannels to achieve narrow feature sizes. In order to pattern Au nanostripes via NEM, the PDMS stamp was kept on a cleaned Si wafer and an appropriate weight was applied on top amounting to a pressure of 450 Pa (see schematic in Figure III.52a). SEM image of the patterned region (Figure III.52b) shows, in contrast to the images in Figure III.48, pairs of stripes of width 70 nm, filled with nanocrystals. As seen in the magnified image of a stripe, the size of the crystals is varied (5 - 10 nm) but the nanocrystals are seen tightly packed into thread-like features. In conformity with the nanochannel formation, pairs of parallel stripes ~70 nm wide were seen with an internal separation of ~430 nm and between ~990 nm (see Figure III.52b). Considering that solvent evaporation from narrow channels (height or width < 100 nm) is not trivial [109], the present method provides a ready recipe in contrast to methods based on solvent evaporation [110].
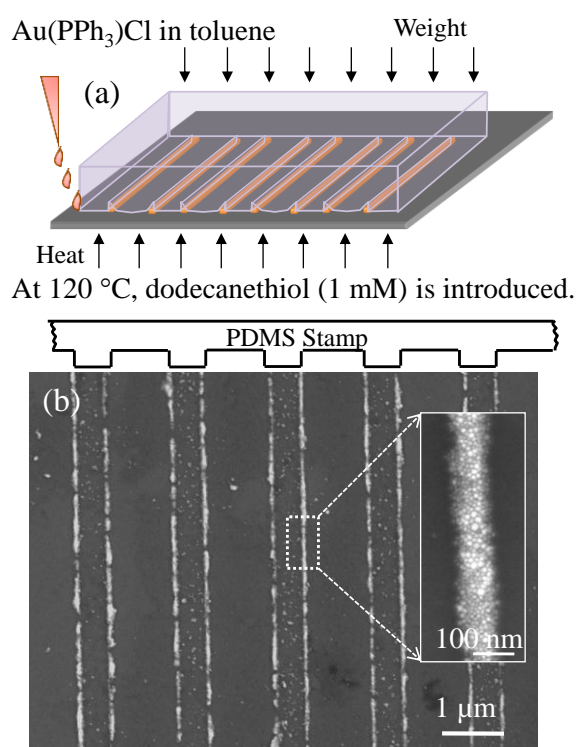
Figure III.52 NEM of Au nanocrystals - (a) Schematic showing the formation of nanochannels in the NEM process, (b) A SEM image of patterned Au nanocrystals formed on Si substrate. A magnified view an individual stripe is in the inset. Other conditions were similar to the process described in Figure III.48.

Clearly, the above method need not be limited to Au nor to the size range mentioned. It should be possible to extend the two step *in situ* synthesis and thermolysis for the other M-thiolates which are poorly soluble.

Direct NIL using Pd thiolate

Since its inception, NIL has been used for imprinting polymers [111]. Of late, there has been considerable interest in direct imprinting of metal-organic compounds, as the number of process steps are reduced. For realizing the direct imprinting, several precursors have been tried out. Metal methacrylates [112], alkoxides [113,114] etc., are the notable ones, which have been primarily used for metal oxide imprinting. These precursors utilize polymer additives to make the precursor imprintable. The additives may induce polymer crosslinking during imprinting, thus trapping the metal precursor in the patterned structure. One immediate consequence of such method is the higher decomposition temperature required to crack the polymer. Also, the impurities left behind are difficult to get rid of. Another way is to imprint nanoparticle inks [35,115] directly and sinter the particles to lead to continuous structures. The stabilizing ligands around the nanoparticles cannot be removed smoothly and thus sintering usually leads to inferior properties of the imprinted features. Considering the above factors, it is interesting to directly imprint using a molecular ink, which by itself is imprintable, without any additives. Analogous to the glass transition (Tg) in polymeric systems, the chosen precursor, Pd thiolates possessing crystalline lamellar structures also undergo melting [116]. Pd benzyl thiolate was chosen for this study, in order to increase the metal content in the final imprinted structure. The recipe presented here can not only be used for directly patterning Pd but also for creating versatile hierarchical and stacked nanostructures (Figure III.53).
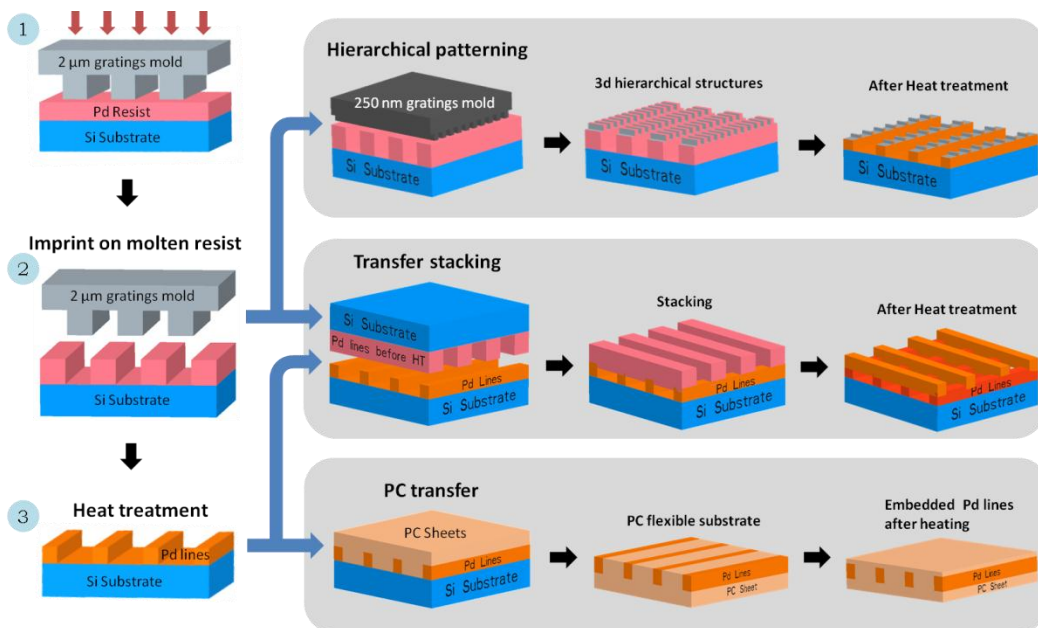
Figure III.53 Schematic illustration of the direct imprinting, hierarchical patterning and transfer stacking.

In order to find out the melting temperature of the imprinting precursor, a DSC measurement was performed (Figure III.54). A sharp endothermic (–ve) peak was observed at around ~120 °C, coinciding with melting of the Pd thiolate (cycle 1). The compound was then cooled back to 30 °C and after a short while, the second cycle of heating was performed, which led to a DSC trace much shallower with no evident peak. In the third cycle, the peak due to melting further diminished and when the temperature was raised to 250 °C, a distinct endothermic peak was observed due to decomposition. In the case of linear alkanethiolates of Pd, the melting of the thiolates is well studied [116] and was observed at around 85 °C for dodecylthiolate. The irreversible nature of the melting transition in the present case plays an important role in preserving the integrity of the patterns while thermolysis. At the same time, second shallow (i.e., surface) melting can be employed in creating interesting and versatile hierarchical structures as well (*vide infra*).
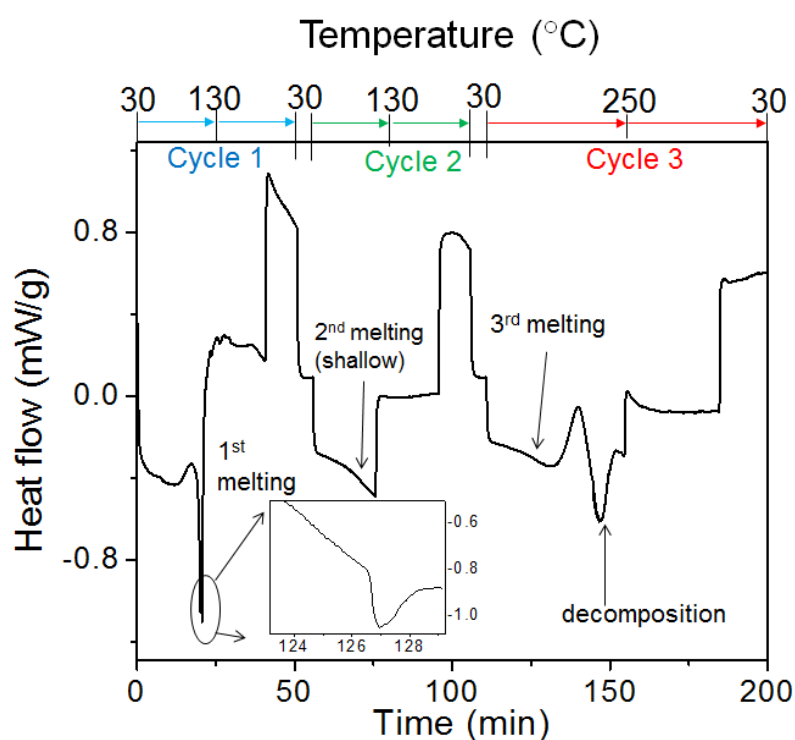
Figure III.54 DSC of the Pd thiolate for various melting cycles (details in the text). The first melting curve is shown enlarged in the inset.

Pd benzylthiolate dissolves well in many common solvents such as toluene, chloroform, acetone etc., and forms smooth films when spincoated. The thickness of the film is highly controllable with the concentration of the precursor and the spin speed (Table III.4).

Table III.4 Direct nanoimprinting conditions for various patterns of Pd.

Sl. No	Mold	Conc. of Pd resist (M)	Spin speed (rpm)	Thickness (nm)	Imprinting conditions			Pd feature size (nm)	Ref. (Fig.)
					Temp (°C)	Pressure (bar)	Time (min)		
2D structures									
1	2 µm gratings	0.28	400	501	120	50	1200	1040	III.62
2	250 nm gratings	0.28	3000	323	120	50	1500	100	III.55
3	100 nm gratings	0.1	3000	135	120	40	1800	40	III.58
4	200 nm dimples	0.28	3000	323	120	50	1800	85	III.56
5	Nanotubes	0.28	3000	323	120	50	1200	100	III.57
6	Hexagonal hole array	0.05	6000	68	120	50	1500	23	III.58
Hierarchical structures									
7	250 nm on 2 µm gratings	0.28	400	501	I, 120	50	1200	1040	III.59
					II, 90	30	2400	50	
8	Rice leaf	0.28	400	501	I, 120	50	1200	1700	III.60
					II, 92	30	2400	90	
Transfer stacking									
9	Stack 1: 2 um	0.28	1500	501	130	30	1500	1803	III.61
10	Stack 2: 2 um	0.28	2000	501	130	25	1500	1705	III.61
11	Stack 1: 250 nm	0.28	3000	501	90	40	1500	150	III.61
Transfer imprinting to flexible polycarbonate (PC)									
12	Pd lines transferred to PC	-	-	-	150	50	600	1700	III.62
13	Embedded Pd lines in PC	-	-	-	150	50	600	1700	III.62

The spin coated film was imprinted using a Si mold with 250 nm grating structures, at about melting temperature (~120 °C) applying a pressure of ~50 bar. During imprinting, the molten precursor flowed into and filled the channels in the Si mold, and after imprinting process, the setup was cooled down. The Si stamp was demolded leading to the Pd thiolate patterns on the substrates. Henceforth, the process is named as melting induced direct NIL (MDNIL). As-imprinted patterns were ~210 nm wide (Figure III.55a and b) with a thickness

of ~185 nm (Figure III.55c). After thermolysis at 250 °C for 1 hr, the obtained Pd patterns shrunk to ~100 nm (Figure III.55d and e), with a thickness of ~70 nm (Figure III.55f). In other words, the lateral shrinkage was 47%, whereas the vertical shrinkage, 38%, all due to the loss of the organic moieties. Thus, the distance between the features increased, while the pitch of the grating remained the same. An excellent imprinting yield of nearly 100% was obtained and this can be clearly seen in the photograph of the imprinted features over an area of 2 x 2 cm^2 (Figure III.55a inset). The diffracted color of the ambient light is uniform across the large patterned area.
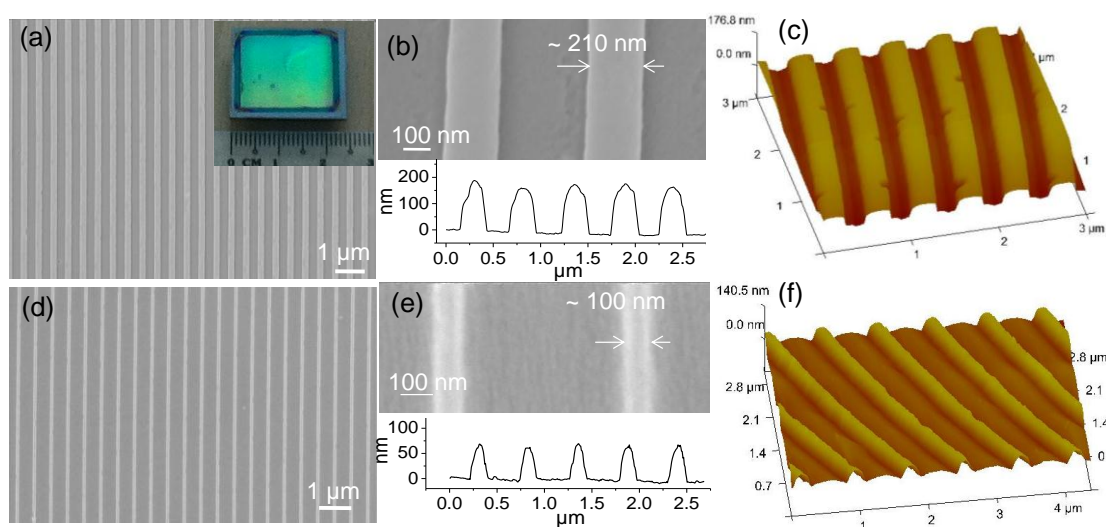
Figure III.55 Direct nanoimprinting of Pd – SEM images of the (a) as-imprinted line gratings of Pd benzylthiolate and (d) after heat treatment with (b),(e) showing magnified view and *z*-profiles. (c), (f) 3D AFM images of the same. Inset in (a) shows the digital photograph of large-area i.e., 2x2 cm^2 uniformly imprinted pattern. The color is due to interference of the diffracted ambient light.

Various morphologies can be directly imprinted by suitably selecting the imprinting Si mold. Circular tall pillars of 1:2 aspect ratio were imprinted (Figure III.56) using the similar imprinting procedure (Table III.4). After imprinting and demolding, the imprinted pillars (~260 nm tall, ~150 nm wide) were intact and the aspect ratio is vividly seen in the case of a broken pillar shown in the inset (Figure III.56a and b). After heat treatment, the pillars height reduced to ~160 nm and the width was ~85 nm (Figure III.56c and d). Apart from solid Pd nanostructures, hollow Pd nanotubes can also be imprinted directly. Figure III.57a shows the optical images of the Pd nanotubes. The SEM images in Figure III.57b shows the aspect ratio and the nanotube morphology in a tilted view (inset). The width of the wall of the as-imprinted nanotube is ~200 nm, which decreases to ~100 nm after heat treatment (Figure III.57c). The height of the nanotube was ~280 nm and reduced to ~90 nm after heat

treatment; this can be seen from the overlaid AFM profiles and the magnified views in Figure III.57b and c. Uniform filling of the molten Pd precursor is the key for the successful imprinting of various morphologies including nanotubes. The isolated features obtained by NIL are unique to NIL; MIMIC for instance needs continuous flow channels and cannot be used for creating patterns of unconnected features.
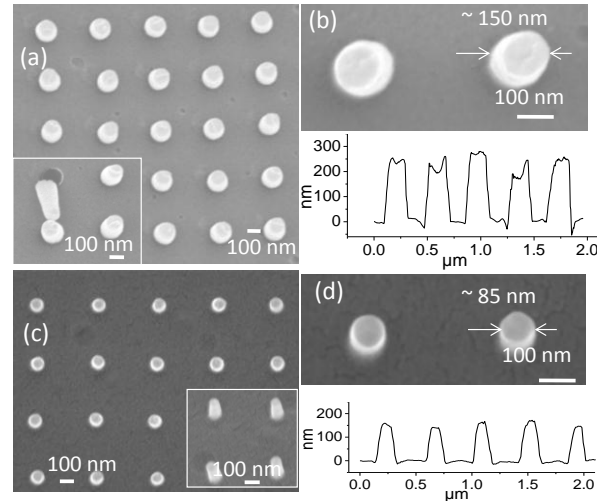
Figure III.56 SEM image of the imprinted Pd pillars of high aspect ratio (a) before and (c) after heat treatment, with the magnified SEM images and AFM *z*-profiles in (b) and (d) respectively. In the inset of (a), a broken pillar can be seen.
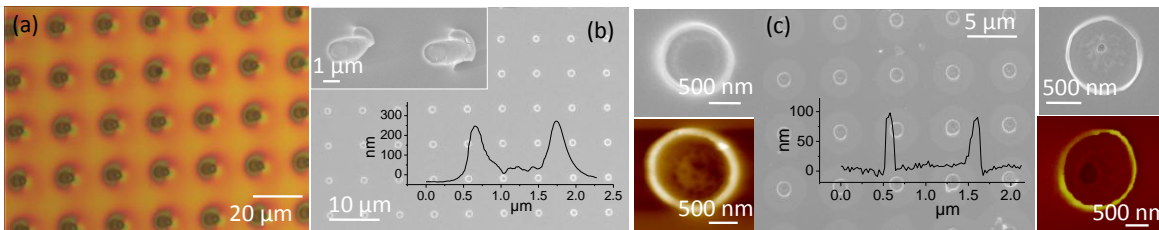
Figure III.57 (a) Optical images of imprinted Pd nanotubes over large area. SEM image of the (b) as-imprinted Pd nanotubes and (c) after heat treatment with AFM z-profiles overlaid; magnified SEM and AFM images shown alongside.

Sub-50 nm direct imprinting is of technological importance in the fields of nanoelectronics as well as nanophotonics. Imprinted Pd lines of ~40 nm width (after shrinkage) can be obtained routinely (Figure III.58a and b). Using a mold with feature size ~35 nm, Pd nanolines (width, ~30 nm) were obtained (Figure III.58c and d). Similarly, Pd hexagonal nano-hole arrays can be uniformly imprinted over large areas (Figure III.58e) and after heat treatment the structure is preserved (Figure III.58f) with an average wall width of ~23 nm. These structures resemble metallic photonic crystals with hexagonal hole-type arrays, which are of interest as they can have a larger photonic band gap.
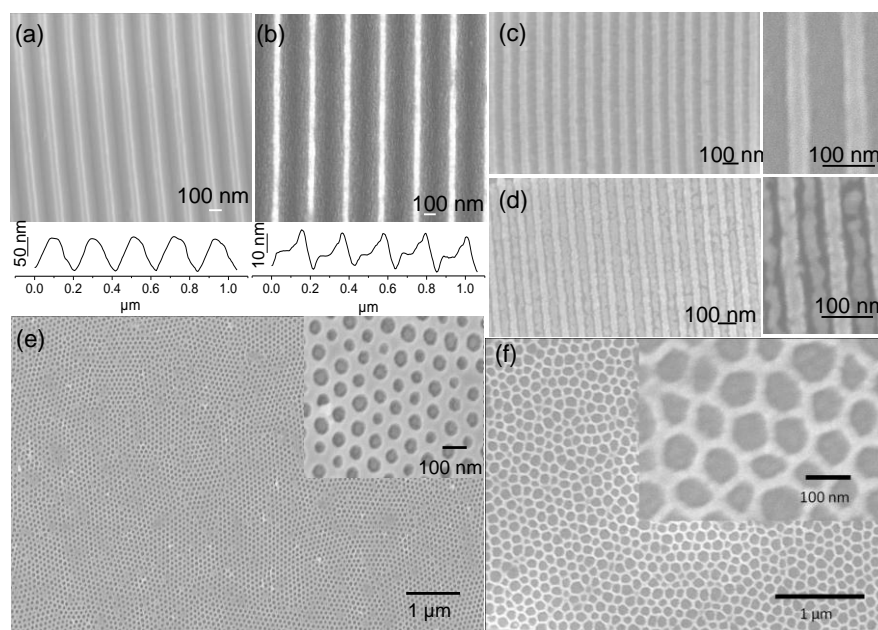
Figure III.58 Sub-50 nm direct imprinting of Pd - Imprinted Pd features using 100 nm mold (l) before and (m) after heat treatment. AFM z-profiles are shown below. SEM images of 35 nm features (n) as-imprinted and (o) after heat treatment, with magnified images shown alongside. Hexagonal hole array imprinted in Pd benzylthiolate (p) before and (q) after heat treatment. The minimum wall thickness between the holes after heat treatment is ~23 nm.

Ordered hierarchical and complex metal nanostructures have potential magnetic [117], catalytic [118], optical applications [119]. Hierarchical structuring on polymers is well known and an important use of such structures can be noted here; a plastic film with hierarchical surface topography is used in aircrafts to reduce drag [120]. In literature, hierarchical patterning of polymers has been achieved by sequential imprinting steps [121]. Laser patterning has been utilized for direct hierarchical structuring of metals [122], employing high energy pulses of laser. The MDNIL method presented here, can be employed for hierarchical patterning of Pd taking advantage of the hysteritic melting behavior of the Pd thiolate precursor (Figure III.54). This is illustrated in Figure III.59, where 2 μm grating was used as a primary mold to imprint Pd line gratings, over which finer gratings (~160 nm) were imprinted using a secondary mold (Figure III.59a). The temperature, pressure and time of imprinting were optimized such that the primary structure did not collapse while imprinting the secondary structure. As shown in Figure III.59b and c, the secondary lines are ~50 nm wide and ~25 nm tall over the primary line gratings of width ~1.04 μm after heat treatment. The shrinkage is not exactly the same as was observed for simple 2D imprinting (Figure III.55) as the imprinting conditions are slightly different.
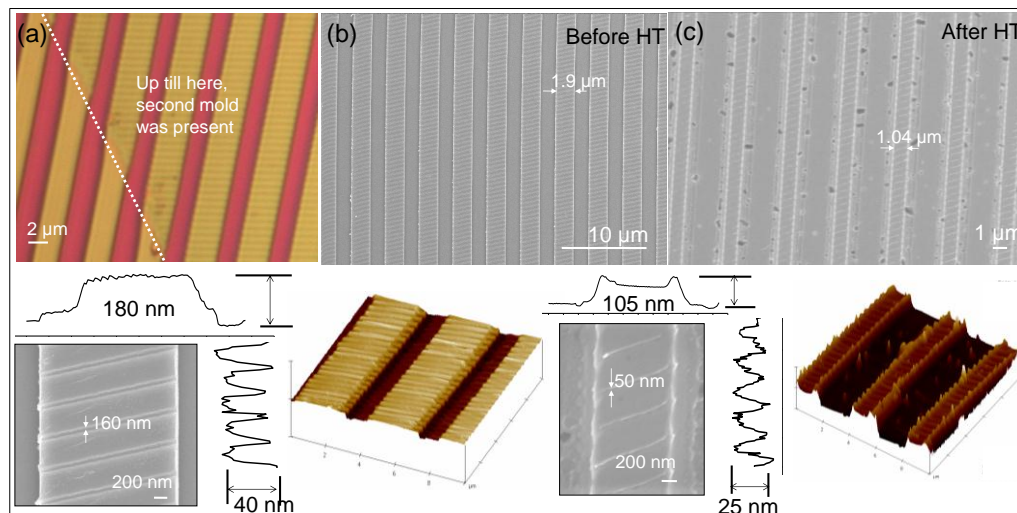
Figure III.59 (a) Optical image demonstrating large area of Pd hierarchical structures with a primary mold of 2 μm gratings and secondary mold of 250 nm gratings. SEM and AFM images of Pd hierarchical structures; (b) Before heat treatment with primary lines of 2 μm and secondary lines of 160 nm, and corresponding height of 180 nm and 40 nm respectively. (c) After heat treatment with primary lines of 1.04 μm and secondary lines of 50 nm, and corresponding height of 105 nm and 25 nm respectively.

Of late, metallic photonic crystals have been a subject of intense research owing to the advantage of the integration of plasmonics with photonics [123]. This has rendered the 3D and hierarchical structuring of metals quite interesting and many self-assembly as well as lithographic methods have been employed for this purpose. NSOM studies on such hierarchical structures have evidenced amazing optical devices [124,125] such as optical cavities, antennas, waveguides etc. Owing to the optical beam sizes ranging few μms in general, large area patterns with nanodomains are a stringent condition. Especially, woodpile or chiral structuring of metals at the nanoscale, creates optical bandgaps which are otherwise not possible [126]. Stacked patterns of the Pd gratings were created by MDNIL method. Initially, Pd thiolate was imprinted using a 2 μm grating mold and heat treated in a similar way as in Figure III.55. In the second imprinting step instead of using a Si mold, another as-imprinted (without heat treatment) grating of Pd (2 μm) was used as a mold for imprinting (Figure III.60a). Under the optimal applied pressure (25 bar) and temperature (130 °C), the Pd thiolate lines on the second mold melted and got transferred to the bottom substrate, during imprinting. Thus obtained patterns after transfer stacking can be subjected to heat treatment (Figure III.60b). Another round of transfer stacking was performed using double stacked Pd lines as substrate and freshly imprinted Pd thiolate grating as mold (Figure III.60c and d). Here, an analogy can be drawn with the adhesion driven transfer printing [127] where the adhesion of the transferred nanostructures can be switched between the host

and the substrate kinetically. Here, the transfer stacking is mediated due to the melting of Pd thiolate which facilitates the transfer to the bottom Pd lines. Importantly by MDNIL, the transfer stacking procedure is reproducible and can be done with even finer features. Figure III.60e and f show a 250 nm grating of Pd stacked over another 250 nm Pd grating as-imprinted and after heat treatment. Such stacked metal structures are of much demand as photonic crystals.
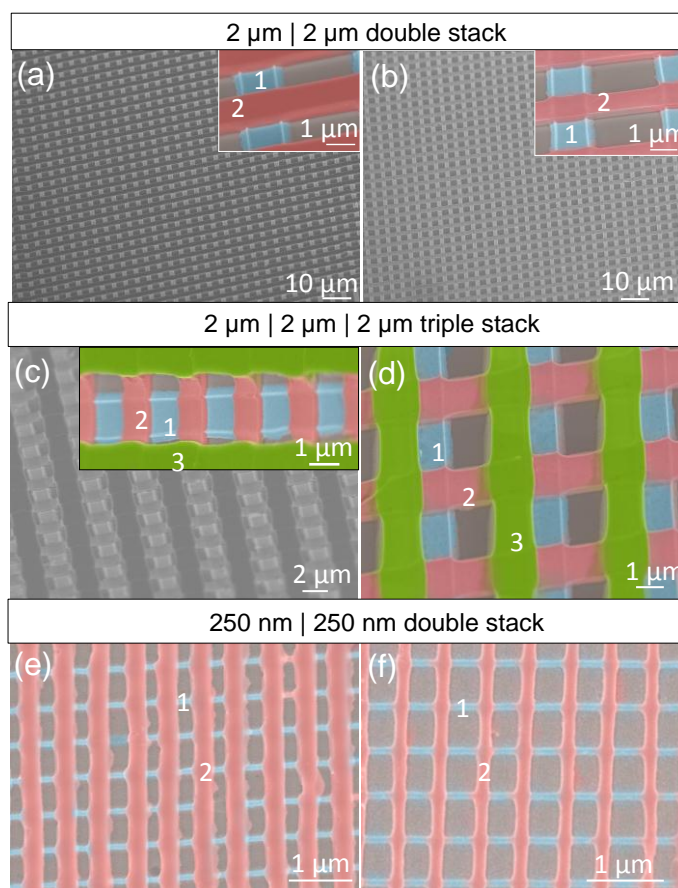
Figure III.60 Transfer stacking - (a) optical image of the transfer stacked 2 µm Pd lines with the insets showing magnified views, (b) 3D AFM image, (c) SEM of the same and (d) after heat treatment. (e) Transfer printed 3rd stack; inset shows magnified tilted view and (f) after heat treatment. A 250 nm grating stacked over another 250 nm grating (g) before and (h) after heat treatment. Images are false colored for illustration; blue colored (1st i.e., primary line grating), light red colored (2nd stack) and green colored (3rd stack).

All the direct imprinted structures till date have been patterned on flat substrates. Flexible substrates carrying such metal patterns find many applications as illustrated previously. But, when the flexible substrates are subjected to high temperature heat treatment (during thermolysis), they undergo degradation as they cannot withstand the temperature. In fact, this factor limits the imprintability of various direct write precursors onto flexible substrates owing to high processing temperatures. In order to circumvent this

problem, transfer imprinting method was employed. This method involves transferring the imprinted and thermolysed Pd patterns to a flexible substrate. Here the substrate chosen was polycarbonate (PC). PC possesses a glass transition temperature of Tg~150 °C. Utilising the Pd patterns on Si as mold (Figure III.61a and b) and PC as substrate, imprinting was performed. When PC substrate was taken through Tg, softened PC flowed into the channels thus contacting the Pd lines all over. After cooling down the setup, PC substrate got demolded carrying the transferred Pd lines on surface (Figure III.61c). The Pd line shown in cross-section in Figure III.62d clearly illustrates the PC in intimate contact with Pd on all the three sides. Embedding the Pd lines under the PC surface was achieved by heating the PC substrate carrying the Pd lines above the Tg. The PC flowed and covered the Pd lines all around thus embedding them. Due to the charging from the insulating PC substrate, cross section SEM was not possible. Optical images (Figure III.61e-h) taken from the top of the PC surface did not show any Pd lines. While focusing beneath the surface of PC, gratings were visible, revealing the embedded Pd lines (Figure III.61g). The transfer imprinting method is general and can be extended to transfer of any patterned materials to flexible substrates.
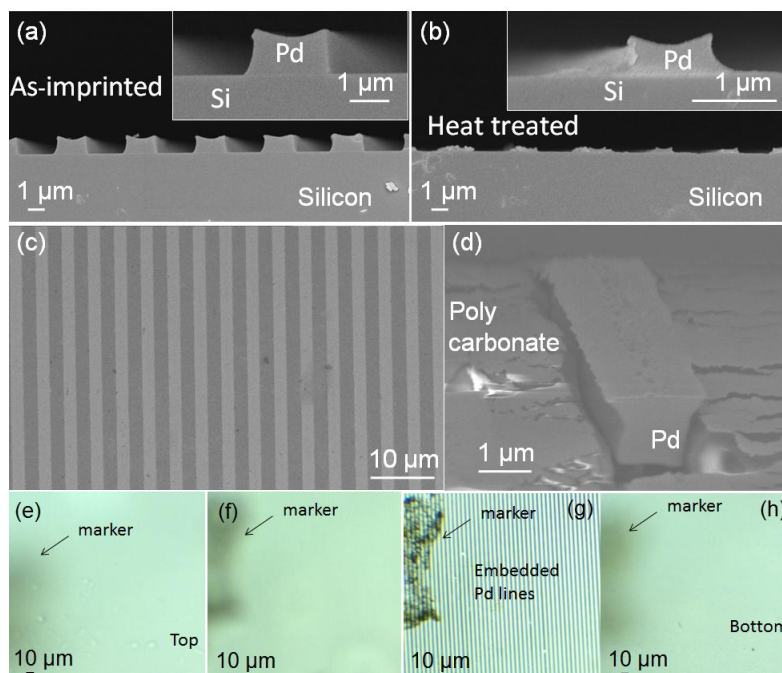
Figure III.61 Transfer imprinting of Pd lines to flexible substrate - cross-section SEM images of the 2 μm Pd gratings (a) as-imprinted and (b) after heat treatment, with magnified views in insets. (c) Pd lines transferred to polycarbonate (PC) substrate and (d) cross-sectional view showing the partially embedded Pd line into PC substrate. (e-f) Optical micrographs of the Pd lines embedded inside PC substrate. Images taken while different planes of the substrate were in optical focus, from top surface to the bottom surface of the PC. Arrow marks indicate the dust particle as an identification markers.

III.5. CONCLUSIONS

Single source precursors amenable to patterning are utilised in direct EBL, direct micromolding, direct nanoimprinting lithography techniques. Two classes of such single source precursors namely, metal anions complexed with tetraoctylammonium bromide (M-ToABr) and metal thiolates (M-Thiolates) were discussed in this part. These precursors can lead to thin nanocrystalline films and micro/nanopatterns of various materials involving a single process step namely thermolysis in a controlled atmosphere. The single source precursors' chemistry has been amended to produce various materials such as metals, metal sulfides, oxides, nitrides. Thin precursor films coated on a substrate serve as e-beam resists for direct writing due to extreme e-beam sensitivity of the hydrocarbon chain. The direct write method involves only a single (at best two) process steps with an excellent control on chemical purity and morphology of the resulting patterns. Direct write precursors possess better sensitivity, 3 orders of magnitude better as compared to conventional polymeric resists in EBL. Instead of coating as a film on a substrate, the precursor solutions may be flowed into micromold capillaries to produce patterns of the desired material covering large areas. Nanoimprinting was done to create versatile hierarchical and 3D patterned nanostructures using Pd thiolate.Simple and complex hierarchical patterns over cm^2 areas were achieved on flat as well as flexible substrates. The approach is generic and should be extendable to materials not explored in this study.

REFERENCES

[1]   K.-C. Kim, I.-B. Lee, D.-J. Kang, and S. Maeng, Etri Journal 29 (2007) 814.

[2]   M. Cavallini, C. Albonetti, and F. Biscarini, Advanced Materials 21 (2009) 1043.

[3]   P. R. Willmott and J. R. Huber, Reviews of Modern Physics 72 (2000) 315.

[4]   J. S. Ritch, T. Chivers, M. Afzaal, and P. O'Brien, Chemical Society Reviews 36 (2007) 1622.

[5]   J. J. Schneider, R. C. Hoffmann, J. Engstler, S. Dilfer, A. Klyszcz, E. Erdem, P. Jakes, and R. A. Eichel, Journal of Materials Chemistry 19 (2009) 1449.

[6]   M. S. M. Saifullah, K. R. V. Subramanian, D. J. Kang, D. Anderson, W. T. S. Huck, G. A. C. Jones, and M. E. Welland, Advanced Materials 17 (2005) 1757.

[7]   A. F. Roland, M. Alexander, H. Eberhardt, R. M. Michael, A. Oliver, M. Thomas, B. Eberhard, W. Sevil, R. P. Colin, and P. Simon, Chemistry - A European Journal 2 (1996) 1353.

[8]   P. Greco, M. Cavallini, P. Stoliar, S. D. Quiroga, S. Dutta, S. Zacchini, M. C. Iapalucci, V. Morandi, S. Milita, P. G. Merli, and F. Biscarini, Journal of the American Chemical Society 130 (2008) 1177.

[9]   R. Nomura, K. Kanaya, and H. Matsuda, Industrial & Engineering Chemistry Research 28 (2002) 877.

[10]   C. N. R. Rao and K. P. R. Pisharody, Progress in Solid State Chemistry 10 (1976) 207.

[11]   H. Fischmeister, Acta Chemica Scandinavica 13 (1959) 852.

[12]   B. D. Morreale, B. H. Howard, O. Iyoha, R. M. Enick, L. Chen, and D. S. Sholl, Industrial and Engineering Chemistry Research 46 (2007) 6313.

[13]   F. Gronvold and E. Rost, Acta Crystallographica 15 (1962) 11.

[14]   Hamilton, Hugh, Gavin, and Charles, International Patent (2007)

[15]   J. J. Bladon, A. Lamola, F. W. Lytle, W. Sonnenberg, J. N. Robinson, and G. Philipose, Journal of the Electrochemical Society 143 (1996) 1206.

[16]   A. Zubkov, T. Fujino, N. Sato, and K. Yamada, Journal of Chemical Thermodynamics 30 (1998) 571.

[17]   I. J. Ferrer, P. Diaz-Chao, A. Pascual, and C. Sanchez, Thin Solid Films 515 (2007) 5783.

[18]   H. Kyama and T. Iwata, Japanese Patent 08/095,209, 1996.

[19]   Y. Tonomura and J. Handa, Mitsubishi Paper Mills Ltd, Japanese Patent 03/126,035, 1991.

[20]   R. Yamamoto, Japanese Patent 61/215661, 1986.

[21]   F. Groenvold, E. F. Westrum Jr, and R. Radebaugh, Journal of Chemical and Engineering Data 14 (1969) 205.

[22]   F. R. Grønvold, Erling, Acta Chemica Scandinavica 10 (1956) 1620.

[23]   P. Diaz-Chao, I. J. Ferrer, J. R. Ares, and C. Sanchez, Journal of Physical Chemistry C 113 (2009) 5329.

[24]   P. O'Brien and J. Waters, Chemical Vapor Deposition 12 (2006) 620.

[25]   A. Birri, B. Harvey, G. Hogarth, E. Subasi, and F. UÇ§ur, Journal of Organometallic Chemistry 692 (2007) 2448.

[26]   S. Dey and V. K. Jain, Platinum Metals Review 48 (2004) 16.

[27]   N. Ghavale, S. Dey, A. Wadawale, and V. K. Jain, Organometallics 27 (2008) 3297.

[28]   M. C. Gather, A. Köhnen, A. Falcou, H. Becker, and K. Meerholz, Advanced Functional Materials 17 (2007) 191.

[29]   M. H. V. Werts, M. Lambert, J.-P. Bourgoin, and M. Brust, Nano Letters 2 (2002) 43.

[30]   M. T. Reetz, M. Winter, G. n. Dumpich, J. Lohau, and S. Friedrichowski, Journal of the American Chemical Society 119 (1997) 4539.

[31]   M. K. Corbierre, J. Beerens, and R. B. Lennox, Chem. Mater. 17 (2005) 5774.

[32]   T. J. Stark, T. M. Mayer, D. P. Griffis, and P. E. Russell, J. Vac. Sci. Technol., B 9 (1991) 3475.

[33]   M. Nedelcu, M. S. M. Saifullah, D. G. Hasko, A. Jang, D. Anderson, W. T. S. Huck, G. A. C. Jones, M. E. Welland, D. J. Kang, and U. Steiner, Advanced Functional Materials 20 (2010) 2317.

[34]   E. Kim, Y. Xia, and G. M. Whitesides, Nature 376 (1995) 581.

[35]   S. H. Ko, I. Park, H. Pan, C. P. Grigoropoulos, A. P. Pisano, C. K. Luscombe, and J. M. J. Frechet, Nano Letters 7 (2007) 1869.

[36]   O. F. Göbel, M. Nedelcu, and U. Steiner, Advanced Functional Materials 17 (2007) 1131.

[37]   M. J. Hampton, S. S. Williams, Z. Zhou, J. Nunes, D.-H. Ko, J. L. Templeton, E. T. Samulski, and J. M. DeSimone, Advanced Materials 20 (2008) 2667.

[38]   Su Hui Lim, M S M Saifullah, Hazrat Hussain, Wei Wei Loh, and H. Y. Low, Nanotechnology 21 (2010) 285303.

[39]   Q. Xu, B. D. Gates, and G. M. Whitesides, Journal of the American Chemical Society 126 (2004) 1332.

[40]   T. W. Odom, V. R. Thalladi, J. C. Love, and G. M. Whitesides, Journal of the American Chemical Society 124 (2002) 12112.

[41]   H. W. Li, B. V. O. Muir, G. Fichet, and W. T. S. Huck, Langmuir 19 (2003) 1963.

[42]   M. Geissler, J. M. McLellan, and Y. Xia, Nano Letters 5 (2005) 31.

[43]   C. M. Bruinink, M. Peter, P. A. Maury, M. De Boer, L. Kuipers, J. Huskens, and D. N. Reinhoudt, Advanced Functional Materials 16 (2006) 1555.

[44]   J. Kong, M. G. Chapline, and H. Dai, Advanced Materials 13 (2001) 1386.

[45]   M. A. Meitl, Z. T. Zhu, V. Kumar, K. J. Lee, X. Feng, Y. Y. Huang, I. Adesida, R. G. Nuzzo, and J. A. Rogers, Nature Materials 5 (2006) 33.

[46]   H. Mizuno and J. M. Buriak, Journal of the American Chemical Society 130 (2008) 17656.

[47]   A. L. Das, R. Mukherjee, V. Katiyer, M. Kulkarni, A. Ghatak, and A. Sharma, Advanced Materials 19 (2007) 1943.

[48]   S. Donthu, Z. Pan, B. Myers, G. Shekhawat, N. Wu, and V. Dravid, Nano Letters 5 (2005) 1710.

[49]   M. S. M. Saifullah, K. R. V. Subramanian, D. J. Kang, D. Anderson, W. T. S. Huck, G. A. C. Jones, and M. E. Welland, Advanced Materials 17 (2005) 1757.

[50]   G. Carotenuto, B. Martorana, P. Perlo, and L. Nicolais, Journal of Materials Chemistry 13 (2003) 2927.

[51]   M. Nakamoto, M. Yamamoto, and M. Fukusumi, Chemical Communications 15 (2002) 1622.

[52]   P. C. Hidber, W. Helbig, E. Kim, and G. M. Whitesides, Langmuir 12 (1996) 1375.

[53]   M. S. Hussain and E. O. Schlemper, Acta Crystallographica Section C-Crystal Structure Communications 43 (1987) 450.

[54]   P. Braunstein, H. Lehner, and D. Matt, Inorganic Synthesis 27 (1990) 218.

[55]   V. Belova, A. Khol'kin, and T. Zhidkova, Theoretical Foundations of Chemical Engineering 41 (2007) 743.

[56]   Y. J. Park and D. J. Fray, Journal of Hazardous Materials 164 (2009) 1152.

[57]   M. W. Mathias Brust, Donald Bethell, David J. Schiffrin and Robin Whyman, Journal of the Chemical Society, Chemical Communications 7 (1994) 801.

[58]   E. G. Castro, R. V. Salvatierra, W. H. Schreiner, M. M. Oliveira, and A. J. G. Zarbin, Chemistry of Materials 22 (2009) 360.

[59]   E. Coronado, A. Ribera, J. Garcia-Martinez, N. Linares, and L. M. Liz-Marzan, Journal of Materials Chemistry 18 (2008) 5682.

[60]   P. J. G. Goulet and R. B. Lennox, Journal of the American Chemical Society 132 (2010) 9582.

[61]   F. J. Ibanez and F. P. Zamborini, ACS Nano 2 (2008) 1543.

[62]   In addition, using the Au anionic complex with ToABr as a CVD precursor, there have been attempts to deposit Au nanoparticles by thermolysis at elevated temperatures (R. G. Palgrave and I. P. Parkin, Gold Bulletin 41 (2008) 66).

[63]   Y. Xia, Y. Xiong, B. Lim, and S. E. Skrabalak, Angewandte Chemie International Edition 48 (2009) 60.

[64]   T. Bhuvana and G. U. Kulkarni, ACS Nano 2 (2008) 457.

[65]   K. G. Thomas, J. Zajicek, and P. V. Kamat, Langmuir 18 (2002) 3722.

[66]   M. B. Mooiman, Precious Metals 1993 (1993) 411.

[67]   K. Kondo, T. Ourachi, T. Kaneiwa, and M. Matsumoto, Solvent Extraction Research and Development-Japan 7 (2000) 176.

[68]   L. E. Cox and D. G. Peters, Inorganic Chemistry 9 (1970) 1927.

[69]   The amount of carbon in the deposited Pt for ion- and electron beam-induced processes can vary in the range from 40–55% and 60–75% according to the ref (R. M.Langford, T. X. Wang and D.Ozkaya, Microelectronic Engineering (2007) 84, 784-788); for instance in the ref. (K. A. Telari, B. R.Rogers, H. Fang, L. Shen, R. A. Weller and D. N. Braski, Journal of Vacuum Science and Technology B (2002) 20, 590-595), 66% carbon is left behind in the Pt deposit.

[70]   D. S. Gardner, J. Onuki, K. Kudoo, Y. Misawa, and Q. T. Vu, Thin Solid Films 262 (1995) 104.

[71]   In contrast to literature reports which make use of additional sulfiding agents, Na_2S (T. G. Schaaff and A. J. Rodinone, Journal of Physical Chemistry B 107 (2003) 10416), here thermolysing in H_2 lead to the sulfidic phase. Without either of the two mentioned, a simple air treatment will yield Ag nanoparticles (G. Carotenuto, B. Martorana, P. Perlo, and L. J. Nicolais, Materials Chemistry 13 (2003) 2927).

[72]   V. D. Ashok, T. Ghoshal, and S. K. De, The Journal of Physical Chemistry C 113 (2009) 10967.

[73]   S. Strite and H. Morkoc, Journal of Vacuum Science & Technology B: Microelectronics and Nanometer Structures 10 (1992) 1237.

[74]   K. Suzuki, T. Kaneko, H. Yoshida, H. Morita, and H. Fujimori, Journal of Alloys and Compounds 224 (1995) 232.

[75]   S. Angappane, J. Park, Y. Jang, T. Hyeon, and J.-G. Park, Journal of Physics: Condensed Matter 20 (2008) 295209.

[76]   WO/2009/088522, MEDINA, Rolando, United States, 2009.

[77]   S. Yasin, D. G. Hasko, and H. Ahmed, Vol. 17, Marco Island, Florida (USA), 1999, p. 3390.

[78]   J. Marqués-Hueso, R. Abargues, J. Canet-Ferrer, S. d. Agouram, J. L. s. Valdés, and J. P. Martínez-Pastor, Langmuir 26 (2009) 2825.

[79]   M. K. Corbierre, J. Beerens, and R. B. Lennox, Chemistry of Materials 17 (2005) 5774.

[80]   J. K. W. Yang and K. K. Berggren, Journal of Vacuum Science & Technology B: Microelectronics and Nanometer Structures 25 (2007) 2025.

[81]   Z. L. Wang, Journal of Physics: Condensed Matter 16 (2004) R829.

[82]   V. Auzelyte, H. Sigg, B. Schmitt, and H. H. Solak, Nanotechnology 21 (2010) 215302.

[83]   O. F. Goìˆbel, D. H. A. Blank, and J. E. ten Elshof, ACS Applied Materials & Interfaces 2 (2010) 536.

[84]   J. Yang, E. Sargent, S. Kelley, and J. Y. Ying, Nature Materials 8 (2009) 683.

[85]   P. John Thomas, A. Lavanya, V. Sabareesh, and G. U. Kulkarni, Proceedings of the Indian Academy of Sciences: Chemical Sciences 113 (2001) 611.

[86]   P. J. Thomas, A. Lavanya, V. Sabareesh, and G. U. Kulkarni, Proc. Indian Acad. Sci., Chem. Sci. 113 (2001) 611.

[87]   M. Nakamoto, M. Yamamoto, and M. Fukusumi, Chemical Communications (2002) 1622.

[88]   K. Osakada and T. Yamamoto, Journal of the Chemical Society, Chemical Communications (1987) 1117.

[89]   G. Carotenuto, L. Pasquini, E. Milella, M. Pentimalli, R. Lamanna, and L. Nicolais, European Physical Journal B 31 (2003) 545.

[90]   S. Ono, T. Osaka, K. Naitoh, and Y. Nakagishi, Journal of the Electrochemical Society 146 (1999) 160.

[91]   C. H. Yang, Y. Y. Wang, and C. C. Wan, Journal of the Electrochemical Society 146 (1999) 4473.

[92]   H. S. Chen, Y. J. Huang, and C. C. Wan, Plating and Surface Finishing 90 (2003) 50.

[93]   T. Bhuvana, L. Gregoratti, S. Heun, M. Dalmiglio, and G. U. Kulkarni, Langmuir 25 (2008) 1259.

[94]   Y. Sun and J. A. Rogers, Advanced Materials 19 (2007) 1897.

[95]   A. Nathan and B. R. Chalamala, Proceedings of the IEEE 93 (2005) 1235.

[96]   A. Nathan and B. R. Chalamala, Proceedings of the IEEE 93 (2005) 1391.

[97]   R. H. Reuss, B. R. Chalamala, A. Moussessian, M. G. Kane, A. Kumar, D. C. Zhang, J. A. Rogers, M. Hatalis, D. Temple, G. Moddel, B. J. Eliasson, M. J. Estes, J. Kunze, E. S. Handy, E. S. Harmon, D. B. Salzman, J. M. Woodall, M. A. Alam, J. Y. Murthy, S. C. Jacobsen, M. Olivier, D. Markus, P. M. Campbell, and E. Snow, Proceedings of the IEEE 93 (2005) 1239.

[98]   A. J. Baca, J. H. Ahn, Y. Sun, M. A. Meitl, E. Menard, H. S. Kim, W. M. Choi, D. H. Kim, Y. Huang, and J. A. Rogers, Angewandte Chemie - International Edition 47 (2008) 5524.

[99]   O. Cherniavskaya, A. Adzic, C. Knutson, B. J. Gross, L. Zang, R. Liu, and D. M. Adams, Langmuir 18 (2002) 7029.

[100] J. N. Lee, C. Park, and G. M. Whitesides, Analytical Chemistry 75 (2003) 6544.

[101] C. Y. Hui, A. Jagota, Y. Y. Lin, and E. J. Kramer, Langmuir 18 (2002) 1394.

[102] E. Favre, European Polymer Journal 32 (1996) 1183.

[103] E. Boisselier and D. Astruc, Chemical Society Reviews 38 (2009) 1759.

[104] C. J. Murphy, A. M. Gole, J. W. Stone, P. N. Sisco, A. M. Alkilany, E. C. Goldsmith, and S. C. Baxter, Accounts of Chemical Research 41 (2008) 1721.

[105] N. L. Rosi, D. A. Giljohann, C. S. Thaxton, A. K. R. Lytton-Jean, M. S. Han, and C. A. Mirkin, Science 312 (2006) 1027.

[106] M. Brust, Nature Materials 4 (2005) 364.

[107] C. N. R. Rao, G. U. Kulkarni, P. J. Thomas, and P. P. Edwards, Chemical Society Reviews 29 (2000) 27.

[108] P. J. Thomas, G. U. Kulkarni, and C. N. R. Rao, The Journal of Physical Chemistry B 104 (2000) 8138.

[109] W. Sparreboom, A. van den Berg, and J. C. T. Eijkel, Nature Nanotechnology 4 (2009) 713.

[110]   A. Akey, C. Lu, L. Yang, and I. P. Herman, Nano Letters 10 (2010) 1517.

[111]   M. D. Austin, H. Ge, W. Wu, M. Li, Z. Yu, D. Wasserman, S. A. Lyon, and S. Y. Chou, Applied Physics Letters 84 (2004) 5299.

[112]   L. Su Hui, M. S. M. Saifullah, H. Hussain, W. W. Loh, and L. Hong Yee, Nanotechnology 21 (2010) 285303.

[113]   T. Kunitake and S.-W. Lee, Analytica Chimica Acta 504 (2004) 1.

[114]   H.-H. Park, D.-G. Choi, X. Zhang, S. Jeon, S.-J. Park, S.-W. Lee, S. Kim, K.-d. Kim, J.-H. Choi, J. Lee, D. K. Yun, K. J. Lee, H.-H. Park, R. H. Hill, and J.-H. Jeong, Journal of Materials Chemistry 20 (2010) 1921.

[115]   C.-C. Liang, M.-Y. Liao, W.-Y. Chen, T.-C. Cheng, W.-H. Chang, and C.-H. Lin, Opt. Express 19 (2011) 4768.

[116]   P. J. Thomas, A. Lavanya, V. Sabareesh, and G. U. Kulkarni, Proceedings of the Indian Academy of Sciences-Chemical Sciences 113 (2001) 611.

[117]   G. Ctistis, E. Papaioannou, P. Patoka, J. Gutek, P. Fumagalli, and M. Giersig, Nano Letters 9 (2008) 1.

[118]   R. Wang, C. Wang, W.-B. Cai, and Y. Ding, Advanced Materials 22 (2010) 1845.

[119]   Y. Tan, J. Gu, X. Zang, W. Xu, K. Shi, L. Xu, and D. Zhang, Angewandte Chemie International Edition 50 (2011) 8307.

[120]   P. Ball, NATURE 400 (1999) 507.

[121]   Z. Fengxiang and L. Hong Yee, Nanotechnology 17 (2006) 1884.

[122]   M. Bieda, E. Beyer, and A. F. Lasagni, Journal of Engineering Materials and Technology 132 (2010) 031015.

[123]   I. El-Kady, M. M. Sigalas, R. Biswas, K. M. Ho, and C. M. Soukoulis, Physical Review B 62 (2000) 15299.

[124]   J.-S. Kim and J.-J. Kim, Journal of Lightwave Technology 22 (2004) 840.

[125]   S. Grilli, S. Coppola, V. Vespini, F. Merola, A. Finizio, and P. Ferraro, Proceedings of the National Academy of Sciences 108 (2011) 15106.

[126]   R. Hillebrand and U. Gösele, Science 305 (2004) 187.

[127]   M. A. Meitl, Z.-T. Zhu, V. Kumar, K. J. Lee, X. Feng, Y. Y. Huang, I. Adesida, R. G. Nuzzo, and J. A. Rogers, Nature Materials 5 (2006) 33.

PART IV

Device Fabrication with Nanomaterials*

SUMMARY

Six prototype devices have been fabricated using functional nanostructures presented in Parts II and III. A practically useful semi-transparent strain gauge with high gauge factor was fabricated using Pd μ-stripes fabricated via micromolding. The strain sensing mechanism originates from the varying strength of the interparticle coupling with strain. A flexible H_2 sensor based on Pd films and patterns was devised to study the mechanism of H_2 sensing. The sensor could sense as low as 50 ppm of gas concentration. Hydrophobic hierarchical structures with anisotropic wetting have been formulated using the nanoimprinted Pd structures. From the Au nanocrystalline stripes obtained by direct write EBL, a nanoscale half wave rectifier with high rectification ratio and a tunable threshold voltage was obtained. Single crystalline Au microplates described in Part II, have been employed as top contacting electrodes for examining electrical transport through monolayers of self-assembled molecules and a large number of vertically grown semiconductor nanowires, in capacitor geometry. The micro-sandwich device stands as a highly stable molecular test-bed providing ample room for dynamic thermal and mechanical analysis of molecules. Moreover, the method of top-contacting can be generalized for various molecules and 1D-nanoobjects.

IV.1 FLEXIBLE STRAIN SENSORS AND CONDUITS

IV.1.1 Introduction

Flexible electronics, in contrast to conventional electronics, makes use of material components with wide range of response to bending, stretching or twisting; either respond sensitively or strive remain constant [1]. While those respond are to be found in device parts such as touch screen, the latter are important in conduits and interconnects. In a laboratory setting, the strain gauge factor distinguishes the two performances. The gauge factor for a resistive sensor is the relative change in its resistance divided by the strain applied [2]. Obviously in a flexible circuit, the conduits and interconnects are expected to exhibit near zero gauge factor over repeated bending, unlike user interface components for which high gauge factors are desirable [3,4]. The literature is abundant with examples of both classes of materials. Based on constant resistance interconnects, Rogers and coworkers fabricated foldable inorganic light emitting diodes on a PET substrate capable of functioning at bent radii down to 0.7 mm with no change in performance [5]. Likewise, GaN high electron mobility transistors [6], graphene FETs [7], GaAs MESFETs [8], solar cells [9,10], photodetectors [11], resistance switching memory devices [12], nanogenerators [13,14] ultrahigh frequency electronics [15] etc., have been fabricated on flexible substrates. Transparent conducting electrodes for organic solar photovoltaics have been made using graphene on a PET substrate where, the conductance of the electrodes decreased by only 7.9% after 100 bending cycles [16]. Various semiconductor nanostructures have also been explored for the purpose of high performance flexible electronics [17].

The sensors with high strain gauge factors are important in flexible electronics as well as in stand-alone devices. The latter have been in use for structural health monitoring [18] of critical infrastructures - highways, buildings, bridges, aircraft, ships, and pipelines, particularly during earthquakes, hurricanes, and other natural disasters. As regards resistive sensors (capacitive sensors and optical sensors being examples of other types of strain sensors), thin metal films have served as strain gauges for decades [19], and recently bimetal alloys (e.g., Ni-Ag [20], Ni-Cr [21]) have replaced them for want of better adherence and corrosion resistance. Fibre-concrete composites [22] are yet another class of strain sensors. Microcrystalline and amorphous Si strain sensors are also well known [23]. Conducting polymer based sensors have been developed [24] and in another example, conductive-polymer strain sensors for touch input sheets have been fabricated which are sensitive to bending radius of 20 mm [25]. In this context, several nanomaterials are being projected for

highly sensitive sensors. Single ZnO nanowire [3], single walled carbon nanotubes [26], networked Au nanoparticle coatings [27], self-assembled monolayers of nanoparticles [28,29], have served as sensor elements. Bridging ZnO nanorods into circuits, strain driven transistors have been fabricated with high on-off ratios particularly at strains >1.4% [30]. ZnO embedded paper composite is shown to work as strain sensor with a gauge factor of ~21 [31].

IV.1.2 Scope of the present investigation

Metal or metal-based strain gauges albeit low gauge factors (2-5) are preferred due to their temperature stability. In addition, metal based sensors usually have low operating voltages. In order to improve the gauge factor, nanoparticulate metal structures have to be employed as sensor element [32]. Here the fabrication and performance of patterned Pd μ-stripes (described in Part III) are investigated, which based on the heat treatment employed during patterning, should serve as highly sensitive strain sensor or as reliable conduits. The molding can be carried out under varying thermolysis conditions, in order to realize the strain sensing action. As the device consists of grating structures, it can be reasonably transparent.

IV.1.3 Experimental details

A flexible polyimide (~20 μm thick) was used as a substrate for molding Pd μ-stripes. Polyimide was cleaned by sonicating in acetone, isopropyl alcohol and double-distilled water and dried under flowing argon. The polydimethylsiloxane (PDMS) stamp fabrication and the precursor ink preparation are discussed in Part III.3. Approximately, 60 μL of the Pd hexadecylthiolate, $Pd(SC_{16}H_{33})_2$ solution (10mM in toluene) was dropped at one edge of the PDMS stamp kept on the substrate to fill the channels spontaneously by capillary action. The set up was gradually heated on a hot plate to reach the desired temperature (180, 195, 210 or 230 °C) and was held for 30 min. Following cooling to room temperature, the stamp was removed leaving behind the patterns on the substrate. Au contact pads were deposited using a shadow mask of 6 μm width. Metallic contacts were drawn from the Au pads using silver epoxy (SPI suppliers, USA) and the resistance measurements were done using a digital multimeter (TestLink) with computer control.

IV.1.4 Results and discussion

Pd μ-stripes were patterned onto a flexible polyimide substrate by direct micromolding. Pd hexadecylthiolate in toluene (10 mM) served as a precursor for molding using a PDMS stamp (see scheme in Figure IV.1a), which upon thermolysis at 195 °C led to

nanocrystalline Pd µ-stripes inside the microchannels (nanoparticle size, 8±2 nm, see Figure IV.2). As is well known, polyimide can easily withstand such temperatures without losing its flexibility [9]. Although the thermolysis of the precursor is expected to remove the hydrocarbon by desorption [33], depending on the temperature, some amount of carbon is usually left behind (see Table IV.1). For the 195 ºC treatment, it is as high as 58.6 at%.
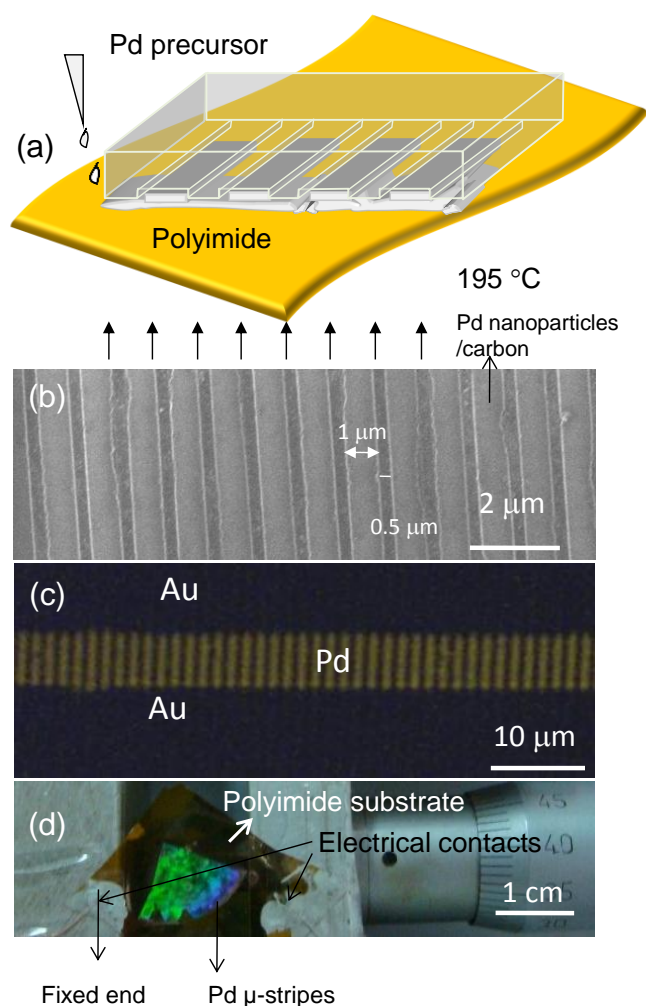
Figure IV.1 (a) Schematic showing direct micromolding of Pd hexadecylthiolate onto a polyimide substrate. (b) SEM image of the formed stripes on polyimide substrate. (c) An optical image of the Pd µ-stripes across the Au electrodes. (d) A photograph of the device used for bending experiments. The color from diffraction of ambient light by the µ-stripes are visible.

In this sense, the Pd µ-stripes are nanocomposites of Pd nanoparticles in carbon matrix (*vide infra*). The formed µ-stripes were ~1.1 µm wide with a spacing of ~400 nm, in conformity with the PDMS mold (Figure IV.1b). A pair of Au electrodes was deposited onto the µ-stripes by shadow masking such that as many as ~7500 stripes ran perpendicular to the 6 µm gap (Figure IV.1c). Figure IV.1d shows a photograph of the fabricated flexible strain sensor device with µ-stripes exhibiting brilliant colors in ambient light because of diffraction.
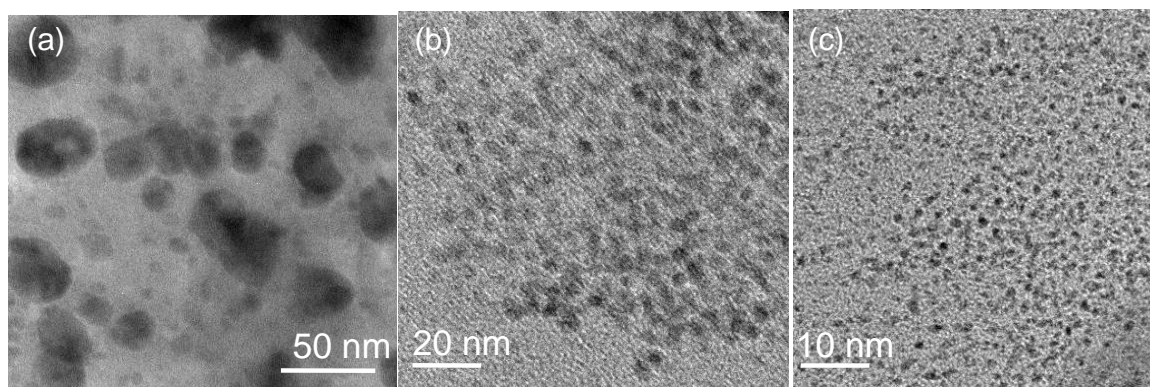
Figure IV.2 Transmission electron microscopy (TEM) images of the Pd nanoparticles obtained by thermolysing the Pd hexadecylthiolate at (a) 230 °C, (b) 195 °C and (c) 180 °C.

Table IV.1 Carbon content in the circuits with the corresponding thermolysis temperatures.

Sl. No.	Thermolysis temperature (°C)	Carbon content from EDS (%)
1	230	37.7
2	210	46.9
3	195	58.6
4	180	62.5

The resistance of the sensor device was measured in the ambient at room temperature for varying bent radii, under both tension and compression (Figures IV.3a and b). With the device held flat, the collective resistance of the stripes was 4.34 MΩ. When the µ-stripes were subjected to tensile strain (Figure IV.3a) - the bending radius decreasing from ∞ (flat) to below 0.5 cm, the resistance of the device gradually increased to 6.82 MΩ as shown in Figure IV.3c. On the other hand, under compressive strain, the resistance of the device decreased gradually to 2.48 MΩ also shown in Figure IV.3c. The release of either strain brought the device back to its original flat position with characteristic resistance. Notably the change in the resistance is not linear as is observed in conventional metal strain gauges (*vide infra*). The change in resistance expressed as normalized values are shown in Figure IV.3d against % strain for the µ-stripes obtained by thermolysis at 195 °C. The slope of the plot is the gauge factor that defines the performance of the sensor device. For the data shown in Figure IV.3d, the gauge factor was estimated to be ~390 for tensile strain and ~249 for compressive strain, which are commendable values. The gauge factor values obtained from the µ-stripes are considerably higher compared to conventional metal and alloy strain gauges (1-5). Further, the sensor is remarkably sensitive to even small strains like ~0.09%.
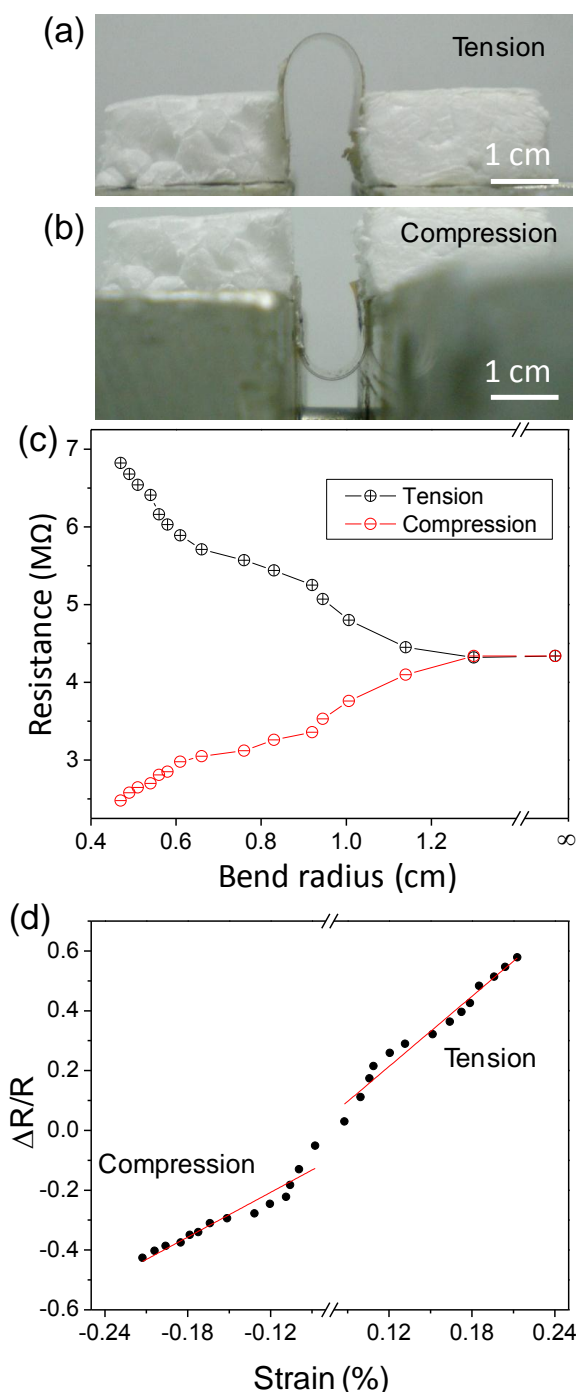
Figure IV.3 Digital photographs of the device with Pd μ-stripes (thermolysis temperature, 195 °C) under (a) tension and (b) compression. One end of the device was moved with the aid of a screw gauge (see Figure IV.1d) while the other end was held fixed. (c) Variation in resistance with bend radius during tension and compression. (d) Normalized change in resistance as a function of strain. The % strain (ε) was calculated as $\varepsilon = d/2r$ [25], d being the substrate thickness and r, the radius of curvature.

Low temperature conductance measurements revealed the activation energy for the transport to be ~ 25 meV (Figure IV.4). This value is in line with the activation energies obtained for metal-containing diamond-like-carbon films [34].
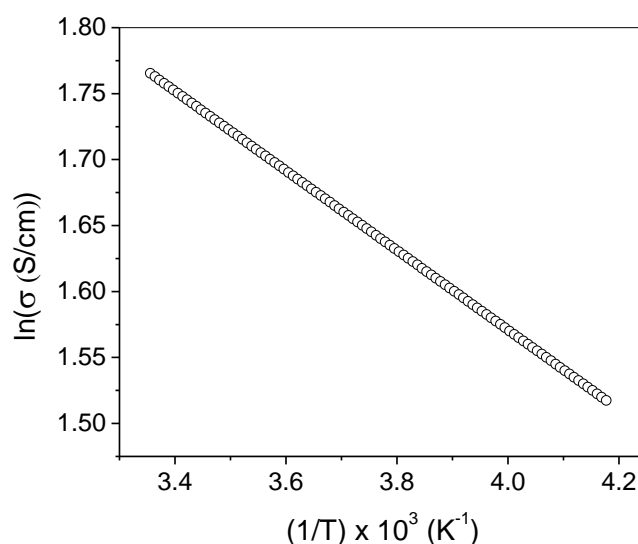
Figure IV.4 Arrehenius plot of conductance for Pd-thiolate film obtained by thermolysis at 195 °C. The activation energy from the slope is found to be ~25 meV.
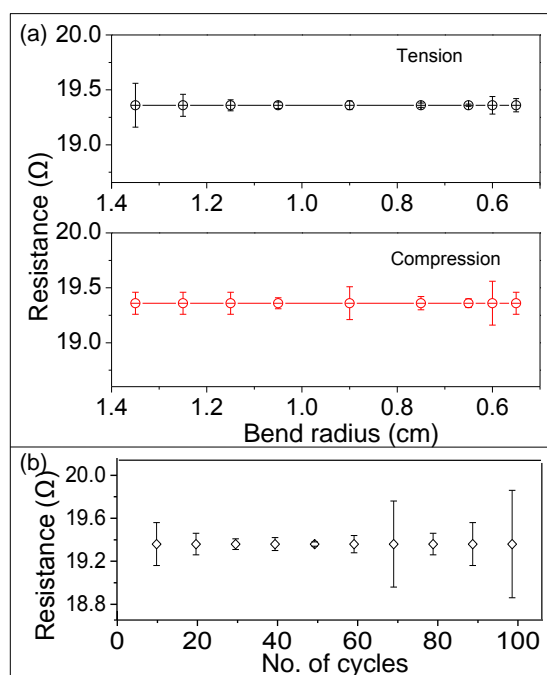
Figure IV.5 Pd μ-stripes obtained from 230 °C thermolysis exhibiting near constant resistance (a) for different bend radii under tension and compression and (b) over many cycles at a tensile bend radius of 1.1 cm. The error bars stands for the changes in the resistance value during the measurement.

The results obtained for sensors produced with different thermolysis temperature are discussed further on. Higher temperatures (230-250 °C) produce metallic stripes composed of larger nanoparticles (Figure IV.2), with conductivity close to that of the bulk Pd, with only little carbon left behind (see Table IV.1). When molding was carried out on the flexible substrate, the obtained stripes were metallic as expected but interestingly, showed no

response to bending. Indeed, with either strain, the resistance remained nearly constant at its base value (19.4±0.2 Ω) (Figure IV.5a). Interestingly, the μ-stripes were stable even after 100 cycles of bending (Figure IV.5b). This observation is well contrasting with the sensor action shown in Figure IV.3.

It was observed in separate experiments that the stripes produced with thermolysis temperatures in the range 195-230 °C were poorly conducting and exhibited little response to strain. The stripes obtained from a 180 °C treatment were not only highly insulating but also were poorly sensing the strain (Figure IV.6). These results are shown in Figure IV.7 and discussed below.
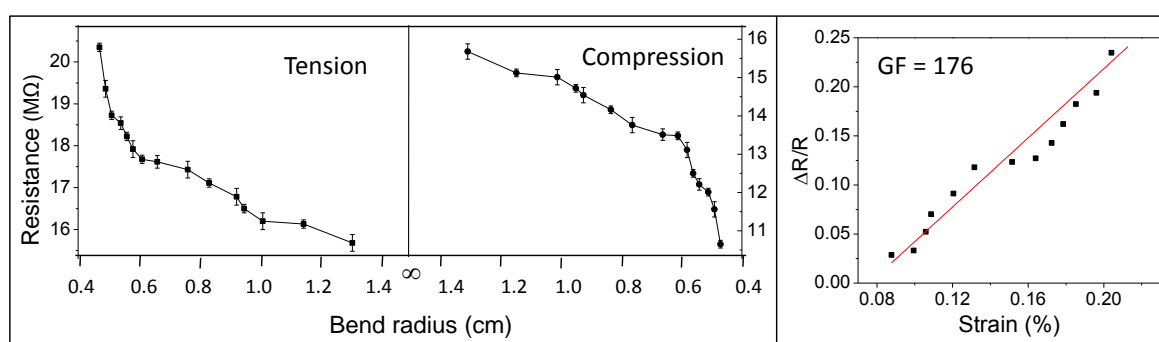
Figure IV.6 Strain response of the Pd μ-stripes obtained by micromolding at 180 °C, under tensile and compressive strains. The base resistance of the stripes is ~15.65 MΩ and the gauge factor for tensile strain is ~176.

As shown in Figures IV.3 and IV.5, the temperature of thermolysis decides the electrical property of the μ-stripes and thus the sensing ability. Thermolysis influences the constitution of the μ-stripe in two ways namely, the Pd nanoparticle size and the nature of the carbon matrix that is left behind after thermolysis. The decomposition of Pd thiolate [35,36] occurs by reductive elimination of thiol molecules leaving behind Pd as revealed by thermogravimetric analysis (Figure III.24 in Part III). The thiol molecules essentially undergo homolytic dissociation and desorb as disulfide molecules [35,36]. However, when the temperature is not high enough, partial decomposition may be expected where Pd nanoparticles are to be found amidst carbonaceous species, as shown by Raman measurements as well as by SEM and STEM (see Figure IV.8). Thus at 195 °C, only small nanoparticles are produced (~6 - 10 nm, Figure IV.2). There is discernible contrast between SEM and STEM images from this sample, although individual nanoparticles could not be made out in carbon matrix due to the small size (Figure IV.8b and c).
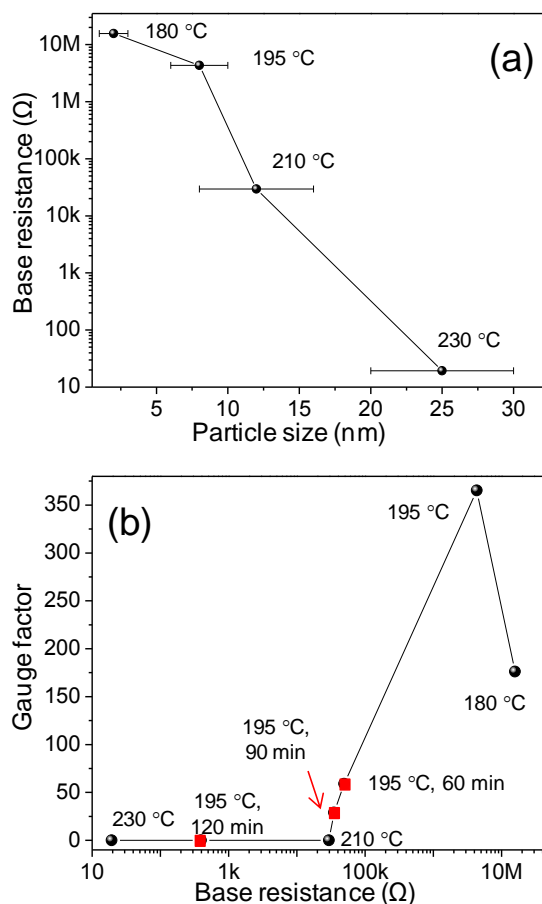
Figure IV.7 (a) Strain sensor base resistance (resistance while being flat) vs Pd particle size in µ-stripes. (b) Gauge factor as a function of the base resistance of Pd µ-stripes. The thermolysis temperatures used for producing the stripes are indicated alongside (time, 30 min). Three data points (squares) in (b) refer to thermolysis at 195 °C for 60, 90 and 120 min.

Further, at this temperature the hydrocarbon decomposition appears to be incomplete and as a result, the overall carbon content remains comparable to the precursor state itself (58.6 at%, Table IV.1). In the Raman spectrum (Figure IV.8a), two broad peaks of carbon were observed corresponding to D peak around 1360 cm^{-1} and G peak at around 1584 cm^{-1}. Both the bands are broader in the case of the film thermolysed at 195 °C compared to the one thermolysed at 230 °C, suggesting the presence of a significant portion of amorphous carbon in the deposited layer. Also, there is considerable intensity associated with the D-band, related to the degree of disorder from the sp^3 hybridized carbon [37] which is essentially non-conducting. The particle size increased vividly with the thermolysis temperature while the resistance of the stripes decreased (Figure IV.7a). Thus, the µ-stripes exhibit a wide range of resistance depending on the thermolysis temperature. The stripes

resulting from the 230 °C thermolysis are essentially metallic (~19.3 Ω, Figure IV.3d) and exhibited no change in resistance with change in bend radius which means that the gauge factor is zero in this case. These properties owe much to the bigger Pd nanoparticles (~20-30 nm, Figure IV.2) and less carbon (37.7 at%), a good fraction of it being sp^2 as evident from the Raman data (Figure IV.8a). The intensity increase of the G peak originates from the formation of conductive sp^2 carbon atoms resulting in higher conductivity [37]. The ratio I(D)/I(G) measures the sp^3/sp^2 carbon [38]. As can be readily seen from the spectra, I(D)/I(G) ratio decreases from 0.63 to 0.5, sp^3 content decreases and sp^2 content increases in the film thermolysed at 230 °C.
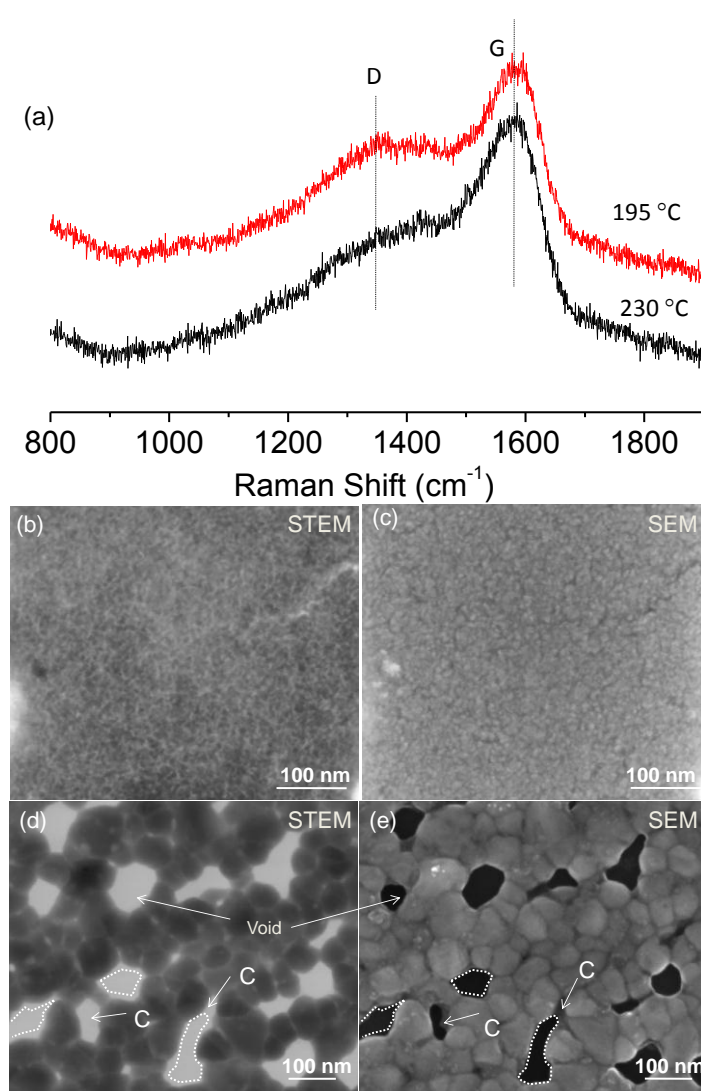
Figure IV.8 (a) Raman spectra of the carbon species obtained following thermolysis of the Pd precursor. (b, d) STEM and (c, e) SEM images of the Pd nanoparticle/carbon matrix obtained at thermolysis temperatures of 195 °C and 230 °C respectively. Areas marked by the dashed line indicate the boundaries of void regions. 'C' indicates carbonaceous matrix surrounding Pd nanoparticles connecting them.

Under STEM (Figure IV.8e), Pd nanocrystals revealed themselves as dark features gently separated from each other with light-grey regions marking the boundaries. When compared with the SEM image in Figure IV.8d, it is clear that the particle boundaries contain a lighter material around, which going by the EDS data, must be a carbonaceous species. The presence of a carbonaceous layer around Pd nanocrystals is seen vividly in the void regions, as marked by dashed lines. Thus, the voids look bigger in STEM than in SEM. The carbonaceous species appears to be loosely bound, which may get washed away in solvents as was the case while preparing for TEM measurement. Thus, the presence of carbon around the Pd nanoparticles is clearly seen from the STEM images (Figure IV.8a and b). This was also evident in the case of 210 °C treated sample (Figure IV.9). The stripes resulting from the 210 °C thermolysis exhibit a slightly higher resistance (20 kΩ) than those obtained from 230 °C thermolysis, as the metal particles are relatively smaller, ~8-16 nm (see Figure IV.7a). The surrounding carbon may be less sp^2 in nature. Interestingly, the applied strain has only little influence on their resistance with the estimated gauge factor of 0.11 (see Figure IV.7b). The thermolysis time also seems to have an influence of the particle size and the nature of carbon (see square data points in Figure IV.7b). Among the different samples, when the time duration was increased from 30 min to 60, 90 and 120 min at 195 °C, the base resistance decreased to 49.3, 35.0 and 0.39 kΩ, respectively with the corresponding gauge factors of 59, 29 and 0.1.
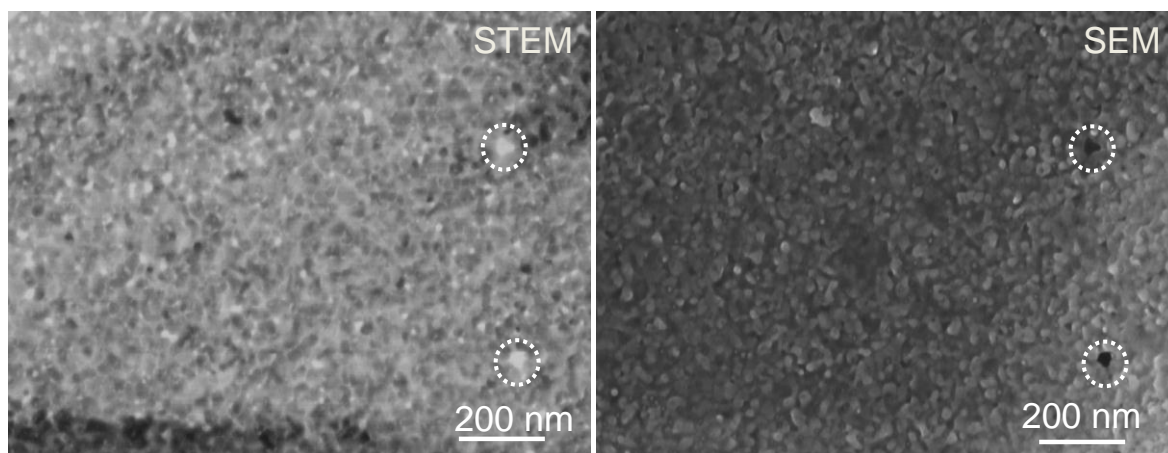
Figure IV.9 STEM and SEM images of Pd nanoparticles obtained at 210 °C thermolysis. The voids marked by circles look bigger in STEM as the carbonaceous material is transparent to e-beam.

Given the constitution of these µ-stripes, the strain seems to induce a change in the electronic coupling between the nanoparticles. With the µ-stripes obtained from the 195 °C thermolysis, the scenario is so well set with the nanoparticle size and the nature and content

of carbon that, the electronic coupling becomes most sensitive to any tiny change in the nanoparticle environment (see schematic illustration in Figure IV.10). Also, the resistance change with strain resembles closely the exponential nature of a tunnel junction. This is relatively more expressed in the tensile strain as the nanoparticles move away from each other and the coupling becomes weaker. In the compressive regime, the nanoparticles are forced to come closer, which because of the surrounding carbon matrix is hindered more so at very short distances. This observation is in line with Vossmeyer et al. [27], who found that the tensile strain brought larger changes in resistance than compressive strain in the case of Au nanoparticle networks. This was attributed to the dislocations which are produced when the interparticle distance can no longer be buffered by the organic material between the metal cores. Steric repulsion and other interactions may dominate this regime.
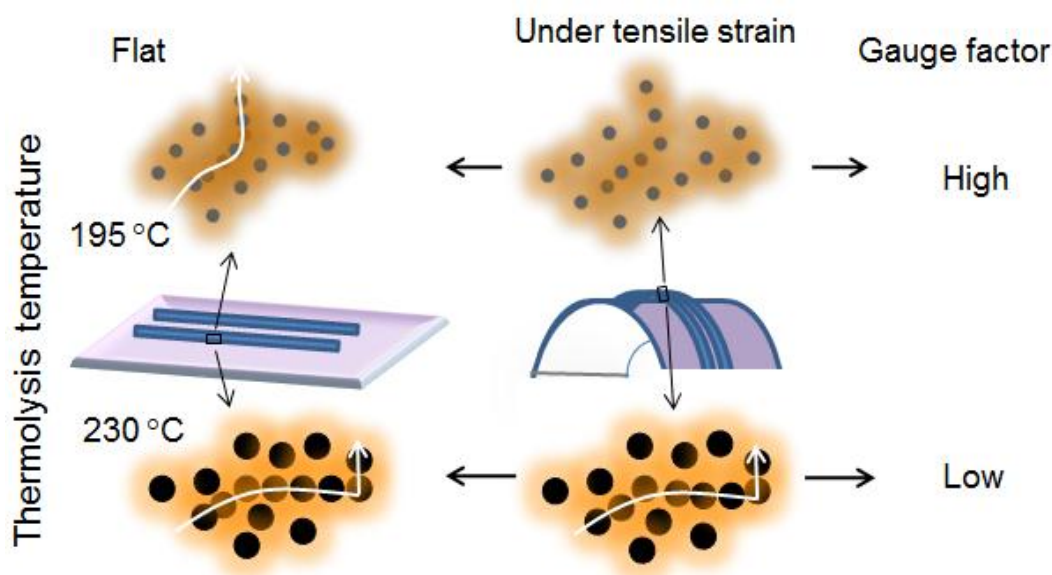
Figure IV.10 Schematic showing the Pd nanoparticle environment in the µ-stripes patterned on a polyimide shown on flat and bent substrates. Lower thermolysis results in smaller Pd particles surrounded with less conducting carbon species. While there may be higher number of conducting paths (shown by white arrow), they easily break open under tensile strain. The opposite situation may be considered for compression strain. Higher thermolysis temperatures give rise to bigger particles with well conducting carbon. In this case, the conducting paths are less affected during strain.

If the base resistance becomes even higher as in the case of stripes resulting from 180 °C (see Figure IV.7), the interparticle coupling is nearly lost making the sensing action less effective, as the particle size for this sample is much smaller, ~2 ±1 nm (see TEM image in Figure IV.2c). The results presented here may be compared with a strain sensor from the literature which was based on tungsten nanoparticles embedded in amorphous carbon [39]. In the latter, decreasing metal density of nanoparticles led to an increase in the gauge factor,

the maximum value being 30. Another important aspect is the µ-stripe/electrode interface. In a strain sensor, ohmic contact of the electrodes with sensing elements is highly desirable [40] so that the observed changes in resistance arise mainly from the sensing element without the influence of the contacts. In the present case i.e. Pd µ-stripes, the linear I–V characteristics (Figure IV.11) obtained are typical of an ohmic contact. In the case of sample treated at 230 °C which led to highly conducting Pd µ-stripes (results shown in Figure IV.5), the resistance did not change with bending, the standard deviation being less than ~0.2 Ω for different bend radii (Figure IV.5a), clearly indicating the reliability of the contacts. As the Au electrodes were made by the same method in all cases (by thermal evaporation of Au onto the stripes), the contacts should be similar in all cases.
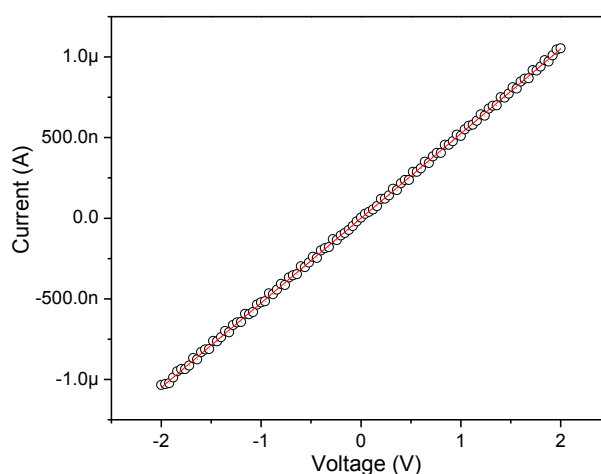
Figure IV.11 Typical current-voltage characteristics of Pd nanocrystalline sample thermolysed at 195 °C, with a base resistance of 2 MΩ.

Instead of µ-stripes, films derived from thermolysis at 195 °C have been tried out (Figure IV.12). Pd film on polyimide substrate was prepared by drop coating the precursor and subjecting it to thermolysis at 195 °C. Although the film exhibited a comparable resistance value as the µ-stripes, the obtained gauge factor was way below. The gauge factor for tension is 0.1 and for compression is 0.3. Further, the film failed to regain its original resistance, when released to flat condition from the tensile strain. This observation emphasizes the importance of molding the sensor element in the form of µ-stripes. The confinement of the material in the latter perhaps leads to a better translation of the strain into change in resistance. Table IV.2 lists the performance parameters of typical strain sensors reported in the literature. For example, a strain sensor based on a single SWNT exhibited gauge factor of 269 at a working voltage of 5 V [26]. ZnO nanorod based strain sensor with very high gauge factor was found to operate at 2 V [41]. In contrast, the sensor reported here typically works at 0.2 V! The fabrication process is also much simpler.
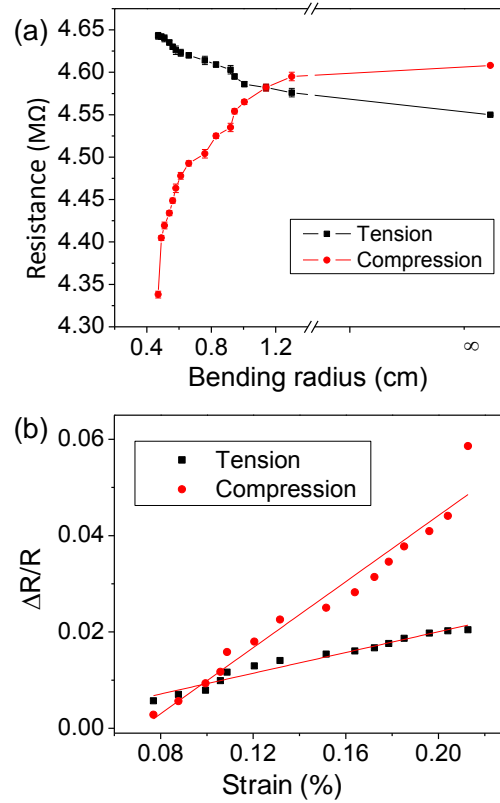
Figure IV.12 μ-stripes vs a film, (a) Variation in resistance with bend radius during tension and compression. (b) Normalized change in resistance as a function of strain.

Table IV.2 A comparative study of typical 2-terminal strain gauge sensors reported in the literature

Material	Maximum working range of strain (%)	Gauge factor	Operating voltage/range (V)	Ref.
Ni wire (commercial)	0.15	~ 2	6	[42]
Piezoresistive doped nanocrystalline Si	0.2	30	5	[43]
Si nanowire	3	~ 20	~ 3	[44]
ZnO nanowire	1.2	1250	~ 2	[3]
ZnO nanorod	1.4	6.7×10^8	2	[41]
Piezoresistive carbon filament	1.5	~ 10	~ 2.4	[45]
MWCNT/epoxy composite	2	~ 75	10	[46]
SWNT	0.08	210	0.05	[47]
SWNT	0.24	269	5	[26]
Pd μ-stripes	0.22	390	0.2	Present work

Another noteworthy feature is that the temperature coefficient of resistance for our sensor (see Figure IV.13) is around 0.00228 K^{-1}, lower than the bulk Pd (0.00572 K^{-1}). Thus, temperature variations of the ambient will have little effect on the performance of the sensor.
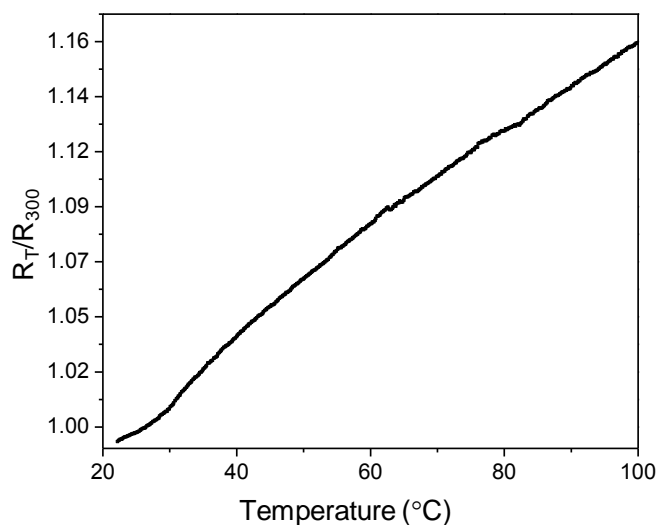
Figure IV.13 Estimation of the temperature coefficient of resistance (TCR): Normalized resistance of the thermolysed Pd film vs temperature. The TCR obtained is ~0.00228 K^{-1}

Further, the substrate (polyimide) with the μ-stripe grating structure on top possesses favorable transparency in the visible range (see dashed square regions in the Figure in IV.14). A strain sensor being transparent may offer additional advantages, particularly in transparent electronics.
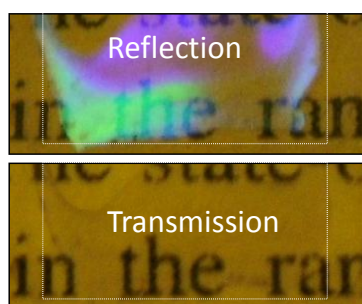
Figure IV.14 Digital photographs of the strain sensor device in reflection and transmission geometries. The text beneath the sensor can be read indicating the transparent nature of the device.

IV.1.5 Conclusions

In conclusion, the above study has shown how a practically useful strain gauge may be produced based on Pd μ-stripe grating structures. The merit lies in the simple process of direct micromolding with well controlled electrical properties which in turn give a control on the gauge factor itself. Here, the decomposition chemistry of the Pd alkanethiolate precursor

plays a key role. By thermolysing the molded stripes at 230 ºC, well conducting Pd µ-stripes (zero gauge factor) were produced which are robust and can withstand bending over many cycles with resistance unchanged. This corresponds to a situation where the Pd nanoparticles are well coupled with little carbon around. Such highly conducting stripes may find applications as flexible electrodes. By thermolysing at 195 ºC on the other hand, high resistance stripes were produced with gauge factor ~400. The sensor action is primarily derived from the changing coupling between the Pd nanoparticles in the carbon matrix. The confinement of the materials in the form of µ-stripes seems important; a film obtained under similar thermolysis conditions, shows only a small gauge factor (0.1). Clearly, the strain sensor reported here is comparable to the existing commercial metallic strain gauges in terms of working range of strains, and superior in terms of the gauge factor. Comparing with the sensors based on nanomaterials, the employed fabrication process is much simpler, inexpensive and it neither requires high temperature processing nor sophisticated equipment. Thus, it is a direct, single step, solution-based process with good control over the electronic property of the strain sensor element. As the sensor is highly flexible, it can easily adapt to any surface topology and the base resistance may be redefined for the assumed shape.

IV.2 H$_2$ SENSOR

IV.2.1 Introduction

Palladium – hydrogen interaction is unique and well known. Pd has high diffusion and sticking coefficients but a low activation barrier for H$_2$ adsorption and forms a range of PdH$_x$ phases which possess lower work functions and increased volume compared to the metal. Further, the hydride phases are electrically more resistive, a property which is exploited as a transducer signal [48-50]. In particular, Pd nanostructures have been used in a variety of innovative ways as resistor-based H$_2$ sensors. To date, a lot of literature is available for the detection of H$_2$ using Pd nanostructures in the form of thin films [51-55], nanotubes [56,57], single nanowire [58-61] and polycrystalline nanowires [50,62-66] etc. Nanoparticle based films prepared by physical [52,53,67] or chemical [68] methods have also been used. Kiefer et al. exploited the volume expansion property and fabricated a hydrogen sensor that relied on the closing of a nanotrench cut across a Pd stripe using FIB [60]. Pd clusters supported on alkanethiol SAM forms a molecular device for H$_2$ sensing [67]. In addition, bilayer structure of metal-free pthalocyanine/Pd [69] and Sm/Pd [70] have been studied. Pd based nanocomposites are also employed for efficient detection of H$_2$.

Examples include CNTs decorated with Pd particles [71], Si-nanowires functionalized with Pd [72], TiO$_2$ nanofibers decorated Pd [73], Pd dispersed over Si and microporous-Si [74-76]. There are also some reports on the usage of Pd metal based metal-semiconductor diodes [77,78] and MOSFET [79] acting as H$_2$ sensors. The response time of different sensors is varied over large scale, 68 ms [67] to tens of seconds [52,53] for H$_2$ concentrations in the range, 0.1% to 5%.

The sensing behavior is of two types [52,53], depending on whether the resistance increases or decreases upon exposure to H$_2$. The former response is associated with the surface hydride formation which is of higher resistivity than Pd itself. This behavior is observed in case of Pd films consisting of particles (or clusters) which are closely packed and surface hydride formation takes place along the boundaries of grains [50,51,53,58,59,61]. A decrease in resistance can be expected in such cases where the particles are sparsely packed and their connectivity is improved by the hydride formation due to volume expansion [62,64,67]. These mechanisms are also termed as electronic and geometric effects, respectively [52]. Interestingly in some cases, a switch over behavior has been observed depending on the H$_2$ gas concentration [52,73]. Following the initial jump in resistance (rise or fall), the saturation behavior is quite varied from system to system. The resistance may remain constant upon continued exposure to H$_2$ [67,80] or revert back gradually [69,80]. This behavior is intimately linked to particle connectivity and the hydride phase [59,80].

IV.2.2 Scope of the present investigation

As such, the H$_2$ response is clearly discernible based on the initial jump itself. Another interesting aspect relates to the shape of the response immediately after the H$_2$ loading or unloading, which is less documented in the literature. For instance, the data presented in Ref. [53] shows a pulse-like behavior when H$_2$ is introduced, while occasionally such a behavior has been also observed while switching from H$_2$ to N$_2$ as well [69]. Often, withdrawal of H$_2$ leads to a monotonic trend in resistance approaching the base value. The shape of the response while changing the gas atmosphere, from H$_2$ to N$_2$ was investigated in detail in order to understand the mechanism of H$_2$ response with Pd. Nanocrystalline Pd films and patterns supported on glass substrates were employed for this study. The specialty of these samples is that they are essentially nanocomposites of Pd nanocrystals in carbonaceous matrix whose base resistance and hence the H$_2$ response could be varied depending on the initial treatment. The carbonaceous layer is electrically conducting and

permeable to gas molecules (H$_2$ or N$_2$) to allow access to the nanocrystal surface while keeping the nanocrystals apart. This offers an interesting synergy to study the electrical response to H$_2$ adsorption. Also, employing fine nanopatterns of Pd, gas sensing up to low concentrations should be possible.

IV.2.3 Experimental details

For the experiments involving 15-100 % of H$_2$ gas exposure, the substrate carrying Pd film/patterns was placed in a glass tube and the electrical connections were taken out through an air-tight seal (Figure IV.15). The tube was connected with H$_2$ and N$_2$ supply tubes through a change-over valve. The gas pressure during the flow was maintained at one atmosphere. The electrical measurements were done by using a digital multimeter with a computer control. For the experiments involving < 5% H$_2$ gas exposure, concentration of H$_2$ was controlled by the Brooks mass flow controllers.
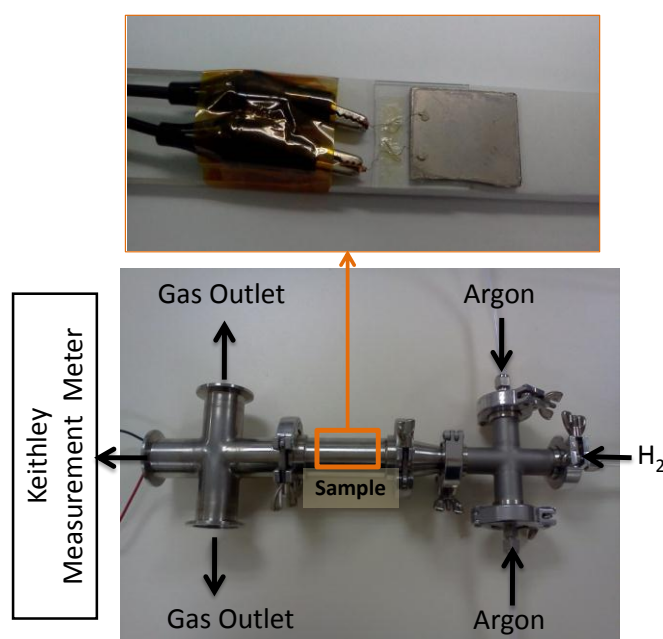
Figure IV.15 Setup of the Hydrogen sensing chamber.

IV.2.4 Results and discussion

Pd hexadecylthiolate coated as a film on a glass substrate and subjected to thermolysis at various temperatures (195 °C, 210 °C and 250 °C) in air. The Pd films obtained after thermolysis at 195 °C and 210 °C contains nanoparticles as discussed in Part IV.1. The size of the nanoparticles was below 10 nm at 195 °C which appeared grown in size, 10 to 40

nm at 210 °C (Figure IV.2). The 250 °C film contained more of the bigger nanocrystals (Figure IV.16a), many with multi-domains as evident in the HRTEM image (Figure IV.16b).
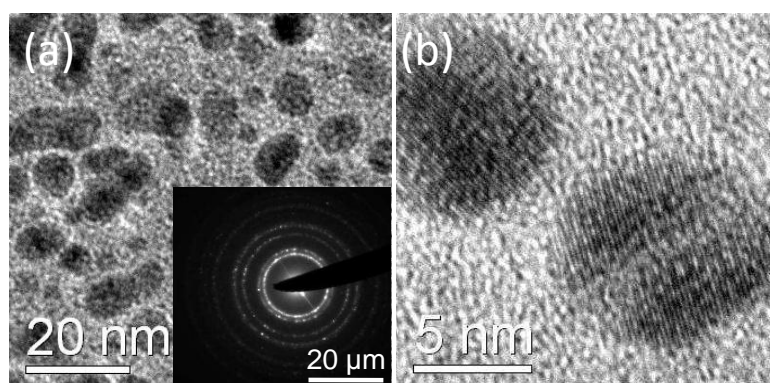
Figure IV.16 (a) TEM images of Pd nanocrystals formed by the thermolysis of Pd hexadecylthiolate in air for 1 hr at 250 °C. The inset shows the ED pattern from the nanocrystals indicating the evolution of crystallinity with thermolysis. (b) HRTEM image revealing the *d*(111) planes (2.245 Å) of Pd. The nanocrystal at the bottom in (b) contains two domains.

The structure of the as-prepared films was examined using SEM (Figure IV.17). The SEM image in Figure IV.17a shows well connected nanocrystals arranged into sheet-like structures. Interestingly, the EDS measurement indicated the presence of a carbonaceous species up to 40 at% (the variations between different films were within 10%) with negligible amount of sulfur (< 3%). Raman spectrum of the film in Figure IV.17b shows two broad bands centered around 1336 and 1583 cm^{-1} corresponding to the D (breathing mode of sp^2 carbons) and G bands, respectively which are characteristic of amorphous carbon [81,82]. The ratio I(D)/I(G) which is a measure of the disorder, is ~1.06 in the present case. Such values have been obtained for microcrystallites of carbon [83,84].
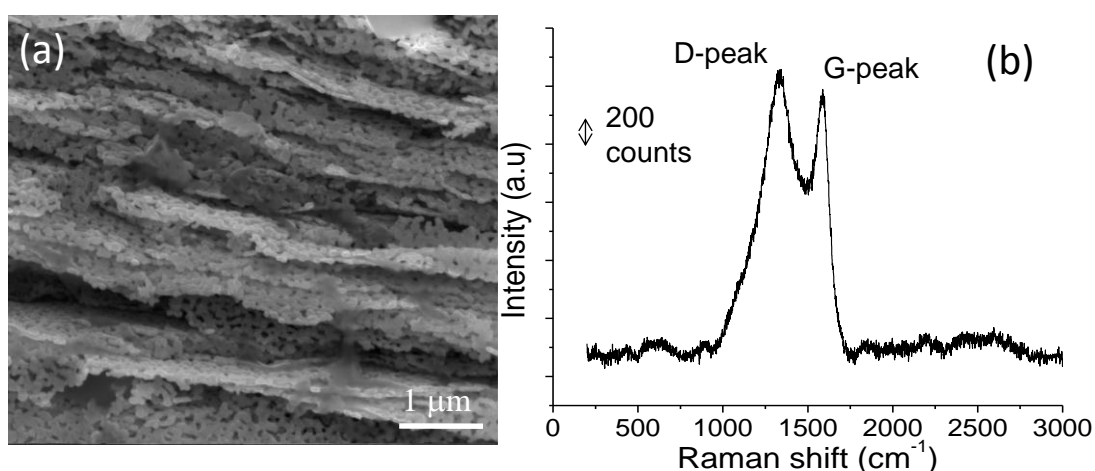
Figure IV.17 (a) SEM image of the scrapped off thermolysed film. (b) Raman spectrum from the thermolysed Pd film indicating the carbon D and G bands.

The resistances of the Pd films prepared at different thermolysis temperatures were measured. In general, higher thermolysis temperatures produced films with lower resistances (few Ωs). What is noteworthy is that the carbon layer (arising from partial decomposition of the precursor) around the Pd nanocrystals is well conducting. Films with base resistances in the range, 3 to 115 Ω were tried out for hydrogen sensing. As an example, the response of a Pd nanocrystalline film (~18 Ω) on successive exposures to H_2 and N_2 atmospheres is shown in Figure IV.18. As H_2 is introduced into the glass tube containing the sensor element, the resistance increased suddenly to ~22 Ω within 8 s. This amounts to a 23% jump, comparable to the literature values [56,67]. On continued exposure to hydrogen, the resistance decreased rather gradually to 21.7 Ω in 224 s. Upon purging with nitrogen, the fall in resistance became much faster to eventually reach the base value in ~12 min. The response was quite repetitive (see Figure IV.18). The response time observed is ~8 s, typical for a Pd based sensor [53].
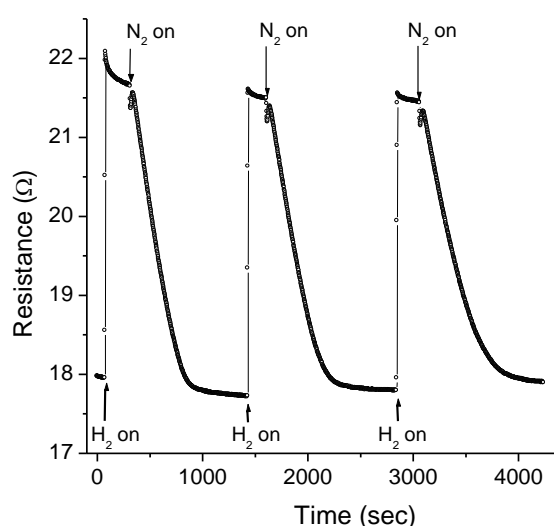
Figure IV.18 The response curve of a thermolysed nanocrystalline Pd film (base resistance, 18 Ω) for consecutive H_2 and N_2 atmospheres.

The change-over from hydrogen to nitrogen in each cycle is accompanied by an interesting feature (Figure IV.19), hitherto not well documented. The response curve shown in the figure is marked with regions, a to g, where 'b' refers to the onset of hydrogen response while 'c' stands for the highest response. With the introduction of nitrogen (point d), the resistance of the film, instead of showing monotonic decrease as found in earlier reports [51,67], exhibits a kink-like feature (d-e-f); first decreased to a small extent (21.66 Ω, point e) only to recover sharply within 20 s (21.55 Ω, point f). The decrease thereafter is akin to the reported behavior. The kink feature is indeed striking. Its possible origin is

explained using the schematic shown in Figure IV.19. The film is considered to be a close packed arrangement of Pd nanocrystals, amidst amorphous carbon (see Figure IV.17), permeable to H$_2$ as shown in the schematic diagram (a-b) in Figure IV.19. Some conducting paths get established depending on particle proximity. When the film is exposed to H$_2$ (point b), surface and subsurface hydride formation [85] takes place resulting in a jump in the resistance (see schematic diagram, Figure IV.19b-c).
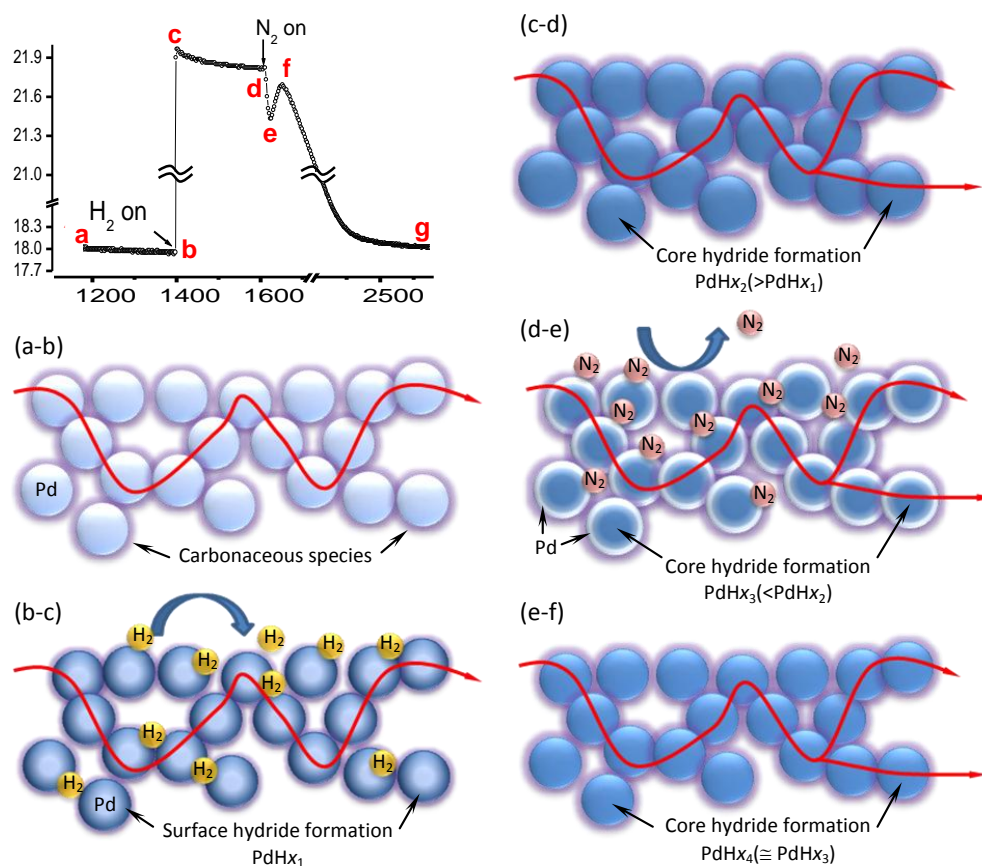
Figure IV.19 A detailed plot of the response curve where the different stages have been marked. Point a, nanocrystalline Pd film; b, onset of hydrogen response; c, maximum response; d, onset of nitrogen response; d-e-f, the kink feature; g, complete recovery in nitrogen. Schematic of the Pd nanocrystalline film corresponding to the different stages of the response curve is shown. In the following figure, the extent of hydride formation is represented by varying shades of blue color. Accordingly, the resistance recovers. (a-b) The thermolysed film with Pd nanocrystals (light blue) surrounded by the carbonaceous species (violet). The red line is one possible conduction path. (b-c) The completion of the surface hydride formation (dark blue) leads to the maximum in hydrogen response. (c-d) Core hydride formation (dark blue) with continued flow of hydrogen. New paths may also establish due to particle volume expansion (d-e) Upon switching to nitrogen, the vicinal layer is depleted of hydrogen (light blue) while the core (dark blue) is still nearly unchanged. The resistance drops due to improved electrical contact (e-f) Hydrogen from the core equilibrates through the particle volume (medium blue), as more and more hydrogen is forced to desorb. Here the content of hydrogen in Pd nanoparticle is different at different stages from a to g, which is indicated by x_i, $i = 1, 2, 3,$ and 4, and $x_1 < x_2 > x_3 \cong x_4$.

On continued exposure to H$_2$, a complete conversion to Pd hydride takes place leading to volume expansion and improved interparticle connectivity. The resistance decreases gradually (Figure IV.19c-d). As N$_2$ gushes in (point d), hydrogen from the surface of the nanocrystal desorbs creating a hydrogen-deficient but more conducting hydride species, leading to a sudden drop in the resistance (Figure IV.19d-e). Before the volume and hence the connectivity could adopt to the new situation, hydrogen from the core equilibrates across the particle volume (Figure IV.19e-f), leading to an immediate rise in resistance, but to a lesser extent in this case. The depletion of hydrogen from the surface and its backfilling readily by the hydride core, thus gives rise to the observed kink feature in the response curve.

All the films examined exhibited good response curves with distinct kink features. In Figure IV.20, the hydrogen response and the kink feature with respect to the base resistances of the Pd films was examined. The jump in the resistance seen immediately after exposure to hydrogen (b to c in Figure IV.19), is found to vary linearly with the base resistance (Figure IV.20a) indicating similar response mechanism being prevalent in all the films. The surface area of the particles and the width of the conduction paths seem to play a greater role, both however being closely linked to the particles size. Interestingly, the effect of size is of opposite nature in the two cases. Smaller particles may have higher surface area but larger ones, wider conduction paths. These effects are possibly additive, giving rise to a linear behavior in Figure IV.20. The slope of plot is ~0.2, thus corresponding to nearly ~21% sensitivity irrespective of the base resistance of the examined films. As the origin of the kink feature is also closely linked to the surface area and the particle connectivity, a linear behavior in its variation was observed as well (Figure IV.20b).
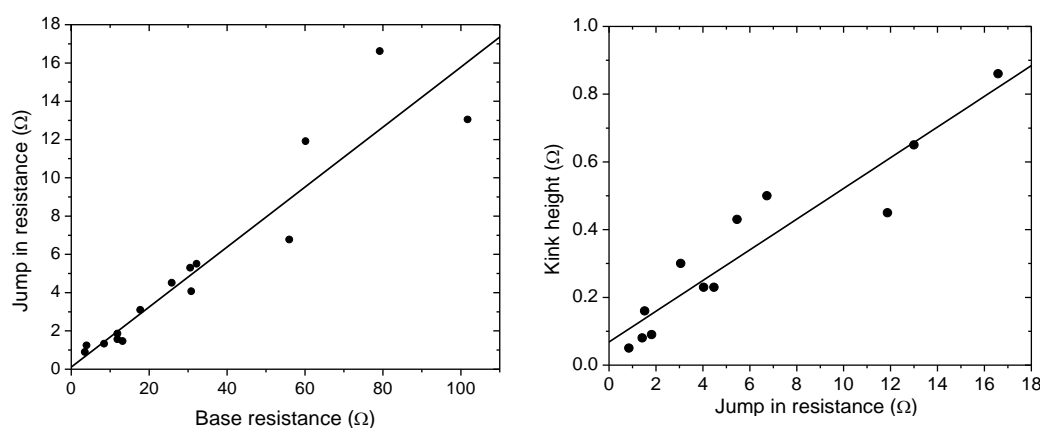
Figure IV.20 (a) Variation of the resistance jump (b to c in Figure IV.19) with the base resistance of the films, and (b) Variation of the dip in the resistance at the kink with the resistance jump.

The origin of the kink feature was investigated further. The formation of the hydride species itself was controlled by exposing to hydrogen for varying intervals, 5 to 300 s, before switching over to N$_2$ (Figure IV.21). When H$_2$ exposure was limited to 5 and 10 s, there was no kink formation following entry of N$_2$. It is to be noted that these time periods are shorter than the typical time required (~12 s) to achieve maximum resistance jump from the base value. For a H$_2$ exposure of 15 s, a mild feature was seen emerging after the initial jump in resistance. For higher loading times of H$_2$, 25 s or more, a regular kink formation was seen upon N$_2$ introduction. Thereafter the kink formation is almost independent of the H$_2$ on-time. This observation implies that the kink formation is closely linked to the saturation of Pd nanocrystals with hydrogen, in other words, complete conversion of surface, sub-surface and core Pd to its hydride. With 5, 10 and 15 s exposure of the Pd film to H$_2$, only the vicinal layer of the nanocrystal is converted to the hydride species which readily gives up hydrogen on introduction of N$_2$. In such a case, the kink recovery (e-f in Figure IV.19) is not to be expected.
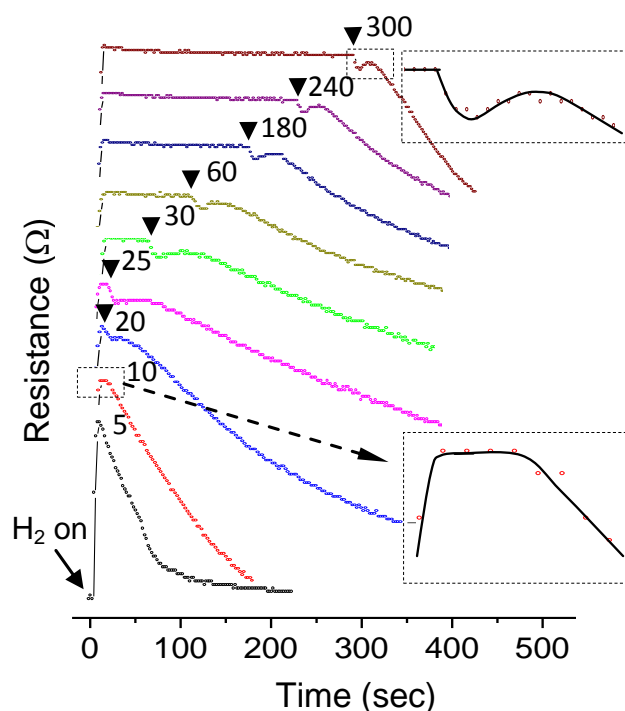
Figure IV.21 Variation in the nature of the kink with the time of exposure to H$_2$. Down arrows indicate switch over from H$_2$ to N$_2$ atmosphere. The response curves are shown on top of one another for the sake of comparison.

Figure IV.22 shows the nature of the kink response in Pd nanocrystalline films with different base resistances, namely 12 and 60 Ω (Figure IV.22). The kink shape in the two cases is different. The film with 12 Ω base resistance (see Figure IV.22a) behaves similar to the one shown in Figure IV.19. On the other hand, the film with 60 Ω base resistance shows

a kink whose resistance after recovery is higher than that before the kink (see Figure IV.22b). The latter contains nanocrystals of smaller size (~5 nm) where the conduction paths are likely to be more affected than in the low resistance film (particle size, ~15 - 20 nm).
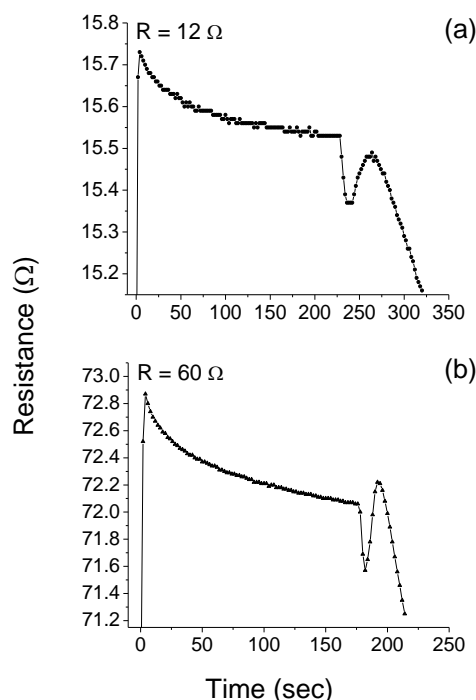
Figure IV.22 The nature of the kink in Pd films with different base resistances (R).

The nature of the kink was also studied by changing the concentration of H$_2$ from being 100% in the above experiments to below 50% by mixing with N$_2$. As shown in Figure IV.23a, the kink feature is mildly visible even down to 25%, but ceases to exist for concentrations below 15%. It is also observed that the jump in resistance and its steepness decreases with lowering H$_2$ concentration. Thus, the sensitivity decreases to ~6% and the response time increases to ~100s for H$_2$ concentration of 15%. The inset in Figure IV.23 shows the details of the kink feature for 25%, 40% and 50% of H$_2$ with respect to d, e and f stages (as discussed in Figure IV.19). With decreasing H$_2$ concentration, the resistance change as well as the time required to reach the kink minimum (d to e), decrease considerably. This observation clearly implies that the depletion of H$_2$ from the surface is a function of H$_2$ loading in the nanocrystal itself. The effect of the purging atmosphere on the kink feature was also examined. When Ar was used in place of N$_2$, there was hardly any difference in the kink feature. On the other hand, when O$_2$ or dry air was used for purging, the kink feature was not observed. It is possible that the surface of the nanocrystal gets oxidized to some extent and can influence adversely the kink formation.
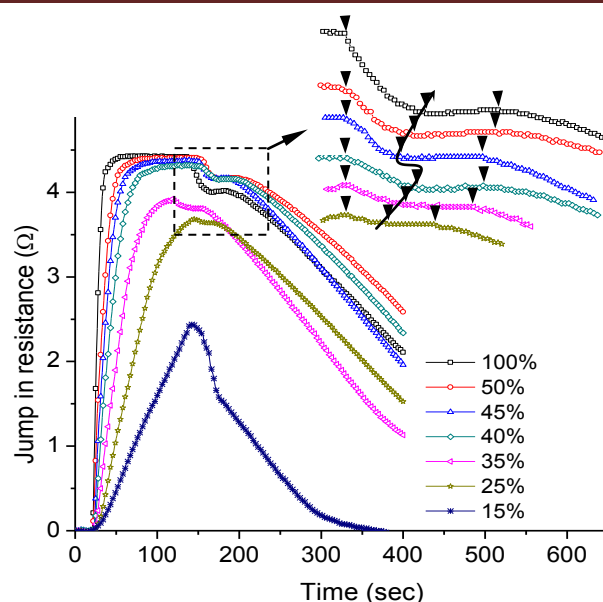
Figure IV.23 The formation of kink feature as a function of H$_2$ concentration. The inset shows the kink for 15, 25, 35, 40, 45 and 50% of H$_2$ and the arrow marks with d, e and f correspond to the kink states shown in Figure IV.19.

As seen from this study, the presence of an amorphous carbon layer around the Pd nanocrystals makes the sensor action interesting. Upon H$_2$ exposure, the molecules permeate through the carbon layer to reach the Pd nanocrystal surface and convert to PdH$_x$ species, which is expressed as a jump in the resistance. On continued exposure to H$_2$, there is gradual diffusion of hydrogen down to the nanocrystal core and eventually complete conversion to the hydride species resulting in volume expansion and improved interparticle connectivity. This is seen as a gradual decrease in resistance after the initial jump. These observations are in line with the literature reports [80]. Now, a change-over of atmosphere to N$_2$ makes the Pd nanocrystal surface layer get depleted of hydrogen, thus more conducting. This phenomenon has been sensitively picked up by our nanocrystalline films exhibiting a short but sudden drop in resistance which is termed as kink feature. Hydrogen from the core hydride diffuses outwardly to the surface layers to equilibrate across the entire nanocrystal volume. The resistance therefore, regains to some extent. Importantly, the kink feature is unique to this study and owes much to the nature of the carbon layer. As seen from Raman data, this layer is essentially disordered carbon which is expected to be porous (typical hydrogen response times being few seconds) allowing facile transaction of molecules across the Pd nanocrystals, even if the latter were hidden deep within the film. Such a situation cannot be expected in the case of a pure Pd nanocrystalline film. The carbon layer is highly conducting (the resistance of the films being typically few ohms), collating the electrical response from individual nanocrystals in the conducting path and transmitting into electrodes. Importantly,

here the carbon species does not seem to chemically modify the Pd nanocrystal surface, as the observed response to hydrogen is significant.

Pd nanowires for H$_2$ sensing

Sensing can be improved by facilitating the hydrogen diffusion in the surface sites of Pd to form hydride. Therefore, increasing the surface area of Pd thin film allows more H$_2$ absorption which is important in sensing and also in H$_2$ storage, metal-hydride batteries and H$_2$ purification. As discussed in Part III.4.2, Pd nanostructures can be patterned using nanoimprint lithography (NIL) which is not only a simple method that can directly pattern Pd but also provides a better controllability for desired surface structures.
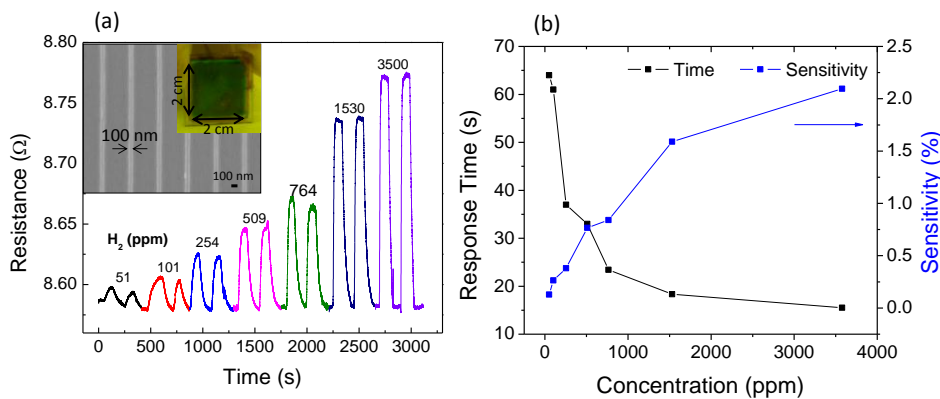
Figure IV.24 (a) Real-time electrical resistance response of Pd nanowires on glass to H$_2$ gas within a concentration range of 51-3500 ppm at room temperature. Inset shows SEM images of the 100 nm Pd nanowires. (b) Response time and sensitivity as a function of H$_2$ concentration range from 51-3500 ppm.
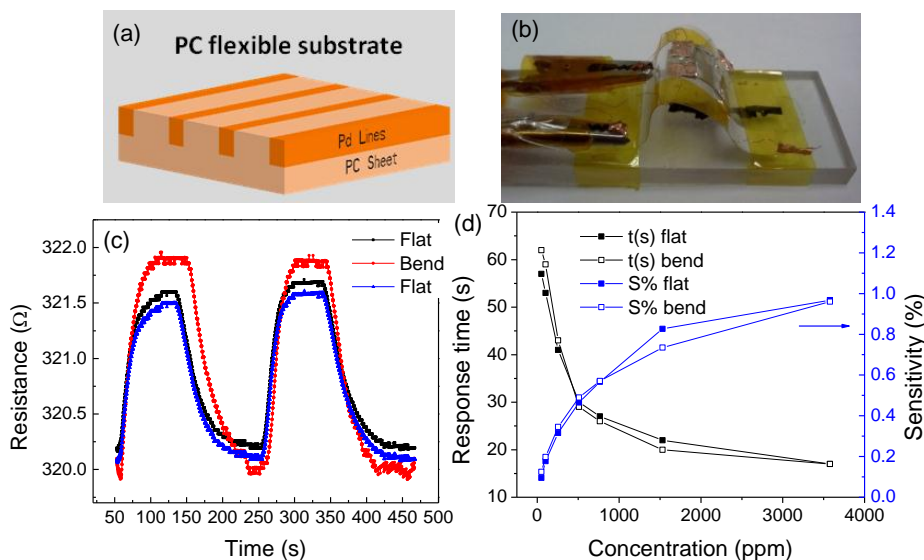
Figure IV.25 (a) Schematic showing the flexible PC substrate carrying Pd nanowires. (b) Photograph of the same in bent configuration, attached to a glass substrate with kapton tape. (c) Electrical resistance response to present of H$_2$ concentration at 500 ppm when sample is placed flat to bend to flat. (d) Response time and sensitivity as a function of H$_2$ concentration range from 51-3500 ppm for flexible sample.

Employing Pd nanowires (~100 nm wide) on a glass substrate over 2x2 cm^2 (Figure IV.24a inset), H$_2$ gas sensing was performed. The sensor exhibits a fast response time of 15 s at 0.1% H$_2$, which is well below the explosion limit. Importantly, it can sense even a very low H$_2$ concentration of ~50 ppm at about 65 s (Figure IV.24a). The sensitivity and response time for various concentrations are shown in Figure IV.24b. Flexible PC substrate carrying Pd nanowires can also be fabricated using NIL (as discussed in Part III.4.2). Thus a flexible Pd nanowire H$_2$ sensor has been developed which is as sensitive as rigid sensors on glass substrates, even when it is bent (Figure IV.25).

IV.2.5 Conclusions

In the present study, Pd hexadecylthiolate films were subjected to thermolysis in air at 195 °C, 210 °C and 230 °C to obtain Pd nanocrystalline films with resistances ranging from 3 to 115 Ω. HRTEM, SEM and STEM imaging revealed the presence of Pd nanocrystals surrounded by a carbonaceous species (up to 40 at% by EDS). Raman spectra of the films were typical of disordered carbon with broad D and G peaks (ratio ~ 1). The presence of carbon, porous and conducting, around Pd nanocrystals seems vital to our study of hydrogen response. As H$_2$ was introduced, the resistance of the film increased suddenly as expected (rise time ~ 8 s), and thereafter declined gradually with continued exposure to H$_2$. While the jump is ascribed to the formation of a less conducting surface hydride, the latter behavior arises due to volume expansion and increased particle connectivity associated with complete conversion to Pd hydride. The response was found to increase linearly with the base resistance, typical sensitivity being ~ 21%. This value is comparable with the literature reports, indicating that the carbon layer has negligible interaction with the Pd surface in the films. The response curve was also studied further in detail. The change of atmosphere to N$_2$, interestingly, gave rise to a kink-like feature : sudden decrease in resistance for a short while and reverting back, in the electrical response. This feature originates due to the depletion of hydrogen from the Pd hydride nanocrystal (decrease in resistance) and subsequent equilibration of hydrogen from the core throughout the nanocrystal volume (reverting back). The carbon layer here plays an important role. Being porous, it allows gas molecules to have an easy access to the nanocrystal surface throughout the film while collating the response from individual nanocrystals. Thus, it enabled to virtually take snapshots of hydrogen diffusing in and coming out of the nanocrystal volume. Employing nanowires of Pd fabricated using direct NIL, a flexible H$_2$ sensor sensitive down to 50 ppm of gas concentration, has been developed.

IV.3 HIERARCHICALLY PATTERNED HYDROPHOBIC METAL SURFACES

IV.3.1 Introduction

Hierarchical patterning on surfaces allows for the tunability of the surface hydrophobicity and wettability. Particularly, anisotropic wetting achievable by hierarchical patterning, has the advantage of restricting the liquid flow to a desired direction and has potential applications in microfluidic devices [86], where the surface topography of the channels can be used for the manipulation of the interaction of bio/nanomaterials flowing inside the channel [87]. Hydrophobic metal surfaces are generally achieved by surface coatings or hierarchical structuring, the former being the most widely used. It is rather difficult to pattern metals hierarchically in an ordered manner over large areas, using conventional lithography techniques. To achieve this, micro and nanostructuring using biological scaffolds by physical and chemical deposition methods have been tried out. Direct laser writing and LIGA have been methods of choice on thicker resists. For layer by layer patterning, optical and e-beam lithographies have been employed. In the case of optical lithography, a significant fraction of the cost is towards making of a qualified mask with feature sizes down to few nms, way beyond the normal optical limits. Development of mask-less lithography techniques as such laser interference lithography (LIL) or holographic lithography, electron beam lithography (EBL) provided an alternative. LIL involves the splitting and recombination of a laser beams to produce a standing wave, creating a periodic pattern on photoresist. This technique offers an advantage of resolution of sub-100 nm over large areas but suffers from the disadvantage in that the pattern choice is limited to periodic patterns obtainable by interference. Recently, laser patterning has met with some success for direct hierarchical structuring of metals [88], employing high energy pulses of laser. NIL, foreseen as next generation lithography, has been gaining successful attention for large area patterning, as it is simple and can afford a resolution of few nms. As discussed in Part III, MDNIL can be used for hierarchical patterning of metal surfaces, which will be tested for its hydrophobic nature.

IV.3.2 Scope of the present investigation

A pristine metal surface being hydrophobic presents several advantages. Thus far, hydrophobicity on metal surfaces has been achieved using various chemical methods such as surface coatings by SAMs [89], polymers/organic molecules [90] and physical methods such as plasma surface modification [91], laser patterning [92] have been used. MDNIL is a

versatile method for producing hydrophobic metal surface while not compromising with chemical purity, stability and edge roughness of the patterns.

IV.3.3 Results and discussion

Using MDNIL method, a hierarchical pattern mimicking rice leaf structure was obtained. Natural rice leaf possess papillae of about 5-8 µm arranged in parallel order with innumberable pins of nanometer scale, due to which the leaf exhibits anisotropic dewetting. For this purpose, a primary grating was imprinted with 2 µm mold, over which fine dimples were imprinted using a 200 nm mold (Figure IV.26).
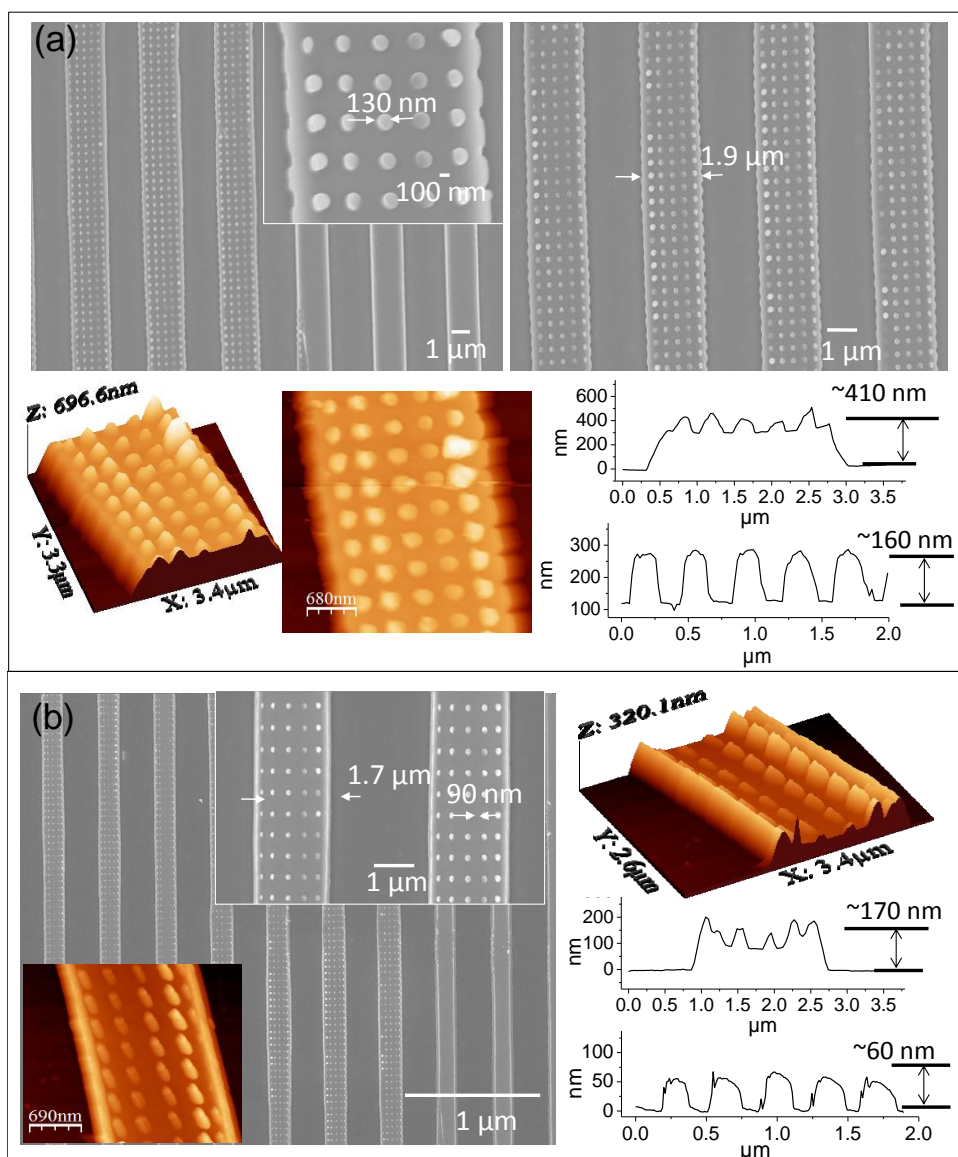
Figure IV.26 Biomimicking - (a) SEM images of rice leaf pattern with primary lines of 1.9 µm and secondary pillars of 130 nm, and corresponding height of 410 nm and 160 nm marked in the AFM profiles. (b) After heat treatment of rice leaf structures giving primary lines of 1.7 µm and secondary pillars of 90 nm, and corresponding height of 170 nm and 60 nm.
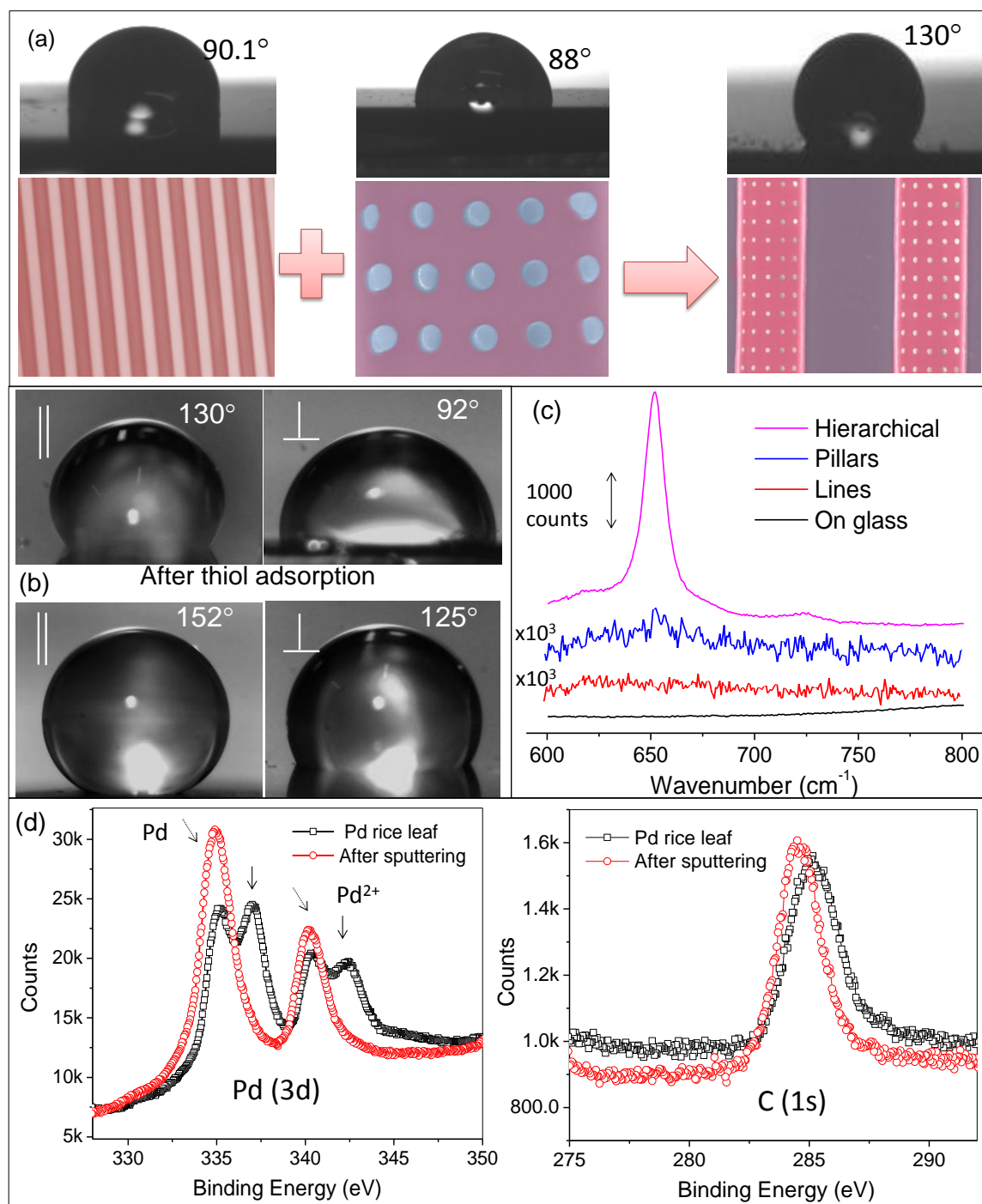
Figure IV.27 Contact angles of the Pd lines and dimples separately and the rice leaf where dimples were patterned over lines. On the metallic rice leaf, the contact angle was ~130°. The images are artificially colored for clarity. (b) The contact angles in parallel and perpendicular direction of the metallic rice leaf lines differing due to anisotropic wetting. After hexadecanethiol absorption, the contact angle increased in both directions. (c) Surface enhanced Raman spectra (ν(C-S)) of the adsorbed thiol molecule from hierarchical rice leaf along with control samples. (d) Pd 3d and C1s core level spectra from the Pd rice leaf sample before and after sputtering.

The contact angle of the as-imprinted rice leaf structure is 137° and is comparable to the one obtained with the natural rice leaf [93]. After thermolysis, the contact angle reduced to ~130°, owing to the hydrophilic nature of the Pd metal surface. The patterns are well-ordered and smooth, unlike the ones produced by laser flashing [92]. As can be seen from Figure IV.27, the contact angles of the either line patterns or dimple patterns alone possess much lower contact angles (90.1° and 88° respectively) as compared to the hierarchical Pd pattern.

The anisotropic wettability is generally studied by static contact angles of water droplets measured in the directions parallel and perpendicular to the stripes. For natural rice leaf, the values are 138.5° and 131.7° respectively [93]. For the metallic structure fabricated here, the contact angles are 130° and 92° respectively in parallel and perpendicular directions, thus clearly deciphering the anisotropic wetting. The hydrophobicity arises due to the physical structure. In order to understand the role of chemical impurity, XPS was performed on the rice leaf (Figure IV.27d). Along with Pd(0) peaks at 335.2 ($3d_{5/2}$) and 340.6 ($3d_{3/2}$) eV, Pd^{2+} peaks at 336.9 and 342.4 eV [94] were also observed. Sulfur was absent but small amount of carbon (285.1 eV) was seen. Upon Ar^+ sputtering for 1 min, Pd^{2+} peaks disappeared revealing the pristine nature of the underlying bulk structure.

In order to further increase the hydrophobicity, a monolayer of hexadecanethiol molecule was adsorbed onto the metallic rice leaf by immersion in 1 mM of the thiol solution in ethanol. After 3 hours of immersion, the substrate was taken out rinsed and then the contact angles were measured. As can be seen from Figure IV.27b, the contact angles increased in both parallel and perpendicular directions to 152° and 125° respectively. The hierarchical structure is also found to enhance the Raman signal of the thiol molecules adsorbed (Figure IV.27c).

IV.3.4 Conclusions

Hydrophobic hierarchical metal (Pd) structures with anisotropic wetting property have been formulated. The contact angle was further increased by chemical modification of the surface i.e., adsorbing a monolayer of thiol. The patterned structure acts as a Raman enhancing substrate.

IV.4 NON VOLATILE MEMORY DEVICES

IV.4.1 Introduction

A memory device in simple terms, can store the information via a change in some material property. Non-volatility implies the ability to store even when the power to the device is off. Many examples of non-volatile memory devices are used in day-to-day life, for e.g., optical disks (CD, DVD), magnetic hard disk drives, flash memory (thumbdrive, SD card) etc. Digital memory is stored in the form of '0's and '1's, which correspond to OFF and ON states of the memory device respectively [95]. There is an ever increasing demand for higher memory storage capacity with the year-2020 target, various memory technologies have been compared [96]. The comparison was done taking into account the important properties of memory devices such as cost per GB, endurance, retention, ON/OFF ratios, power consumption etc [96]. Currently, the magnetic memory and NAND flash are projected as possible candidates for future memory requirements, while resistive switching and phase change memory are still at the laboratory research stage [96]. Memristive switching [97], a class of non-volatile resistive switching has been investigated recently in various nanoscale [98] and microscale [99] devices composed of inorganic [100,101], polymer [13,102], organic [103,104] and of late carbon compounds [105,106] as well. In fact, memristance as a new physical entity was proposed by Chua way back in 1971 [107]. These memory devices exhibit hysteretic current voltage characteristics and possess nonvolatile memory states. Various materials such as TiO_2, Ta_2O_5, Co_3O_4, SiO_2 and NiO etc., have been discussed as active elements for non-volatile memory devices [108]. The switching phenomenon in such devices has been identified primarily due to two different mechanisms; the electrochemical reduction of the solid electrolyte/active electrode and the vacancy/defect migration from one electrode to the other [108]. Electrochemical reduction is popularly called as filamentary mode of conduction and the devices in this class are called as atomic switches [109]. The latter are again categorized as gap-type and gap-less atomic switches depending on whether there exists a nanometric gap between the electrode and active materials or not. Atomic switch is present at the edge/interface of the conducting metal filament (which preferably starts from one electrode) and the second electrode. The dissolution and formation of the filament controls the switching property of the device. Popular materials exhibiting such switching are Ag_2S, Cu_2S, GeSe doped with Ag nanoparticles etc.[110] Owing to the demands of the ultrahigh density and packing of the memory devices, cross-bar electrodes have proven to be the best alternative to lateral geometry of laying electrodes even though

the former geometry suffers from cross talk and sneak paths [111]. Another effective way to increase the data density is to increase the number of memory states which can be stored in each bit. So, instead of two states 0 and 1, if many states can be stored such as 0,1,2,3,4,5…. etc., the data density can be improved from being 2^n to 3^n, 4^n, 5^n… etc., where n is the number of the memory cells [112]. It also implies that the memory density can be increased without the physical constraints of scaling [113] and that the junctions can be reasonably far away so as to prevent the cross-talk. Redox molecules [114], small molecular layers of AlQ_3 [115], molecules with azo functional groups [116] etc., have been shown to exhibit multiple state switching apart from inorganic junctions such as Cu_xO [117], TaO_x [118], TiO_x [119], ZrO_x [30] etc., which can store multiple states based on current compliance, switching voltage or the random circuit breakage model.

IV.4.2 Scope of the present investigation

Inorganic compounds are known to offer high ON/OFF ratios, good endurance and retention in the case of two-state switching. On the other hand, molecules exhibit often multiple resistance switching but are too fragile and unstable under the electric field [97,120]. Thus taking molecules to real applications has been a challenging task. Here, an intermediate i.e, a metal-organic precursor possessing a metal center and organic moiety has been investigated for its use as a memory element with the ability to store multiple states.

IV.4.3 Results and discussion

Pd hexadecylthiolate solution (50 mM in toluene) was drop coated as a film (~1 μm thick) over Au gap (~6 μm) electrodes (see schematic in Figure IV.28a). It is an insulating metal-organic compound, which shows very less current (<1 pA). As discussed in Part III, thermolysis can lead to nucleation of Pd nanoparticles with their size and density related to the extent of thermolysis. In this study, the formed Pd thiolate films were subjected to heat treatment in the ambient at 200 °C for 10 min, following which they became conducting with a typical resistance of few MΩs and the I-Vs of the film showed non-linear behavior (Figure IV.28b). The film was then subjected to electrical activation at a constant applied bias of ~20 V (Figure IV.28c). Prior to this, lower bias activation (i.e., at 8, 10 and 15 V) was tried, but was not successful. In the case of 20 V activation, the current displayed frequent jumps with time; after 50 s, the current was almost constant. In the case of cross-bar geometry (Figure IV.28a), the bottom set of electrodes were defined first over which Pd thiolate was spin/dropcoated (~0.5 − 1 μm). After the thermolysis, the top set of electrodes

were deposited using shadow masking. Each cross bar junction occupied ~600 x 600 μm^2 area. Following the electrical activation, I-V data was measured in the form of a cycle, sweeping voltage from 0 → -1.5 → 1.5 → 0 V with a dwell time of 1 ms at each of the 100 data points (Figure IV.28d). At about ~1.3 V, the device exhibits high current and thus it has switched to a low resistance state. On the negative bias, at ~1.2 V, the device switched back to high resistance state. This is a representative example from a cross-bar device. It has been observed that, once the device is switched to low resistance i.e., ON state, it can be switched to high resistance i.e., OFF state at higher positive voltages (~25 V). This means that applying –ve voltage is not necessarily required for switching, thus the device can be called as unipolar. The voltage which takes the device to ON state is called setting voltage (V_{set}) and the one which turns OFF the device is called resetting voltage (V_{reset}). In the case of the device with lateral geometry i.e., ~6 μm gap electrode, the V_{set} was ~4 V. In order to prevent any effect on the ON or OFF states, a small read voltage of ~0.1 V was employed (Figure IV.28e).
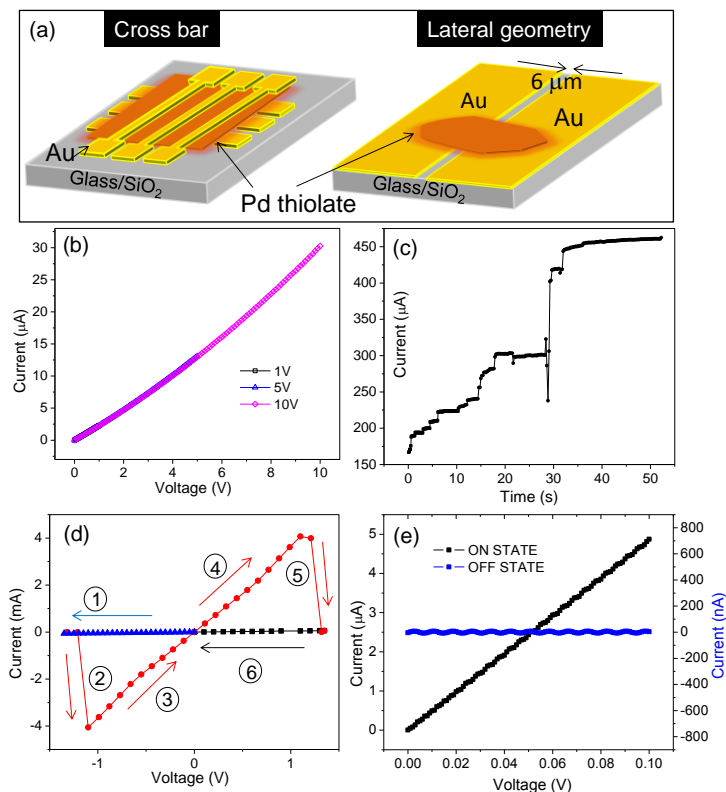
Figure IV.28 Schematic illustrating the Pd thiolate memory device geometry; cross-bar and lateral gap electrodes. (b) Virgin I-V curves of the device and (c) Current-time characteristics for monitoring the electrical activation of the device at a constant applied bias of 20 V. (d) I-V characteristics after electrical activation of the device, voltage sweep from 0 to -1.5 to 1.5 to 0). (e) I-V's of the device in the ON-state and OFF-state. Small oscillations and some EMI from surroundings are overlapped.
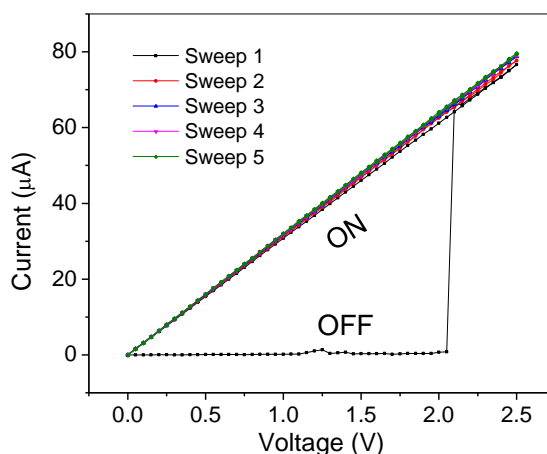
Figure IV.29 (a) Sequential I-V characteristics on the positive bias showing slight increment of current in consecutive I-V.

In order to understand the effect of an extended application of bias in the ON state, a series of I-V data was recorded from 0 $\rightarrow$ 2.5 $\rightarrow$ 0 V (on another device). As shown in Figure IV.29, after the first sweep, the device switched to the ON state, and the second sweep followed the same trend but with a small increment in the current. The hysteresis still prevailing, the subsequent I-V curves were seen building up on the trace of the preceding I-V curve. The switching was non-volatile and the device remembered the history it had been taken through.
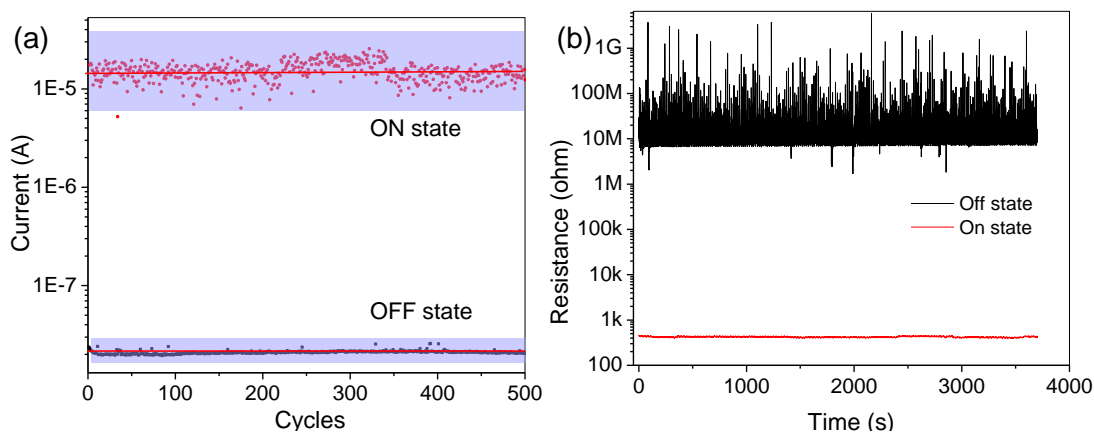
Figure IV.30 (a) Endurance and (b) retention characteristics of the fabricated memory device.

By applying alternate pulses of V_{set} (4 V) and V_{reset} (25 V) with a pulse width ~ 1 ms, the device was tested with a small read voltage (0.1 V) for evaluating whether the device has switched to either ON or OFF state, according to the voltage pulse applied. Briefly, the sequence of the voltage pulses was write (4 V)/read (0.1 V)/erase (25V)/read (0.1 V). This is called endurance performance of a memory device. As shown in Figure IV.30a, up to 500

cycles, an average current ON/OFF ratio of 0.58 x 10^3 was maintained. Another important property of a memory device is its retention i.e., how long the ON or the OFF state can be retained once switched to that state. This is shown in Figure IV.30b for a third device, where the resistance in the ON and OFF states do not change much with time in two separate measurements (reading voltage, 0.1V). This marks the utility of Pd thiolate for nonvolatile memory applications such as write-read-erase as well as write once-read many.
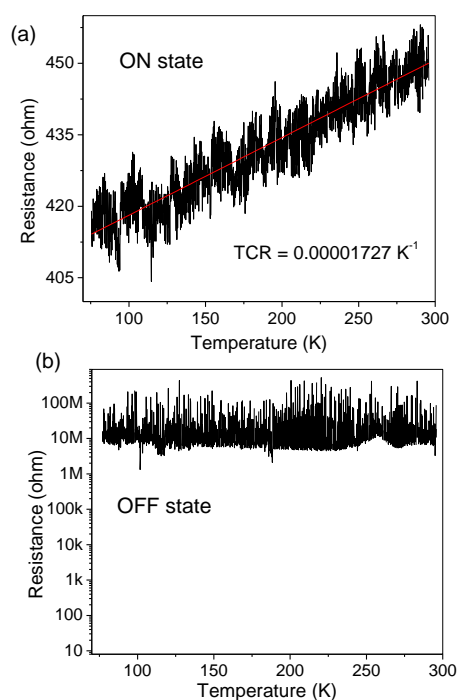
Figure IV.31 Low temperature measurements on the memory device in (a) ON and (b) OFF states.
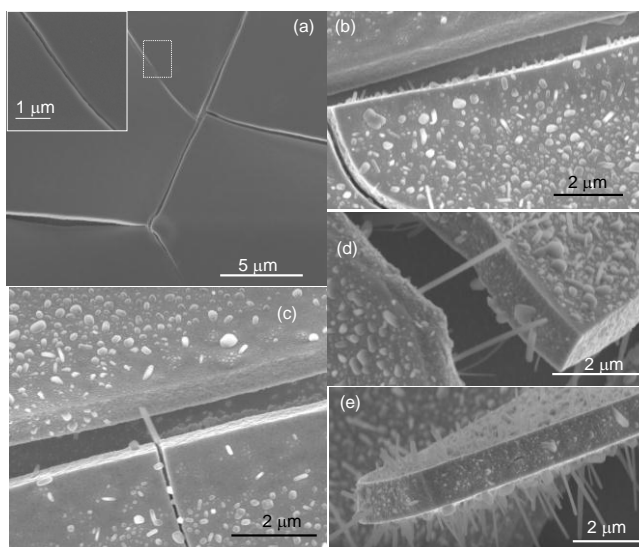
Figure IV.32 SEM images of the Pd thiolate memory device (a) before electrical analysis, (b-e) after electrical switching, (e) shows a tilted view from a broken piece of the film showing the emanation of Pd filaments from all directions.

In order to understand the conduction mechanism and thus the switching phenomenon, low temperature measurements were performed. In the ON state (Figure IV.31a), the resistance of the device increased with increasing temperature nearly linearly, following Matheissans rule, while in OFF state (Figure IV.31b), it was independent of temperature, which may be attributed to tunneling type of conduction. The temperature coefficient of resistance (TCR) in the ON state was quite low (0.00001727 K^{-1}) indicating that it is a disordered system. The active material being a partially thermolysed metal-organic compound, this ON state behavior hints at filamentary conduction. Detailed noise measurements have been done in the literature on such resistive switching models with inorganic compounds [121,122] and the noise has been attributed to the percolation nature of the filaments [123].

The morphology of the device was examined after electrical analysis with SEM. For this purpose, the as-made Pd thiolate film after thermolysis was imaged first. As shown in Figure IV.32a, the film surface was smooth but with cracks of dimensions ranging from few tens of nms to few μms. After electrical switching, the film exhibited rough surface and importantly, some filamentous structures were seen growing along the cracks (Figure IV.32b). As can be seen from the Figures IV.32c and d, the filaments were long enough to bridge the cracks. The diameter of the filaments was varied (~50 -150 nm). From a broken piece of the film (Figure IV.32e), the filaments were seen emanating from all over the surface, i.e., top, bottom, sides of the film in large numbers. These filaments are primarily composed of Pd and may form due to Pd particles and the associated movements under applied electric field.
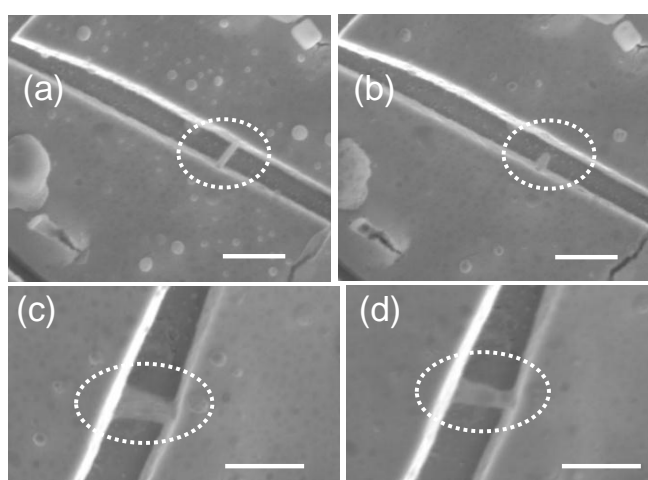
Figure IV.33 *In situ* SEM images while switching. (a) On state and (b) after switching OFF with a high voltage (V_{reset}) pulse. (c) and (d) show the filament thinning when a slightly lower voltage than V_{reset} was applied. All scale bars correspond to 1 μm. Circles indicate the region of interest.

In an attempt to directly visualize the filament formation, measurements were performed dynamically inside the SEM chamber. The memory device in the ON state has a Pd filament across the crack as shown in Figure IV.33a. After applying a pulse of 25 V, the filament broke and was retained with the bottom crack wall (Figure IV.33b). In another instance, a thick filament (Figure IV.33c) thinned down with the application of ~20 V reset (Figure IV.33d). Thus there is ample evidence that the switching in the Pd thiolate memory device might be due to the filaments of Pd and their breaking due to joule heating.
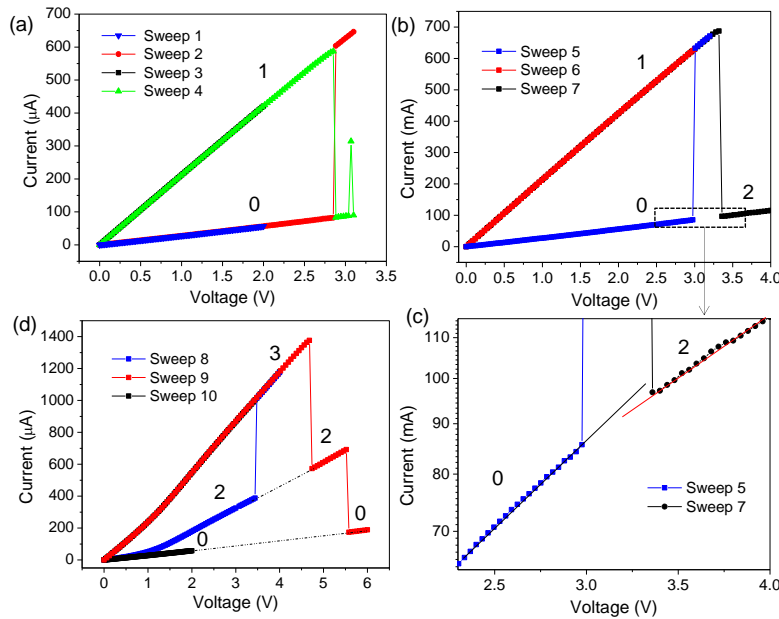
Figure IV.34 I-V sweeps on the positive bias, showing various resistance states. (a-d) are sequential.

In the above instances, switching of Pd thiolate memory device between two different resistance states (0 and 1) and their nonvolatile retention has been discussed. Interestingly, multiple state switching is also possible with this system as detailed below. Using Pd thiolate memory device (on a ~6 μm gap electrode), the possibility of storing multiple resistance states (0,1,2,3,4 etc) was investigated. After electrical activation using ~20 V bias (as discussed in Figure 1), the I-V of the device (state 0) is shown in Figure IV.34a (blue curve). With increase in applied bias, at about ~2.85 V, the device switched to a more conductive state (state 1) which was retained till the bias increased to ~2.85 V where the device switched back to the low conductive state (state 0). In subsequent sweeps (Figure IV.34b), application of ~2.95 V was required to switch the device back to state 1. This observation implies that Pd thiolate memory device remembers its history, a property perhaps similar to a neural synapse. It appears that fresh Pd filaments could form at a V_{set} of 2.85 V in the pristine device while reforming the ruptured filaments takes a V_{set} of ~2.95 V. At about

~3.32 V (Figure IV.34c), the attained state 1 could retrace back to a low conducting state which was non-linear (state 2) as shown in a magnified plot in Figure IV.34c. At ~3.44 V, the state 2 switched to a different high conducting state (state 3). At about ~4.68 V, state 3 reverted back to state 2 only to come back to state 0 at ~5.52 V. Application of higher voltages (8 – 10 V), leads to many different resistance states separated by a small but definite resistance window. In order to reduce the switching voltages, multiple state memory device was fabricated in cross-bar geometry. Approximately 8 memory states were identifiable in the cross-bar device within a voltage range of 0-3.5 V as shown in Figure IV.35, where the conductance is plotted against the voltage applied. The numbers in the graph indicate the difference ($\times 10^{-5}$ μS) between consecutive memory states.
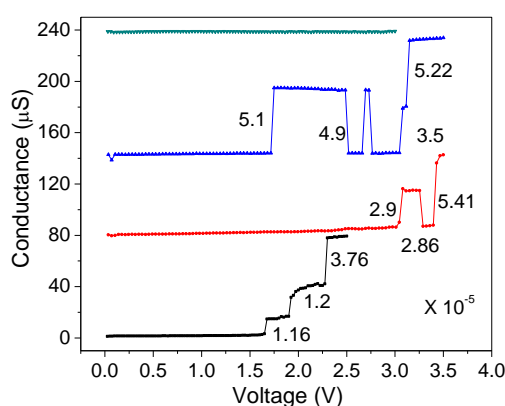
Figure IV.35 Conductance-voltage plots of Pd thiolate memory device.

There is a growing interest in using a hanging electrode (such as an AFM tip) for read/write/erase processes so as to miniaturize the memory device structure [124,125]. Probe based memory has been demonstrated by IBM via creating indentations on a polymer surface which signify state 1 whereas no indentation representing state 0 [126]. Importantly, films of active materials can be used as such, without the need of patterning, unlike conventional memory device fabrication. Over the Pd thiolate films (on Au as bottom electrode), using C-AFM tip as top electrode (see schematic in Figure IV.36a), voltage sweeps were done from -1 to +1 V where the switching behavior was noticed similar to the previously fabricated devices (Figure IV.36c). The V_{set}, V_{read} and V_{reset} could be brought down from V to mV range, due to the extremely small area being probed. Further, various writing voltages were applied over different areas on the film and were read using a small voltage sweep i.e. 0.5 mV (Figure IV.36e). There was a progressive increment in the read current with the writing voltage pulse, the trend being nearly exponential. It can be understood in the following way. The defined resistance of a state with a given write voltage

decreases which may imply that small writing voltages bridge the cracks with few and perhaps thinner filaments while increased writing voltages may thicken thus formed bridges and increase the current gradually. As shown in Figure IV.36f, from a different Pd thiolate memory device up to five resistance states are shown using a read voltage sweep i.e. from 0 to 0.8 mV, which are written with different voltages (i.e., 0.2, 0.8, 2 and 2.5 V). As described in Figure IV.36e, many more resistance states can be designed with higher write voltages. Apart from C-AFM I-V's, reading of the switched resistance states was performed using EFM phase signal (see schematic in Figure IV.36b). After switching the Pd thiolate on specified locations of dots, EFM phase image was recorded with a reading bias of 0.1 mV at a scan speed of 0.3 μm/s. Darker contrast features were seen on the written areas and the contrast was increasing with increasing write voltage (Figure IV.36c). The EFM phase showed the same darker contrast when read with a negative reading bias (-0.1 mV) indicating that there is no residual charge inherent to the material and that the charge has been driven by the top electrode while writing.
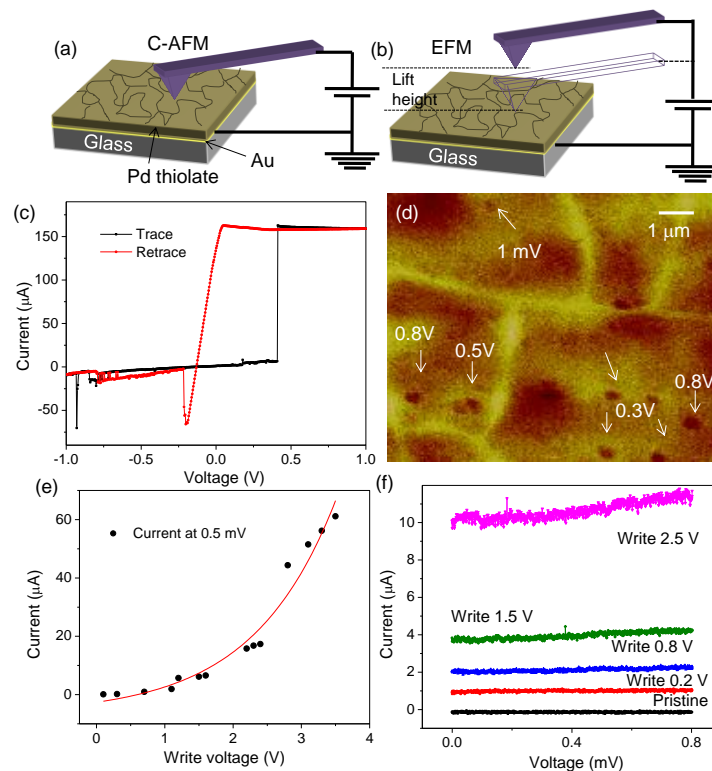
Figure IV.36 Schematic of the (a) C-AFM and (b) EFM measurement on Pd thiolate films. (c) I-V characteristics of the Pd thiolate film using C-AFM. (d) EFM phase image showing contrast in the regions which have been modified with voltage writing. Reading scan was done using 0.1 mV, after writing the dots with various write voltages. The image was recorded at a lift height of ~250 nm. Bright lines are cracks present on the film (e) Current at 0.5 mV versus write voltages for creating multiple states. (f) Typical five resistance states along with pristine, read with a small voltage sweeps. The writing voltages are indicated on the figure.

IV.4.4 Conclusions

Non-volatile memory devices with commendable memory characteristics such as large on-off ratio, high endurance and retention have been fabricated using Pd hexadecylthiolate films. The films were cast in between gap electrodes in a lateral or cross-bar geometry to lead to the memory device after electrical activation. The as-formed films possess cracks and the switching mechanism is based on Pd filament formation across the cracks. The device can be used to store multiple memory states which is of great significance for multivalued logic. Using a AFM tip as top electrode, the operating voltages can be brought down and the number of feasible memory states can be improved enormously.

IV.5 AN ELECTRICAL RECTIFIER BASED ON Au NANOPARTICLE ARRAY FABRICATED USING DIRECT–WRITE EBL

IV.5.1 Introduction

The method of rectifying an alternating current is historically perhaps the first step towards electronics. The evolution of this tiny circuit element namely diode has seen several generations starting from vacuum tubes to semiconductor p–n junctions [127]. During the last decade or so, since the advent of nanotechnology, several nanomaterials have been tried out for diode action. These include ZnO nanowires [128], carbon nanotube (CNT) [129], grapheme [130], tailored donor–acceptor molecules [131], nanoparticle–polymer composites [132] etc. These devices essentially rely on asymmetric junction formation at the nanomaterial–electrode interface [133] or a junction formed within the nanomaterial due to differential doping [128]. In addition, nanoparticle arrays [134] particularly of Au and Ag, stabilized by organic spacers have been employed for electrical rectification [135-137]. In contrast to the 'colloidal state', metal nanoparticles assembled onto a substrate as an ordered array represent a quasi 2D system where the interparticle coupling [138], depending on its strength, can give rise to collective properties [139] unique to the nanoparticle organization [140]. The interparticle coupling is tuned [141] by suitably choosing the linker molecule [136] or by dynamically changing its length/conjugation [142,143]. While the nanoparticle arrays can be directly contacted by laying metal electrode pads [136], the use of scanning probe methods is not uncommon [137,144]. Electrical rectification is one among the range of interesting properties in metal nanoparticle arrays, other important properties being the metal–insulator transition [145], magnetic transitions [146], single electron tunneling [147], linear and non–linear optical response [148] and more recently acoustic rectification [149]. A survey of the literature shows that the nanoparticle arrays are usually obtained by the self–

assembly methods [150-152] by drop–drying the nanoparticle dispersion [152] on a desired substrate or at air–water interface using the Langmuir–Blodgett method [148]. Instead of 2D, Au nanoparticle wire arrays have been fabricated by convective self–assembly method with tunable conductivity [153]. Recently, ink–jet printing has been employed to produce Au nanoparticle arrays which work as immunosensors [154]. Micromolding nanoparticle superlattices has also been demonstrated [155]. Dip–pen lithography has been used to draw Au nanoparticle lines [156]. Extended arrays have been produced using nanosphere lithography [157], diblock copolymer micelles [158] etc.

In this context, as described in Part III, direct write techniques become handy as they cut down the number of process steps. For direct write ion or e–beam lithography (EBL), various metal–organic precursors have been explored as negative resists, the notable ones for Au being Au(I) thiolate thin films [159] and Au loaded block copolymer micelles [160]. These methods have led to patterning Au nanoparticles into regular extended arrays. However, the obtained nanoparticle arrays have not been reported to show any rectifying action.

IV.5.2 Scope of the present investigation

A list of metal nanoparticle based electrical rectifiers is presented in Table IV.3. Making a 'stand-alone' nanoparticle device reproducible both in fabrication and performance, is indeed a herculean task and this has been achieved in this work in a simple and elegant way. As described in Part III, a highly versatile, single–step direct write EBL process employing a single source precursor is performed wherein the nucleation and growth of Au nanoparticles into close packed arrays takes place in confined boundaries defined by patterning. In particular, micron wide stripes of Au nanoparticle (size, ~25 nm) arrays were fabricated which exhibit electrical rectifier action with high rectification ratio. This is for the first time, a metal nanoparticle rectifier with highly commendable characteristics has been developed. In addition, the transferability of the patterned arrays is demonstrated onto a polymer substrate, where the latter could undergo swelling and deswelling causing variation of inter–nanoparticle spacing and hence the electrical transport.

IV.5.3 Results and discussion

For the purpose of constructing a two–terminal device, Au nanoparticle array stripes were defined by EBL in between a pair of Au contact pads (see optical image with rectifier electrical connections indicated, as the inset of Figure IV.37a) and the current–voltage

Table IV.3 Nanoparticle rectifiers reported in the literature (present work is also shown for comparison)

S. No	Nanoparticle system	Method of probing	RR	V_{TH}	Current/ current density	f	Ref
1.	Co-Al nanoparticles	STM	100– 1000	~0.9	<100 nA	NA	[144]
2.	Au nanoparticles embedded in SiO_2	STM	NA	~2.5	<100 pA	NA	[161]
3.	Langmuir monolayers of Au nanoparticles	Lateral electrodes	NA	~0.2	<100 nA	NA	[136]
4.	Functionalized Nanoparticle Films	STM	66	~1	<50 nA	NA	[162]
5.	Au nanoclusters capped with thiols	C-AFM	13.5 365 (bilayer)	0.24	NA	NA	[137]
6.	Molecular Junctions (Au-dithiocarbamate-Au nanoparticle)	Hg drop electrode	1.35	~0.4	Few A/cm^2	NA	[163]
7.	Diode between ZnO nanoparticles	STM	31.5	~1.5	nA	NA	[164]
8.	Au nanoparticle ordered array patterned by EBL	Lateral contacts	3.15 x 10^5	~4.3	0.5 A/cm^2	Up to 10 Hz	Present work

NA: Not available; RR: Rectification ratio; V_{TH} : Forward threshold voltage; f: frequency response

characteristics were measured. The current was low initially (~0.4 nA) and a sharp rise was observed beyond a forward voltage of +4.3V, while in the negative bias region, the current remained at fraction of a nA up to –5 V for this device. The current rectification ratio, which is the ratio of forward to reverse currents at a given bias, is estimated to be ~3 x 10^5 (at ± 4.5 V), which is considerably higher than the reported values from nanoparticle arrays [136,137]. The device characteristics are highly stable and reproducible both in fabrication

and performance (see characteristics of the second device in Figure IV.38). Some devices showed rectification in the negative bias region and others, in the positive bias region; of course, this observation is only relative as the choice of electrode polarity, positive or negative, is simply arbitrary (*vide infra*). Another device (third one) was tested by cycling between +4.5 V and –4.5 V continuously (Figure IV.37b). Over the observed 100 cycles, the rectifier action was well preserved, with the positive bias (+4.5 V) current being much higher than that at the negative bias (–4.5 V). Low temperature resistance measurements have been carried out on the rectifier device in order to understand the nature of the conducting and insulating states. When the device resistance was measured applying +4.5 V, the resistance decreased with decreasing temperature (see Figure IV.37c), resembling metallic behavior. On the other hand, the device resistance remained almost independent of temperature, when measured at –4.5 V (Figure IV.37c).
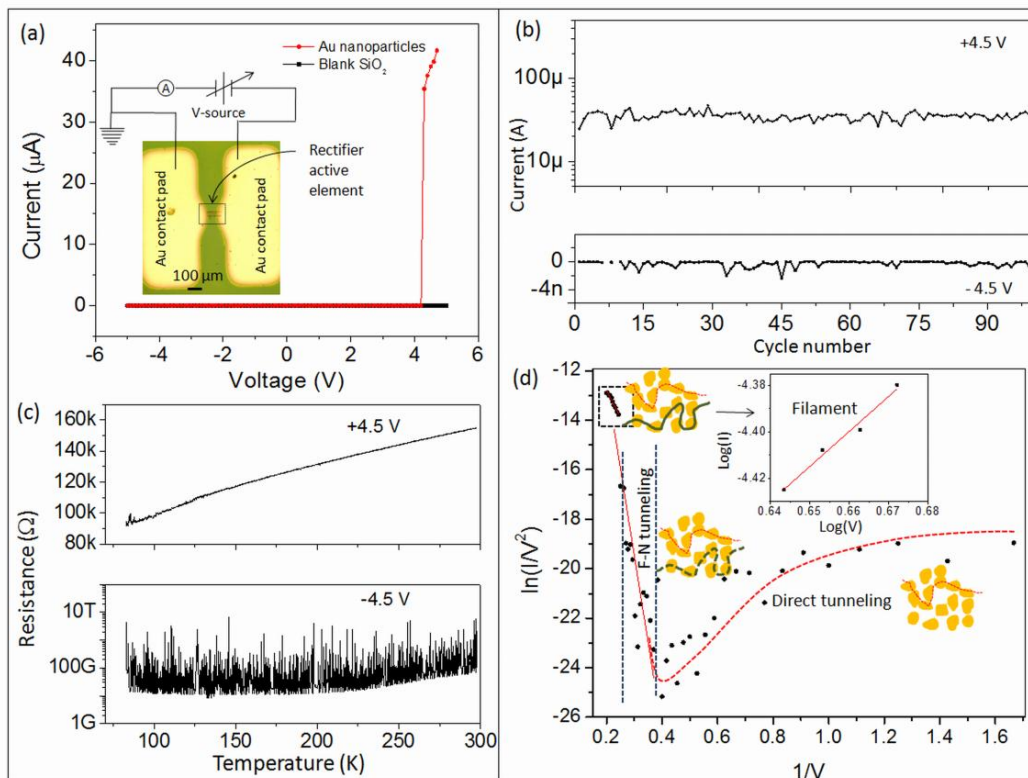
Figure IV.37 (a) Two probe I–V characteristics of the Au nanoparticle array stripes patterned by direct–write EBL (red, e–dosage ~783 μC/cm^2) on a SiO$_2$ (300 nm)/Si substrate along with that from the blank substrate (black). Inset shows an optical image of the device along with the schematic of the circuit. (b) Switching the applied voltage, +4.5 V and –4.5 V, in cycles and monitoring the current. (c) Low temperature resistance measurements on the rectifying device performed at +4.5 V and -4.5 V. (d) A F–N plot of the Au nanoparticle rectifier. Three regions, namely direct tunneling, F–N tunneling and filament mode of conduction are marked and schematics of conduction are shown along with. Inset shows log (I) vs log (V) plot above the threshold voltage.

Various reports in the literature have described rectification involving nanoparticles as due to different widths of the tunnel barriers on either sides of the nanoparticles [137] or due to asymmetric coupling of the nanoparticles at the electrode interfaces [165]. Where some slight movements are possible such as in Langmuir monolayers, collective realignment of the nanoparticle dipoles can lead to current rectification [136]. In the nanoparticle devices presented here, the direct–write EBL process produces well separated nanoparticles with no possibility of direct contact between the nanoparticles. As the electrodes are identical and the spacer molecules are practically absent, one cannot invoke rectification mechanisms relying on electrode or spacer induced asymmetries. Besides, the observed high rectification ratio of 10^5 cannot be expected from such asymmetries alone [166]. There might be other mechanisms at play. In the present device at negative or near zero bias, the conduction may rely on paths where the interparticle separations are of the order of ~1 nm, suitable for tunneling, leading to the low current region. As the conduction is due to tunneling, the resistance is nearly independent of temperature under such bias conditions (Figure IV.37c, at –4.5 V).The unsymmetrical nature of the I–V characteristics and the anisotropic shape of the nanoparticles along with the large interparticle spacings (1–25 nm) prompted us to think that besides direct tunneling, there must exist a Fowler–Nordheim (F–N) type polarity dependent tunneling. This is corroborated by the F–N plot shown in Figure IV.37d, the shape of which owes much to the changing shape of the tunnel barrier under varying bias [167,168]. Three regions were identified distinctly in bias dependent characteristics – direct tunneling (up to ~2.5 V), F–N tunneling (~2.5 to ~4.2 V) and transient filament formation due to field induced electromigration ($\geq$ 4.3 V).
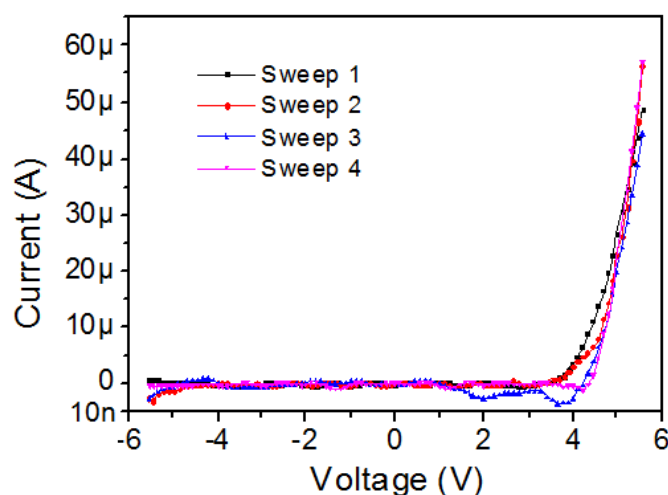
Figure IV.38 Successive I-V curves of another nanoparticle rectifier device from -5 V to +5 V. Threshold voltage of ~4.2 V was observed.

Although the particle asymmetry is not along any particular direction, under the electric field, percolative paths set in and link only the relevant nanoparticles, thus bringing in an unintentional asymmetry, for which the contact electrodes (being identical) have little role to play. The percolative path of F–N tunneling may involve sharp corners and rounded surfaces of the nanoparticles from one electrode to the other, the direction of easy flow of current (forward path) being along the path (see schematic diagrams in Figure IV.37d). The F–N tunneling equation is written as [167] :

$$In\left(\frac{I}{V^2}\right) = In\left(\frac{\alpha A(\beta^2/\phi)}{d^2}\right) - \frac{Bd\phi^{3/2}}{\beta}\frac{1}{V}$$

where I is the current; α, the emission area; V, the voltage (~2.5 V to ~4.2 V); d, the distance between the electrodes (~92 μm); ϕ, the work function of gold (5.1 eV); A and B are the constants given by 1.56×10^{-10} AV^{-2} eV and 6.83×10^3 V eV$^{-3/2}$ μm^{-1} respectively and β is the field enhancement factor. A plot of ln(I/V^2) versus (1/V) is linear in the range, 2.5 V to 4.2 V (see Figure IV.37d), the slope of which gave $\beta \sim 10^5$. In F–N tunneling involving metal nanostructures, such high values for β may be expected [169,170].

As the voltage is increased beyond 4.2 V, an additional mode of conduction by filament formation is possible. Such filaments may get formed due to electromigration as the electrical stress from the applied voltage can induce slight changes in the alignments of the nanoparticles or in the particle shape [136,171], with some contribution from joule heating as well. A plot of log (I) versus log (V) for the voltage range, 4.3 to 4.7 V, is found to be linear with a slope close to 1 (~1.3) indicating ohmic conduction [172] (see inset in Figure IV.37d). The low temperature measurement shown in Figure IV.37c for V = +4.5 V also confirms the metallic behavior. Only filament formation can account for the observed colossal increase in current to few μA. However, these filaments are not permanent contacts as no such features were seen in the SEM image of the device after operation. The fact that the current diminishes to less than few nA once the voltage is withdrawn (or opposite bias is applied), itself implies that these filaments are transient, present only under high bias condition. As the width of the nanoparticle array is limited to few μms, many such filaments cannot also be expected, thus limiting the diode action to perhaps only one or just few. Whether one or few paths, they ought to be unidirectional to bring in the desired asymmetry, which also means that paths in the opposite direction cannot be favored. This is essentially a morphology controlled device. Among the fabricated devices, some show rectification at positive bias voltages, while others on the negative bias; however this observation may not be of much significance as the electrode polarity is arbitrary as noted earlier.
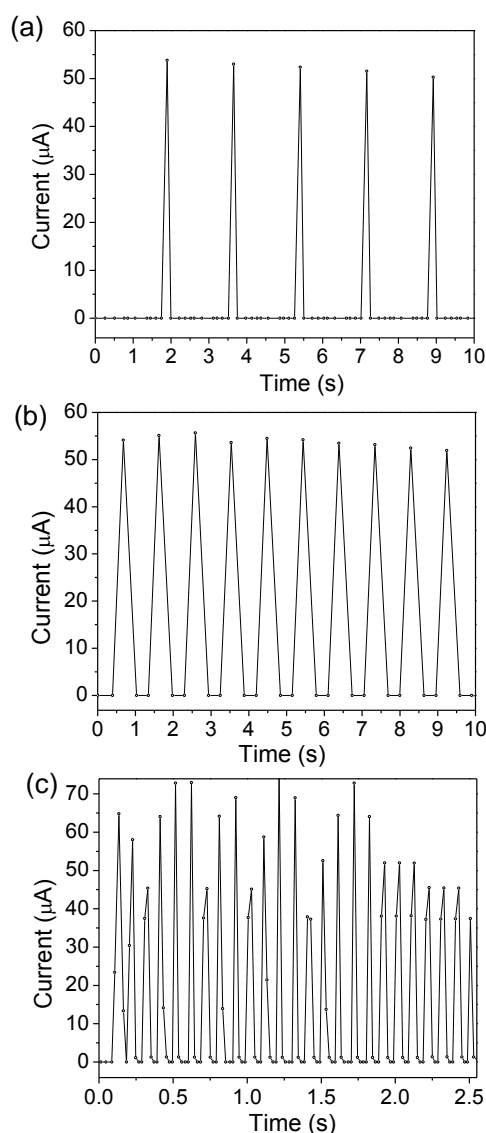
Figure IV.39 Rectification at different frequencies: Current vs time curves at a fixed applied voltage of 4.5 V for sine–wave of frequencies of (a) 0.5 Hz, (b) 1 Hz and (c) 10 Hz.

The rectifier action was studied for different sine wave frequencies (Figure IV.39). At lower frequencies, 0.5 and 1 Hz (Figure IV.39a and b respectively), the half–wave rectification was quite convincing, while at 10 Hz, small variations were seen in the forward bias current value. At higher frequencies (100 Hz or above), the device did not show a good response (not shown). Here, we compare the performance of our device with the literature reports on nanomaterial based rectifier systems, specifically the stand–alone devices which do not make use of other equipment such as scanning probe microscopes (Table IV.4). Compared to most devices listed in Table IV.4, the present device has relatively high threshold voltage, current and the rectification ratio, comparable to a CNT device [129]. Unlike the case of CNT based diodes, fabricating the active element and establishing electrical contacts with this device is rather straight forward.

Table IV.4 Comparison with typical stand–alone rectifiers reported in the literature

S. No.	Nanoparticle system	RR	V_{TH}	Current/ Current density	f	Ref
1	Graphene–metal junction	NA	~0.3	nA	NA	[133]
2	Graphene diode	NA	~0.3	µA	NA	[129]
3	SWNT p–n junction diode	NA	~0.2	µA	NA	[173]
4	SWNT diodes	10^5	~3	µA	1–1000 Hz	[174]
5	Organic polymer diode	10^3	~1.8	Few A/cm^2	NA	[175]
6	Molecular Junctions (Au–dithiocarbamate–Au nanoparticle)	1.35	~0.4	Few A/cm^2	NA	[163]
7	SAM–Based Tunneling Junctions	130	~0.6	mA/cm^2	NA	[176]
8	Langmuir monolayers of Au nanoparticles	NA	~0.2	<100 nA	NA	[136]
9	Polymer – Au nanoparticle composite	15	~0.1	mA/cm^2	NA	[132]
10	Fully tunable CNT diode	NA	~4.3	nA	NA	[129]
11	Au nanoparticle ordered array patterned by EBL	3.15 x10^5	~4.3	0.5 A/cm^2	Up to 10 Hz	Present work

NA: not available; RR: Rectification ratio; V_{TH} : Forward threshold voltage; f: frequency response

Tunability of the low–current region is an additional advantage with the present nanoparticle array rectifier. The I–V sweeps between ±5 V obtained after intermittently applying electrical stress at 8 V show that the low–current region can be made to shrink. From the magnified view in Figure IV.40a, the shrinkage was rather sudden after the first and second stress and becomes gradual thereafter, which is quantitatively shown in Figure IV.40b. By applying a stress of 15 V, the I–V data was made relatively linear! The shrinkage of the low–current region and increase in the forward current imply increased physical connectivity between the nanoparticles, involving permanent filament formation along the nanoparticle chain induced electrically. This observation further corroborates the mechanism of rectification explained earlier. E–beam dosage was also employed as a tool to vary the

nanoparticle size, spacing and thus the threshold voltage of the rectifier. At a lower e–dosage i.e., 78 μC/cm^2, smaller nanoparticles (mean size, ~19 nm) with lesser spacing were obtained (Figure IV.40c). The I–V curve showed a threshold voltage of 2.2 V (Figure IV.40d). At a much higher e–dosage (1566 μC/cm^2), the rectification was lost (Figure IV.41).
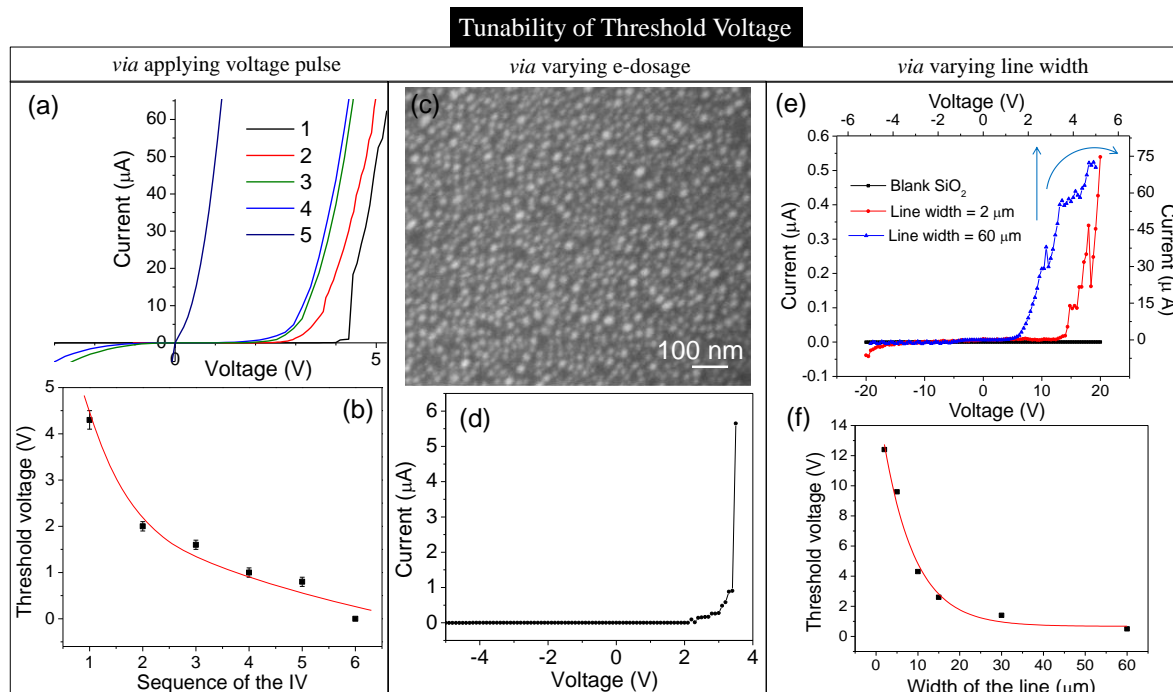
Figure IV.40 Tunability of threshold voltage – (a) Sequential I–V characteristics from –5V to +5V. After each sweep, an electrical stress of 8 V was applied. The low–current region being shrunk as higher voltages are applied. I–V characteristic named 5 was obtained after stressing with 15V. (b) The threshold voltage of the rectifier device for the successive sweeps plotted vs sweep number (the line drawn is only a guide to eye). A lower threshold voltage could also be obtained by varying the e–dosage use for Au nanoparticle array formation. (c) SEM image of the Au nanoparticle array produced by e–dosage of 78 μC/cm^2. (d) I–V characteristics of the resulting rectifier. (e) I-V characteristics of rectifiers with varying line-widths of Au nanoparticle arrays. (f) Threshold voltage versus line width of the nanoparticle array.
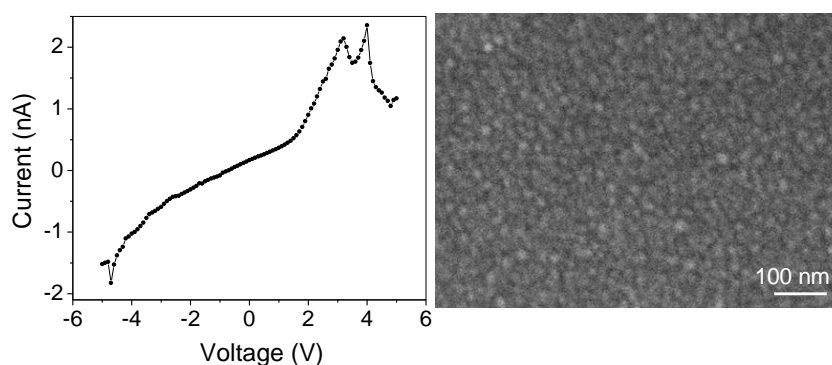
Figure IV.41 I-V characteristics of the rectifier obtained at an e-dosage of 1566 μC/cm2. As seen in the SEM image on right, Au nanoparticles are densely packed, with direct contact between them. The rectification is no more present.

In order to understand the effect of line width of the Au nanoparticle array on the rectifier characteristics, a systematic study was performed with different line widths of the nanoparticle rectifier stripes i.e., 2, 5, 15, 30 and 60 μm (in addition to 10 μm). As the width of the array increased, the threshold voltage decreased (Figure IV.40e and f). For instance, in the case of 60 μm, the rectifier characteristics showed a threshold voltage of ~0.5 V, much lower than that seen in the case of 10 μm stripes (~4.3 V). The increased width of the rectifier element thus leads to more F-N tunnel paths. Concomitantly, the current also increased considerably (see Figure IV.40e and IV.42).
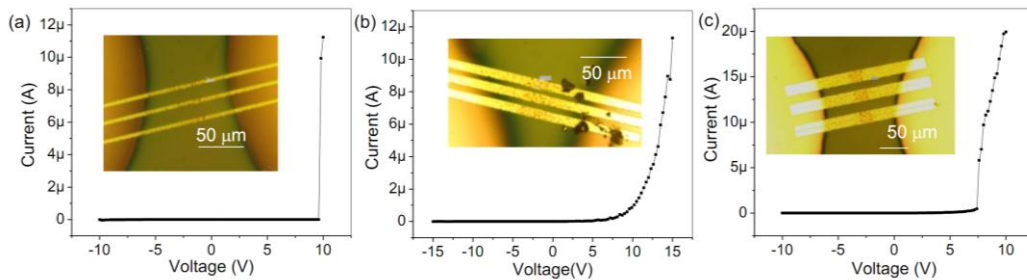
Figure IV.42 I-V characteristics of the rectifier with Au nanoparticle stripes of width (a) 5 μm, (b) 15 μm and (c) 30 μm. The insets show the respective optical images.
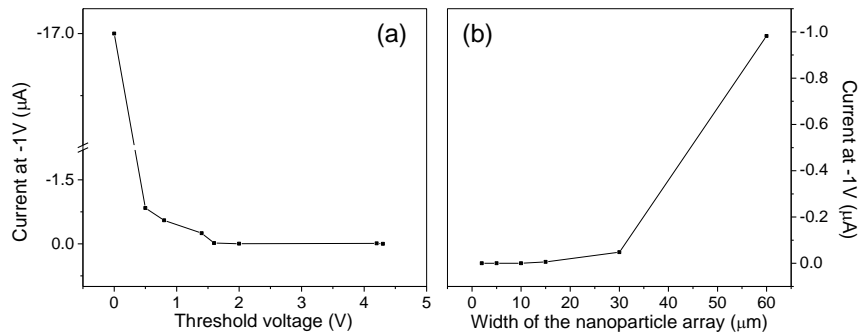
Figure IV.43 Current in the negative bias (at -1V) with (a) threshold voltage and (b) nanoparticle array width for various rectifier devices presented in the study.

Indeed, the variation of threshold voltage exhibits a smooth trend with the line width (Figure IV.40f). On the other hand, with the line width of 2 μm, the threshold voltage is beyond 12 V and the forward current is also comparatively less! The other important observation is that the reverse current increases with the line width, as expected due to increased direct tunneling paths (Figure IV.43). Also, the current in the reverse bias increases with the decreasing threshold voltage. We observe good rectification at threshold voltages ≥ 1.5V (Figure IV.43). A different contact scheme was attempted as well. Instead of Au, Ni metal was used for contacting the nanocrystal array. The diode action was repeatable with nearly similar characteristics. This further strengthened the notion of Au nanoparticle based rectification.

The Au nanoparticle array stripes were transferred (obtained with ~783 $\mu C/cm^2$) to a flexible substrate i.e., poly(dimethylsiloxane) (PDMS). By masking the stripes on PDMS, Au deposition was done to define the contact pads (Figure IV.44a). Upon closely examining the stripes (inset in Figure IV.44b),we observe wrinkles on the PDMS surface which are a result of the PDMS shrinkage during curing [177]. This is expected to have some influence on the interparticle spacing. Although our efforts using SEM were unsuccessful because of surface charging of the substrate, there is enough evidence in the literature that PDMS shrinkage can cause a mismatch in the registry of the transferred patterns [178]. Thus, the I–V characteristics in Figure IV.44c, no longer shows a flat gap region near zero bias (compared with Figure IV.37a) but exhibits a finite slope extending on both sides of zero bias indicating that the conducting paths now involve nanoparticles in contact, though the contact may be very subtle. At a higher positive bias (~ +3.1 V), however, the slope increased (Figure IV.44b) further pointing to a similar mechanism that prevails in devices hosted on SiO_2/Si substrates.
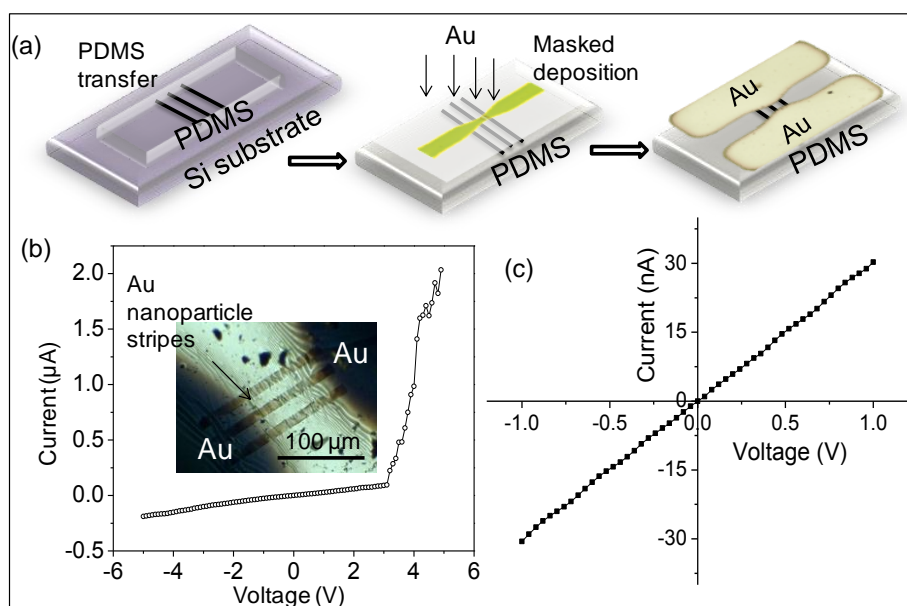
Figure IV.44 (a) Schematic showing the transfer of patterned Au nanoparticles onto a PDMS substrate and masked deposition of Au contact pads. (b) I–V characteristics of the device obtained in different voltage ranges. Optical image in the transmission mode of the obtained device is shown as inset. The wrinkles developed due to shrinkage of PDMS. (c) I–V characteristics in the low bias region showing no blockade.

As PDMS is flexible, the nanoparticle contact can be manipulated (Figure IV.45). One simple way to do this is to swell PDMS by an organic solvent such as toluene [179]. A brief exposure to toluene brought down the current in the device to under 50 pA (red curve, Figure IV.45a), indicating that nanoparticle contacts along the conducting paths were

weakened due to swelling of the substrate. Interestingly, the current in the device nearly regained as the substrate gradually put out toluene by evaporation (Figure IV.45a). The substrate was reversibly swollen and deswollen in many cycles and the effect on I–V characteristics was observed (Figure IV.45b).
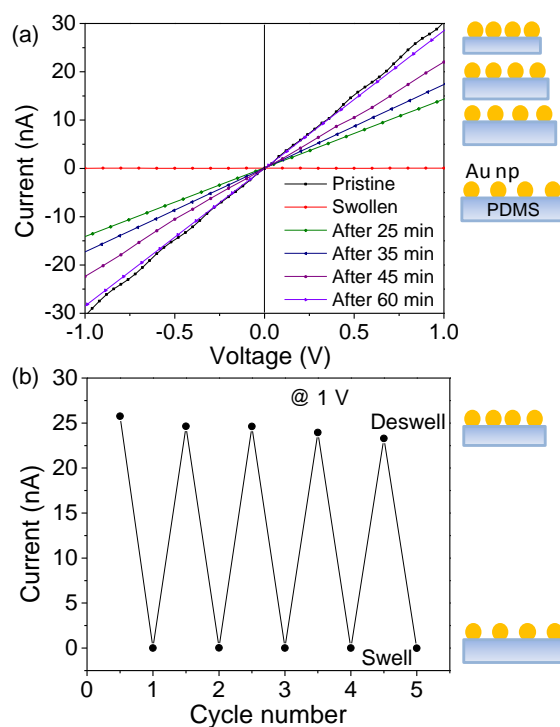
Figure IV.45 (a) I–V characteristics collected during deswelling of toluene–treated PDMS carrying the rectifier device, at different time intervals. (b) Swell–deswell cycles monitored with the device. The schematic illustrations are shown alongside.

Finally, for specific applications, nanoparticle arrays can be made electrically continuous on chosen substrates by filling in interparticle regions with electroless deposition of Au (Figure IV.46). In order to realize electrically continuous conduits of Au, electroless deposition of Au was employed onto the preformed Au nanoparticles. Patterns defined by EBL lead to Au nanoparticles in specific sites, which act as seeds for further electroless deposition of Au. Figure IV.46a shows the XRD pattern of electrolessly deposited Au onto EBL defined Au nanoparticle array. Electroless deposition preserves the (111) orientation of the as-made Au nanoparticles, as shown by huge peak of (111) in XRD. SEM images showing Au nanoparticles before and after electroless deposition are shown as insets in Figure IV.46a. Current-voltage characteristics shown in Figure IV.46b reveal highly conducting nature, following electroless deposition.
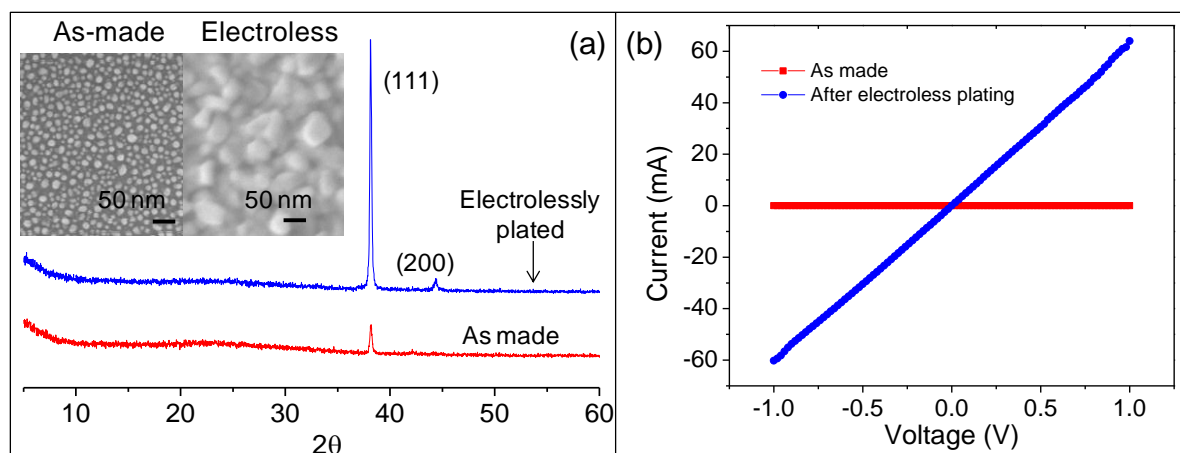
Figure IV.46 (a) XRD patterns of the e-beam exposed, developed and thermolysed Au-ToABr film (red) along with that after electroless Au deposition (blue). Insets show the particle morphology in the two cases (b) Current-Voltage measurements on the as-made film along with that after electroless Au deposition. Well-connected nanoparticles in the latter produce large current.

IV.5.4 Conclusions

Patterned regions of Au nanoparticle arrays with a reasonable control on particle size and spacing were produced. The rectifier contains nanoparticles of different shapes with sharp corners and blunt surfaces, yet maintaining several nanometer wide spacing, a property which was exploited in fabricating a diode. Electrical transport measurements across patterned Au nanoparticle array stripes (~10 μm wide) have shown rectification with a rectification ratio of 3×10^5 and the forward bias threshold voltage of +4.3 V. The threshold voltage can be tuned by applying higher voltage stress, by varying e-dosage or the line width. Tunability of the threshold voltage represents an important property of rectifier and is extremely useful for complementary logic circuits using nanoelectronics. The proposed mechanism of rectification is F–N tunneling, which leads to transient filament formation due to field induced electromigration after the threshold voltage. Low temperature measurements above threshold voltage have confirmed the metallic state of conduction. Finally, the device fabrication described in this article opens up many possibilities where the interparticle spacing as monitored through the tunnel current serves as a guiding factor for an application. It was demonstrated that how swelling and deswelling of a PDMS substrate carrying the device and exposed to toluene can be monitored. The simplicity of this *all–gold* device fabrication by direct write EBL is clearly an attraction.

IV.6 FREE STANDING AU MICROPLATES AS LARGE AREA TOP-CONTACTING ELECTRODES FOR MOLECULAR ELECTRONICS

IV.6.1 Introduction

Transcending Moore's law, molecules are the choice of future nanoelectronics, as they represent ultimate miniaturized active elements [180]. Beginning from the seminal work by Aviram and Ratner in 1974 [181] there have been hundred reports on molecules in electronics. Various molecules starting from simple alkanethiols to conjugated monolayers have been investigated for electrical transport using different experimental methods as well as theoretical simulations for applications in interconnects, diodes, transistors, logic circuits, photovoltaics, lubricants as well as for negative differential resistance and memory applications [143]. In this context, several nanofabrication methods [182] and device architectures [183] have been explored for making molecular test beds [184]. For contacting molecules, generally a densely packed self-assembled monolayer (SAM) of the molecules is formed on a substrate, followed by deposition of noble or semi-noble metal onto the SAM [185]. Unfortunately this approach suffers from electrical shorts through defect areas in the SAM which leads to the yield of working devices to be astonishingly low i.e., <1% [186]. Although possible damage to the molecules can be minimized using methods like cold evaporation of the top metal [187], nanopore model for top electrode [188] but very difficult to completely avoid. Scanning probe methods [189], hanging mercury electrode [190], cross wire junctions [191], break junctions [143], self-assembled nanogaps formed by nanorods coupled to molecules [192], multi-layer edge devices where molecules are bridged vertically [182], surface diffusion mediated soft contact deposition [193], nanotransfer printing [187] etc., are some of the other methods which have been utilized towards this end. Large area molecular junctions were proposed using a PEDOT:PSS layer [194] or a graphene interlayer [195,196] beneath the top Au electrode to prevent shorts. A eutectic liquid metal (Ga-In) stabilized inside microchannels has also been proposed [176,197] to serve as large area electrode with conformal contact to molecules. Metal free electrodes were proposed to circumvent the problem of electromigration of metal forming shorts. All carbon molecular junctions have been investigated in this context, but the specific contact resistance was higher [198]. Vertical nanogaps created with Si top and bottom electrodes (on SiO_2) have been utilized for measuring molecular properties [199], but it was found later that SiO_2 was also participating in the conduction along with molecules [200]. Most reports dealing with molecular electronics report the electrical characteristics of simple alkanethiols first, much

like the toddler way of starting. The tunneling current density, J, of alkanethiol molecules shows an exponential dependence, described by [$J \propto \exp(-\beta N)$] on the number of carbons atoms, N, in the alkyl chain, where β is the decay constant. The exponential decay factor β is considered as one of the good indication for testing the accuracy of a molecular test bed.

IV.6.2 Scope of the present investigation

While the afore-discussed device architectures are useful for studying molecular conduction processes, they do not possess exposed regions of molecules for chemical sensing. Alternatively, exotic materials such as strained semiconductor nanomembranes [168] were also proposed as top electrodes recently. A simple and easy-to-fabricate method with self-standing top electrode, for local electrical measurement of molecules not forming electrical shorts and not embedding the molecules, is still a challenge, which is the thrust of the present work. For this purpose, single crystalline Au electrode was chosen instead of conventionally employed polycrystalline Au. The method of simple and reproducible chemical synthesis of large area single crystalline Au microplates of controllable sizes (as described in Part II) has propelled the present work where the microplates find their place either as a top electrode for molecules. This proposed device promises an unprecedented synergic combination of versatility and off the shelf independence.

IV.6.3 Results and Discussion

Figure IV.47a schematically describes the fabrication steps of the proposed micro-sandwich molecular device. The device fabrication starts with well cleaned glass slides which were deposited with a thin (~40 nm) layer of Au by PVD; this serves as bottom electrode of the micro-sandwich. Shadow masking resulted in two electrically isolated Au pads. Single crystalline Au microplates were synthesized chemically using a single step thermolysis of $(AuCl_4)^-$–tetraoctylammonium bromide complex in air, as described in Part II, possessing hexagonal and triangular shapes with areas extending over ~80,000 μm^2 and thickness in the range 30–1000 nm. As noted previously, the microplates are self-supporting and can be easily manipulated using simple metal pins attached to a 3-axis differential micrometer driven stage-Nanomax TS or manually using an improvised micromanipulating tool developed by longitudinally inserting a chemically etched sharp Cu wire into a capillary tube. A microplate was marshaled (using any of the methods stated above) towards the gap at the end of one Au contact pad on glass. Then, a carbon fibre (~6-10 μm thick and ~150 to 200 μm long), coated with Pd hexadecylthiolate on both ends, and air-dried was placed with

its one end over the Au microplate electrode and the other end resting over the adjacent electrically isolated Au contact pad. Then the assembled system was heated on a hot plate in ambient at 250 °C for 1 hr. Pd hexadecylthiolate acts as a nanosolder [201] after thermolysis leading to a robust electrical contact between the C-fibre and the Au electrodes. The fabricated device (Figure IV.47c and d) can be stored without any considerable degradation and can be used directly for molecular self-assembly after a simple rinse with toluene. To assay the micro-sandwich ability to incisively study the electrical properties of assembled molecules, alkanethiol molecules were chosen as a model system, as copious amount of literature is extant on these molecules using CAFM, STM, nanopores, break junctions, cross bars and other molecular test beds [180,202]. The molecules were self-assembled between the top and bottom electrodes, formed by the Au microplate and the Au contact pad respectively, by immersing the device in a 50 mM solution of the required alkanethiol or alkanedithiol in toluene overnight (Figure IV.47b).
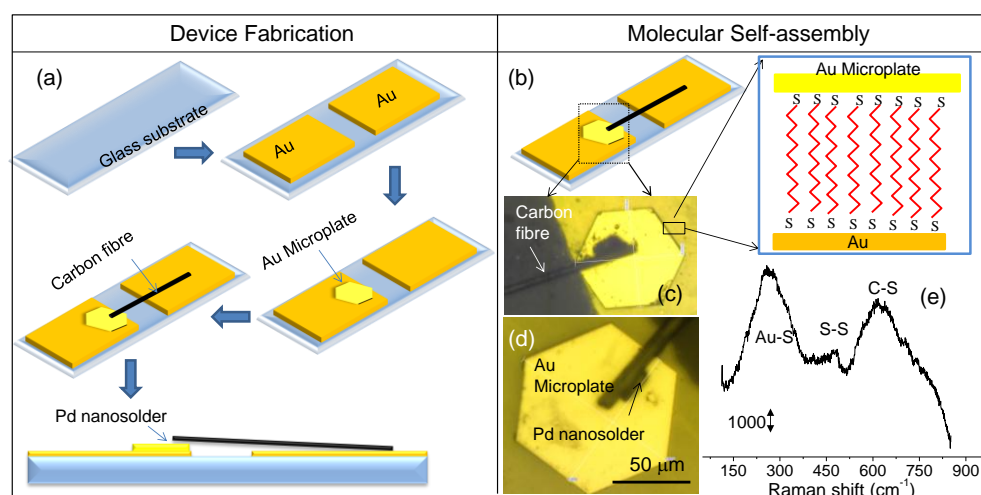
Figure IV.47 Schematic of device fabrication steps and molecular self-assembly – (a) A cleaned glass slide was deposited with Au gap electrodes by shadow masking using PVD. This is preceded by the placement of large crystalline Au microplates as top electrodes. Carbon fibre is attached in between the Au plate and the pad with a nanosolder. (b) Alkanedithiol molecules assembled between the Au electrodes by immersion. (c) Optical image of the made device. (d) Magnified view of the microplate and (e) Raman spectrum showing the characteristic peaks of the assembled molecules.

After the self-assembly, the device was washed carefully with excess toluene and gently dried with N_2 and then the devices were ready for further electrical and mechanical analysis. Raman spectroscopy was performed on a device to characterize the assembled dithiol molecules. The spectrogram (Figure IV.47e) showed two broad peaks at about ~248 and ~618 cm^{-1} corresponding to that of Au-S, C-S stretch respectively. In addition, a S-S

shoulder stretch (~510 cm^{-1}) was observed which could be due to dimer formation in dithiols. A schematic of the self-assembled molecules between the electrodes is shown in Figure IV.47b.

Various alkanedithiol (hexanedithiol-C6D, octanedithiol C8D and decanedithiol C10D) and alkanemonothiol (C10M, C12M, C14M) molecules have been brought into the Au microplate micro-sandwich device. Figure IV.48a shows the I-V characteristics of the microplate sandwich device with and without C8D molecules. Clearly with molecules in between, the current is much diminished compared to that seen during direct contact between the Au microplate and bottom Au electrode. The temperature independent I-V characteristics of octanedithiol molecule indicate the tunneling conduction [185] (Figure IV.48b). The current density (J) was obtained by dividing the current (I) by the area (A) of the microplate electrode. For instance, an area of the microplate ~2344 μm^2 and a current of 0.0027 A (at 0.5 V from Figure IV.48b) resulted in a current density of $0.00428/(2344 \times 10^{-12})$ = 1.826 x 10^6 A/m^2. Assuming a molecular packing density of 4.67 x10^{18} molecules per m^2, total number of molecules = 2343.8 x 4.67 x 10^{18} x 10^{-12} = 10945.5 x 10^6 molecules and thus the current per molecule = total current / number of molecules = 0.25 pA. The resistance per molecule comes to be 2 x10^3 GΩ, which is comparable with the value reported for this molecule in large area junctions using nanopore, Hg junctions or polymer under layer [203]. The J-V data plotted in Figure IV.48c, demonstrate the exponential dependence of the current density on the length of the alkanethiols, which further reaffirms the non-resonant direct tunneling to be the predominant mechanism for conduction. The J-V characteristics depend mainly on the molecular length and also on the type of contact with the disparity between monothiol and dithiol molecules arising out of the differences of chemisorbed and physisorbed interface with either the Au contact pad or the Au top electrode. Mostly, the molecules will prefer to get chemisorbed on to the atomically flat top Au microplate electrode over the bottom Au because of the surface geometry. The difference in the conductances of C10M and C10D; with C10D having a higher conductance than of C10M junctions is in tune with the typical metal–molecule contact properties of physisorbtion vs. chemisorbtion contacts at the Au-molecule contacts [204]. Figure IV.48d shows a semi-log plot of the current density J measured as a function of the number of carbon atoms in the molecules. The decay coefficient per carbon atom (β) was determined from the slope of the linear fits when semi-log of J was plotted against the number of carbon atoms. The value of β was separately obtained from the linear fits of the plots of monothiols and dithiols. The

obtained value for β was 0.95± 0.12 and 0.44 ± 0.13 for dithiols and monothiols respectively which is in good agreement with previously reported values for alkanethiol junctions [202]. From the plot in Figure IV.48d, R_a (= Resistance x area, i.e., resistance value compensated for the molecular junction area) was extracted and plotted versus the number of carbon atoms. The extrapolation of R_a to the number of carbons as zero on x-axis, i.e., to a state of zero molecule length, gives R_c, the specific contact resistance. The values of R_c for monothiols and dithiols were found to be 6.4×10^{-7} and 4.7×10^{-9} Ohm.cm^2 respectively. The contact resistance was lower for dithiols owing to the chemisorbtion on both top and bottom Au electrodes and the values can be compared with metal top contacts for molecules [205] and conducting probe based methods [198,206].
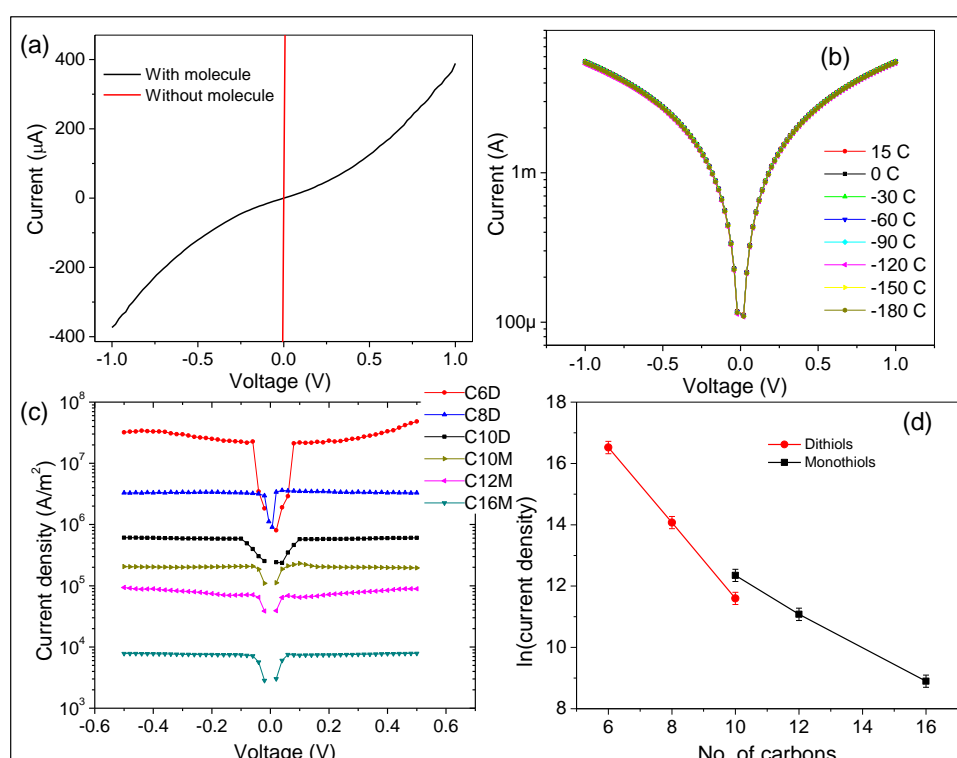
Figure IV.48 (a) I-V characteristics of octanedithiol (C8D) molecule along with the blank Au microplate electrode when placed on Au contact pad without any molecule in between. (b) Temperature independent I-V characteristics of the C8D molecule showing the typical tunneling behavior. (c) J-V data of molecular devices with dithiols (C6D, C8D, C10D) and monothiols (C10M, C12M, and C16M). (d) A semi-log plot of *J* versus the number of carbon atoms, the slope of which, gives the β for both monothiols and dithiols.

Stability of the molecular sandwich:

Although the literature is plenteous in methods and techniques which can electrically characterize the molecular monolayers, there is relatively less emphasis on the retention, electrical and mechanical stability including the shelf life of the device before and after self-assembly. This requires the electrode system to be mechanically robust while preserving the

electrical contact with molecules. Encapsulating the micro-sandwich device after self-assembly of the molecules, proved to be the most viable method to improve the durability and operational stability. The encapsulation was done by covering up electrode setup with a thin poly(dimethylsiloxane) i.e., PDMS sheet (~10 microns thick). As such, the fabrication of very thin PDMS sheet is not easy as it self-wrinkles/folds while peeling off, because of its extremely sticky nature. Here, the thin sheet of PDMS was fabricated by spin coating the PDMS on a preformed thin layer of poly(vinyl alcohol) (PVA). PVA (1 wt% solution in water) was spincoated as a thin film; it was chosen due of its differential solubility with PDMS. The thin film of PDMS was formed by spincoating the degassed mixture of elastomer and curing agent (in 10:1 ratio) on PVA thin film and was cured at room temperature for 12 hrs. Further, PVA was removed by dissolving in water, releasing the PDMS thin film. Thus obtained PDMS sheet was carefully placed over the fully formed device after self-assembly by observing under a microscope. The PDMS sheet conformally encapsulated the device (Figure IV.49b) protecting it from considerable physical perturbations. Figure IV.49a shows the current-voltage characteristics before encapsulation and after 1000 s post encapsulation. It is clearly visible that the current increased considerably. This could be attributed to the change in the distance between the two electrodes due to extra weight of the PDMS sheet. The decrease in the distance between the two electrodes could contribute to increased tunneling current. It was clear from the optical image (Figure IV.49b) that the thin layer of PDMS has conformal contact around the electrode arrangement. The conformity of the encapsulation was tested by dipping the device in ethanol for 10 min and even after that there is no considerable change in the resistance of the device. This particular arrangement allows for the freedom of long shelf life.
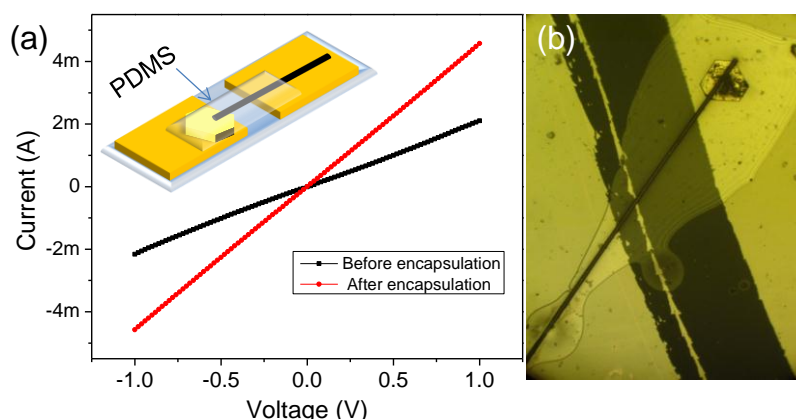
Figure IV.49 (a) I-V characteristics of the device before and after encapsulation by PDMS sheet and (b) Optical image of the PDMS encapsulated device with the polymer conforming to the Au microplate.

For the presented molecular devices, endurance [196], retention and stability were studied using the case of C8D devices. By applying opposite bias pulses of 1 V continuously while measuring the current (positive current I^+, at +1 V and the negative current I^-, at -1 V) with an interval of 1 s. Up to 10^4s, the device was robust without any significant degradation (Figure IV.50a).
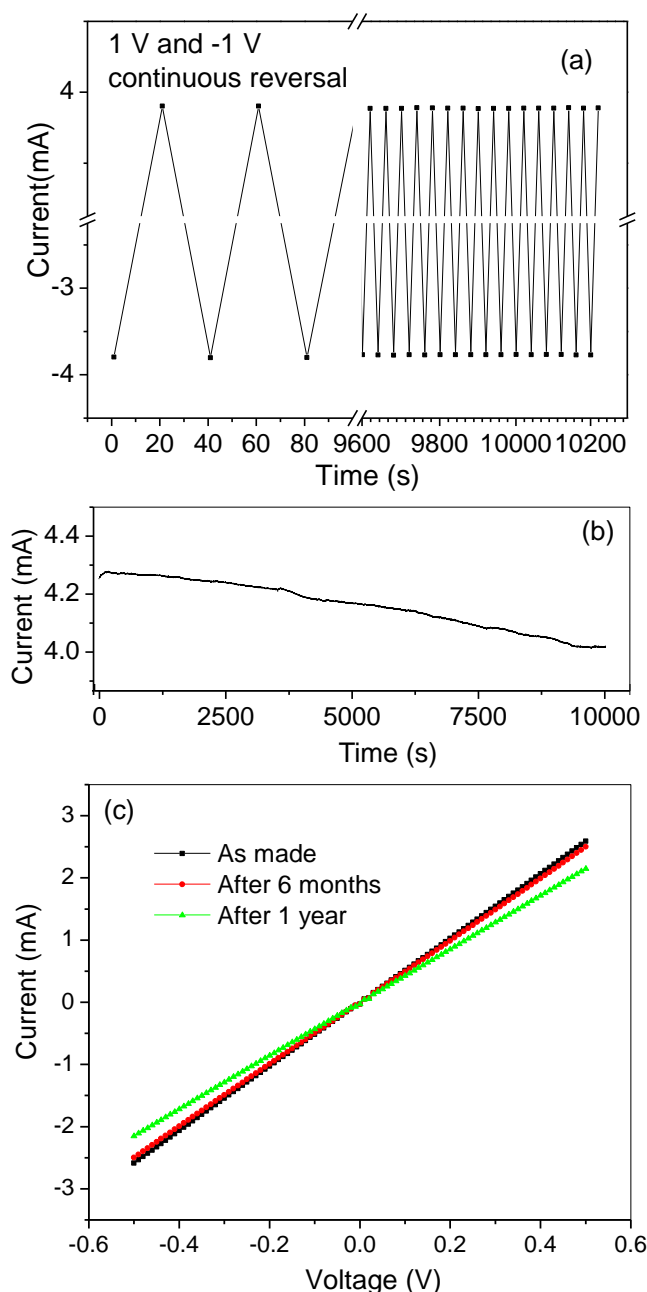
Figure IV.50 (a) Endurance characteristics of the molecular sandwich obtained by applying the voltage pulses of +1 V and -1V and monitoring the current while switching the pulses. The measurement was done for 10000 sec with an interval $\Delta t = 20s$. (b) Retention characteristics of the molecular junction obtained via current measurement at a constant applied bias of 1 V. (c) Retention characteristics of another device showing the pristine IV characteristics and the IV obtained after 6 months and 1 year of storing in ambient conditions at room temperature.

The molecular device sustains voltage stressing cum continuous voltage pulsing and does not form electrical shorts due to electromigration. This might be due to the single crystalline, atomically flat nature of the Au microplate electrode and thus the SAM contacts the top electrode very efficiently. Figure IV.50b shows the results of operational stability of C8D device obtained by measuring the current as a function of time at a constant applied bias of 1 V for 10^4 s. Figure IV.50c shows the comparison of the IV characteristics of the pristine device and the device after storing it in ambient conditions for 1 year without considerable degradation in the current characteristics. These results demonstrate the exceptional and improved stability of the encapsulated molecular device.

Dynamic thermal and mechanical analysis of the molecular sandwich:

The dynamic analysis of the thermal and mechanical loads on the molecules has also been appreciably studied and researched for its profound applications in a variety of fields. Thermal analysis of the phase transitions in the alkanethiol SAMs has been intensely investigated using spectroscopy [207-209], thermal desorption spectroscopy [210], scanning tunneling microscopy [211] along with the electrical analysis [196,212]. It has been predicted that above 350 K i.e., 77 °C, there is an irreversible transition due to the desorbtion of the SAM from the metallic surface, whereas below 350 K, the transitions are reversible and occur due to gradual untilting of the chains combined with the emergence of gauche defects in the chains [207]. The molecular sandwich devices have been probed for the thermal stability and phase transitions (Figure IV.51).
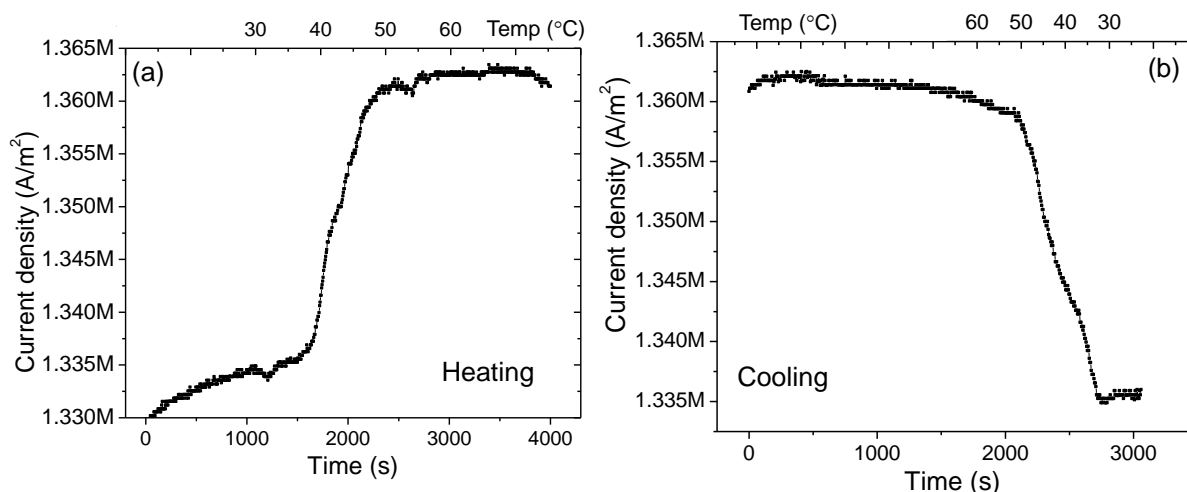
Figure IV.51 Current versus temperature/time while (a) heating and (b) cooling the sandwich device from room temperature to 60 °C showing reversible change in resistance of the molecules in the encapsulated device.

When the device was heated while measuring the current, there was an increase in the current above 45 °C (Figure IV.51a). After heating to about 60 °C, the device was cooled back to understand if the change in current was reversible. Indeed, the current retraced back while cooling back to room temperature, giving rise to almost similar current at room temperature what was measured before heating the device (Figure IV.51b).
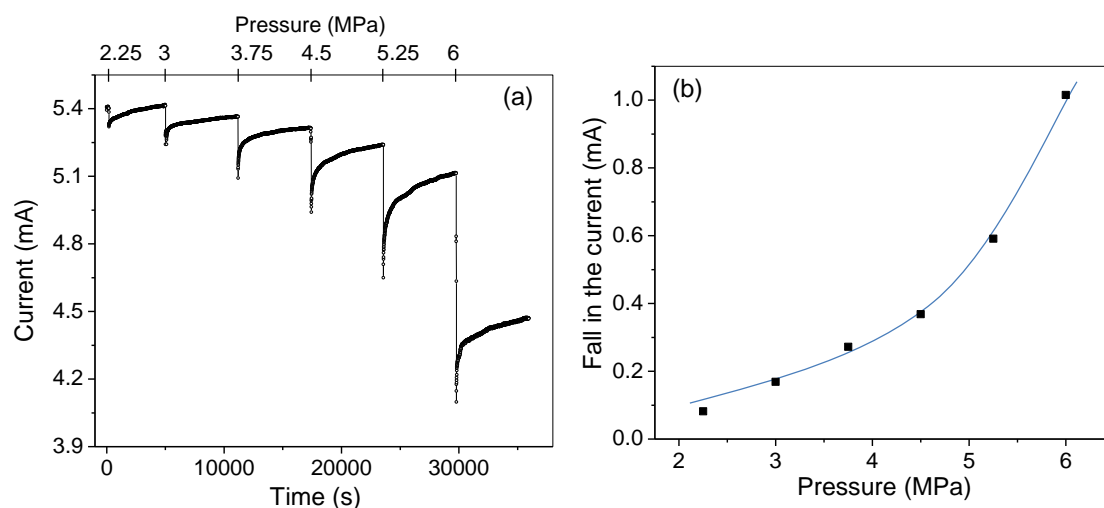
Figure IV.52 (a) The change in conductivity of the molecules assembled in the device with mechanical loading. (b) The fall in the current vs the loaded weight (the line drawn is a guide to eye).

A preliminary study was carried out to see the response of the SAM to mechanical loads in terms of real-time analysis of the electrical response while compressing. It has been shown that an array of self-assembled molecules has an inherent anelastic nature having a linear combination of elastic and damping component [213]. This is considered to be the reason why the molecules take some time to recover from a mechanically distorted state and show considerable hysteresis during the compression-relaxation cycle [213,214]. Here, this was studied with the encapsulated molecular (octanedithiol) sandwich device by putting load via placing series of known weights over the molecular test bed. For this purpose over the thin layer of PDMS, a thicker (~30-50 µm) layer of PDMS was placed for the cushioning action so as to prevent the weight from disturbing the electrodes set up. The change in the electrical conduction of the molecules was measured while loading dynamically for predicting the response of the molecules to loading, as the conduction through the molecules may vary commensurately with the mechanical deformation developed by cooperative tilting and gauche defects [215]. In the literature, for studying compression of molecules, experimental process is based on fixed relative displacement [213] but in the present experiment, the loading resulted in force acting directly upon the sandwiched molecules.

There is a sharp decrease in the current while loading as the molecules get compressed and tend to come closer and in turn develop defects in the assembly. The defects along the molecular chain may cause extra scattering. But the chemisorbed molecules spontaneously reorganize themselves and concomitantly, the current in the circuit regains. But this takes place quite gradually [213,214]. This is clear from the Figure IV.52b where the degree of decrease in the current is proportional to the weight being loaded; the heavier the weight, the more the fall. The time constant as such could not be calculated as the curve profiles were slightly different for different weights. Preliminary analysis shows that the relaxation curve consists of two slopes; one could be related to the relaxation of impact of the load and the other due to gradual relaxation of SAM. Above 6 MPa of load pressure, the sandwich device got destroyed due to the physical displacement of the top electrode.

Electrical analysis of biomolecules using molecular sandwich:
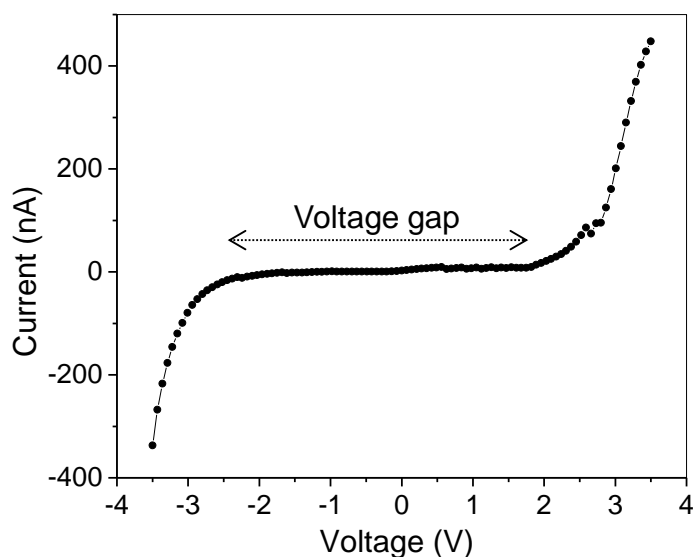
Figure IV.53 Current versus voltage characteristics of the 30A thiolated ss-DNA molecule.

Apart from alkanethiol monolayers, biomolecules can also be probed using the molecular sandwich assembly. Among other biomolecules, there is a lot of interest in the DNA nanoelectronics due to its exciting properties in that it can adopt various states and conformations and thus becomes a storehouse or blueprint of life [216,217]. Of course, it has been a challenging task to get the reliable data by contacting large number of DNA molecules due to experimental difficulties in fabricating such nanogaps [217,218]. As an attempt to top contact vertical DNA SAMs, Hg electrodes have been employed [219]. Here, thiolated single-stranded 30-mer DNA possessing 30 adenine units was electrically analysed using the molecular sandwich. Thiol-modified oligonucleotides are usually in the protected

form with the disulfide linkages which minimizes the oxidation, but this usually results in dimer formation. To use the free thiolends, the thiolated oligonucleotides were treated with the deprotecting agent dithiothreitol (DTT). The DNA solution (6.7 ng/μL) was mixed with DTT (100 mM) solution in phosphate buffer (pH = 8.3), following which the DTT was desalted/removed by filtration. In the current-voltage characteristics, a distinct blockade was observed at low bias (Figure IV.53). This has been a distinctive electrical feature of DNA called as 'voltage gap'. Such a voltage gap has been observed in electrical analysis of DNA when measured as a single molecule using CNT electrodes [220] as well as using a number of DNA molecules by various methods as documented in the review [217]. The origin of the voltage gap has been attributed to the offset between the electrode's Fermi level and the molecular energy bands of the DNA molecule [221].

IV.6.4 Conclusions

An innovative large area contact sandwiched metal-molecule-metal electrode arrangement is proposed for electrical analysis of molecules. The top contact was essentially a single-crystalline and atomically smooth Au microplate contacted with C-fibre. The device works in capacitor geometry with SAM in between the top and bottom metal electrodes. It could be used off-the-shelf any time for further studies without any processing. The electrical characteristics of the alkanethiols, dithiols and DNA were tested and the exponential decay parameter, β value, verified that the device was indeed a decent molecular testbed. Polymer encapsulation of the device greatly enhanced the stability of the device. This device promises new ways of analysis particularly involving dynamic studies such as thermal phase transitions. As a proof-of-concept, a simple electrical analysis of the molecular sandwich capacitor indeed becomes a handy tool to study the effect of load on molecules. The major advantage of the proposed device is its ability to be stocked after fabrication for off-the-peg self-assembly. Also, both the top and bottom electrodes can be designed as Au microplates, for improving the device performance.

IV.7 LARGE AREA OHMIC TOP CONTACTS TO VERTICALLY GROWN NANOWIRES USING A FREE-STANDING AU MICROPLATE ELECTRODE

IV.7.1 Introduction

One-dimensional structures such as carbon nanotubes and semiconductor nanowires (NWs) are explicitly foreseen as realistic candidates for modern electronic applications [222]. Vertically grown nanotubes and NWs especially are of paramount importance in applications such as energy storage [223], sensing [224], power generation [225], light emitting diodes [226], and solid state lighting [227]. Voltage generation using piezoresponsive materials has also been shown to be most effective in vertical geometry [228]. While contacting every individual NW and sourcing the tiny charge or signal from it are important for effective usage in technological applications [229], it is extremely challenging to employ the pick-and-place method in routine device fabrication. Thus, top contacting vertically grown NWs is still a pertinent issue in the literature [222]. Although drawing individual contacts out is desirable, it is not usually required; a canopy of networked contacts serves most applications. An additional complication is often posed by the typically large variation in the heights of the vertical NWs [230,231]. In this work, the top contacting of an array of vertically grown NWs of varying heights is demonstrated while overcoming the fabrication drawbacks.

Top contacting individual NWs has been achieved using scanning probe techniques - conducting atomic force microscope [232,233] and scanning tunneling microscope [234], and of late, nanoprobe [235] and air-bridge connection [236]. While these techniques have been largely successful, they are time consuming and, importantly, may not give rise to stand-alone devices. An alternate but somewhat compromising method is to top-contact a number of vertical NWs using large area electrodes. Deposition of a metal film, say by physical vapor deposition, would not work as the metal seeps through the voids in between the NWs and shorts with the bottom electrode. In order to avoid this, the NWs are typically first embedded in a dielectric layer such as a polymer. Planarazation is then performed to get NWs of the desired length [237]. Following etching of the polymer to expose the tips of the NWs, a metal film is deposited on top as the contact pad [7]. ZnO NWs based power generators have been realised by the above method. Recently, a flexible CNT film was used as a top electrode for pillared CuI structures in a solar cell [238].

IV.7.2 Scope of the present investigation

A simple and generic method for top contacting vertically grown nanowires of uneven heights is not attended to hitherto in the literature. Also, the NWs need to be exposed for certain applications. Here a method of bringing even shorter NWs into ohmic contact.is described. The NW sample in this study was chosen to have a broad distribution in the height of the NWs and the effort was to bring maximum number of NWs into contact.

IV.7.3 Results and Discussion

A simple, lithography free method which makes use of large, flat, single-crystalline Au hexagonal microplates is discussed here to contact vertical NWs via electrical activation. As a case study, InAs NWs are used, which were grown by chemical beam epitaxy employing Au catalyst particles on an InAs(111)A substrate with trimethylindium and tert-butylarsine as metal–organic precursors [239]. The Au catalyst particles have been realized by thermal dewetting of nominally 0.5 nm thick gold films. The resulting nanoparticles have a wide diameter range, which implies that the diameter of the NWs is varied, the mean value being 75 ± 14 nm. The NW growth is Au-assisted, with a Au catalyst particle at the top of each NW [239]. The as-grown NWs are not of the same height, the mean height being 0.600 μm with a relatively large variation of ±0.250 μm (Figure IV.54). While setting top contact with the tallest NWs could be achieved by just placing a flat electrode, the NWs of smaller heights pose a challenge.
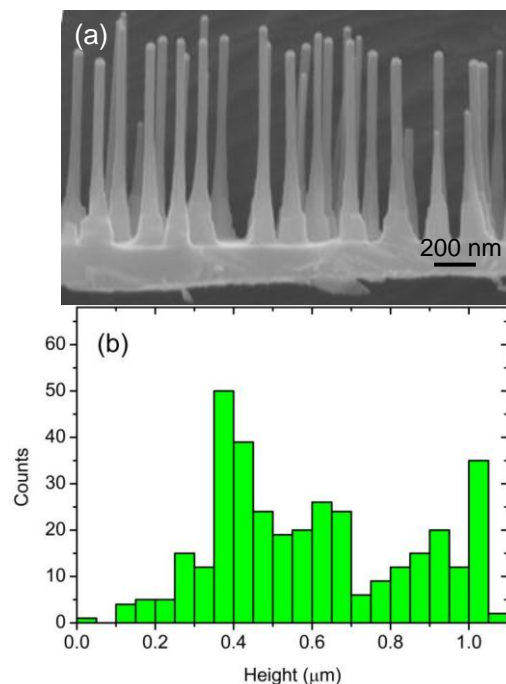
Figure IV.54 (a) SEM image of the InAs NWs viewed at right angle. (b) Height distribution histogram of the sample.
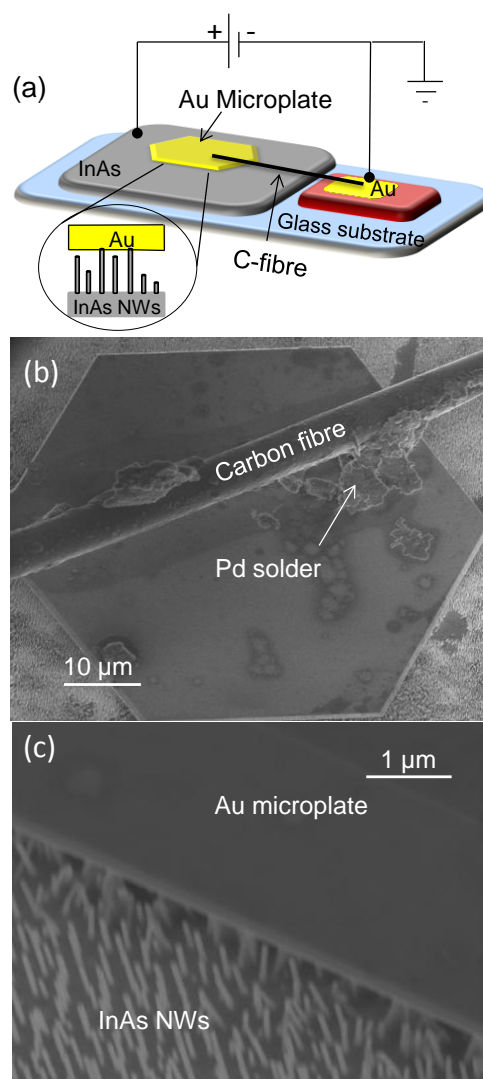
Figure IV.55 (a) Schematic showing the device configuration of Au microplate/InAs NW sandwich. (b) SEM image of the actual sandwich device, with the clear image of the soldered point between Au microplate and C-fibre with the Pd solder trace. The Pd metal in between the carbon fibre and the microplate is also clearly evident. (c) InAs NWs beneath the Au microplate captured along the edges (Imaging done at tilt angle of 60°).

As described in Part IV.6, a Au microplate was connected with a conducting C-fibre with a slight modification that the C-fibre was soldered to Au microplate prior to the device assembly and the Au-microplate could be lifted with the aid of C-fibre. The device consists of a clean glass slide as the base for the InAs substrate carrying InAs NWs and a Au (~ 40 nm thick) coated glass slide (of similar thickness as the InAs substrate, ~300 μm) juxtaposed with a separation of several tens of μms for electrical isolation (see Figure IV.55a). Both, the height of NWs and the thickness of Au coating are insignificant compared to the thickness of substrates and therefore are not critical process parameters. Such small differences were taken care by the bending of the long C-fibre. The arrangement was such that the C-fibre

contacted the Au microplate electrode only from the top and no NWs directly. The soldered Au microplate was lifted by holding the fibre from the free end, manually using a 3-axis micromanipulating tool (Nanomax TS) and placed gently onto the InAs substrate such that the microplate rested on the NWs (Figure IV.55c), and the free end of the fibre on the Au coated glass slide. Subsequently, the latter was also soldered using a drop of the Pd precursor. Thus a sandwich device comprising Au microplate/InAs NWs/InAs substrate was made. The density of the NWs was measured to be ~12 μm^{-2}, and given that the area of the microplate used for the experiment was ~1000 μm^{2}, the total number of NWs under the microplate comes out to be ~12000. From the SEM image in Figure IV.55c, one may visualize the NWs underneath the microplate edges indicating that they preserve the contact without being mechanically crushed. This can be rationalized by considering that the critical load for an ideal elastic column, often called the Euler load for failure [240] due to buckling, is given by P= π^{2} EI/L_e^{2} where E is Young's modulus and the moment of inertia, I= πR^{4}/4, R is diameter of the NW. The effective length L_e is $L_e = KL$, where L is the actual length of the column or the nanowire, K is column effective length factor (For one end fixed and the other end pinned, K ~ 0.7). The buckling behavior of NWs in this work can be approached by considering the NW to be a nanocolumn fixed at the base and pinned at the top (usually called a fixed pinned column), where P=2.04 π^{2}EI/L^{2}. The critical load for a single InAs NW (dia, ~75 nm; height, 1 μm), calculated according to the Euler load for failure turns out to be 2x10^{-4} N. The top Au plate corresponds to a load of 3x10^{-27} N per NW, safely below the critical value.

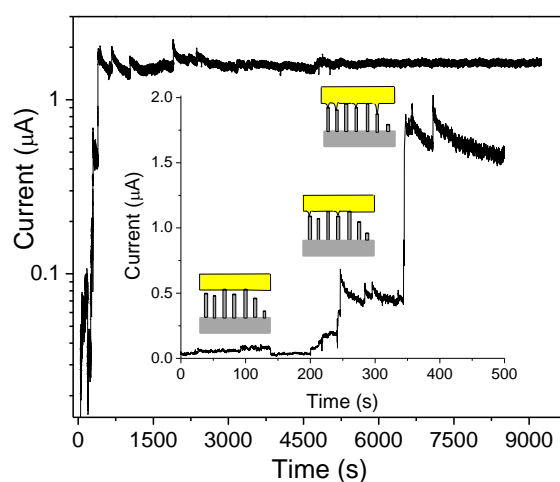**Figure IV.56** Current of the sandwich device recorded as a function of time, applying 0.5 mV for current induced electrical activation at a data collection rate of 1000 points per second for more than 9000 s. Note the logarithmic current scale. Inset shows zoom-in for the first 500 s (linear current scale) and schematic illustrations at various stages of NWs establishing contact with the top microplate electrode.

The prevalent contact by the tallest NWs produced a tiny current of ~37 nA, when 0.5 mV bias was applied to the InAs substrate carrying the NWs (the Au microplate was held at ground potential, see Figure IV.55a). The current got stabilized at ~84 nA after 45 s. The total resistance of the NWs in contact works out to be 5.9 kΩ, and considering the known approximate resistance of the individual NW (~25 kΩ) [241], the fraction of NW in contact is only ~0.04% of the total number of NWs under the microplate electrode. According to the height distribution histogram of the NWs (see Figure IV.54), this corresponds to the tallest NWs and those which fall short of that height by a few nm. Little distortions may be caused by the microplate in contact, which evens out the small differences in heights of NWs. With the voltage on (0.5 mV), the current through the sandwich device began to increase with time which implies either opening up of more conducting channels or annealing of the set contacts, or both. This aspect was studied in detail (Figure IV.56). In the initial 240 s, the current increased gradually to 179 nA and jumped to 672 nA at around 246 s. While a gradual increase may be taken to represent annealing of set contacts, a jump in current may correspond to more NWs coming in contact with the top electrode. The NWs which are within a short distance from the top electrode could be electrically contacted, and going by a similar estimate as before, this fraction comes out to be ~0.3% of the total. This type of contact can be visualized as analogous to atomic wire formation observed in STM studies [242], under an applied bias between a sharp tip and a flat substrate (Au nanoparticle terminated InAs NW as 'tip' and the Au microplate as the 'substrate' respectively, in the present case). Further continued application of the bias led to a sudden rise in the current from 0.82 to 1.87 µA at about ~344 s. Such noticeable rise in current indicates that a large number of NWs came into contact. It was estimated that ~1% of all NWs are in contact at this point (see the schematic illustration in the inset of Figure IV.56). In terms of distance from the microplate, this fraction covers a range of few tens of nm, from the Au nanoparticle tip (Figure IV.54). Given such large distances, it is reasonable to think that an electromigration process may be responsible - from microplate electrode to the Au nanoparticle tip. Such stalactite formation from the electrodes has been discussed in the context of molecular systems [243], although the distances involved in those cases are much smaller. Indeed, electromigration i.e., migration of metal under applied field is considered as a serious mode of failure in printed circuit boards as it forms shorts [244]. Usually in electromigration, dendritic or stalactite filaments bridge towards the positive electrode in an applied DC field [245]. From Figure IV.56, it may be seen that the current

eventually settles around ~1.8 µA but for small sudden variations. This marks the stabilization of the contact between the microplate electrode and the NWs. There may be instances of incomplete electromigration with the Au stalactites being very close but not yet contacting the InAs NWs, and in such cases tunneling may also be a contributing factor for overall conduction. As the measurements of nanowire height are based on SEM, nanometric accuracy was not possible. Tunneling, if exists, is relevant within 1 nm, and given the accuracy of heights measured, no concrete conclusions can be drawn with regard to the role of tunneling in transport. Further, tunneling will contribute in the range of few nanoamps while jumps in current observed are tens to hundreds of nanoamps. However, much shorter NWs could not make it owing to large gaps from the electrode. The latter fraction is astonishingly high, ~99%!
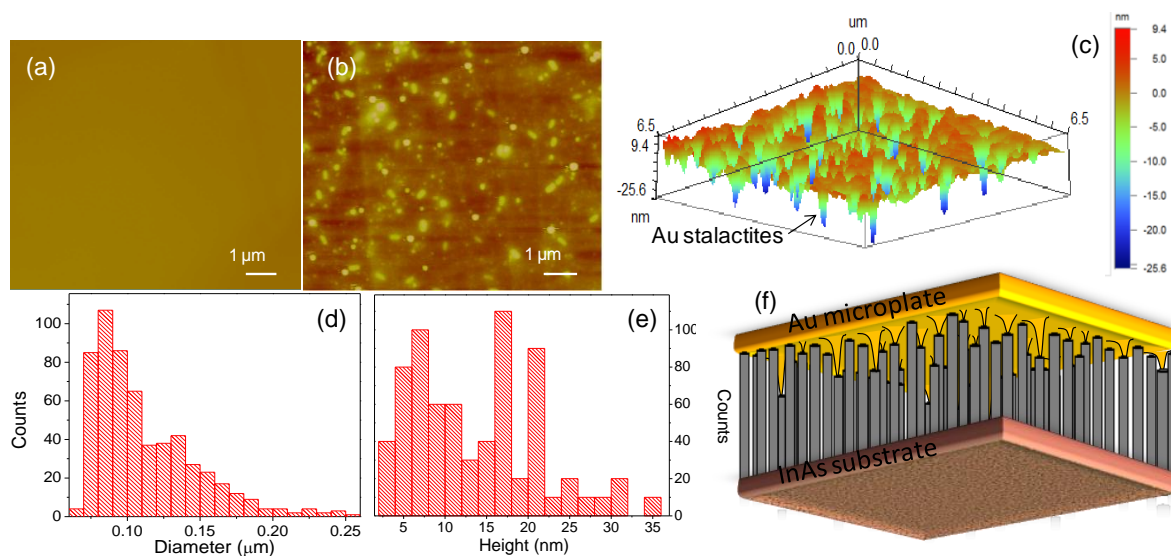
Figure IV.57 AFM images of the Au microplate top electrode surface, (a) before and (b) after electrical activation. (c) shows the planar view of stalactites on Au microplate surface (Image is turned upside down for better understanding). (d) and (e) are the histograms of the stalactites tip diameter and height. (f) is the schematic of the sandwich device with the microplate/InAs NWs and the developed stalactites.

The device was dismantled and the microplate surface which was in contact with the NWs, was examined (Figure IV.57). In contrast to the smooth pristine surface (Figure IV.57a), the surface after contacting, is filled with bright features in the AFM topography image (see Figure IV.57b). These features represent local topographical deviations from the atomically flat surface. The AFM image (shown upside down) in Figure IV.57c clearly shows the stalactites pointing down with lengths up to ~25 nm. From the histogram in Figure IV.57d, the mean tip diameter of the stalactite filament is ~70 nm, which corresponds roughly to the average diameter of the individual InAs NWs (~75 nm). The height histogram

of the stalactites which could be responsible for the contact with NWs is shown in Figure IV.57e. The stalactite induced contact is illustrated more vividly in Figure IV.57f. Good agreement between the results of Figures IV.56 and IV.57 is observed: stalactites with a length of up to 25 nm were found, and NWs with a maximum distance from the microplate of a few tens of nms are contacted. Also, the NW tips were examined for evidence of any sharp dendritic or stalactite features originating from the catalyst particles on the heads of InAs NWs (Figure IV.58); microscopy indicates that the NWs and the catalyst particles at the tips of NWs are intact without any deformation. Also, the stalactites' magnitude is too large to originate from the catalyst particle. Thus, the stalactite contacts are predominantly originating from the Au microplate electrode only. This corroborates our interpretation.
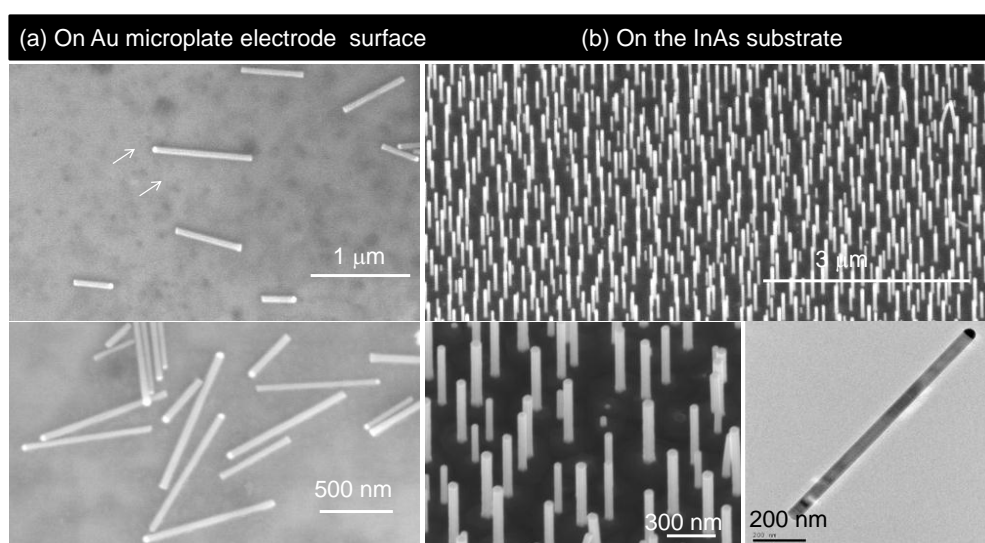
Figure IV.58 (a) SEM images of the Au microplate electrode after dismantling showing some of the NWs which came off due to mechanical pulling of the electrode surface. Importantly the NW and the catalyst particle are intact without any deformation. Arrows indicate few of the dark spots on Au microplate which correspond to Au stalactites as were seen in AFM images (in Figure 3). (b) SEM images of the NWs on the InAs substrate after electrical analysis, TEM image is also shown which shows clearly the catalyst particle at the tip.

The above method of applying a tiny bias (0.5 mV) and observing the current through the device with time was carried out essentially to understand the contacting process. While the above results gave an insight into the process, finally, only 1% of NWs could be brought into electrical contact and this over a period of ~50 min! In order to increase the yield of contacted NWs, increasing the bias and applying it continuously (Figure IV.59) would not do as the current carrying capacity of NWs is limited. It is reported that NWs start melting when the joule heat generated locally exceeds typically a few tens to hundreds of μW [246].
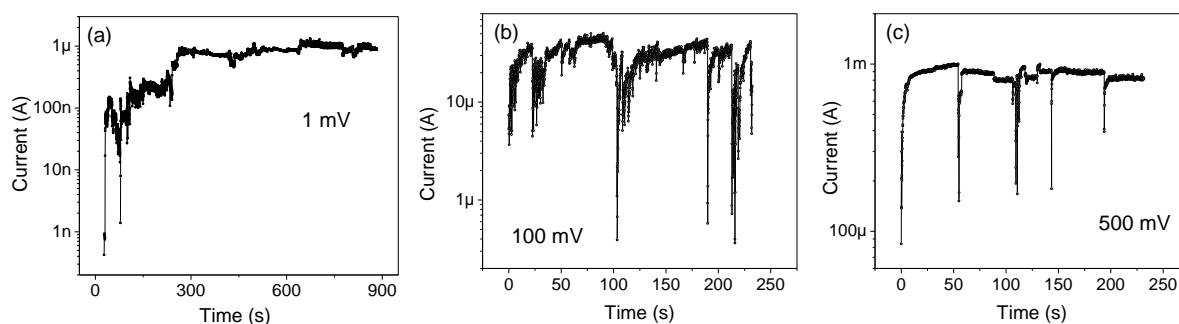
Figure IV.59 Current-time characteristics of the NW sandwich device at various applied constant bias, (a) 1 mV; (b) 100 mV and (c) 500 mV. At higher voltages, the current was higher indicating that more number of NWs have come into contact, but the contacts are not stable enough. There were frequent dips in the current indicating rupture of the contacts and/or NW tip melting due to joule heating.
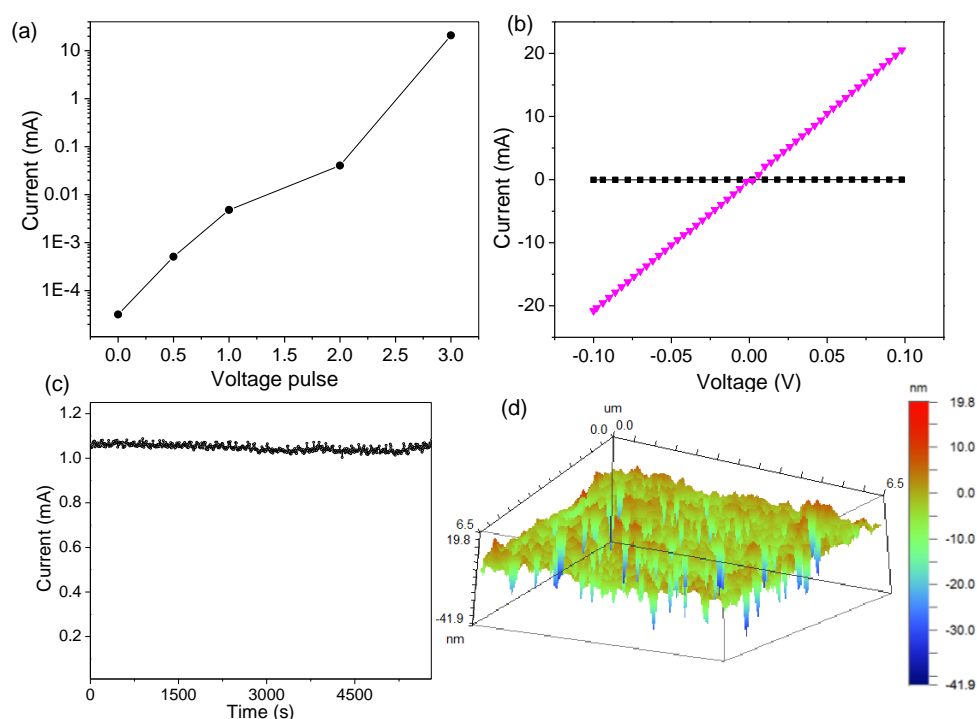
Figure IV.60 Voltage induced electrical activation: (a) Current at 0.1 V plotted versus the voltage pulse used for contact initiation. All pulses were of duration ~10 s. (b) I-V characteristics of the sandwich device, before (squares) and after applying a voltage pulse of 3 V (triangles). When 3 V was pulsed for 10 s, the current improved significantly. (c) Current-time plot showing the retention of the contact of the NWs (read voltage, 5 mV). (d) AFM planar image of stalactites on Au microplate surface (Image is shown upside down).

In order to avoid such a situation, voltage was switched from a continuous application to short bias pulses. For a given sample to reach its steady state condition, the required voltage was arrived empirically by applying short (10 s) voltage pulses starting

from 0.5 up to 3 V. The state of the device after pulsing was examined using a reading voltage of 0.1 V (Figure IV.60a). Initially after pulsing with 0.5 V, the current was low (~510 nA) and non-linear. By increasing the pulsing voltage, not only there was an increase in the current (see Figure IV.60a) but also nearly linear I-V behavior was achieved as shown in Figure IV.60b. Thus a higher voltage (3 V) in short pulses (10 s) was applied leading to success in bringing ~50% of the NWs into ohmic contact (see linear behavior in Figure IV.60b). These contacts were robust, because the current remained steady (1.08 ± 0.02 mA at 5 mV) even after 100 min (see Figure IV.60c). A further increase in voltage (4 V) did not improve the number of NWs coming into contact significantly. This is an empirical observation and the conditions of pulsing voltage may vary depending on the density of the NWs, area of the microplate, height distribution of the NWs etc. The swiftness of the contact development in this case indicates that the above discussed processes - direct contact and electromigration - take place simultaneously. The microplate electrode surface from this device indeed showed stalactites which are more longer (up to ~62 nm) with a higher density (Figure IV.60d).The fraction of NW in contact achieved by this process can be compared with that obtained with the airbridge [236] or the planarization method [237].

IV.7.3 Conclusions

A simple method for top contacting a large number of NWs in vertical geometry has been devised using a mesoscopic Au electrode. In spite of widely distributed heights of the NWs, almost 50% of the NWs were brought into contact without damage. The surface of NWs is free and can be exposed to gases for specific applications in contrast to conventional top contact methods where NWs are constrained in a dielectric polymer environment. This method is distinctly different in that it is lithography-free and does not require sophisticated nanomanipulation techniques. The device is essentially self-standing which paves the way to up-scale circumventing the stumbling block for the development of NWs/nanotubes from growth to applications.

References

[1]   R. H. Reuss, B. R. Chalamala, A. Moussessian, M. G. Kane, A. Kumar, D. C. Zhang, J. A. Rogers, M. Hatalis, D. Temple, G. Moddel, B. J. Eliasson, M. J. Estes, J. Kunze, E. S. Handy, E. S. Harmon, D. B. Salzman, J. M. Woodall, M. A. Alam, J. Y. Murthy, S. C. Jacobsen, M. Olivier, D. Markus, P. M. Campbell, and E. Snow, Proceedings of the IEEE: Macroelectronics: Perspectives on Technology and Applications 93 (2005) 1239.

[2]   A. L. Window, Strain Gauge Technology, Elsevier Applied Science, Essex (England), 1992.

[3]   M. J. Hampton, S. S. Williams, Z. Zhou, J. Nunes, D.-H. Ko, J. L. Templeton, E. T. Samulski, and J. M. DeSimone, Advanced Materials 20 (2008) 2667.

[4]   E. Laukhina, R. Pfattner, L. R. Ferreras, S. Galli, M. Mas-Torrent, N. Masciocchi, V. Laukhin, C. Rovira, and J. Veciana, Advanced Materials 22 (2010) 977.

[5]   S. I. Park, A. P. Le, J. Wu, Y. Huang, X. Li, and J. A. Rogers, Advanced Materials 22 (2010) 3062.

[6]   K. J. Lee, M. A. Meitl, J. H. Ahn, J. A. Rogers, R. G. Nuzzo, V. Kumar, and I. Adesida, Journal of Applied Physics 100 (2006) 124507.

[7]   X. Wang, K. Kim, Y. Wang, M. Stadermann, A. Noy, A. V. Hamza, J. Yang, and D. J. Sirbuly, Nano Letters 10 (2010) 4901.

[8]   Y. Sun, S. Kim, I. Adesida, and J. A. Rogers, Applied Physics Letters 87 (2005) 1.

[9]   A. N. Tiwari, A. Romeo, D. Baetzner, and H. Zogg, Progress in Photovoltaics: Research and Applications 9 (2001) 211.

[10]   Z. Liu, V. Subramania, and M. Misra, The Journal of Physical Chemistry C 113 (2009) 14028.

[11]   L. Tong, C. Li, F. e. Chen, H. Bai, L. Zhao, and G. Shi, The Journal of Physical Chemistry C 113 (2009) 7411.

[12]   J. Yun, K. Cho, B. Park, B. H. Park, and S. Kim, Journal of Materials Chemistry 19 (2009) 2082.

[13]   K. Tae-Wook, C. Hyejung, O. Seung-Hwan, J. Minseok, W. Gunuk, C. Byungjin, K. Dong-Yu, H. Hyunsang, and L. Takhee, Nanotechnology 20 (2009) 025201.

[14]   D. Choi, M. Y. Choi, W. M. Choi, H. J. Shin, H. K. Park, J. K. Seo, J. Park, S. M. Yoon, S. Chae, Y. H. Lee, S. W. Kim, J. Y. Choi, S. Y. Lee, and J. M. Kim, Advanced Materials 22 (2010) 2187.

[15]   T. Takahashi, K. Takei, E. Adabi, Z. Fan, A. M. Niknejad, and A. Javey, ACS Nano 4 (2010) 5855.

[16]   L. Gomez De Arco, Y. Zhang, C. W. Schlenker, K. Ryu, M. E. Thompson, and C. Zhou, ACS Nano 4 (2010) 2865.

[17]   J. H. Ahn, H. S. Kim, K. J. Lee, S. Jeon, S. J. Kang, Y. Sun, R. G. Nuzzo, and J. A. Rogers, Science 314 (2006) 1754.

[18]   K. Inpil, M. J. Schulz, J. H. Kim, V. Shanov, and D. Shi, Smart Materials and Structures 15 (2006) 737.

[19]   J. C. Anderson, Journal of Vacuum Science & Technology A: Vacuum, Surfaces, and Films 4 (1986) 610.

[20]   H. Chiriac, M. Urse, F. Rusu, C. Hison, and M. Neagu, Sensors and Actuators A: Physical 76 (1999) 376.

[21]   D. J. Lichtenwalner, A. E. Hydrick, and A. I. Kingon, Sensors and Actuators A: Physical 135 (2007) 593.

[22]   D. D. L. Chung, Smart Materials and Structures 4 (1995) 59.

[23] Z. Lisong, J. Soyoun, E. Brandon, and T. N. Jackson, IEEE Transactions on Electron Devices 53 (2006) 380.

[24] G. Latessa, F. Brunetti, A. Reale, G. Saggio, and A. Di Carlo, Sensors and Actuators B: Chemical 139 (2009) 304.

[25] T. Seiichi, T. Takahata, M. Muraki, E. Iwase, K. Matsumoto, and I. Shimoyama, Journal of Micromechanics and Microengineering 20 (2010) 075017.

[26] N.-K. Chang, C.-C. Su, and S.-H. Chang, Applied Physics Letters 92 (2008) 063501.

[27] T. Vossmeyer, C. Stolte, M. Ijeh, A. Kornowski, and H. Weller, Advanced Functional Materials 18 (2008) 1611.

[28] P. Siffalovic, L. Chitu, K. Vegso, E. Majkova, M. Jergel, M. Weis, S. Luby, I. Capek, J. Keckes, G. A. Maier, A. Satka, J. Perlich, and S. V. Roth, Nanotechnology 21 (2010) 385702.

[29] K. E. Mueggenburg, X.-M. Lin, R. H. Goldsmith, and H. M. Jaeger, Nature Materials 6 (2007) 656.

[30] M. Liu, Z. Abid, W. Wang, X. He, Q. Liu, and W. Guan, Applied Physics Letters 94 (2009) 233106.

[31] H. Gullapalli, V. S. M. Vemuru, A. Kumar, A. Botello-Mendez, R. Vajtai, M. Terrones, S. Nagarajaiah, and P. M. Ajayan, Small 6 (2010) 1641.

[32] C. Li, P. J. Hesketh, and G. J. Maclay, Journal of Vacuum Science & Technology A: Vacuum, Surfaces, and Films 12 (1994) 813.

[33] T. Bhuvana and G. U. Kulkarni, ACS Nano 2 (2008) 457.

[34] T. Takeno, Y. Hoshi, H. Miki, and T. Takagi, Diamond and Related Materials 17 (2008) 1669.

[35] G. Carotenuto, B. Martorana, P. Perlo, and L. Nicolais, Journal of Materials Chemistry 13 (2003) 2927.

[36] M. Nakamoto, M. Yamamoto, and M. Fukusumi, Chemical Communications 15 (2002) 1622.

[37] Y. Cai, D. Wolfkuỉhler, A. Myalitsin, J. Perlich, A. Meyer, and C. Klinke, ACS Nano 5 (2011) 67.

[38] J. Robertson, Materials Science and Engineering: R: Reports 37 (2002) 129.

[39] T. Ohno, T. Takeno, H. Miki, and T. Takagi, International Journal of Applied Electromagnetics and Mechanics 33 (2010) 665.

[40] X. Han, G. Jing, X. Zhang, R. Ma, X. Song, J. Xu, Z. Liao, N. Wang, and D. Yu, Nano Research 2 (2009) 553.

[41] N. Liu, G. Fang, W. Zeng, H. Long, L. Yuan, and X. Zhao, The Journal of Physical Chemistry C 115 (2011) 570.

[42] IPA Pvt Ltd, Bangalore (http://ipaindia.com/)

[43] P. Alpuim, S. A. Filonovich, C. M. Costa, P. F. Rocha, M. I. Vasilevskiy, S. Lanceros-Mendez, C. Frias, A. T. Marques, R. Soares, and C. Costa, Journal of Non-Crystalline Solids 354 (2008) 2585.

[44] F. Xu, J. W. Durham, B. J. Wiley, and Y. Zhu, ACS Nano 5 (2011) 1556.

[45] S. Xiaoping and D. D. L. Chung, Smart Materials and Structures 5 (1996) 243.

[46] H. G. W. Malte, T. B. Samuel, B. Lars, A. Rainer, and S. Karl, Nanotechnology 19 (2008) 475503.

[47] C. Stampfer, T. Helbling, D. Obergfell, B. SchÃberle, M. K. Tripp, A. Jungen, S. Roth, V. M. Bright, and C. Hierold, Nano Letters 6 (2006) 233.

[48] H. Lin, T. Gao, J. Fantini, and M. J. Sailor, Langmuir 20 (2004) 5104.

[49] X. Wei, T. Wei, H. Xiao, and Y. S. Lin, Sensors and Actuators, B: Chemical 134 (2008) 687.

[50] F. Yang, D. K. Taggart, and R. M. Penner, Nano Letters 9 (2009) 2177.

[51] R. K. Joshi, S. Krishnan, M. Yoshimura, and A. Kumar, Nanoscale Research Letters 4 (2009) 1191.

[52] M. Khanuja, S. Kala, B. R. Mehta, and F. E. Kruis, Nanotechnology 20 (2009)

[53] M. Khanuja, D. Varandani, and B. R. Mehta, Applied Physics Letters 91 (2007)

[54] S. V. Patel, J. L. Gland, and J. W. Schwank, Langmuir 15 (1999) 3307.

[55] J. Van Lith, A. Lassesson, S. A. Brown, M. Schulze, J. G. Partridge, and A. Ayesh, Applied Physics Letters 91 (2007)

[56] S. Yu, U. Welp, L. Z. Hua, A. Rydh, W. K. Kwok, and H. H. Wang, Chemistry of Materials 17 (2005) 3445.

[57] S. Cherevko, N. Kulyk, J. Fu, and C. H. Chung, Sensors and Actuators B-Chemical 136 (2009) 388.

[58] K. J. Jeon, M. Jeun, E. Lee, J. M. Lee, K. I. Lee, P. Von Allmen, and W. Lee, Nanotechnology 19 (2008)

[59] K. J. Jeon, J. M. Lee, E. Lee, and W. Lee, Nanotechnology 20 (2009)

[60] T. Kiefer, F. Favier, O. Vazquez-Mena, G. Villanueva, and J. Brugger, Nanotechnology 19 (2008)

[61] D. B. Wolfe, J. C. Love, K. E. Paul, M. L. Chabinyc, and G. M. Whitesides, Applied Physics Letters 80 (2002) 2222.

[62] F. Favier, E. C. Walter, M. P. Zach, T. Benter, and R. M. Penner, Science 293 (2001) 2227.

[63] Y. Im, C. Lee, R. P. Vasquez, M. A. Bangar, N. V. Myung, E. J. Menke, R. M. Penner, and M. Yun, Small 2 (2006) 356.

[64] E. C. Walter, F. Favier, and R. M. Penner, Analytical Chemistry 74 (2002) 1546.

[65] M. Yun, N. V. Myung, R. P. Vasquez, C. Lee, E. Menke, and R. M. Penner, Nano Letters 4 (2004) 419.

[66] R. Dasari and F. P. Zamborini, Journal of the American Chemical Society 130 (2008) 16138.

[67] T. Xu, M. P. Zach, Z. L. Xiao, D. Rosenmann, U. Welp, W. K. Kwok, and G. W. Crabtree, Applied Physics Letters 86 (2005) 1.

[68] F. J. Ibanez and F. P. Zamborini, Langmuir 22 (2006) 9789.

[69] W. P. Jakubik, M. W. Urbanìƒczyk, J. Bodzenta, and M. A. Pietrzyk, Sensors and Actuators, B: Chemical 105 (2005) 340.

[70] P. Kumar and L. K. Malhotra, Materials Chemistry and Physics 88 (2004) 106.

[71] Y. Sun and H. H. Wang, Advanced Materials 19 (2007) 2818.

[72] Z. H. Chen, J. S. Jie, L. B. Luo, H. Wang, C. S. Lee, and S. T. Lee, Nanotechnology 18 (2007)

[73] W. Jia, L. Su, Y. Ding, A. Schempf, Y. Wang, and Y. Lei, Journal of Physical Chemistry C 113 (2009) 16402.

[74] G. Kaltenpoth, P. Schnabel, E. Menke, E. C. Walter, M. Grunze, and R. M. Penner, Analytical Chemistry 75 (2003) 4756.

[75] F. Rahimi and A. Iraji Zad, Journal of Physics D: Applied Physics 40 (2007) 7201.

[76] P. K. Sekhar, A. Sine, and S. Bhansali, Sensors and Actuators, B: Chemical 127 (2007) 74.

[77] S. Y. Chiu, H. W. Huang, K. C. Liang, T. H. Huang, K. P. Liu, J. H. Tsai, and W. S. Lour, Semiconductor Science and Technology 24 (2009)

[78] S. N. Das and A. K. Pal, Journal of Physics D: Applied Physics 40 (2007) 7291.

[79] Y. Y. Tsai, K. W. Lin, H. I. Chen, I. P. Liu, C. W. Hung, T. P. Chen, T. H. Tsai, L. Y. Chen, K. Y. Chu, and W. C. Liu, Sensors and Actuators, B: Chemical 134 (2008) 750.

[80] E. Nowicka, Vacuum 48 (1997) 199.

[81] J. Robertson, Materials Science & Engineering R-Reports 37 (2002) 129.

[82]   A. C. Ferrari and J. Robertson, Physical Review B 61 (2000) 14095.

[83]   J. J. Blackstock, A. A. Rostami, A. M. Nowak, R. L. McCreery, M. R. Freeman, and M. T. McDermott, Analytical Chemistry 76 (2004) 2544.

[84]   Y. Wang, D. C. Alsmeyer, and R. L. McCreery, Chemistry of Materials 2 (1990) 557.

[85]   L. C. F.-T. E. Charles H. Sykes, Sanjini U. Nanayakkara, Brent A. Mantooth, Ryan M. Nevin, and Paul S. Weiss, Proc Natl Acad Sci U S A 102 (2005) 17907.

[86]   L. Ionov, N. Houbenov, A. Sidorenko, M. Stamm, and S. Minko, Advanced Functional Materials 16 (2006) 1153.

[87]   F. Bahador, M. H. Steven, L. Jaejong, and P. Sunggook, Journal of Micromechanics and Microengineering 21 (2011) 035016.

[88]   M. Bieda, E. Beyer, and A. F. Lasagni, Journal of Engineering Materials and Technology 132 (2010) 031015.

[89]   J. C. Love, L. A. Estroff, J. K. Kriebel, R. G. Nuzzo, and G. M. Whitesides, Chemical Reviews 105 (2005) 1103.

[90]   P. A. Levkin, F. Svec, and J. M. J. Fréchet, Advanced Functional Materials 19 (2009) 1993.

[91]   X. Chao-Hua, J. Shun-Tian, Z. Jing, and M. Jian-Zhong, Science and Technology of Advanced Materials 11 (2010) 033002.

[92]   R. Jagdheesh, B. Pathiraj, E. Karatay, G. R. B. E. Römer, and A. J. Huisint Veld, Langmuir 27 (2011) 8464.

[93]   D. Zhu, X. Li, G. Zhang, X. Zhang, X. Zhang, T. Wang, and B. Yang, Langmuir 26 (2010) 14276.

[94]   T. Bhuvana, L. Gregoratti, S. Heun, M. Dalmiglio, and G. U. Kulkarni, Langmuir 25 (2008) 1259.

[95]   G. W. Burr, B. N. Kurdi, J. C. Scott, C. H. Lam, K. Gopalakrishnan, and R. S. Shenoy, Ibm Journal of Research and Development 52 (2008) 449.

[96]   M. H. Kryder and K. Chang Soo, IEEE Transactions on Magnetics 45 (2009) 3406.

[97]   J. J. Yang, M. D. Pickett, X. Li, A. A. OhlbergDouglas, D. R. Stewart, and R. S. Williams, Nature Nanotechnology 3 (2008) 429.

[98]   D. B. Strukov, G. S. Snider, D. R. Stewart, and R. S. Williams, Nature 453 (2008) 80.

[99]   T. Prodromakis, K. Michelakis, and C. Toumazou, Electronics Letters 46 (2010) 63.

[100]   T. Mikolajick, M. Salinga, M. Kund, and T. Kever, Advanced Engineering Materials 11 (2009) 235.

[101]   S. H. Jo, K.-H. Kim, and W. Lu, Nano Letters 9 (2009) 870.

[102]   T. Berzina, A. Smerieri, G. Ruggeri, M. Bernabo, V. Erokhin, and M. P. Fontana, Materials Science & Engineering C-Materials for Biological Applications 30 (2010) 407.

[103]   T. Berzina, A. Smerieri, M. Bernabo, A. Pucci, G. Ruggeri, V. Erokhin, and M. P. Fontana, Journal of Applied Physics 105 (2009) 124515.

[104]   K. Gorshkov, T. Berzina, V. Erokhin, and M. P. Fontana, Procedia Computer Science 7 (2011) 248.

[105]   S. K. Hong, J. E. Kim, S. O. Kim, S.-Y. Choi, and B. J. Cho, Ieee Electron Device Letters 31 (2010) 1005.

[106]   H. Y. Jeong, J. Y. Kim, J. W. Kim, J. O. Hwang, J.-E. Kim, J. Y. Lee, T. H. Yoon, B. J. Cho, S. O. Kim, R. S. Ruoff, and S.-Y. Choi, Nano Letters 10 (2010) 4381.

[107]   L. Chua, IEEE Transactions on Circuit Theory 18 (1971) 507.

[108]   W. Rainer, Microelectronic Engineering 86 (2009) 1925.

[109] T. Hino, T. Hasegawa, K. Terabe, T. Tsuruoka, A. Nayak, T. Ohno, and M. Aono, Science and Technology of Advanced Materials 12 (2011)

[110] R. Waser and M. Aono, Nature Materials 6 (2007) 833.

[111] E. Linn, R. Rosezin, C. Kugeler, and R. Waser, Nature Materials 9 (2010) 403.

[112] Y. Jung, S.-H. Lee, A. T. Jennings, and R. Agarwal, Nano Letters 8 (2008) 2056.

[113] M. J. Rozenberg, I. H. Inoue, and M. J. Sánchez, Physical Review Letters 92 (2004) 178302.

[114] C. Li, W. Fan, B. Lei, D. Zhang, S. Han, T. Tang, X. Liu, Z. Liu, S. Asano, M. Meyyappan, J. Han, and C. Zhou, Applied Physics Letters 84 (2004) 1949.

[115] J.-G. Park, W.-S. Nam, S.-H. Seo, Y.-G. Kim, Y.-H. Oh, G.-S. Lee, and U.-G. Paik, Nano Letters 9 (2009) 1713.

[116] C.-P. Hsiung, H.-W. Liao, J.-Y. Gan, T.-B. Wu, J.-C. Hwang, F. Chen, and M.-J. Tsai, ACS Nano 4 (2010) 5414.

[117] S.-Y. Wang, C.-W. Huang, D.-Y. Lee, T.-Y. Tseng, and T.-C. Chang, Journal of Applied Physics 108 (2010) 114110.

[118] Y. C. Yang, C. Chen, F. Zeng, and F. Pan, Journal of Applied Physics 107 (2010) 093701.

[119] S. C. Chae, J. S. Lee, W. S. Choi, S. B. Lee, S. H. Chang, H. Shin, B. Kahng, and T. W. Noh, Applied Physics Letters 95 (2009) 093508.

[120] C. Yong, J. Gun-Young, A. A. O. Douglas, L. Xuema, R. S. Duncan, O. J. Jan, A. N. Kent, J. F. Stoddart, and R. S. Williams, Nanotechnology 14 (2003) 462.

[121] M. Terai, Y. Sakotsubo, Y. Saito, S. Kotsuji, and H. Hada, IEEE Electron Device Letters 31 (2010) 1302.

[122] Z. Fang, H. Y. Yu, J. A. Chroboczek, G. Ghibaudo, J. Buckley, B. DeSalvo, X. Li, and D. L. Kwong, Electron Devices, IEEE Transactions on 59 (2012) 850.

[123] S. B. Lee, S. Park, J. S. Lee, S. C. Chae, S. H. Chang, M. H. Jung, Y. Jo, B. Kahng, B. S. Kang, M. J. Lee, and T. W. Noh, Applied Physics Letters 95 (2009) 122112.

[124] C. D. Wright, L. Wang, P. Shah, M. M. Aziz, E. Varesi, R. Bez, M. Moroni, and F. Cazzaniga, Nanotechnology, IEEE Transactions on 10 (2011) 900.

[125] K. Tanaka, Y. Kurihashi, T. Uda, Y. Daimon, N. Odagawa, R. Hirose, Y. Hiranaga, and Y. Cho, Japanese Journal of Applied Physics 47 (2008) 3311.

[126] A. Knoll, P. Bächtold, J. Bonan, G. Cherubini, M. Despont, U. Drechsler, U. Dürig, B. Gotsmann, W. Häberle, C. Hagleitner, D. Jubin, M. A. Lantz, A. Pantazi, H. Pozidis, H. Rothuizen, A. Sebastian, R. Stutz, P. Vettiger, D. Wiesmann, and E. S. Eleftheriou, Microelectronic Engineering 83 (2006) 1692.

[127] J. Millman, ed., Vacuum-tube and semiconductor electronics, McGraw-Hill, 1958.

[128] B. Pradhan, Applied Physics Letters 89 (2006) 233109.

[129] C.-H. Liu, C.-C. Wu, and Z. Zhong, Nano Letters 11 (2011) 1782.

[130] D. Dragoman, Journal of Applied Physics 108 (2010) 084316.

[131] I. Díez-Pérez, J. Hihath, Y. Lee, L. Yu, L. Adamska, M. A. Kozhushner, I. I. Oleynik, and N. Tao, Nature Chemistry 1 (2009) 635.

[132] J. L. Dewald, W. T. Wondmagegn, A. V. Ellis, and S. A. Curran, Synthetic Metals 155 (2005) 39.

[133] A. Nourbakhsh, M. Cantoro, A. Hadipour, T. Vosch, M. H. van der Veen, M. M. Heyns, B. F. Sels, and S. De Gendt, Applied Physics Letters 97 (2010) 163101.

[134] C. N. R. Rao, G. U. Kulkarni, P. J. Thomas, and P. P. Edwards, Chemical Society Reviews 29 (2000) 27.

[135] S. Chen, Proceedings of SPIE 4807 (2002) 93.

[136] S. Chen, Analytica Chimica Acta 496 (2003) 29.

[137] S. Pal, M. K. Sanyal, N. S. John, and G. U. Kulkarni, Physical Review B 71 (2005) 121404.

[138] V. V. Agrawal, N. Varghese, G. U. Kulkarni, and C. N. R. Rao, Langmuir 24 (2008) 2494.

[139] S. A. Maier, Journal of Applied Physics 98 (2005) 011101.

[140] While this is also true for semiconductor nanoparticles (A. P. Alivisatos, Science 271 (1996) 933–937; A. L. Rogach, in Semiconductor Nanocrystal Quantum Dots: Synthesis, Assembly, Spectroscopy. Springer, Austria, 2008), in this article, we restrict to metal nanoparticles.

[141] C. Salzemann, W. Zhai, N. Goubet, and M.-P. Pileni, The Journal of Physical Chemistry Letters 1 (2009) 149.

[142] V. V. Agrawal, G. U. Kulkarni, and C. N. R. Rao, The Journal of Physical Chemistry B 109 (2005) 7300.

[143] R. L. McCreery, Chemistry of Materials 16 (2004) 4477.

[144] A. Iovan, V. Korenivski, and D. B. Haviland, Journal of Applied Physics 99 (2006) 08E502.

[145] C. P. Collier, R. J. Saykally, J. J. Shiang, S. E. Henrichs, and J. R. Heath, Science 277 (1997) 1978.

[146] S. Sun, C. B. Murray, D. Weller, L. Folks, and A. Moser, Science 287 (2000) 1989.

[147] C. T. Black, C. B. Murray, R. L. Sandstrom, and S. Sun, Science 290 (2000) 1131.

[148] G. Markovich, C. P. Collier, S. E. Henrichs, F. Remacle, R. D. Levine, and J. R. Heath, Accounts of Chemical Research 32 (1999) 415.

[149] B. Liang, X. S. Guo, J. Tu, D. Zhang, and J. C. Cheng, Nature Materials 9 (2010) 989.

[150] M. Grzelczak, J. Vermant, E. M. Furst, and L. M. Liz-Marzán, ACS Nano 4 (2010) 3591.

[151] S. Kinge, M. Crego-Calama, and D. N. Reinhoudt, ChemPhysChem 9 (2008) 20.

[152] X. M. Lin, H. M. Jaeger, C. M. Sorensen, and K. J. Klabunde, The Journal of Physical Chemistry B 105 (2001) 3353.

[153] A. Dong, J. Chen, S. J. Oh, W.-k. Koh, F. Xiu, X. Ye, D.-K. Ko, K. L. Wang, C. R. Kagan, and C. B. Murray, Nano Letters 11 (2011) 841.

[154] G. C. Jensen, C. E. Krause, G. A. Sotzing, and J. F. Rusling, Physical Chemistry Chemical Physics 13 (2011) 4888.

[155] W. Cheng, N. Park, M. T. Walter, M. R. Hartman, and D. Luo, Nature Nanotechnology 3 (2008) 682.

[156] P. J. Thomas, G. U. Kulkarni, and C. N. R. Rao, Journal of Materials Chemistry 14 (2004) 625.

[157] B. J. Y. Tan, C. H. Sow, T. S. Koh, K. C. Chin, A. T. S. Wee, and C. K. Ong, The Journal of Physical Chemistry B 109 (2005) 11100.

[158] S.-H. Yun, S. I. Yoo, J. C. Jung, W.-C. Zin, and B.-H. Sohn, Chemistry of Materials 18 (2006) 5646.

[159] M. K. Corbierre, J. Beerens, and R. B. Lennox, Chemistry of Materials 17 (2005) 5774.

[160] R. Glass, M. Arnold, J. Blümmel, A. Küller, M. Möller, and J. P. Spatz, Advanced Functional Materials 13 (2003) 569.

[161] F. Ruffino, M. G. Grimaldi, F. Giannazzo, F. Roccaforte, and V. Raineri, Applied Physics Letters 89 (2006) 263108.

[162] T. Reda, A. F. Collings, C. Barton, and P. Lukins, The Journal of Physical Chemistry B 107 (2003) 13774.

[163] D. Gao, F. Scholz, H.-G. Nothofer, W. E. Ford, U. Scherf, J. M. Wessels, A. Yasuda, and F. von Wrochem, Journal of the American Chemical Society 133 (2011) 5921.

[164] M. Kallol and J. P. Amlan, Nanotechnology 20 (2009) 185203.

[165] G. J. Ashwell, W. D. Tyrrell, and A. J. Whittam, Journal of Materials Chemistry 13 (2003) 2855.

[166] G. J. Ashwell and A. Mohib, Journal of the American Chemical Society 127 (2005) 16238.

[167] J. M. Beebe, B. Kim, J. W. Gadzuk, C. Daniel Frisbie, and J. G. Kushmerick, Physical Review Letters 97 (2006) 026801.

[168] C. C. Bof Bufon, J. D. Arias Espinoza, D. J. Thurmer, M. Bauer, C. Deneke, U. Zschieschang, H. Klauk, and O. G. Schmidt, Nano Letters 11 (2011) 3727.

[169] L. Hong, L. Huiqin, L. Ming, and M. Dali, in 8th International Conference on Electronic Packaging Technology, ICEPT 2007, 2007, p. 1.

[170] T.-i. Kim, J.-h. Kim, S. J. Son, and S.-m. Seo, Nanotechnology 19 (2008) 295302.

[171] C. Dong-Uk, S. Kumar, and K. Gil-Ho, in 9th IEEE Conference on Nanotechnology, IEEE-NANO 2009, 2009, p. 261.

[172] D. I. Son, D. H. Park, J. B. Kim, J.-W. Choi, T. W. Kim, B. Angadi, Y. Yi, and W. K. Choi, The Journal of Physical Chemistry C 115 (2011) 2341.

[173] J. Lee, P. Gipp, and C. Heller, Applied Physics Letters 85 (2004) 145.

[174] G. Mallick, M. H. Griep, P. M. Ajayan, and S. P. Karna, Applied Physics Letters 96 (2010) 233109.

[175] E. Yeow Hwee Teo, Z. Chunfu, L. Siew Lay, K. En-Tang, C. Daniel, and Z. Chunxiang, IEEE Electron Device Letters 30 (2009) 487.

[176] C. A. Nijhuis, W. F. Reus, J. R. Barber, M. D. Dickey, and G. M. Whitesides, Nano Letters 10 (2010) 3611.

[177] C. H. Lee, D. R. Kim, and X. Zheng, Proceedings of the National Academy of Sciences 107 (2010) 9950.

[178] C. Moraes and et al., Journal of Micromechanics and Microengineering 19 (2009) 065015.

[179] J. N. Lee, C. Park, and G. M. Whitesides, Analytical Chemistry 75 (2003) 6544.

[180] J. R. Heath and M. A. Ratner, Physics Today 56 (2003) 43.

[181] A. Aviram and M. A. Ratner, Chemical Physics Letters 29 (1974) 277.

[182] P. Tyagi, Journal of Materials Chemistry 21 (2011)

[183] H. Song, M. A. Reed, and T. Lee, Advanced Materials 23 (2011) 1583.

[184] A. H. Flood, J. F. Stoddart, D. W. Steuerman, and J. R. Heath, Science 306 (2004) 2055.

[185] N. J. Tao, Nature Nanotechnology 1 (2006) 173.

[186] T. W. Kim, G. Wang, and T. Lee, Nanotechnology, IEEE Transactions on 7 (2008) 140.

[187] J. W. P. Hsu, Y. L. Loo, D. V. Lang, and J. A. Rogers, Vol. 21, AVS, Salt Lake City, Utah (USA), 2003, p. 1928.

[188] T. Lee, W. Wang, and M. A. Reed, Annals of the New York Academy of Sciences 1006 (2003) 21.

[189] A. M. Rawlett, T. J. Hopson, L. A. Nagahara, R. K. Tsui, G. K. Ramachandran, and S. M. Lindsay, Applied Physics Letters 81 (2002) 3043.

[190] K. Slowinski, H. K. Y. Fong, and M. Majda, Journal of the American Chemical Society 121 (1999) 7257.

[191] H. P. Yoon, M. M. Maitani, O. M. Cabarcos, L. Cai, T. S. Mayer, and D. L. Allara, Nano Letters 10 (2010) 2897.

[192] T. Qingxin, T. Yanhong, J. Titoo, H. Tue, W. Qing, M.-P. Kasper, and B. Thomas, Nanotechnology 20 (2009) 245205.

[193] A. P. Bonifas and R. L. McCreery, Nature Nanotechnology 5 (2010) 612.

[194] H. B. Akkerman, P. W. M. Blom, D. M. de Leeuw, and B. de Boer, Nature 441 (2006) 69.

[195] T. Li, J. R. Hauptmann, Z. Wei, S. Petersen, N. Bovet, T. Vosch, J. Nygård, W. Hu, Y. Liu, T. Bjørnholm, K. Nørgaard, and B. W. Laursen, Advanced Materials (2012) n/a.

[196] G. Wang, Y. Kim, M. Choe, T.-W. Kim, and T. Lee, Advanced Materials 23 (2011) 683.

[197] R. C. Chiechi, E. A. Weiss, M. D. Dickey, and G. M. Whitesides, Angewandte Chemie International Edition 47 (2008) 142.

[198] H. Yan, A. J. Bergren, and R. L. McCreery, Journal of the American Chemical Society 133 (2011) 19168.

[199] D. A. Corley, T. He, and J. M. Tour, ACS Nano 4 (2010) 1879.

[200] J. Yao, L. Zhong, D. Natelson, and J. M. Tour, Journal of the American Chemical Society 133 (2010) 941.

[201] T. Bhuvana, K. C. Smith, T. S. Fisher, and G. U. Kulkarni, Nanoscale 1 (2009) 271.

[202] A. Salomon, D. Cahen, S. Lindsay, J. Tomfohr, V. B. Engelkes, and C. D. Frisbie, Advanced Materials 15 (2003) 1881.

[203] B. A. Hylke and B. Bert de, Journal of Physics: Condensed Matter 20 (2008) 013001.

[204] V. B. Engelkes, J. M. Beebe, and C. D. Frisbie, Journal of the American Chemical Society 126 (2004) 14287.

[205] G. Wang, T.-W. Kim, Y. H. Jang, and T. Lee, The Journal of Physical Chemistry C 112 (2008) 13010.

[206] D. J. Wold, R. Haag, M. A. Rampi, and C. D. Frisbie, The Journal of Physical Chemistry B 106 (2002) 2813.

[207] F. Bensebaa, T. H. Ellis, A. Badia, and R. B. Lennox, Vol. 13, AVS, Denver, Colorado (USA), 1995, p. 1331.

[208] M. Byloos, H. Al-Maznai, and M. Morin, The Journal of Physical Chemistry B 105 (2001) 5900.

[209] S. Subramanian and S. Sampath, Analytical and Bioanalytical Chemistry 388 (2007) 135.

[210] N. Sandhyarani and T. Pradeep, International Reviews in Physical Chemistry 22 (2003) 221.

[211] Y. Qian, G. Yang, J. Yu, T. A. Jung, and G.-y. Liu, Langmuir 19 (2003) 6056.

[212] H. B. Akkerman, A. J. Kronemeijer, J. Harkema, P. A. van Hal, E. C. P. Smits, D. M. de Leeuw, and P. W. M. Blom, Organic Electronics 11 (2010) 146.

[213] S. A. Joyce, R. C. Thomas, J. E. Houston, T. A. Michalske, and R. M. Crooks, Physical Review Letters 68 (1992) 2790.

[214] D. Devaprakasam and S. K. Biswas, Review of Scientific Instruments 76 (2005) 035102.

[215] G. Oncins, C. Vericat, and F. Sanz, The Journal of Chemical Physics 128 (2008) 044701.

[216] M. Taniguchi and T. Kawai, Physica E: Low-dimensional Systems and Nanostructures 33 (2006) 1.

[217] M. Waleed Shinwari, M. Jamal Deen, E. B. Starikov, and G. Cuniberti, Advanced Functional Materials 20 (2010) 1865.

[218] A. K. Mahapatro, G. U. Lee, K. J. Jeong, and D. B. Janes, Applied Physics Letters 95 (2009) 083106.

[219] V. Ostatna and E. Palecek, Langmuir 22 (2006) 6481.

[220] H. Watanabe, C. Manabe, T. Shigematsu, K. Shimotani, and M. Shimizu, Applied Physics Letters 79 (2001) 2462.

[221] D. Porath, A. Bezryadin, S. de Vries, and C. Dekker, Nature 403 (2000) 635.

[222] C. Thelander, P. Agarwal, S. Brongersma, J. Eymery, L. F. Feiner, A. Forchel, M. Scheffler, W. Riess, B. J. Ohlsson, U. Goesele, and L. Samuelson, Materials Today 9 (2006) 28.

[223] S. R. Gowda, A. Leela Mohana Reddy, X. Zhan, and P. M. Ajayan, Nano Letters 11 (2011) 3329.

[224] C. R. Field, H. J. In, N. J. Begue, and P. E. Pehrsson, Analytical Chemistry 83 (2011) 4724.

[225] D. Choi, M.-Y. Choi, H.-J. Shin, S.-M. Yoon, J.-S. Seo, J.-Y. Choi, S. Y. Lee, J. M. Kim, and S.-W. Kim, The Journal of Physical Chemistry C 114 (2009) 1379.

[226] E. Lai, W. Kim, and P. Yang, Nano Research 1 (2008) 123.

[227] Q. Li and G. T. Wang, Nano Letters 10 (2010) 1554.

[228] S. Xu, Y. Qin, C. Xu, Y. Wei, R. Yang, and Z. L. Wang, Nat Nano 5 (2010) 366.

[229] E. M. Freer, O. Grachev, X. Duan, S. Martin, and D. P. Stumbo, Nat Nano 5 (2010) 525.

[230] L. E. Jensen, M. T. Björk, S. Jeppesen, A. I. Persson, B. J. Ohlsson, and L. Samuelson, Nano Letters 4 (2004) 1961.

[231] S. Roddaro, P. Caroff, G. Biasiol, F. Rossi, C. Bocchi, K. Nilsson, L. Fröberg, J. B. Wagner, L. Samuelson, L.-E. Wernersson, and L. Sorba, Nanotechnology 20 (2009) 285303.

[232] D. Erts, B. Polyakov, B. Daly, M. A. Morris, S. Ellingboe, J. Boland, and J. D. Holmes, The Journal of Physical Chemistry B 110 (2005) 820.

[233] O. Moutanabbir, S. Senz, R. Scholz, M. Alexe, Y. Kim, E. Pippel, Y. Wang, C. Wiethoff, T. Nabbefeld, F. Meyer zu Heringdorf, and M. Horn-von Hoegen, ACS Nano 5 (2011) 1313.

[234] A. A. Talin, B. S. Swartzentruber, F. Leonard, X. Wang, and S. D. Hersee, Journal of Vacuum Science and Technology B 27 (2009) 2040.

[235] A. A. Talin, F. Léonard, A. M. Katzenmeyer, B. S. Swartzentruber, S. T. Picraux, M. E. Toimil-Molares, J. G. Cederberg, X. Wang, S. D. Hersee, and A. Rishinaramangalum, Semiconductor Science and Technology 25 (2010) 024015.

[236] P. Offermans, M. Crego-Calama, and S. H. Brongersma, Nano Letters 10 (2010) 2412.

[237] A. C. E. Chia and R. R. LaPierre, Nanotechnology 22 (2011) 245304.

[238] Y. Tan, J. Gu, X. Zang, W. Xu, K. Shi, L. Xu, and D. Zhang, Angewandte Chemie International Edition 50 (2011) 8307.

[239] D. Ercolani, F. Rossi, A. Li, S. Roddaro, V. Grillo, G. Salviati, F. Beltram, and L. Sorba, Nanotechnology 20 (2009) 505605.

[240] K. Kato, Journal of the Japan Society of Mechanical Engineers 19 (1915) 41.

[241] C. Thelander, K. A. Dick, M. T. Borgström, L. E. Fröberg, P. Caroff, H. A. Nilsson, and L. Samuelson, Nanotechnology 21 (2010) 205703.

[242] G. Rubio-Bollinger, S. R. Bahn, N. Agrait, K. W. Jacobsen, and S. Vieira, Physical Review Letters 87 (2001) 026101.

[243] R. M. Metzger, Journal of Materials Chemistry 18 (2008) 4364.

[244] S. J. Krumbein, IEEE Transactions on Components, Hybrids, and Manufacturing Technology 11 (1988) 5.

[245] B. J. Klein, Journal of Physics F: Metal Physics 3 (1973) 691.

[246] S. Meister, D. T. Schoen, M. A. Topinka, A. M. Minor, and Y. Cui, Nano Letters 8 (2008) 4562.

PART V

Outlook

"In all chaos there is cosmos, in all disorder a secret order" – Carl Jung

The thesis is essentially a detailed description of various methodologies for employing metal-organic complexes as simple single source precursors for producing interesting metal nanostructures and functional nanomaterials in patterns. The last part of the thesis has dealt with realising prototype devices from the various functional nanostructures thus made.

The chemistry of metal organic complexes in the form of crystals and films is a field by itself and has reached its maturity in the last few decades. Using such complexes for direct preparation of specific inorganic compounds is also well known. Various nanomaterials such as metals, oxides, nitrides and sulphides etc., synthesized through these routes are being utilized in applications. This thesis work makes a step forward - by employing the metal-organic complexes in lithography and realising their active response and participation in lithography processes. Some complexes have been tried out for nanomaterial synthesis for the first time. Anisotropic giant metal nanostructures may be considered as useful by-product of these studies!

There are some untied knots or possibilities which deserve continued exploration. For instance, extending sub-micron resolution achieved with direct write lithography methods as detailed in Part III, to finer resolutions (sub-20 nm) is clearly a possibility. This is otherwise challenging with conventional lift-off resist lithography technology. On the other hand, with direct write resists, employing high resolution charged particle beam techniques such as electron beam lithography or helium ion beam lithography, one can try to make sub-20 nm devices. The other aspect which may blossom into a full study is tuning the nature of the active material by employing known/new chemical recipes, thereby achieve new functionality with devices. Such active materials with well-defined composition, devoid of unwanted defects become amenable to study quantum confinement effects. Another important aspect that could be carried further is to improve the density of devices by vertical stacking using sequential lithography steps, which remains till date as big puzzle with conventional methods.

There are few subtle observations which perhaps deserve more attention. While this work focuses on the end product from a metal-organic precursor, the intermittent phases which occur during conversion under lithography or subsequent processes might be equally interesting because of the disorder. There is nonetheless some mention in this thesis too. For instance, strain sensors and non-volatile memory devices that are presented in Part IV.1 and Part IV.4, are clearly a result of a semi-thermolysed state of the metal-organic complex. It appears that there may be ample opportunities to revisit and derive new functionalities from these processes, dealing with highly non-stoichiometric and disordered phases. Another important aspect is that the feature sizes reported in the thesis are not restrictive by any means; improved lithography tools should take the feature sizes much lower than reported. The above two aspects with greater physical insight may open new horizons in device fabrication.

There are certainly some new directions and additional thoughts which could have substantiated the device section. For the nanoparticle rectifier presented in Part IV.5, the mechanism of asymmetric rectification proposed through an otherwise symmetric device, can be verified by changing the nanoparticle system to being of other metal, say Pd. With respect to molecular electronics, statistical device to device variability and up-scaling the fabrication protocol for making the molecular devices will enable decent addition to the existing technology.

List of Publications

From Thesis work

1. **An electrical rectifier based on Au nanoparticle array fabricated using direct–write EBL**
   B. Radha and G. U. Kulkarni
   Advanced Functional Materials, accepted (2012), doi: 10.1002/adfm.201103170

2. **Large area ohmic top contact to vertically grown InAs NWs using a free-standing mesoscopic Au electrode**
   B. Radha, Deepak Jayaraj, Stefan Heun and G. U. Kulkarni
   ACS Applied Materials and Interfaces, accepted (2012), doi: 10.1021/ am300063j

3. **Giant single crystalline Au microplates**
   B. Radha and G.U. Kulkarni
   Current Science (Special section: Nanomaterials)*, (2012), 102, 70

4. **Metal anion-alkyl ammonium complexes as direct write precursors to produce nanopatterns of metals, nitrides, oxides, sulfides and alloys**
   B. Radha, S. Kiruthika and G. U. Kulkarni,
   Journal of American Chemical Society, (2011), 133, 12706

5. **Flexible and semitransparent strain sensors based on micromolded Pd nanoparticle–carbon μ-stripes**
   B. Radha, Abhay A. Sagade and G. U. Kulkarni,
   ACS Applied Materials and Interfaces, (2011), 3, 2173

6. **Direct micromolding of Pd μ-stripes for electronic applications**
   B. Radha, Abhay A. Sagade, Ritu Gupta and G. U. Kulkarni
   Journal of Nanoscience and Nanotechnology, (2011), 11, 1-6

7. **A Real time microscopy study of the growth of giant Au microplates**
   B. Radha and G. U. Kulkarni
   Crystal Growth and Design, (2011), 11, 320

8. **Movable Au microplates as fluorescence enhancing substrates for live cells**
   B. Radha, M. Arif, R. Datta, T. K. Kundu and G. U. Kulkarni
   Nanoresearch, (2010), 3, 738
   (Highlighted in sciencia.org and Vertical News;
   http://www.verticalnews.com/article.php?articleID=4689669)

9. **Intricate nature of Pd nanocrystal–hydrogen interaction investigated using thermolysed Pd hexadecylthiolate films**.
   Abhay A. Sagade*, **B. Radha***, G. U. Kulkarni (* Equal contribution)
   Sensors and Actuators B, (2010), 149, 345

10. **Micro- and Nanostripes of Self-assembled Au Nanocrystal Superlattices by Direct Micromolding**
    B. Radha and G. U. Kulkarni
    Nanoresearch, (2010), 3, 537
    (Highlighted in Vertical News,
    http://www.verticalnews.com/premium_newsletters/Nanotechnology-Weekly/2010-09-13/65900NA.html)

11. **Patterned synthesis of Pd₄S: chemically robust electrodes and conducting etch masks**
    B. Radha and G. U. Kulkarni
    Advanced Functional Materials, (2010), 20, 879
    (Highlighted in Vertical News http://www.verticalnews.com/article.php?articleID=3676463)

12. **A modified micromolding method for sub-100 nm direct patterning of Pd nanowires**
    B. Radha and G. U. Kulkarni
    Small, (2009), 5, 2271
    (*Research highlight* on this article appeared in **Lab on a chip** 2009, 9, 2623)

13. **Dewetting assisted patterning of polystyrene by soft lithography to create nanotrenches for nanomaterial deposition**
    B. Radha and G. U. Kulkarni,
    ACS Applied. Materials and Interfaces, (2009), 1, 257

14. **Large area 2D and 3D imprinting of Pd metal by NIL**
    B. Radha, S. H. Lim, M S M Saifullah and G. U. Kulkarni, 2012 (under preparation)

15. **Non-volatile multiple state memory devices made of metal organic complex**
    B. Radha, Abhay A. Sagade and G. U. Kulkarni, 2012 (under preparation)

16. **Free standing Au microelectrodes for molecular electronics**
    B. Radha, Deepak Jayaraj and G. U. Kulkarni, 2012 (under preparation)

17. **UV induced ablation of metal organic complex: Versatile applications**
    B. Radha, P K Dwivedi, A. Sharma and G.U. Kulkarni, 2012 (under preparation)

18. **Simple method of creating palladium nanostructures for sensing low hydrogen concentration**
    S. H. Lim, **B. Radha,** M S M Saifullah and G. U. Kulkarni, 2012 (under preparation)

19. **Pd-Carbon Nanotube composite films as Transparent Conducting Electrodes**
    K. C. Smith, **B. Radha,** T.S. Fisher and G.U. Kulkarni, 2012 (under preparation)

Reviews / Book chapters

1. **Metal nanowire grating patterns**
   G. U. Kulkarni and **B. Radha**
   Nanoscale (Invited review), (2010), 2, 2035

2. **Micromolding (Book Chapter)**
   B. Radha and G. U. Kulkarni in Book: Micromanufacturing Processes
   Editor – V. K. Jain, *Taylor and Francis Publishers* (Submitted 2011)

3. **Single Source precursors for single step lithography**
   B. Radha and G. U. Kulkarni, 2012 (Invited review, under preparation)

Patents filed

1. **"Formation of Palladium Sulfide**"
   B. Radha and G. U. Kulkarni, US patent, Application No.12/881, 700
   Date of Filing - September 14, 2010

2. **"Manufacturing Strain Sensitive Sensors and/or Strain Resistant Conduits from a Metal and Carbon Matrix"**
   B. Radha, Abhay A. Sagade and G. U. Kulkarni, International patent, Application No. 1940/CHE/2011; Date of Filing - June 07, 2011

Other Publications

1. **Metallic conduction in NiS$_2$ nanocrystalline structures**
   K. D. M. Rao,* T. Bhuvana,* **B. Radha,** N. Kurra, N. S. Vidhyadiraja and G.U. Kulkarni (* Equal contribution)
   Journal of Physical Chemistry C, (2011), 115, 10462

2. **Inkjet printing of palladium alkanethiolates for facile fabrication of metal interconnects and surface-enhanced Raman scattering substrates**
   T. Bhuvana,* W. Boley,* **B. Radha**, B.D. Dolash, G. Chiu, D. Bergstrom, R. Reifenberger, T.S. Fisher and G.U. Kulkarni (* Equal contribution)
   Micro & Nano Letters, (2010), 5, 296

3. **Pd-Assisted Growth of InAs Nanowires**
   Stefan Heun, **Boya Radha**, Daniele Ercolani, Giridhar U. Kulkarni, Francesca Rossi, Vincenzo Grillo, Giancarlo Salviati, Fabio Beltram and Lucia Sorba
   Crystal Growth and Design, (2010), 10, 4197

4. **Coexistence of Vapor-Liquid-Solid and Vapor-Solid-Solid Growth Modes in Pd-Assisted InAs Nanowires**
   Stefan Heun, **Boya Radha**, Daniele Ercolani, Giridhar U. Kulkarni, Francesca Rossi, Vincenzo Grillo, Giancarlo Salviati, Fabio Beltram and Lucia Sorba
   Small, (2010), 6, 1935

5. **Functionalized Au$_{22}$ clusters: Synthesis, characterization and patterning**
   E. S. Shibu, **B. Radha**, P. Bhyrappa, G. U. Kulkarni and T. Pradeep,
   ACS Applied. Materials and Interfaces, (2009), 1, 2199

* * *